Modelling of Geochemical Reactions during CO_2 WAG Injection in Carbonate Reservoirs

Ayrton S. Ribeiro

Submitted for the degree of

Doctor of Philosophy in Petroleum Engineering

Heriot-Watt University

School of Energy, Geosciences, Infrastructure and Society

Institute of Petroleum Engineering

December 2017

Universidade Federal de Pernambuco

Centro de Tecnologia e Geociências

Departamento de Engenharia Civil

Ayrton S. Ribeiro

Modelling of Geochemical Reactions during CO_2 WAG Injection in Carbonate Reservoirs

Recife, 2017

ABSTRACT

In this thesis calcite dissolution and precipitation are investigated during injection of CO_2 WAG (water alternating gas) in limestone oil reservoirs. First, the equilibrium between calcite and the carbonic acid system is studied in a static environment to understand how variations in chemical composition, temperature and pressure affect the mineral reactions. Then, four models of CO_2 solubility are presented (PHREEQC, CMG GEM, Duan & Sun and Diamond & Akinfiev) and compared against experimental data from the literature. An empirical model that couples the CO_2 solubility to the mineral and aqueous reactions is constructed. After that, reactive transport simulations are performed using PHREEQC and GEM. The injection of carbonated water in a limestone reservoir is simulated with PHREEQC to assess the behaviour of calcite reactions. The obtained results are explained and also observed in a similar model using GEM. Additional simulations are performed in GEM concerning single-phase injection (seawater and pure CO2 injections) and their analyses are used to assist in the interpretation of the more complex CO2 WAG and CO2 SWAG (simultaneous water and gas injection). Different WAG slug sizes are simulated and simple relationships between the WAG ratio (volumetric ratio between injected water and injected gas at reservoir conditions) and the dissolved calcite are determined. Sensitivity of the porosity change and scale deposition is assessed during grid refinement. A dissolution zone around the injector wellbore is obtained for the WAG process that is dependent on the WAG scheme. Later, reactive transport simulations performed in GEM are extended to 3-phase non-isothermal flow in 2D and re-analysed. The impact of heat exchange on the dissolution is investigated for different time step sizes. More WAG scenarios are simulated and a relationship between the WAG scheme and dissolution similar to 1D simulations is obtained. The final model is completed by adding layers with different properties to investigate how the communication between layers affects the reactions. The dissolution zone and porosity increase are determined based on the flow capacities and front velocities of the layers, while the depth of more sever scale risks are located by considering also the gravity segregation of injected fluids. Finally, different geological scenarios, well operations and initial reservoir conditions are simulated.

RESUMO

Nesta tese, a dissolução e precipitação de calcita são investigadas durante a injeção de CO_2 WAG (gás e água alternados) em reservatórios carbonáticos de petróleo. Primeiro, o equilíbrio entre a calcita e o sistema de ácido carbônico é estudado em um ambiente estático para entender como as variações na composição química, temperatura e pressão afetam as reações minerais. Em seguida, são apresentados quatro modelos de solubilidade do CO_2 (PHREEQC, CMG GEM, Duan & Sun e Diamond & Akinfiev) e comparados com dados experimentais da literatura. É construído um modelo empírico que combina a solubilidade em CO_2 com as reações minerais e aquosas. Depois disso, simulações de transporte reativo são realizadas usando PHREEQC e GEM. A injeção de água carbonatada em um reservatório de calcário é simulada com PHREEQC para avaliar o comportamento das reações de calcita. Os resultados obtidos são explicados e também observados em um modelo similar usando GEM. Simulações adicionais são realizadas no GEM sobre injeção monofásica (injeções de água do mar e de CO_2 puro) e suas análises são usadas para auxiliar na interpretação do mais complexo CO_2 WAG e do CO_2 SWAG (injeção simultânea de água e gás). Diferentes tamanhos de bancos de WAG são simulados e relações simples entre a razão WAG (razão volumétrica entre água injetada e gás injetado nas condições de reservatório) e a calcita dissolvida são determinadas. A sensibilidade da variação da porosidade e da deposição de incrustações é avaliada durante o refinamento da malha. É obtida uma zona de dissolução em torno do poço injetor para o processo WAG que depende do esquema WAG. Mais tarde, as simulações de transporte reativo realizadas no GEM são ampliadas para o fluxo não-isotérmico trifásico em 2D e reanalisadas. O impacto da troca de calor na dissolução é investigado para diferentes tamanhos de passo de tempo. Mais cenários WAG são simulados e é obtida uma relação entre o esquema WAG e a dissolução semelhante às simulações 1D. O modelo final é completado pela adição de camadas com diferentes propriedades para investigar como a comunicação entre camadas afeta as reações. A zona de dissolução e o aumento da porosidade são determinados com base nas capacidades de fluxo e nas velocidades das frentes das camadas, enquanto a profundidade das incrustações de risco mais severo é localizada ao considerar também a segregação gravitacional dos fluidos injetados. Finalmente, diferentes cenários geológicos, operações de poço e condições iniciais de reservatório são simulados.

To Alessandra, my wife

ACKNOWLEDGMENTS

"A journey of a thousand miles begins with a single step" says the Chinese proverb. Indeed, after completing a decade of studies in four different universities, I recall my first step in this long journey to achieve the degree of Doctor. I started in the department of Physics in UFPA (Brazil) and knew that the path to develop a career in research is not only long but also plenty of difficulties (academic, financial and administrative). The passion for science is what motivates someone to become a scientist, however, only through hard work and persistence one can have success in this path (as in many other career paths, I suppose). Thankfully, there were always inspiring teachers and helpful friends to strengthen my (distinctly ambitious) desire to reach my goals without losing my soul to greed or selfishness. In this short text, I thank the men and women who provided aid, support and friendship in these four years of PhD training.

First, I would like to thank my primary supervisors Leonardo Guimarães and Eric Mackay for introducing me to petroleum engineering and for the training in reservoir simulation and reactive transport. Together with Patrick Corbett, their pursuit of establishing a dual-degree PhD between UFPE and HWU made it possible that I could flew over the Atlantic to achieve international experience and build skills within academic teams of different expertise.

In this sense, I appreciate the financial support of the Foundation CMG (Calgary, Canada), which filled the gap left by an oil company and provided funding during the entire PhD. The Foundation CMG was also important in creating links between partner universities through its annual summit, where I presented my work and met outstanding professors and students.

At UFPE, I must say thanks to my colleagues and friends, especially Aldemir and Rafael. I enjoyed our talks between classes, which ranged from math and computer coding to philosophy and politics. I also acknowledge the department infrastructure and personnel for providing the classes and software required for learning the fundamentals of reservoir engineering and for performing my first simulations. This basic training was very valuable to me for I could start researching on my PhD topic as soon as I arrived at HWU.

At HWU, I arrived just before the 40-years celebration of the Institute of Petroleum Engineering and enjoyed its cumulative experience in many topics as well as its international community. In the group I was part of (Flow Assurance and Scale Team – FAST) I could learn different topics related to scale deposition in a diverse and multicultural group of PhD students and university staff that spans over Europe and Asia. I thank everyone especially the recent doctors Yisheng and Duarte, for the many discussions on reactive transport simulations and for showing that there is life beyond a PhD.

I thank my parents and my brother for this bond of mutual inspiration needed to surpass all the challenges that life has given us. I thank my wife for motivating me to be a better man through her precious love and kindness.

Finally, I recall that the word “Doctor” descends from Latin (*docere*) and means “to teach”. It is a privilege to teach, i.e. to help different individuals to achieve personal development and to grow in the understanding of the different phenomena, which may be ruled by laws of nature or the laws of men. A Doctor or PhD must hold this very close to the heart since the research activity serves as a reminder that the learning process is endless: new findings are constantly being taught from scientists to their peers and to the society in general. To me, it is very fortunate that in the year I complete my PhD is also the time I discover I am going to be a father, for now I have the opportunity and skills to provide service to the ones who need knowledge, starting with my son.

HERIOT WATT UNIVERSITY

ACADEMIC REGISTRY
Research Thesis Submission

Name:	AYRTON SOARES RIBEIRO		
School:	EGIS / IPE		
Version: *(i.e. First, Resubmission, Final)*	Final	Degree Sought:	PhD in Petroleum Engineering

Declaration

In accordance with the appropriate regulations I hereby submit my thesis and I declare that:

1) the thesis embodies the results of my own work and has been composed by myself
2) where appropriate, I have made acknowledgement of the work of others and have made reference to work carried out in collaboration with other persons
3) the thesis is the correct version of the thesis for submission and is the same version as any electronic versions submitted*.
4) my thesis for the award referred to, deposited in the Heriot-Watt University Library, should be made available for loan or photocopying and be available via the Institutional Repository, subject to such conditions as the Librarian may require
5) I understand that as a student of the University I am required to abide by the Regulations of the University and to conform to its discipline.
6) I confirm that the thesis has been verified against plagiarism via an approved plagiarism detection application e.g. Turnitin.

* *Please note that it is the responsibility of the candidate to ensure that the correct version of the thesis is submitted.*

Signature of Candidate:	Ayrton Ribeiro	Date:	

Submission

Submitted By *(name in capitals)*:	
Signature of Individual Submitting:	
Date Submitted:	

For Completion in the Student Service Centre (SSC)

Received in the SSC by *(name in capitals)*:			
Method of Submission *(Handed in to SSC; posted through internal/external mail)*:			
E-thesis Submitted ***(mandatory for final theses)***			
Signature:		Date:	

Please note this form should be bound into the submitted thesis.

TABLE OF CONTENTS

LIST OF PUBLICATIONS BY THE CANDIDATE

RIBEIRO, A. S., MACKAY, E. J., & GUIMARÃES, L. 2016. Predicting Calcite Scaling Risk Due to Dissolution and Re-Precipitation in Carbonate Reservoirs during CO_2 Injection. Presented at SPE International Oilfield Scale Conference and Exhibition, Aberdeen, UK, 11-12 May. SPE-179884-MS

RIBEIRO, A. S., SILVA, D., MACKAY, E. J., & SORBIE, K. S. 2016. The Impact of Vapour-Liquid Equilibria VLE Calculations on Scale Prediction Modelling. Presented at SPE International Oilfield Scale Conference and Exhibition, Aberdeen, UK, 11-12 May. SPE-179885-MS.

JIN, M., **RIBEIRO, A.**, MACKAY, E., GUIMARÃES, L., & BAGUDU, U. 2016. Geochemical modelling of formation damage risk during CO2 injection in saline aquifers, *Journal of Natural Gas Science and Engineering*, 35, Part A, 703-719, ISSN 1875-5100.

RIBEIRO, A. S., SILVA, D., MACKAY, E. J., & SORBIE, K. S. 2017. The Impact of Vapour-Liquid Equilibria VLE Calculations on Scale Prediction Modelling. *SPE Production & Operations*. SPE-179885-PA.

RIBEIRO, A. S., MACKAY, E. J., GUIMARÃES, L., JORDAN, M. & FELLOWS, S. 2017. Scale Risk Management during CO2 WAG in Carbonate Formations. Presented at the 19th European Symposium on Improved Oil Recovery, Stavanger, Norway, 24-27 April 2017.

LIST OF NOMENCLATURE

AIM	adaptive-implicit method
ARD	Advection-Reaction-Dispersion equation
B-dot	Activity model for moderate salinity
CFL	Courant–Friedrichs–Lewy condition
CMG	Computer Modeling Group
Da_I	Damköhler number for advection transport
Da_{II}	Damköhler number for diffusion transport
Debye-Hückel	Activity model for dilute solutions
EOS	equation of state
EOR	enhanced oil recovery
GEM	Compositional Reservoir Simulator, commercial
MatLab™	mathematical software, commercial
Pe	Peclet number
Pitzer	Activity model for high pressure, high temperature and high salinity
PHREEQC	Thermodynamic software, open-source
PV	pore volume or time required for injecting the volume of fluid stored in the reservoir
SWAG	simultaneous water and gas injection
THC	Thermo-Hydro and Chemical coupled transport
THMC	Thermo-Hydro-Mechanical and Chemical coupled transport
WAG	water alternating gas
WAG cycle	time for injecting a pair of water and gas slugs during WAG
WAG ratio (or W_R)	ratio between the volumes of injected water and injected gas at reservoir conditions
WINPROP	PVT Software, commercial

Chapter 1:
Introduction

Carbonate reservoirs retain porosity and permeability characteristics at great depths and therefore are of importance in the exploitation of deeper reservoirs. Consisting mainly of limestone and dolomite (calcium and magnesium carbonates), carbonate reservoirs are typically more geochemically reactive than sandstone reservoirs. Understanding the chemical interaction between carbonate rocks and carbon dioxide (CO_2) in the aqueous phase has been shown to be very important during continuous CO_2 gas injection, carbonated water injection or CO_2 water alternating gas (CO_2 WAG) injection processes (Svec and Grigg, 2001). In regions with high concentrations of CO_2, calcite ($CaCO_3$) will dissolve, increasing the porosity and permeability of the rock. On the other hand, in regions of high Ca concentrations, calcium carbonate precipitates, plugging the pores (Smith et al., 2013). While mineral precipitation can reduce reservoir porosity and permeability and also severely block wellbores (known as scale deposition), high dissolution of the rock matrix can put the wellbore integrity at risk of collapse and also cause CO_2 leakage.

Moreover, as the majority of oil industry knowledge relative to scale management was developed predominantly from sandstone data and applied to sandstone reservoirs, investigation must be carried out to address the specific phenomena related to carbonate reservoirs.

This is important for deepwater projects located in regions like the North Sea or the Campos Basin (Brazil), which had experienced injection of seawater for many years, as scale deposition occurs after many volumes of water are produced. Carbonate scales are precipitated during pressure decrease and temperature increase, and may block and damage equipment such as Venturi flow meters and ESPs (Electric Submersible Pump) (Graham et al., 2002). A North Sea scale prevention treatment will typically have an operational cost of 207 thousand pounds per day plus 2.7 pounds per liter of scale inhibitor used, and takes around 13 months to be complete (Vazquez et al., 2017). In this sense modelling and prediction of scale formation is relevant for reducing the cost

of treatment by using appropriate MICs (minimum inhibitor concentration) before the scale risk becomes severe and damage to equipment occur.

Concerning WAG projects, literature review (Christensen et al., 1998) shows that from 1955 to 1996, out of 59 studies involving field data worldwide, only 11 were reported as either limestones or carbonates formations, while only three studies of this subset had CO_2 as the injected gas. It was also revealed that 12 fields were reported as dolomite and 11 of them had CO_2 flooding.

In a more recent review, Manrique et al. (2007) showed that among 59 CO_2 EOR (continuous or WAG injection) projects in the USA, 39 are in dolomite formations without limestone. This lack of field experience in CO_2 flooding in limestone formations suggests that more research should be conducted to obtain better understanding of mineral reactions during CO_2 WAG in carbonates, since dolomite reacts one order of magnitude slower than calcite (the dominant mineral in limestones) (Pokrovsky et al., 2001). Moreover, CO_2 WAG flooding increases the reactivity of carbonates because of larger contact zones between fluid phases (Qiao et al., 2016).

In this sense, a reactive transport model is a valuable tool to obtain understanding about calcite reactions during CO_2 WAG injection because it can predict them in different scenarios of high pressure or high temperature that are difficult or expensive to investigate experimentally in laboratory conditions or in the field. Moreover, this research can be used to advise operators about possible effects related to fluid-rock interactions in carbonate reservoirs which have calcite as primary rock mineral.

1.1. Problem Statement and Objectives

From the start of the CO_2 injection into a carbonate oil reservoir, dissolution and precipitation of calcite can happen anywhere within the flow path of the injected fluids. The mineral reactions are affected by the physical conditions imposed on the water present in the pores (temperature, pressure and aqueous concentrations). In particular, the pressure is an important variable since its gradient between wells determines the flow according to Darcy´s Law (Bear, 1972; Fanchi, 2006; Chen et al., 2006). Moreover, the enlargement (or shrinkage) of the pores via dissolution (or precipitation) of the rock matrix increases (or decreases) both porosity and permeability, and then either the pressure gradient is altered to maintain the flow rate or the flow rate changes. These mineral reactions may pose problems with injectivity and also scale precipitation

in the producer well, leading to loss of productivity. Therefore, the mineral reactions and the pressure gradient are mutually affected by each other and their behaviour need to be considered simultaneously to improve the understanding of the fluid flow in carbonate reservoirs.

The alternate injection of CO_2 gas and seawater, as a CO_2 WAG process, adds more complexity to the development of carbonate oil reservoirs. First, the switching between water and gas cycles causes oscillations in the pressure and flow rate because the injected fluids have distinct mobilities (i.e. relative permeability divided by viscosity). In addition, gravity segregation can occur since the CO_2 is less dense than seawater (and oil) in most reservoir conditions. Moreover, since the injected fluids reach the reservoir at a higher temperature, heat exchange is constantly happening because the injected fluids (especially water) extract heat from the reservoir rock as they propagate from cooler to warmer regions. These changes in temperature disturb the flow behaviour not only by modifying the physical properties of the fluids such as density and viscosity, but also by enhancing the calcite dissolution and precipitation processes initially caused by the pressure gradient.

In this work, we study the calcite dissolution and precipitation caused by the injection of CO_2 WAG in carbonate oil reservoirs. The precipitation of calcite around the producer wellbore (scale deposition) is of particular interest since most of the literature on scale management refers to injection of seawater only and little attention has been given to the fluid-fluid interactions of CO_2 EOR from the point of view of mineral reactions. Our objective is to answer the following:

- What impacts scale deposition during CO_2 WAG?
- How to model calcite reactions in 3D models of carbonate oil reservoirs?

More importantly, the novelty of this work is a strong understanding of the precipitation of calcite during different flow conditions within CO_2 WAG projects. In addition, we study the porosity increase around the injector, as well as the scale deposition around the producer, caused by different WAG schemes (injection rate and slug sizes). Both dissolution and precipitation are investigated under extreme conditions of pressure (500 to 1000 bar). This pressure range is higher than the values used in similar simulation studies (Wellman et al., 2003, Mohamed and Nasr-El-Din, 2013 and Qiao et al., 2016), which favours the dissolution of CO_2 in water and enhances the calcite reactions. Finally, the analysis of reactions is performed in multiple model

geometries (1D, areal 2D and 3D) and includes gravity segregation, therefore this work goes beyond Mackay and Souza (2014).

1.2. Methods

Our approach of investigation is computational. We chose to perform thermodynamic modelling using PHREEQC (version 3) and reactive transport simulation at reservoir conditions using CMG GEM.

PHREEQC is an open-source software (Parkhurst and Appelo, 2013) which can model accurately aqueous and mineral reactions with a wide range of pressure (up to 1000 atm), temperature (0 to 200 ℃) and salinity (up to 6 molal). In addition, the software considers the Peng-Robinson equation of state to provide CO_2 solubility at high pressure and high salinity (Appelo et al., 2014). The third version of PHREEQC relies on the Pitzer activity model (Pitzer, 1973; Harvie et al., 1984) to produce its high quality equilibrium calculations at extreme conditions. However, PHREEQC reactive flow simulations are limited to the transport of water in unidimensional models.

Thus, we performed reactive transport simulations using CMG GEM, which is a compositional reservoir flow simulator (GEM Manual, 2014) that enables multiphase and multicomponent reactive transport. GEM solves flow equations for water, gas and oil phases numerically using finite-differences approximations. At each iteration, the software is able to solve simultaneously algebraic system of equations to find the chemical equilibrium state for aqueous species as well as for gaseous dissolution/evolution. Moreover, mineral reactions can be modelled using a kinetic law that calculates the change in moles of mineral. The porosity is modified automatically by dividing the variation in moles by the molar density, while permeability can be updated following an empirical law, such as Carman-Kozeny (Bear, 1972; GEM Manual, 2014). Finally, the software has an optional feature of non-isothermal flow simulation that allows heat exchange between fluid components and the porous rock. All these features were used in this work.

1.3. Thesis Outline

The thesis is organised in Chapters of increasing complexity of the flow behaviour. In Chapter 2, we present the chemical reactions that are related to the dissolution of CO_2 in water, known as the carbonic acid system, and how the calcite dissolution reaction is affected by CO_2 and its dissociated ions.

In Chapter 3, there is a study of the CO_2 solubility in water, which includes a comparison between four solubility models (GEM, PHREEQC, Duan & Sun and Diamond & Akinfiev) and experimental data from the literature. After that, reactive transport simulations are performed in subsequent Chapters.

In Chapter 4, we simulate the transport of water and gas in 1D models of limestone reservoir. We simulate injection of seawater, CO_2 gas, carbonated water, CO_2 SWAG (simultaneous water and gas injection) and CO_2 WAG to understand how CO_2 EOR processes cause dissolution of the rock matrix and when and why calcite scale is formed in the producer. Moreover, we simulate several scenarios of different WAG schemes (i.e. different slug sizes) to investigate how the calcite dissolution rate is affected. The sensitivity of the results under grid refinement is analysed.

Then, in Chapter 5, we upgrade the simulations to include an oil phase and perform the 3-phase transport in 2D (a quarter of five-spot scheme) with heat exchange between fluid components and the reservoir rock. The impact of temperature on the reactions is evaluated for different time step sizes. More WAG scenarios are simulated to investigate the dissolution zone around the injector and the reaction rate around the producer during multiphase flow.

In Chapter 6, the model is completed by extension to 3-phase transport in 3D with heat exchange and water vapourisation. We observe the EOR mechanisms of oil vapourisation and gas condensation, which enable the extraction of lighter hydrocarbon components. The impact of vertical cross-flow on the reactions is studied. Scenarios are simulated with different layer configurations (relative position of the less permeable layers), well operations (injection rate and WAG scheme) and initial reservoir conditions (temperature, pressure and salinity).

Finally, Chapter 7 includes the conclusions of this work as well as recommendations for future work in the field of mineral reactions during the development of carbonate oil reservoirs.

Chapter 2:

Modelling of $CaCO_3$ and CO_2 interactions in water

To understand the causes of the mineral reactions during CO_2 WAG in carbonate oilfields, as well as its consequences, one needs first to acknowledge the interactions of calcite ($CaCO_3$) with CO_2 in a static environment, which requires the presence of water to occur. In this Chapter, we present the relevant aqueous and mineral reactions that happen when both CO_2 gas and $CaCO_3$ are dissolved into water.

2.1. The Carbonic Acid System

When gaseous CO_2 is injected in a waterflooded reservoir, part of it dissolves in the aqueous phase and becomes $CO_{2(aq)}$. A small amount of this aqueous species can associate with water to form carbonic acid:

$$CO_{2(g)} \rightarrow CO_{2(aq)} \tag{2.1}$$

$$CO_{2(aq)} + H_2O \rightarrow H_2CO_3 \tag{2.2}$$

In fact, at standard conditions, the concentration of $CO_{2(aq)}$ is about 600 times higher than its associated acid (Appelo and Postma, 2013). To facilitate calculations hereinafter we write $CO_{2(aq)}$ as an approximation of itself plus the carbonic acid and neglect the above chemical reaction.

The carbonic acid system, i.e. the chemical interactions between $CO_{2(aq)}$ and water, can be represented by the following chemical reactions involving ionized carbon species produced via acid dissociation:

$$CO_{2(aq.)} + H_2O = H^+ + HCO_3^- \tag{2.3}$$

$$HCO_3^- = H^+ + CO_3^{-2} \tag{2.4}$$

If we take the associated equilibrium relations, we can build relations between the carbon species according to the pH in equilibrium:

$$K_1 = \frac{[H^+][HCO_3^-]}{[CO_{2(aq)}]} \quad \Rightarrow \quad \frac{[HCO_3^-]}{[CO_{2(aq)}]} = K_1 \times 10^{pH} \tag{2.5}$$

$$K_2 = \frac{[H^+][CO_3^{-2}]}{[HCO_3^-]} \quad \Rightarrow \quad \frac{[CO_3^{-2}]}{[HCO_3^-]} = K_2 \times 10^{pH} \tag{2.6}$$

Here, $[\cdot]$ is a thermodynamic concentration called activity and they are equal to the product of molal concentration (or molality) $m_{\cdot}$ and an activity coefficient $\gamma_{\cdot}$, both associated to the measured ion. The activity coefficient accounts for the interactions of the measured ion with the solution and other ions, which is calculated by an activity model such as Debye-Hückel or Truesdell-Jones (B-dot). However, the Pitzer activity model is a more advanced model for concentrated solutions (> 1 molal) because it incorporates the interaction between triples and pairs of ions.

The K_i is an equilibrium constant and relates the product of activities for a fixed temperature and pressure. For reactions (2.3) and (2.4) the equilibrium constants change slightly $(-1 < \Delta \log K_i < 1$, for for $T(°C) \in [0{,}150]$ and $P(atm) \in [1{,}1000])$, as shown in Figure 2.1.

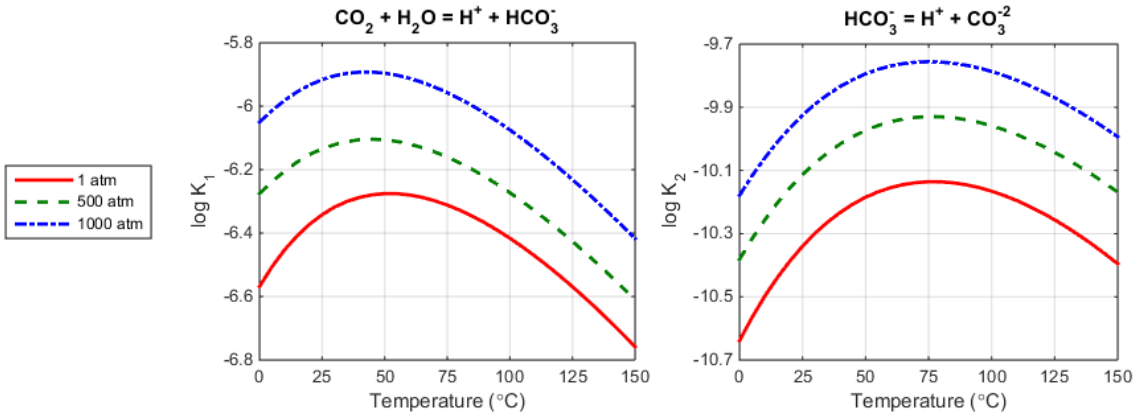

Figure 2.1. Equilibrium constants for the carbonic acid dissociations with varying temperatures and different pressures (calculated using PHREEQC).

Thus, for $K_1 = 10^{-6.3}$ and $K_2 = 10^{-10.3}$ we find

$$\frac{[HCO_3^-]}{[CO_{2(aq)}]} = 10^{pH-6.3} \quad ; \quad \frac{[CO_3^{-2}]}{[HCO_3^-]} = 10^{pH-10.3} \tag{2.7}$$

If we neglect a species when the ratios between it and the others are larger than two orders of magnitude, we get:

For $pH < 4.3$ HCO_3^-, CO_3^{-2} are negligible;

For $4.3 < pH < 8.3$ CO_3^{-2} is negligible;

For $8.3 < pH < 12.3$ $CO_{2(aq)}$ is negligible;

For $12.3 < pH$ $CO_{2(aq)}$, HCO_3^- are negligible.

The dominance of each species with respect to pH can be visualised by plotting the three speciation factors (α_j), i.e. the ratio between each molality (m_j) and the Total Inorganic Carbon (*TIC*) dissolved (Appelo and Postma, 2013; Langmuir, 1997). The α_j can be calculated as follows:

$$m_{CO_2} + m_{HCO_3^-} + m_{CO_3^{-2}} = TIC \tag{2.8}$$

$$\frac{[CO_{2(aq)}]}{\gamma_0} + \frac{[HCO_3^-]}{\gamma_1} + \frac{[CO_3^{-2}]}{\gamma_2} = TIC \tag{2.9}$$

To obtain $\alpha_{HCO_3^-}$, we write all activities in terms of $[HCO_3^-]$ using (2.5) and (2.6)

$$[HCO_3^-]\left(\frac{[H^+]}{\gamma_0 K_1} + \frac{1}{\gamma_1} + \frac{K_2}{\gamma_2[H^+]}\right) = TIC \tag{2.10}$$

$$\alpha_{HCO_3^-} = \frac{\gamma_0\gamma_2[H^+]}{C_T}, \tag{2.11}$$

where $C_T = \gamma_1\gamma_2 K_1^{-1}[H^+]^2 + \gamma_0\gamma_2[H^+] + \gamma_0\gamma_1 K_2$.

Similarly for the others:

$$\alpha_{CO_{2(aq)}} = \frac{\gamma_1\gamma_2 K_1^{-1}[H^+]^2}{C_T} \tag{2.12}$$

$$\alpha_{CO_3^-} = \frac{\gamma_0\gamma_1 K_2}{C_T} \tag{2.13}$$

In Figure 2.2, we show the speciation factors for the ideal case ($\gamma_j \rightarrow 1$).

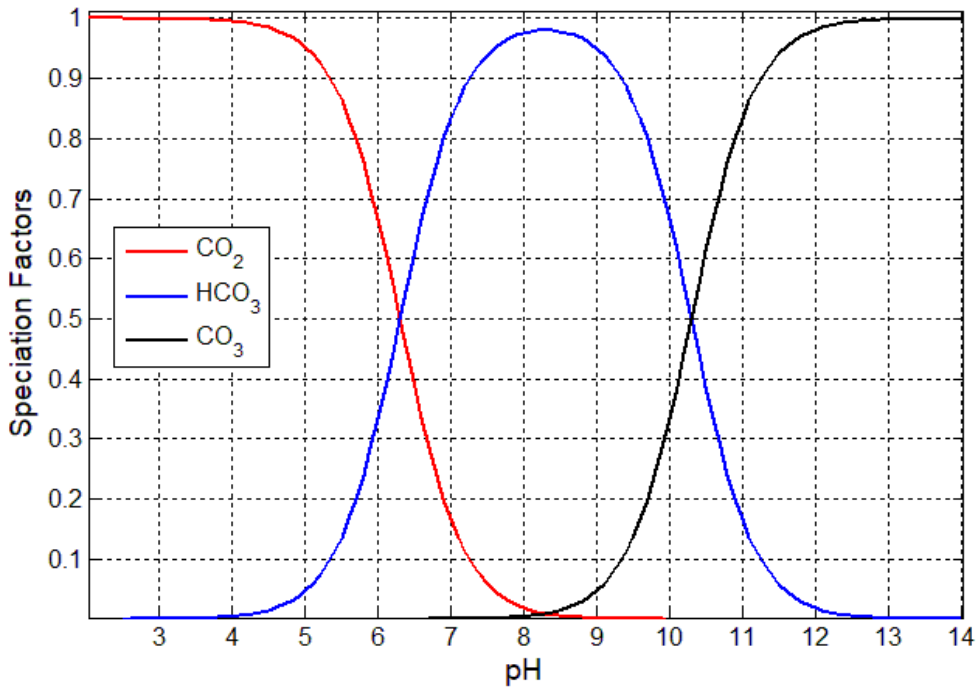

Figure 2.2. Speciation factors of the carbonic acid system as a function of the pH. The points where two speciation factors are equal to 0.5 is localised in pH = - log K.

Since we have pH-dependent reactions, we also include the dissociation of water:

$$H_2O = H^+ + OH^- \tag{2.14}$$

On the other hand, when calcite ($CaCO_{3(s)}$) is added to the system, calcium ions may be produced through mineral dissolution:

$$CaCO_{3(s)} = Ca^{+2} + CO_3^{-2} \tag{2.15}$$

The solubility of calcite decreases with temperature and increases with pressure (Langmuir, 1997), as shown in Figure 2.3. Thus, calcite is much more sensitive to temperature than the species of the carbonic acid system.

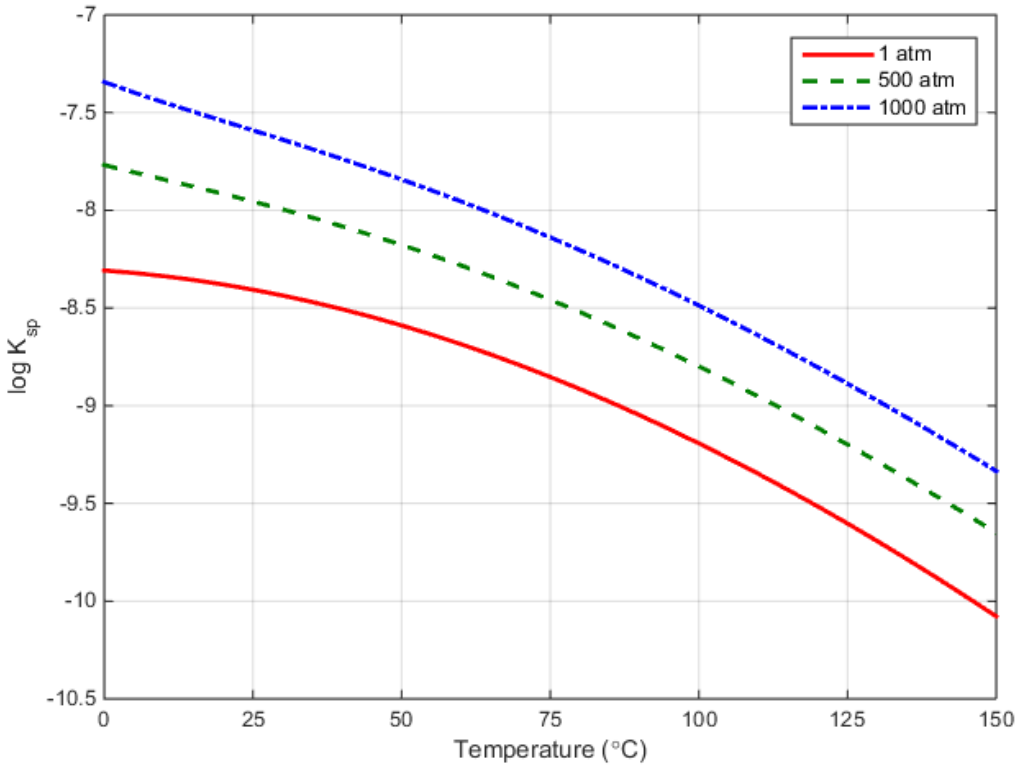

Figure 2.3. Equilibrium constant for calcite dissolution, i.e. reaction (2.15), with varying temperatures and pressures (calculated using PHREEQC).

Moreover, if we combine reactions (2.3), (2.4) and (2.15) we can write a global reaction that relates calcite dissolution to CO_2 aqueous concentration:

$$CaCO_{3(s)} + CO_{2(aq)} + H_2O = Ca^{+2} + 2 \cdot HCO_3^- \quad (2.16)$$

In this form, one can see that calcite dissolution is favoured by higher concentrations of CO_2 in water. Therefore, during the injection of CO_2-bearing fluids in carbonate formations there is a tendency of dissolving calcite near the injection point. However, as the fluids propagate to lower pressure zones CO_2 evolves and changes the direction of the mineral reaction, causing precipitation. Mixing between reservoir fluids with different Ca and HCO_3 concentration may cause similar effects if the activity product of Ca and HCO_3 is larger in the mixture than in each of the individual fluids.

Since the mineral reaction changes the concentrations of carbonate species, all species belonging to the system are linked through equilibrium relations, charge and mass balances. Therefore, if one desires to know what would be the concentration of the

species when equilibrium is reached, a certain number of equations must be solved simultaneously. A general description of how to solve this type of problem was reported by Nghiem et al. (2011).

2.2. Analytical Solutions

In the following, some analytical solutions are obtained for the equilibrium state of the carbonic acid system in the presence of calcite considering some general assumptions which are relevant for CO_2 EOR projects.

Case 1: No aqueous complexes, no gas phase, negligible salinity, $4 < pH < 8$

For these conditions, we can neglect H^+, OH^- and CO_3^{-2}. Thus, we can write a simplified charge balance equation in terms of molalities:

$$2\, m_{Ca^{+2}} = m_{HCO_3^-} \tag{2.17}$$

We can also write a simplified equation for the total dissolved carbon species:

$$m_{CO_2} + m_{HCO_3^-} = CO_{2[init]} + HCO_{3[init]}^- + \left(m_{Ca^{+2}} - Ca_{[init]}^{+2}\right), \tag{2.18}$$

where $CO_{2[init]}, HCO_{3[init]}^-$ and $Ca_{[init]}^{+2}$ are the initial molalities of CO_2, HCO_3 and Ca, respectively. The last term represents the total calcium added to solution and is equal to the additional carbon in moles.

Using (2.17) for initial and equilibrium states we can eliminate the calcium variables from the equation (2.18) to get

$$m_{CO_2} = CO_{2[init]} + \frac{HCO_{3[init]}^-}{2} - \frac{m_{HCO_3^-}}{2}, \tag{2.19}$$

To use a calcite dissolution reaction in terms of only the relevant ions, we can build the equilibrium relation (with an equilibrium constant $K_{sp,1}$) associated to the global reaction (2.16)

$$[Ca^{+2}][HCO_3^-]^2 = [CO_2(aq)]K_{sp,1} \tag{2.20}$$

Thus, combining the last two equations we arrive at

$$K_{sp,1}{}^{-1}\frac{\gamma_{Ca^{+2}}\gamma_1{}^2}{\gamma_0} m_{HCO_3^-}{}^3 + m_{HCO_3^-} = 2 \cdot CO_{2[init]} + HCO_{3[init]}^- \tag{2.21}$$

We can rewrite the independent term by using the total dissolved carbon ($C_T = CO_{2[init]} + HCO_{3[init]}^-$) and the CO_2 speciation factor ($\alpha_{CO_2} = CO_{2[init]}/C_T$):

$$K_{sp,1}{}^{-1}\frac{\gamma_{Ca^{+2}}\gamma_1{}^2}{\gamma_0}m_{HCO_3^-}{}^3 + m_{HCO_3^-} = C_T(1+\alpha_{CO_2}) \tag{2.22}$$

The above cubic equation for the bicarbonate molality ($m_{HCO_3^-}$) is solvable if we assume constant activity coefficients and it has just one real solution. The other relevant species can be determined from

$$\begin{cases} m_{Ca^{+2}} = \dfrac{m_{HCO_3^-}}{2} & (2.23) \\ m_{CO_2} = CO_{2[init.]} - \dfrac{(m_{HCO_3^-} - HCO_{3[init.]}^-)}{2} & (2.24) \end{cases}$$

The cubic equation approximates to a linear equation when $C_T(1+\alpha_{CO_2})$ is low enough. For this condition, $m_{HCO_3^-}$ is approximated by C_T and CO_2 becomes negligible, which means the later dissociates almost completely (see Figure 2.4). This scenario occurs in surface waters since the atmospheric pressure is not high enough to dissolve significant portions of CO_2 and then HCO_3 is the dominant carbon species.

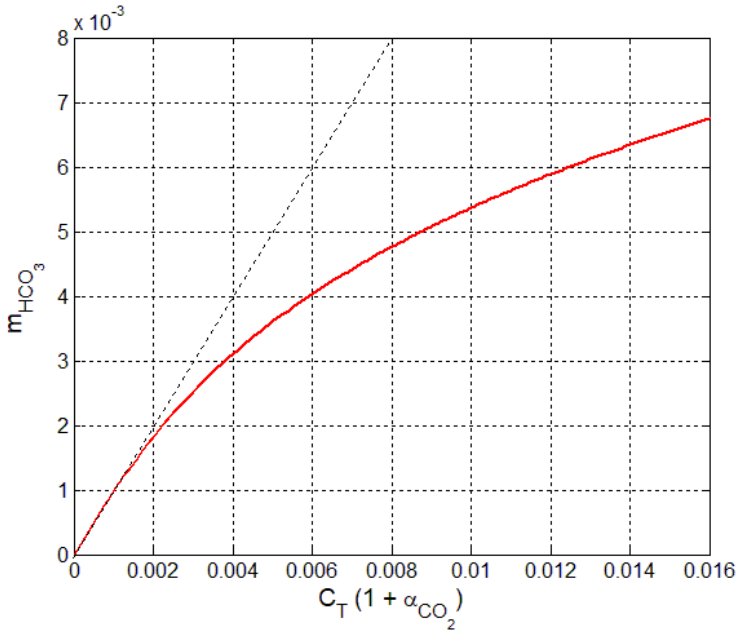

Figure 2.4. Solution of equation (2.22) with $\gamma_j = 1$, for different values of the independent term. Both terms are expressed in units of molality (mol/kgw). In this ideal case, the bicarbonate molality can be approximated by the total dissolved carbon if the latter is less than 2 mM.

Moreover, for increasing C_T (by dissolving CO_2 in a pressurized cell, for example), smaller fractions of CO_2 dissociate until it becomes dominant. However, if one increases the HCO_3 while decreasing the CO_2 (by adding a HCO_3-rich solution) the HCO_3 at equilibrium may decrease if the increase in C_T is not significant.

Case 2: No aqueous complexes, no gas phase, inert species are present, $4 < pH < 8$

Whenever a significant amount of other ions are present in solution the charge balance between them must be included in equation (2.22). This is the only modification needed if the ions do not react with any species of the original system. Therefore, the modified charge balance equation is

$$2\, m_{Ca^{+2}} + \varepsilon = m_{HCO_3^-} \tag{2.25}$$

where ε is the charge balance of non-reactive ions.

Thus, by following the same procedure as before, we update the cubic equation:

$$K_{sp,1}{}^{-1} \frac{\gamma_{Ca^{+2}} \gamma_1{}^2}{\gamma_0} \left(m_{HCO_3^-}{}^3 - \varepsilon \cdot m_{HCO_3^-}{}^2\right) + m_{HCO_3^-} = C_T\left(1 + \alpha_{CO_2}\right) \tag{2.26}$$

and the other species are calculated using

$$\begin{cases} m_{Ca^{+2}} = \dfrac{m_{HCO_3^-}}{2} - \dfrac{\varepsilon}{2} & (2.27) \\ m_{CO_2} = CO_{2[init.]} - \dfrac{(m_{HCO_3^-} - HCO_{3[init.]}^-)}{2} & (2.28) \end{cases}$$

It is worth noting that the charge balance between non-reactive ions plays a role in the amount of calcium in equilibrium and therefore affects calcite dissolution (lower charge yields higher calcium). In fact, lowering the charge balance is equivalent to decreasing the charge difference between bicarbonate and calcium ions:

$$\varepsilon = HCO_{3[init.]}^- - 2 \cdot Ca_{[init.]}^{+2} \tag{2.29}$$

In Figure 2.5 there is a comparison between this simplified analytical model and the complete numerical one, which was run in PHREEQC. In our calculations, all activity coefficients were set to unity. The nonreactive ions are only Na and Cl. C_T was set to 0.4 mol/kgw, while temperature and pressure were 60 ℃ and 500 atm, respectively.

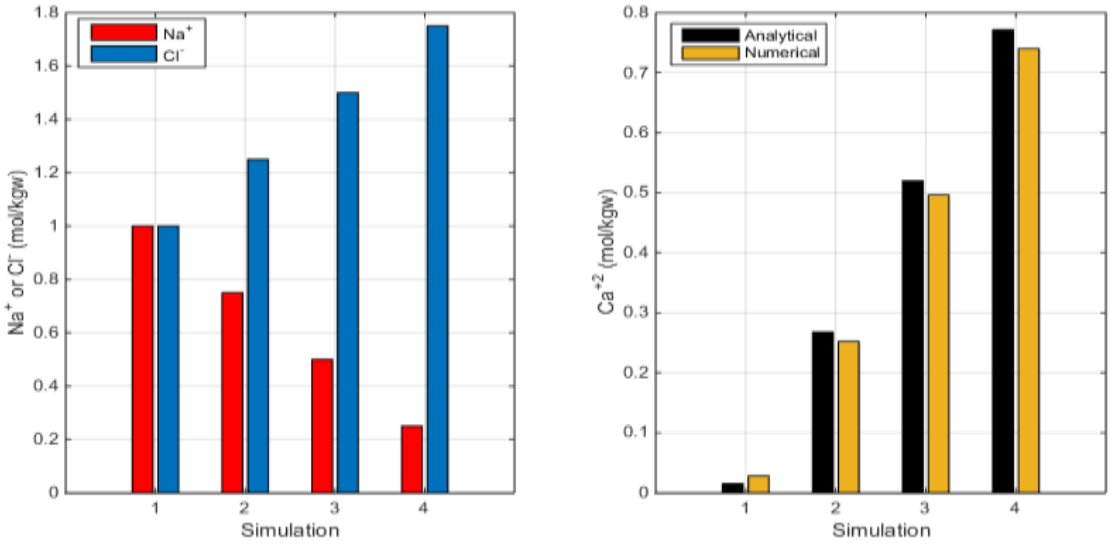

Figure 2.5. Comparison between this formulation (Analytical) and PHREEQC (Numerical) for different charge balance between Na+ and Cl-.

Finally, Table 2.1 summarizes the impact of the physical and chemical changes on calcite solubility in a static environment, which will be important for understanding the calcite reactions during the propagation of water through a carbonate formation.

Table 2.1. Effects on calcite solubility for different perturbations.

Physical/Chemical Perturbation	**Effect on Calcite Solubility**	**Explanation**
Temperature increase	Favours Precipitation	Equilibrium constant decreases
Pressure increase	Favours Dissolution	Equilibrium constant increases
Ca increase	Favours Precipitation	Additional Ca reacts with HCO_3
HCO_3 increase and CO_2 decrease	Favours Precipitation	Additional HCO_3 reacts with Ca
Total Dissolved Carbon increase	Favours Dissolution	Additional CO_2 reacts to produce Ca

2.3. Activity models

Equations (2.22) or (2.26) shows that the calculation of the equilibrium state of the carbonic acid system with calcite requires not only the initial concentrations of CO_2 and HCO_3 (included in C_T and α_{CO_2}) but also thermodynamic parameters: $K_{sp,1}$, γ_0, γ_1 and γ_{Ca}. The computation of the equilibrium constant is straightforward:

$$K_{sp,1} = K_1 \cdot K_{sp} \tag{2.29}$$

On the other hand to obtain the activity coefficients, one needs an activity model. Most activity models use the definition of *ionic strength*:

$$I = {}^1\!/_2 \sum m_j \cdot z_j^2 \tag{2.30}$$

where m_j and z_j are the molality and charge of ion j, while the sum is over all dissolved ions.

The Debye-Hückel activity model accounts for the electrical forces between ions (coulombic interactions) and relies on the ion size, i.e. $å_j$, two temperature dependent parameters (A and B) and I (Debye and Hückel, 1923; Langmuir, 1997):

$$\log \gamma_j = -\frac{A z_j^2 \sqrt{I}}{1 + B å_j \sqrt{I}} \tag{2.31}$$

Note that equation (2.31) requires information from the solution as whole (included in I) and the ion j but not from other ions individually. Its simplicity is advantageous and works well for $I < 0.1$ (less than 5000 ppm of dissolved solids). Above this, one can use the modified version known as Truesdell-Jones model but also called B-dot, as the correction term is the parameter b_j (Truesdell and Jones, 1969):

$$\log \gamma_j = -\frac{A z_j^2 \sqrt{I}}{1 + B a_j \sqrt{I}} + b_j \tag{2.32}$$

In this model the ion size from Debye-Hückel formulation is substituted by a_j, which is now a parameter as well as A, B and b_j. Truesdell-Jones (or B-dot) equation enables the increase of the activity coefficients with ionic strength, which is an effect of

the formation of hydration spheres that traps the water molecules in concentrated solutions such as seawater (Langmuir, 1997). The model provides reasonable approximations for $I < 2$ in dominantly chloride solutions (Parkhurst, 1990). Nevertheless, one may still need a more accurate model to determine the equilibrium state of waters that have concentrations close to the saturation of halite (NaCl). In deep hydrocarbon or water reservoirs the Total Dissolved Solids (TDS) varies from 100 000 to 300 000 ppm, as halite saturates with 6 M of NaCl.

The Pitzer activity model has been said to be the most accepted model for higher ionic strengths (Langmuir, 1997). Its accuracy is given by several interaction parameters which are used to model the interactions between pairs and triples of ions (Pitzer, 1973; Pitzer, 1987; Harvie and Weare, 1980; Harvie et al., 1984; Moller, 1988). Recently, Appelo (2015) has shown that the Pitzer model from Harvie et al. (1984), contained in PHREEQC 3, can be used to model the solubility of different minerals from 0 to 200 °C and up to 1000 atm.

The pressure dependence is important for calculating solubility of minerals and gases, and it is a function of the volume change of reaction (Appelo et al., 2013). In fact, at 25 °C, going from 1 to 500 bar, calcite solubility increase by a factor of about 1.7 (Macdonald and North, 1974).

However, some minerals are still not present in the Pitzer database (interaction parameters) and cannot be modelled, such as the ones containing aluminium. Moreover, PHREEQC fails to model solutions that contains higher concentrations of both Ca and SO_4 in higher pressure (Appelo, 2015).

CMG GEM does not have a Pitzer model at the moment; the user has to choose between Debye-Hückel and Truesdell-Jones, otherwise activity coefficients are set to a constant number (unit value or user-defined).

Chapter 3:
CO_2 solubility modelling

In the previous Chapter we have introduced the main reactions related to the carbonic acid system and how the addition of calcite modifies the equilibrium state by producing or removing inorganic dissolved carbon species from aqueous solutions. The reactions are homogeneous (i.e. occur in a single phase), except for the calcite mineral reactions, which requires a mineral (solid) phase to be in contact with the solution to proceed.

In this Chapter, we consider another heterogeneous reaction: the dissolution of $CO_{2(g)}$ in aqueous solutions. This reaction is considered to be fast and therefore only the equilibrium state needs to be calculated, that is the equilibrium concentration of $CO_{2(aq)}$. Recently, the modelling of the CO_2 solubility in aqueous solution has been the focus of different research groups (Harvie and Weare, 1984; Carroll and Mather, 1992; Harvey, 1996; Garcia, 2001; Bakker, 2003; Diamond and Akinfiev, 2003; Duan and Sun, 2003; Appelo et al., 2013; Zhao et al., 2015), which based their models in a large range of experimental data (Wiebe and Gaddy, 1939 & 1940; Takenouchi and Kennedy, 1964 & 1965; Drummond, 1981; Rumpf et al., 1994; Tong et al., 2013; Zhao et al., 2015).

Nevertheless, to predict accurately the solubility of CO_2 in formation water and injected water is very important for CO_2 EOR and CO_2 storage projects, because the solubility will determine the mass of CO_2 that will be trapped in water and potentially cause mineral reactions, altering the pore sizes and flow properties of the porous media.

3.1. Thermodynamics of gaseous dissolution in aqueous solution

The theoretical solubility of CO_2 (as for any other gas) in an aqueous solution with fixed temperature (T) and pressure (P) can be obtained by finding the equilibrium state for the dissolution process. A fundamental method to determine the equilibrium state consists in minimizing the Gibbs free energy (G), which may be written in terms of the number of moles of each chemical species in the reaction (n_i) and their chemical potentials (μ_i) (Callen, 1985; Castellan, 1986):

$$G(T, P, \{n_i\}) = \sum_i \mu_i n_i \tag{3.1}$$

Then for the dissolution process $\mathrm{CO_2(aq)} \Leftrightarrow \mathrm{CO_2(g)}$ we have that $\mathrm{dG} = 0$ is equivalent to

$$\mu_{aqueous} = \mu_{gas} \tag{3.2}$$

$$\mu_{aqueous}{}^0 + RT \ln\left(a_{CO_2(aq)}\right) = \mu_{gas}{}^0 + RT \ln\left(f_{CO_{2(g)}}\right) \tag{3.3}$$

If we define

$$a_{CO_2(aq)} = \gamma_{CO_2(aq)} m_{CO_2(aq)} \tag{3.4a}$$

$$f_{CO_{2(g)}} = \varphi_{CO_{2(g)}} P_{CO_{2(g)}} \tag{3.4b}$$

and

$$\mu_{aqueous}{}^0 - \mu_{gas}{}^0 = RT \ln K_H \tag{3.5}$$

the solubility is expressed by the following equilibrium relation

$$m_{CO_2(aq)} = \frac{\varphi_{CO_{2(g)}} P_{CO_{2(g)}}}{\gamma_{CO_2(aq)} K_H} \tag{3.6}$$

where $m_{CO_2(aq)}$ and $\gamma_{CO_2(aq)}$ are the molality and activity coefficient of aqueous CO_2, while $\varphi_{CO_{2(g)}}$ and $P_{CO_{2(g)}}$ are the fugacity coefficient and partial pressure of gaseous CO_2. The variable K_H is actually a special type of chemical equilibrium constant called Henry's constant which is fixed for given T and P.

In fact, for low pressures and low salinity both $\varphi_{CO_{2(g)}}$ and $\gamma_{CO_2(aq)}$ converge to unity and we have Henry's Law (Castellan, 1986):

$$m_{CO_2(aq)} \approx \frac{P_{CO_{2(g)}}}{K_H} \quad \text{for dilute solutions at low pressures} \tag{3.7}$$

In addition, the quantity $\left(\mu_{aqueous}{}^0 - \mu_{gas}{}^0\right)$ accounts for the variation of Gibbs free energy at standard temperature and pressure (ΔG^0). Therefore, K_H is a function of ΔG^0 (Castellan, 1986):

$$\Delta G^0 = RT \ln K_H \tag{3.8}$$

For any reaction, ΔG^0 has the following T and P derivatives (Callen, 1985):

$$\frac{\partial(\Delta G^0)}{\partial T} = -\Delta S^0 = \frac{\Delta G^0 - \Delta H^0}{T} \tag{3.9}$$

$$\frac{\partial(\Delta G^0)}{\partial P} = \Delta V^0 \tag{3.10}$$

The derivatives then set the K_H dependence on temperature, known as Van't Hoff's equation (Appelo, 2015),

$$\ln K_H(T) \approx \ln K_H(T = T^0) + \frac{\Delta H^0}{R}\left(\frac{1}{T} - \frac{1}{T^0}\right), \tag{3.11}$$

and the K_H dependency on pressure

$$\ln K_H(P) \approx \ln K_H(P = P^0) + \frac{\Delta V^0}{RT}(P - P^0) \tag{3.12}$$

which are both valid approximations when the variation of enthalpy (ΔH^0) and the variation of volume (ΔV^0), both associated to the chemical reaction, do not change significantly from the standard state.

Because ΔH is usually variable with T we may rather use an empirical expression for the dependence of Henry's constant on temperature (Appelo, 2015). Moreover, during the dissolution process the change in volume is the molar volume of aqueous CO_2 ($V_{CO_2(aq)}$).

$$K_H = K_H(T) \cdot exp\left(\frac{V_{CO_2(aq)}}{RT}(P - P^0)\right) \tag{3.13}$$

and

$$m_{CO_2(aq)} = \frac{\varphi_{CO_2(g)} P_{CO_2(g)}}{\gamma_{CO_2(aq)} K_H(T)} exp\left(-\frac{V_{CO_2(aq)}}{RT}(P - P^0)\right) \tag{3.14}$$

which is similar to the Krichevsky-Kasarnovsky equation (Carroll and Mather, 1992; Tong et al., 2013):

$$ln\left(\frac{f_{CO_2(g)}}{x_{CO_2(aq)}}\right) \approx ln\, K_H(T) + \frac{V^{\infty}_{CO_2(aq)}}{RT}(P - P^0) \tag{3.15}$$

where $x_{CO_{2(aq.)}}$ and $V^{\infty}_{CO_2(aq)}$ are the mole fraction and the molar volume at infinite dilution of aqueous CO_2.

3.2. CO_2 Solubility Models

To model the CO_2 solubility one must take into account the dependence of $\varphi_{CO_{2(g)}}$, $P_{CO_{2(g)}}$, $\gamma_{CO_2(aq)}$ and K_H on T, P and system composition. Because these four parameters are correlated via thermodynamic properties, some of them may be primarily modelled while the others can be treated as constant under a certain change in the physical and chemical conditions.

Among the four parameters, only $\varphi_{CO_{2(g)}}$ is explicitly independent of system composition and is calculated by an equation of state (EOS). On the other hand, although $K_H(T,P), K_H(T)$ and $V^{\infty}_{CO_2(aq)}$ are directly dependent on the physical properties of water (solvent) (Diamond and Akinfiev, 2003; Helgeson and Kirkham, 1976), some authors chose to build empirical model explicitly dependent on T and P only (Plummer and Busenberg, 1982; Duan and Sun, 2003, Harvey, 1996; Garcia, 2001).

In highly saline waters, $\gamma_{CO_2(aq)}$ differs from unity (Diamond and Akinfiev, 2003) and should be calculated by an activity model. For concentrations up to 6 M NaCl, the Pitzer model has been shown to provide accurate activity coefficients (Pitzer, 1987), while other models like the B-dot have reasonable accuracy in solutions up to 2M NaCl (Parkhurst, 1990). Modifications of the Pitzer model (Pitzer, 1973) have been carried out to predict solubilities of minerals and gases in different conditions (Harvie and Weare, 1980; Harvie et al., 1984; Pitzer, 1987; Moller, 1988; Duan et al.,1992) which consider the interactions between Ca, Mg, SO_4, K, Na, Cl, HCO_3 and others relevant species. Alternatively, the general behaviour of lower solubility of gases in higher salinity waters can be modelled by salting-out coefficients (Bakker, 2003).

3.2.1. CMG GEM/WINPROP

The general solubility model implemented in CMG software has optional features that can be activated by the user to improve accuracy for specific systems. For CO_2 the model assumes $\gamma_{CO_2(aq)}$ equal to unity and uses Peng-Robinson EOS to obtain $\varphi_{CO_{2(g)}}$. Moreover, empirical expressions are implemented for K_H (Harvey, 1996) and $V^{\infty}_{CO_2(aq)}$

(Garcia, 2001) as functions of T only. The results are compiled similarly to the Krichevsky-Kasarnovsky equation with water saturation pressure as the reference pressure. In addition, there is an empirical expression for correcting the solubility in high salinity waters which depends on T and Cl concentration which was adapted from the general expression of (Bakker, 2003).

The general empirical expression for $K_H(T)$ used in CMG software is

$$\ln K_{H,CMG}(T) = \ln P^{sat}_{H_2O}(T) + \frac{A}{T_{r,H_2O}} + \frac{B}{T_{r,H_2O}} \cdot \left(1 - T_{r,H_2O}\right) + \\ + \frac{C}{T^{0.41}_{r,H_2O}} \cdot exp\left(1 - T_{r,H_2O}\right)^{0.355} \tag{3.16}$$

where $P^{sat}_{H_2O}(T)$ is the water saturation pressure in MPa calculated by (Saul and Wagner, 1987) and T_{r,H_2O} the reduced temperature, i.e. the temperature divided by the critical temperature of water (both in K). For CO_2, we have $A = -9.4234, B = 4.0087$, $C = 10.3199$ and

$$V^{\infty}_{CO_2(aq)} = 37.51 - 0.9585 \cdot \hat{T} + 0.874 \cdot 10^{-3} \cdot \hat{T}^2 - 0.5044 \cdot 10^{-6} \cdot \hat{T}^3 \tag{3.17}$$

where $V^{\infty}_{CO_2(aq)}$ is in cm^3/mol and $\hat{T}$ is the temperature in ℃.

The correction for high salinity is

$$\frac{\ln K^{SALT}_{H,CMG}(T)}{\ln K_{H,CMG}(T)} = (0.11572 - 0.60293 \cdot 10^{-3} \cdot \hat{T} + \\ +3.5817 \cdot 10^{-6} \cdot \hat{T}^2 - 3.7772 \cdot 10^{-9} \cdot \hat{T}^3) \cdot m_{\mathrm{Cl}} \tag{3.18}$$

where m_{Cl} is the molality of chlorine.

3.2.2. PHREEQC

The CO_2 solubility model in PHREEQC follows a very similar procedure to that used in CMG software (using Peng-Robinson EOS and Krichevsky-Kasarnovsky equation framework). However, $\gamma_{CO_2(aq)}$ is calculated via Pitzer model with simple parameterization reported by (Harvie et al., 1984) for 25℃ but claimed by (Appelo et al., 2015) to be invariant for certain system compositions which were tested. The main

difference is that $V^{\infty}_{CO_2(aq)}$ is a function of T and P. Moreover, the reference pressure for a different empirical expression is used for K_H (Plummer and Busenberg, 1982), though still a function of T.

The empirical expression for $K_H(T)$ in PHREEQC is

$$\log K_{H,PHR}(T) = 109.534 + 0.019913 \cdot T - \frac{6986.04}{T} - \\ - 40.83 \cdot \log T + \frac{669370}{T^2}, \tag{3.19}$$

while the apparent molar volume is used to compute $V^{\infty}_{CO_2(aq)}$:

$$V^{\infty}_{CO_2(aq)} = 41.84 \cdot \left(\begin{array}{c} 2.085 - \frac{4693}{2600 + \hat{P}} - \frac{79.0}{T - 228} + \\ + \frac{279000}{(2600 + \hat{P})(T - 228)} + 0.193 \cdot \frac{\partial \varepsilon_r^{-1}}{\partial \hat{P}} \end{array} \right) \tag{3.20}$$

where $\hat{P}$ is the pressure in bars and ε_r is the relative dielectric constant of pure water calculated by (Bradley and Pitzer, 1979). The value of $\gamma_{CO_2(aq)}$ differs from unity in concentrated solutions because it is calculated by

$$\ln \gamma_{CO_2(aq)} = 0.2 \cdot m_{Na} + 0.366 \cdot (m_{Ca} + m_{Mg}) + 0.194 \cdot m_{SO_4} + \\ + 0.102 \cdot m_K - 0.01 \cdot m_{Cl} - 0.06 \cdot m_{HSO_4} \tag{3.21}$$

3.2.3. Duan & Sun

Duan and Sun (2003) developed a model using their own EOS to calculate $\varphi_{CO_2(g)}$ and applied a different framework to calculate the CO_2 solubility without splitting K_H into two independent functions. In fact, Henry's constant is written in terms of ${\mu_{aqueous}}^0$ and calculated via a multiple parameterisation dependent on both temperature and pressure. A similar procedure is used to determine the Pitzer coefficients which set $\gamma_{CO_2(aq)}$.

The Pitzer model used by Duan & Sun model is

$$\ln \gamma_{CO_2(aq)} = 2\lambda_{CO_2-Na} \cdot (m_{Na} + 2 \cdot m_{Ca} + 2 \cdot m_{Mg} + m_K) + \tag{3.22}$$

$$+\zeta_{CO_2-Na-Cl} \cdot \left(m_{Na} + m_{Ca} + m_{Mg} + m_K\right) - 0.07 \cdot m_{SO_4}$$

while the Pitzer coefficients ($\lambda_{CO_2-Na}, \zeta_{CO_2-Na-Cl}$) and ${\mu_{aqueous}}^0/RT$ [$= \ln K_H$] are set by the empirical expressions of the form

$$Par(T,P) = c_1 + c_2 \cdot T + \frac{c_3}{T} + c_4 \cdot T^2 + \frac{c_5}{(630 - T)} + c_6 \cdot P + c_7 \cdot P \ln T + \frac{c_8 P}{T} + \frac{c_9 P}{630 - T} + \frac{c_{10} \cdot P^2}{(630 - T)^2} + c_{11} \cdot T \ln P \quad (3.23)$$

3.2.4. Diamond & Akinfiev

Diamond and Akinfiev (2003) evaluated 25 literature studies and built their CO_2 solubility model based on only the data they considered to be of good quality. $\varphi_{CO_{2(g)}}$ is obtained using Span & Wagner EOS (Span and Wagner, 1996) while $K_H$is calculated via the virial-like Akinfiev & Diamond EOS (Diamond and Akinfiev, 2003) for specified temperature and pressure. Initially, $\gamma_{CO_2(aq)}$ is calculated using an empirical expression dependent on temperature and $m_{CO_2(aq)}$. Then, $\gamma_{CO_2(aq)}$ is corrected for high salinity brine via Pitzer coefficients dependent on temperature and ionic strength (Akinfiev and Diamond, 2010).

The semi-empirical $K_H$is calculated by

$$\ln K_{H,D\&A}(T,P) = (1+\xi) \ln f^0_{H_2O} + \xi \cdot \ln\left(\frac{RT}{18.0153}\rho^0_{H_2O}\right) + 2 \cdot \rho^0_{H_2O} \cdot \left[a + b \cdot \left(\frac{1000}{T}\right)^{0.5}\right] \quad (3.24)$$

where $f^0_{H_2O}$ and $\rho^0_{H_2O}$ are the fugacity and density of pure water calculated by (Hill, 1990) at specified T and P, while the empirical parameters obtained are $\xi = -0.088, a = -9.3134$ and $b = 11.5477$.

There is an expression for calculating $\gamma_{CO_2(aq)}$ in pure water

$$\ln {\gamma_{CO_2(aq)}}^w = \begin{pmatrix} -0.099085 + 0.48977 \cdot 10^{-3} \cdot T \\ -0.962628 \cdot 10^{-6} \cdot T^2 \end{pmatrix} \cdot m_{CO_2(aq)} + \begin{pmatrix} 0.218384 - 1.024319 \cdot 10^{-3} \cdot T \\ +1.222992 \cdot 10^{-6} \cdot T^2 \end{pmatrix} \cdot {m_{CO_2(aq)}}^2 \quad (3.25)$$

On the other hand for saline waters the expression is

$$\ln \gamma_{CO_2(aq)} = 2m_{CO_2(aq)}\lambda_{11} + 3{m_{CO_2(aq)}}^2\tau_{111} + 2m_{NaCl}B_{12} + \\ +3{m_{NaCl}}^2 C_{122} + 6m_{CO_2(aq)}m_{NaCl}C_{112} \tag{3.26}$$

where the parameters are obtained by fitting to experimental data and are functions of T, P and ionic strength (I).

3.2.5. Summary of CO_2 Solubility Models

In Tables 3.1 and 3.2, we summarize the four models of CO_2 solubility in pure water and its corrections for high salinity waters.

Table 3.1: CO_2 solubility models in pure water.

	CMG	PHREEQC	Duan & Sun	Diamond & Akinfiev
$\boldsymbol{\varphi_{CO_{2(g)}}}$	Peng-Robinson EOS	Peng-Robinson EOS	Duan & Sun EOS	Span & Wagner EOS
$\boldsymbol{K_H(T,P)}$	Krichevsky-Kasarnovsky	Krichevsky-Kasarnovsky	10-parameter expression (Duan and Sun, 2003)	Akinfiev & Diamond virial-like EOS
$\boldsymbol{K_H(T)}$	3-parameter expression (Harvey, 1996)	5-parameter expression (Plummer and Busenberg, 1982)	X	X
$\boldsymbol{V_{CO_2(aq)}}$	4-parameter expression (Garcia, 2001)	5-parameter expression (Helgeson et al., 1981)	X	X
$\boldsymbol{\gamma_{CO_2(aq)}}$	1	1	1	6-parameter expression (Diamond and Akinfiev, 2003)

Table 3.2: CO_2 solubility models corrections for high salinity waters.

	CMG	PHREEQC	Duan & Sun	Diamond & Akinfiev
$K_H(T)$	4-parameter expression (Bakker, 2003)	None	X	X
$\gamma_{CO_2(aq)}$	None	7-parameter Pitzer model (Harvie, 1984)	10-parameter Pitzer model (Duan et al., 1992)	6-parameter expression (Akinfiev and Diamond, 2010)

3.2.6. Comparison with experimental data

We compared the four models with experimental data extracted from the literature (Wiebe and Gaddy, 1939 & 1940; Rumpf et al., 1994; Zhao et al., 2015) and calculated the relative errors between each model and experiments for each data point. PHREEQC and GEM software were used to calculate the CO_2 solubility, while for Duan & Sun and Diamond & Akinfiev, we used the online applications of http://models.kl-edi.ac.cn/models/h2o_co2_nacl/ and http://www.geo.unibe.ch/diamond, respectively. The first set of literature data (Wiebe and Gaddy, 1939 & 1940) is considered of good accuracy according to Diamond and Akinfiev (2003). Moreover, this data is well known and it was used by other authors to validate their models of CO_2 solubility (Duan and Sun, 2003; Appelo, 2015). Results for solubility in pure water (Figure 3.1) show general agreement between experimental data and all models (errors < 6%). This leads to the conclusion that the different EOS in combination with the different models for Henry's constant dependency on P and T are all valid and accurate for these physical conditions ($50 \leq T(℃) \leq 100; P(MPa) \leq 70$).

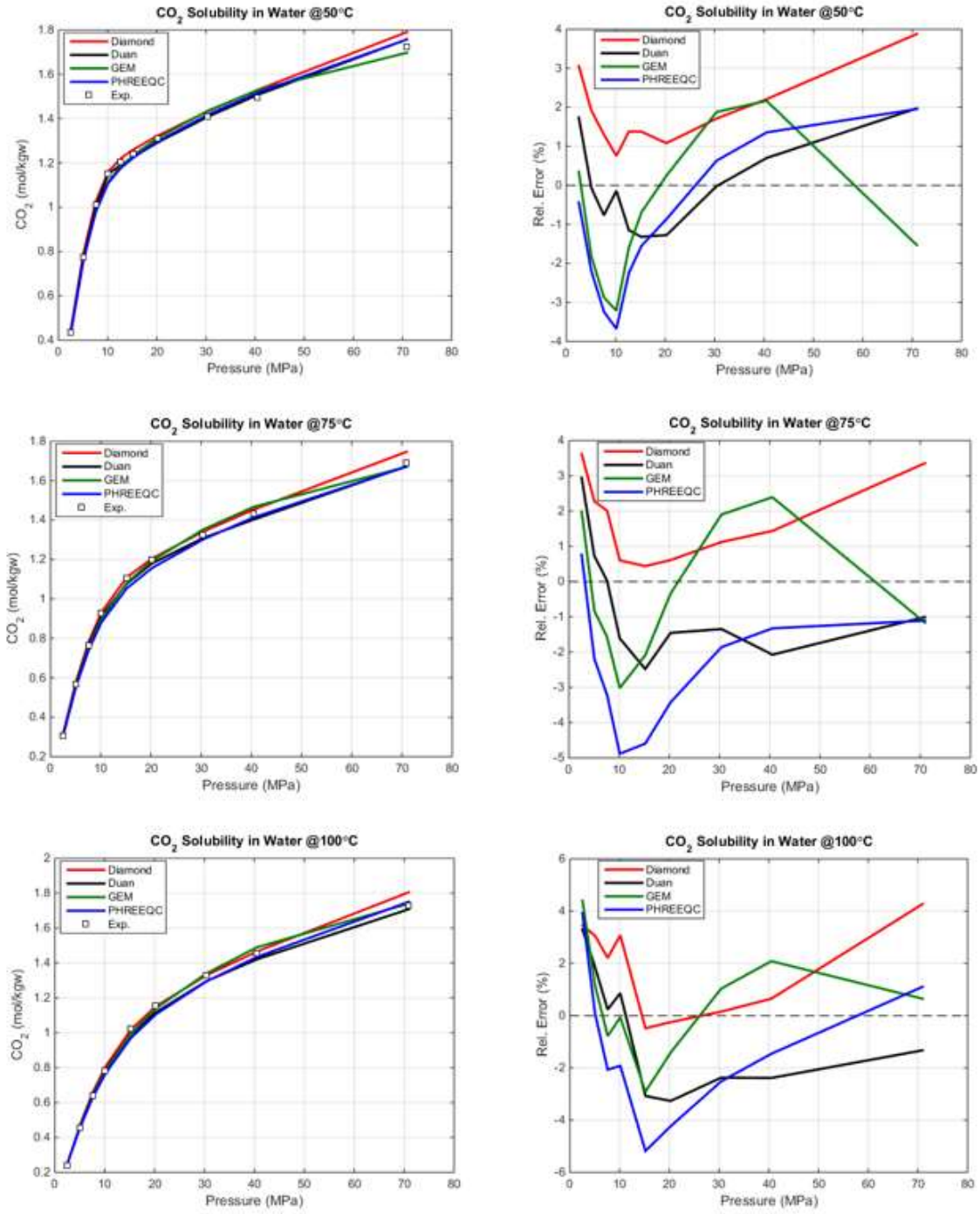

Figure 3.1. CO_2 solubility in pure water at 50℃ (top), 75℃ (middle) and 100℃ (bottom) with different pressures according to four models and experimental data from Wiebe and Gaddy, 1939 & 1940.

However, for higher salinity all models have some degree of difficulty to represent the dynamics of the system at low pressure ($< 10\ MPa$) and show deviations higher than 6% when compared to the literature data (see Figures 3.2 and 3.3). The data (Rumpf et al., 1994) passed in the test of accuracy of Akinfiev and Diamond (2010). One can see that both PHREEQC and GEM overestimate the solubility by more than 10% when the temperature is 140 ℃ or higher. This may be caused by the fugacity coefficient calculated by the Peng-Robinson EOS, which is used by both models. Peng-Robinson EOS is broadly used in the oil & gas industry because many parameters associated to hydrocarbon components have already been determined by fitting experimental data with it. Moreover, the errors given by PHREEQC and GEM decreases as the pressure approaches 10 MPa and therefore the models may still be valid for reservoirs situated at this pressure.

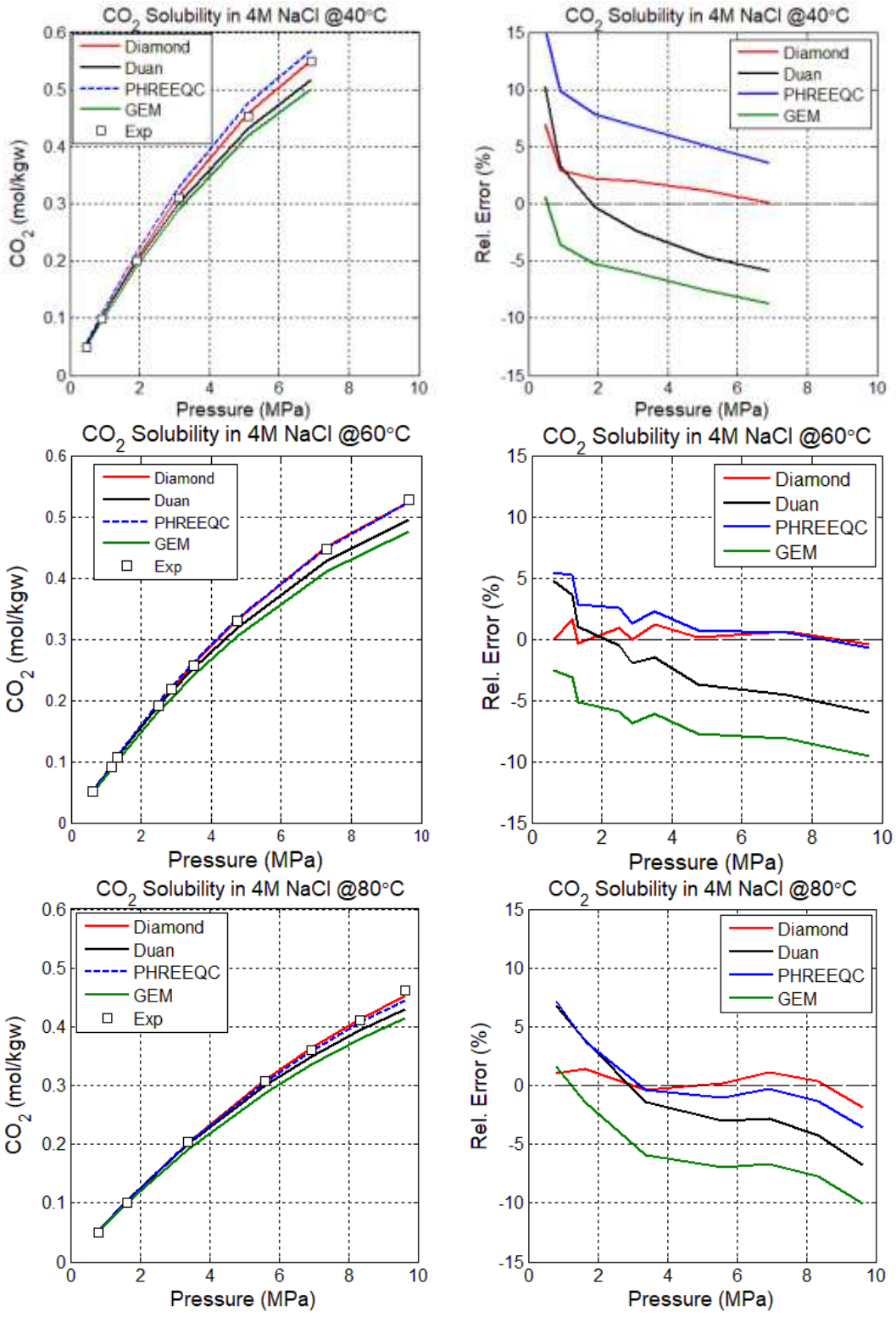

Figure 3.2. CO_2 solubility in 4 M NaCl solution at 40℃ (top), 60℃ (middle) and 80℃ (bottom) with different pressures according to four models and experimental data from Rumpf et al., 1994.

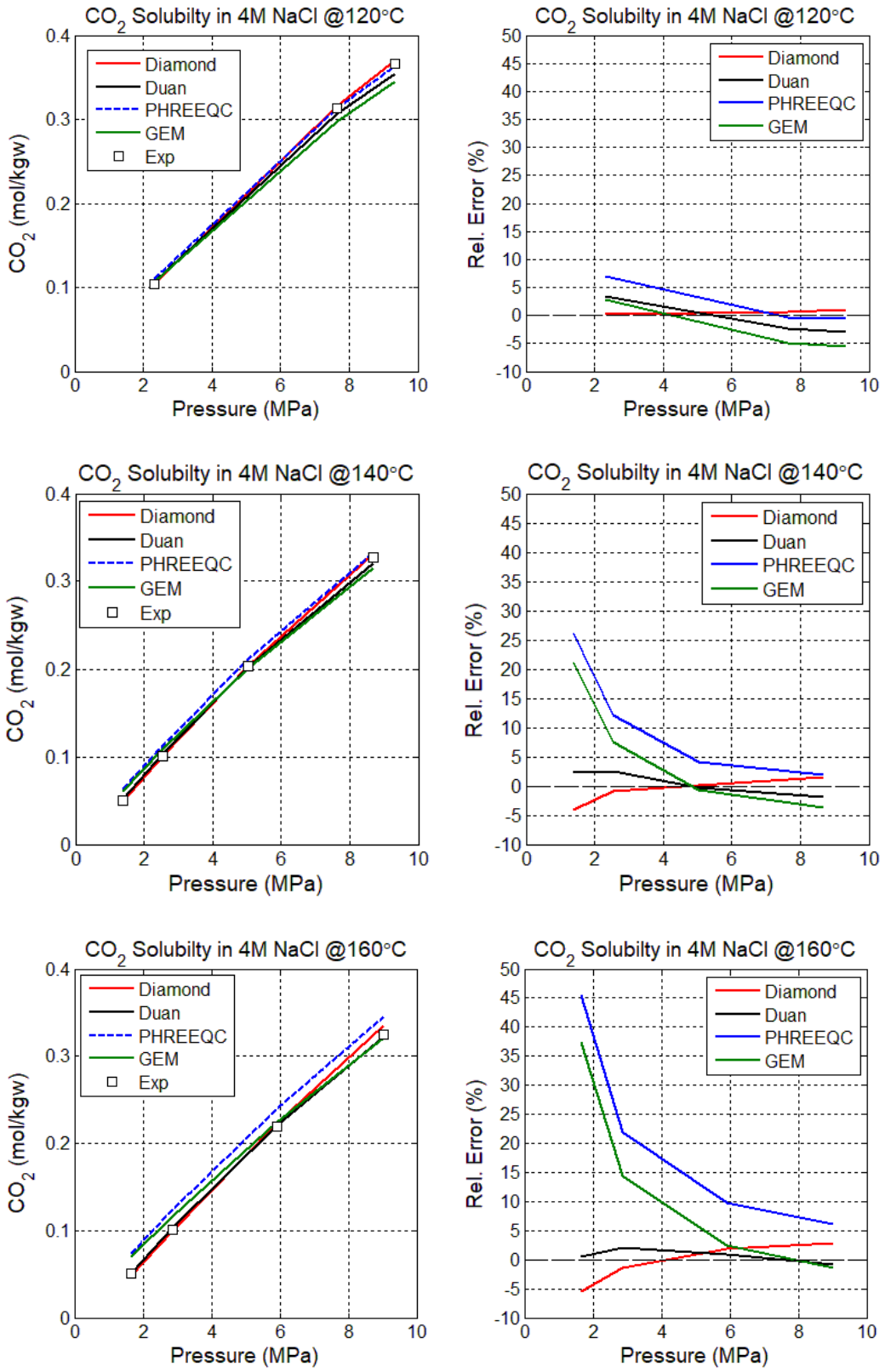

Figure 3.3. CO_2 solubility in 4 M NaCl solution at 120℃ (top), 140℃ (middle) and 160℃ (bottom) with different pressures according to four models and experimental data from Rumpf, 1994.

The strength of a model is given by its ability to reproduce observed behaviour and to predict the behaviour that still needs to be observed. In this sense, a final test for CO_2 solubility may be carried out: to test the model with data that was not available by the time the models were built. The data (Zhao et al., 2015) was not known by Appelo (2015), as he did not compare PHREEQC with it, and is newer than all other models. Since the online application of Duan & Sun is limited to 4.5 M NaCl, we have implemented the model in MatLab™ to calculate the solubility up to 6 M NaCl. Thus, we compared the four models at 15 MPa with increasing NaCl concentrations (see Figure 3.4) to check their reliability for lower pressure reservoirs. All models produced results with good accuracy up to 1M NaCl. We calculated the Absolute Relative Deviation (ARD) for each model and obtained a rank of performance for the given data: Diamond & Akinfiev (1.65%), Duan & Sun (5.81%), PHREEQC (7.97%) and GEM (16.39%).

Again, the performance of PHREEQC and GEM is worse, since they use an EOS which was not specifically built to calculate CO_2 solubility (as Span & Wagner EOS and Duna & Sun EOS were). The problem is more severe for higher salinity (> 4 M NaCl), especially for GEM, which underestimates the solubility by more than 10%. This could be explained by the fact the CMG software do not have the Pitzer model implemented yet (only B-dot and Debye-Hückel are currently available). Although the expression proposed by (Bakker, 2003) shows the decreasing trend in solubility for increasing salinity (salting-out effect), it is overestimated when compared to the other models (which leads to an underestimation in solubility in highly saline waters).

In addition to this, the Pitzer model can make better estimations of mineral precipitation in high salinity waters and was recommended by us in a special report to CMG (shown in Appendix). On the other hand, GEM provides accurate solubility values up to 2 M NaCl, which corresponds to moderate salinity reservoirs (TDS < 100 000 ppm).

Thus, GEM solubility model is accurate to model interactions of CO_2 gas with pure water and seawater, while maximum concentration of CO_2 dissolved in formation water should be taken with care depending on the salinity.

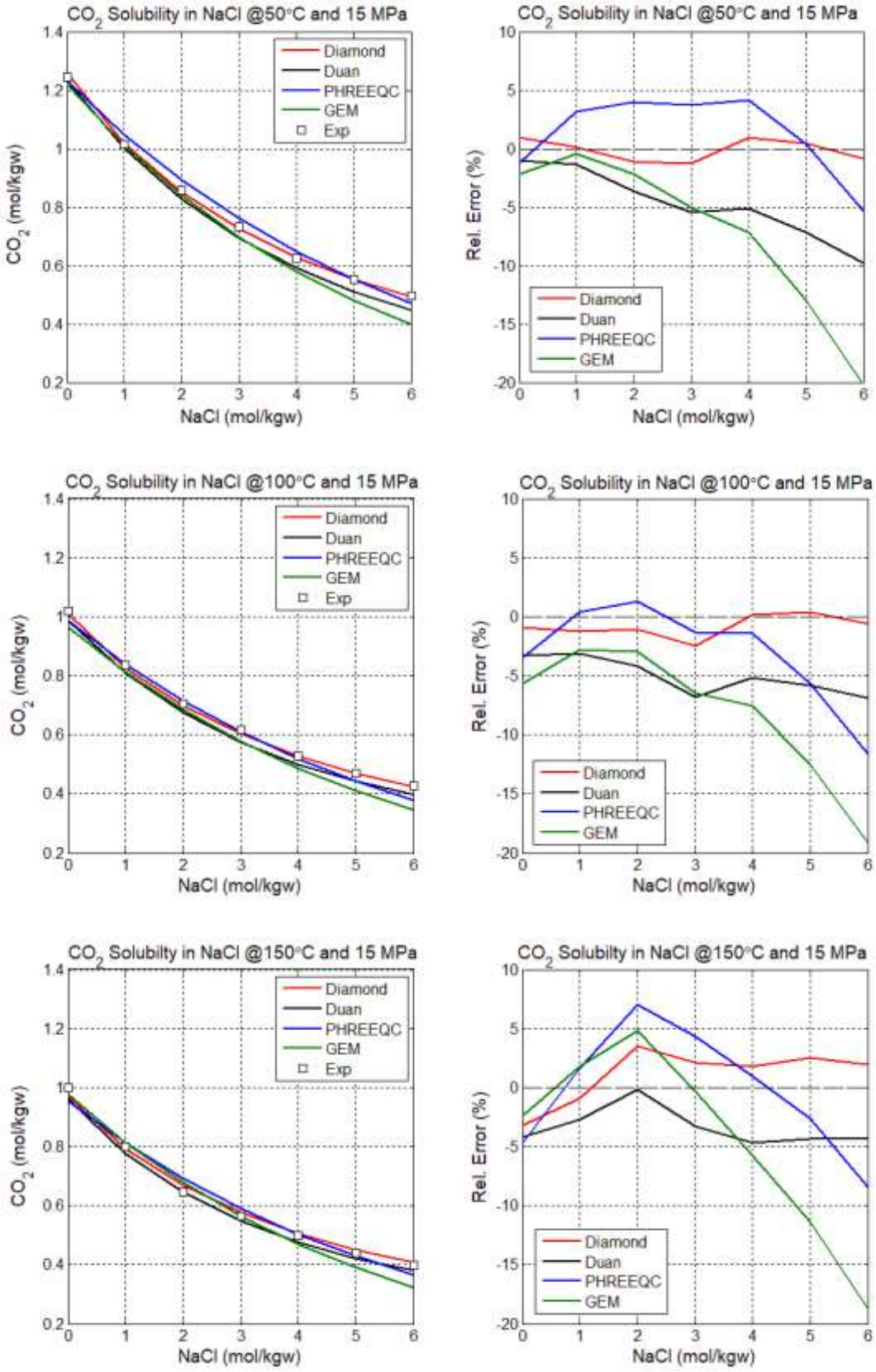

Figure 3.4. CO_2 solubility in NaCl solutions with different concentrations at 15 MPa and 50℃ (top), 100℃ (middle) and 150℃ (bottom) according to four models and experimental data from Rumpf, 1994.

3.3. Simple model for CO_2 and $CaCO_3$ solubilities at high P, T & Salinity

After assessing the main models for gaseous CO_2 solubility at different physical conditions and salinities we are now ready to design a simplified model and to couple it with our simplified $CaCO_3$ solubility model developed in Chapter 2.

The general shape of $K_H(T)$ is a concave curve (or concave downward) with a global maximum at some temperature below the critical temperature of the solvent (Harvey, 1996), which for water is about 374℃. On the other hand, as P increases, $\frac{V^{\infty}_{CO_2(aq)}}{RT}(P - P^0)$ becomes relevant and, because it decreases asymptotically with T, the location of $K_H(T)$ global maximum is moved to lower temperatures. This yields to the conclusion that $m_{CO_2(aq)}$ is a convex function (or concave upward) with a P dependent global minimum (see Figure 3.5).

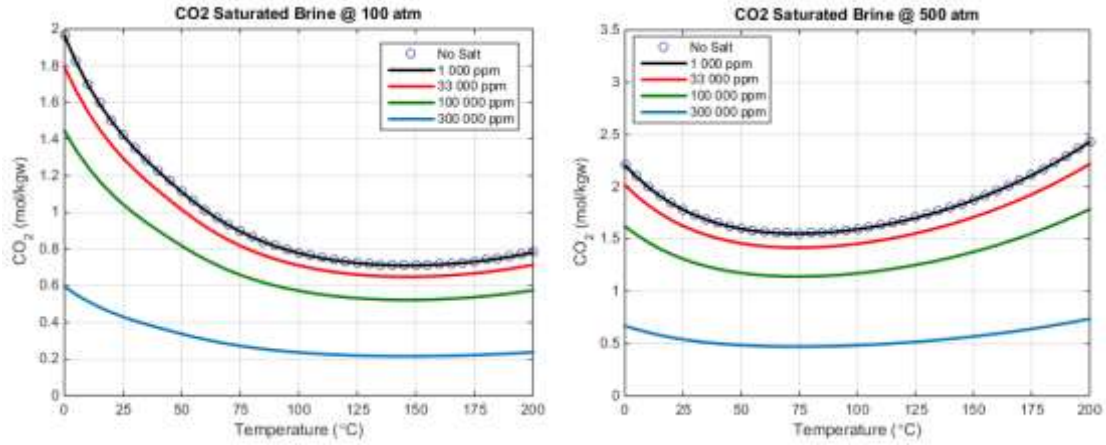

Figure 3.5. CO_2 Solubility with varying temperature for selected brines at 100 (left) and 500 atm (right), calculated by PHREEQC.

Moreover, as previously discussed, the addition of salts to the system decreases the CO_2 solubility by increasing $\gamma_{CO_2(aq)}$. However, the CO_2 solubility in pure water is sufficient to calculate m_{HCO_3} and m_{Ca} (using equations (2.26) and (2.27)) because the activity of aqueous CO_2 in brine is equivalent to its molality in pure water (where $\gamma_{CO_2(aq)} = 1$).

To make our model simple, we would like it to be explicitly dependent on T, P and salinity only. Thus, we chose to find empirical expressions for $K_{sp,1}(T, P)$ and

$m_{CO_2(aq)}(T,P)$ by fitting the calculated values provided by PHREEQC. The fitting procedure was performed by doing two sets of simulations: (a) isobaric and (b) isothermal. For $K_{sp,1}(T,P)$ calculations were done in the logarithmic scale in the range of $0 < T(℃) < 300$ and $1 < P(bar) < 700$:

$$\log K_{sp,1}(T,P) = -4.2 - \frac{5 \cdot T}{1000}\left(1.5 + \frac{T}{100}\right) + \left(7.6 - \frac{T}{100}\right) \cdot \frac{P}{10000} \tag{3.27}$$

On the other hand, for $m_{CO_2(aq)}(T,P)$ we avoided the range of low T and P because the physical properties (like compressibility) diverge near the CO_2 critical point (30.97 ℃ and 73.9 bar). Therefore, we performed the fitting in supercritical conditions and sufficiently far from the critical pressure ($300 < P(bar) < 700$), where the solubility grows linearly with pressure (Wiebe and Gaddy, 1939 & 1940), while the temperature range was $50 < T(℃) < 150$ to avoid the near critical temperature of both CO_2 and H_2O. The selected region comprises solubility values that are close enough to the global minimum in isobaric processes and therefore are easily fitted by quadratic curves.

$$m_{CO_2(aq)}(T,P) = f_1(P) \cdot \left(\frac{T}{150}\right)^2 + f_2(P) \cdot \frac{T}{150} + f_3(P) \tag{3.28}$$

Moreover, by selecting single values for P each isobaric curve was obtained and then polynomials were used to find the P dependent coefficients:

$$f_1(P) = 5.6 \times 10^{-4} \cdot P + 1.551 \tag{3.29a}$$

$$f_2(P) = -1.0 \times 10^{-6} \cdot P^2 + 8.4 \times 10^{-4} \cdot P - 1.37 \tag{3.29b}$$

$$f_3(P) = 1.19 \times 10^{-3} \cdot P + 0.632 \tag{3.29c}$$

Finally, the only parameters that still have to be determined are γ_{Ca} and γ_1, which will correct the concentration of HCO_3 in equilibrium and consequently the concentration of Ca. However, because our approach is to first calculate m_{HCO_3} via a cubic equation (equation (2.26)), which encapsulate the charge balance of non-reactive ions, and then use the solution to obtain m_{Ca} (equation (2.27)), the impact of the activity coefficients will be lower for increasing $-\varepsilon$. To see this, one can write an expression of the relative error in obtaining m_{Ca} between our model and a general one:

$$Rel.Error(\%) = 100 \cdot \frac{\frac{(m_{\mathrm{HCO3}} - \varepsilon)}{2} - \frac{\left(\frac{m_{\mathrm{HCO3}}}{C_\gamma} - \varepsilon\right)}{2}}{\frac{\left(\frac{m_{\mathrm{HCO3}}}{C_\gamma} - \varepsilon\right)}{2}} = 100 \cdot \frac{1 - \frac{1}{C_\gamma}}{\frac{1}{C_\gamma} - \frac{\varepsilon}{m_{\mathrm{HCO3}}}} \quad (3.30)$$

where C_γ represents the correction due to activity coefficients.

Moreover, when $-\varepsilon$ is large equation (2.26) can be approximated by a quadratic equation because the cubic term becomes negligible compared to the quadratic term. Thus, for solutions with a higher difference between non-reactive anions and cations (higher Ca content) we have the following model:

$$m_{HCO_3^-} \approx \sqrt{\frac{2 \cdot \gamma_{CO_2(aq)} m_{CO_2} K_{sp,1}}{-\varepsilon}}; \quad (3.31a)$$

$$m_{\mathrm{Ca}} \approx \frac{\sqrt{\frac{2 \cdot \gamma_{CO_2(aq)} m_{CO_2} K_{sp,1}}{-\varepsilon}} - \varepsilon}{2} \quad (3.31b)$$

The resultant model, i.e. the cubic equation combined with the empirical expressions, provide simple polynomial functions to determine the molality of relevant species of the carbonic acid system (with calcite present) under conditions which most CO_2 EOR projects are planned.

In Figure 3.6, we show the behaviour of calcite solubility at 500 bars in two types of NaCl solutions according to our model and PHREEQC. As expected, there is a higher similarity between the two models for the results involving high salinity brine where values are around $-\varepsilon/2$. However, both models provide compatible values for temperatures above 62 ℃ where the absolute relative error between our model and PHREEQC is lower than 5% (for the lower salinity). Thus, equilibrium calculations from PHREEQC are essential for reservoir simulations that include heat exchange and exhibit a temperature drop around the injector wellbore during injection of colder fluids, like seawater and CO_2.

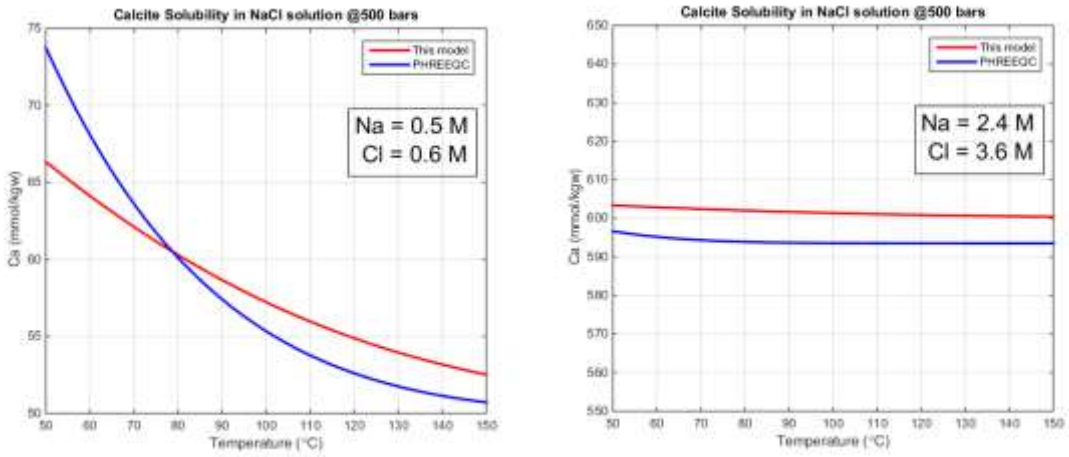

Figure 3.6. Calcite solubility in two NaCl solutions at 500 bars and different temperatures according to our model and PHREEQC. Results are compatible for temperatures higher than 62℃.

Chapter 4:
Reactive Transport of water and gas in 1D

After analysing the thermodynamics of the CO_2-$CaCO_3$-H_2O system, i.e. the physical-chemical interactions within the system in a static environment, we now proceed to the simulation of reactive transport.

To understand the changes in porosity and permeability given by mineral reactions during flow propagation, researchers have been using reactive transport simulations using different software packages (Lichtner, 1985; Steefel and Lasaga, 1994; Xu et al., 2011; Nghiem et al., 2011; Parkhurst and Appelo, 2013; Lichtner et al., 2013). Simulations involving injection of CO_2 in carbonate reservoir have also been carried out and under different scales and scenarios such as coreflooding (Wellman et al., 2003; Izgec et al., 2005; Mohamed and Nasr-El-Din, 2013), injection and production from aquifer (Mackay and Souza, 2014), oil recovery using a quarter of five-spot well pattern (Qiao et al., 2016) and carbon storage in aquifer (André et al., 2007; Tutolo et al, 2015). Although simulations at core-scale have matched experimental results, the flow rate in this condition is limited and lower than simulations at larger scales. Moreover, higher contact between injected water and injected gas in the porous medium causes more mineral dissolution (Mackay and Souza, 2014; Qiao et al., 2016), and that cannot be achieved or observed in shorter scales.

In this Chapter, we perform reactive transport simulations using PHREEQC and CMG GEM to investigate the effects of adding CO_2 and seawater to a carbonate aquifer. As PHREEQC is limited to 1D transport of water only, we used this software to simulate the injection of water saturated with CO_2 (carbonated water). Then, we used GEM to simulate the same scenario and also the injection of seawater, CO_2 gas, CO_2 WAG and CO_2 SWAG (simultaneous water and CO_2 gas injection). Simulation results are compatible for the case of carbonated water, but also reveal the importance of having the capability to simulate multiphase reactive transport, as results for the other scenarios are qualitatively and quantitatively different.

4.1. Fundamentals of reactive transport simulation

The equation that rules the behaviour of the aqueous concentration of a chemical species a in space and time is known as the Advection-Reaction-Dispersion (ARD) equation (Steefel, 2008; Appelo and Postma, 2013) and for a porous media it can be written in the following form

$$\frac{\partial(\emptyset C_a)}{\partial t} + \nabla \cdot (\emptyset \vec{v}_w C_a) - \nabla \cdot \left(\emptyset \overleftrightarrow{D}\, \nabla C_a\right) = R_a \tag{4.1}$$

where $\emptyset$ is the porosity of the medium, C_a is the molal concentration of species a (mol/volume), $\overleftrightarrow{D}$ is the hydrodynamic dispersion tensor (1/length . time), R_a is the kinetic reaction rate of species a (mol/volume . time), $\vec{v}_w$ is the flow velocity of water (length/time).

The ARD equation works under the assumption of incompressible flow, i.e. water has constant density. In addition, for laminar flows we can use Darcy's Law (Bear, 1972)

$$\emptyset \vec{v}_w = \vec{q}_w = -\frac{K}{\mu}\, \nabla P \tag{4.2}$$

where K is the permeability of the medium, μ is the viscosity of water and ∇P is the pressure gradient.

Thus, we can write

$$\frac{\partial(\emptyset C_a)}{\partial t} + \nabla \cdot (\vec{q}_w C_a) - \nabla \cdot \left(\emptyset \overleftrightarrow{D}\, \nabla C_a\right) = R_a \tag{4.3}$$

Finally, for reactions that can be described by single chemical components (Steefel, 2008) we have

$$\frac{\partial(\emptyset C_a)}{\partial t} + \nabla \cdot (\vec{q}_w C_a) - \nabla \cdot \left(\emptyset \overleftrightarrow{D}\, \nabla C_a\right) = kA\left(1 - \frac{C_a}{C_{eq}}\right) \tag{4.4}$$

where k is the rate constant of reaction [mol/area . time], A is the reactive surface area per volume ratio and C_{eq} is the equilibrium concentration for species a.

4.1.1. *Peclet and Damköhler numbers*

For simplicity, we assume the flow is unidimensional, the porous media is homogeneous and that there are no significant changes in the flow or in the porous medium. Thus, we neglect the time derivative and write the equation for stationary flux:

$$q_w \frac{\partial C_a}{\partial x} - \emptyset D \frac{\partial^2 C_a}{\partial x^2} = kA\left(1 - \frac{C_a}{C_{eq}}\right) \tag{4.5}$$

The differential terms on the left side of the equation are called advection and diffusion (or dispersion) terms, respectively. The comparison between the advection and diffusion terms can produce three different solutions for the equation.

- Case 1: Advection dominates over dispersion and diffusion

$$q_w \frac{\partial C_a}{\partial x} = kA\left(1 - \frac{C_a}{C_{eq}}\right) \tag{4.6a}$$

$$\Rightarrow C_a(x) = C_{eq} + (C_{initial} - C_{eq})\exp\left[-\frac{kAx}{q_w C_{eq}}\right] \tag{4.6b}$$

- Case 2: Dispersion or diffusion dominate over advection

$$\emptyset D \frac{\partial^2 C_a}{\partial x^2} = -kA\left(1 - \frac{C_a}{C_{eq}}\right) \tag{4.7a}$$

$$\Rightarrow C_a(x) = C_{eq} + (C_{initial} - C_{eq})\exp\left[-\sqrt{\frac{kA}{\emptyset D C_{eq}}} \cdot x\right] \tag{4.7b}$$

- Case 3: Advection and dispersion/diffusion compete

$$q_w \frac{\partial C_a}{\partial x} - \emptyset D \frac{\partial^2 C_a}{\partial x^2} = kA\left(1 - \frac{C_a}{C_{eq}}\right) \tag{4.8a}$$

$$\Rightarrow C_a(x) = C_{eq} + (C_{initial} - C_{eq})\exp\left[\left(\frac{q_w}{2\emptyset D} - \sqrt{\left(\frac{q_w}{2\emptyset D}\right)^2 + \frac{kA}{\emptyset D C_{eq}}}\right) \cdot x\right] \tag{4.8b}$$

All obtained solutions reproduce an exponential decay with increasing x. If we change the scale by doing $x \rightarrow x'l$, we arrive at

$$\frac{C_a(x) - C_{eq}}{C_{initial} - C_{eq}} = \exp[-Da_I \cdot x'] \tag{4.9}$$

$$\frac{C_a(x) - C_{eq}}{C_{initial} - C_{eq}} = \exp[-\sqrt{Da_{II}} \cdot x'] \tag{4.10}$$

$$\frac{C_a(x) - C_{eq}}{C_{initial} - C_{eq}} = \exp\left[\left(\frac{Pe}{2} - \sqrt{\left(\frac{Pe}{2}\right)^2 + Da_{II}}\right) \cdot x'\right] \tag{4.11}$$

where the exponents are known as Damköhler numbers and Peclet number

$$Da_I = \frac{kAl}{q_w C_{eq}}, \qquad Da_{II} = \frac{kAl^2}{\emptyset D C_{eq}}, \qquad Pe = \frac{q_w l}{\emptyset D} \tag{4.12}$$

The Damköhler numbers are the ratios between resident time (advection time for Da_I or diffusion/dispersion time for Da_{II}) and reaction time, while the Peclet number relates the advection transport against the diffusion/dispersion transport (Steefel, 2008).

These dimensionless numbers can be used to calculate the equilibration length λ, which is an estimation for the distance required to reach equilibrium. This is calculated by multiplying $-l$ by the inverse of the exponent:

$$\lambda_{advection} = \frac{l}{Da_I} = \frac{q_w C_{eq}}{kA} \tag{4.13}$$

$$\lambda_{diffusion} = \frac{l}{\sqrt{Da_{II}}} = \frac{\emptyset D C_{eq}}{kA} \tag{4.14}$$

$$\lambda_{mixed} = \frac{l}{-\frac{Pe}{2} + \sqrt{\left(\frac{Pe}{2}\right)^2 + Da_{II}}} = \frac{1}{-\frac{q_w}{2\emptyset D} + \sqrt{\left(\frac{q_w}{2\emptyset D}\right)^2 + \frac{kA}{\emptyset D C_{eq}}}} \tag{4.15}$$

Note that as $[kA/C_{eq}]$ increases (i.e. higher reaction rate) the distance to reach equilibrium decreases asymptotically to zero. Moreover, for advection-dominated flows, the fluid equilibrates before travelling through the characteristic length l when $Da_I >> 1$ and kinetics are not important (reaction rate is transport controlled), otherwise the

fluid may be not in equilibrium and kinetics must be considered (reaction rate is kinetics controlled).

It is known that for flow velocities higher than 15 cm/day, diffusion can be neglected (Appelo and Postma, 2013) and the dispersion can be treated as a product of the flow velocity and a constant called dispersivity (α):

$$\mathrm{D} = \alpha \mathrm{v} = \alpha \frac{\mathrm{q_w}}{\emptyset} \tag{4.16}$$

and

$$\mathrm{Pe} = \frac{\mathrm{l}}{\alpha}, \qquad \mathrm{Da_{II}} = \mathrm{Da_I} \frac{\mathrm{l}}{\alpha} \tag{4.17}$$

Thus

$$\lambda_{\mathrm{mixed}} = \frac{1}{-\frac{1}{2\alpha} + \sqrt{\left(\frac{1}{2\alpha}\right)^2 + \mathrm{Da_I} \frac{1}{\alpha}}} \tag{4.18}$$

Therefore, for flows with competing advection and dispersion the equilibration length increases with $1/\mathrm{Da_I}$ and α.

4.1.2. *Numerical Dispersion*

Finite-difference operators, which are used to approximate the time and spatial derivatives, introduce errors to numerical simulation. Truncation errors of second order produce effects similar to dispersion and thus the numerical solution of pure advective transport resembles the analytical solution of an advective-dispersion transport (Chen et al., 2006). This additional numerical dispersion can be used to model the physical dispersion by changing the size of the discretisation steps (Fanchi, 2006; Chen et al., 2006, Appelo and Postma, 2013). Peaceman (1977) calculates the numerical dispersion associated to different discretisation schemes for a generic first-order hyperbolic equation:

$$\frac{\partial \mathrm{u}}{\partial \mathrm{t}} + v f' \frac{\partial \mathrm{u}}{\partial \mathrm{x}} = 0 \tag{4.19}$$

where $f = f(u)$ is a linear function.

The discretisation schemes that are stable for $v > 0$ are backward in space (upwind or upstream scheme), while the discretisation in time can be forward (explicit) or backward (implicit). It is interesting to see that a centred discretisation scheme in both space and time is neutrally stable and does not exhibit numerical dispersion. However, truncation errors of higher order cause stable oscillations behind the mixing front (Peaceman, 1977).

Similar to physical dispersion, numerical dispersion can be translated to numerical dispersivity, and for equation 4.19 it is (Peaceman, 1977)

$$\alpha_{num} = \frac{\Delta x}{2} \pm \frac{v f' \cdot \Delta t}{2} \tag{4.20}$$

where the "+" sign applies for implicit discretisation, while the "−" sign represents the explicit scheme. When applied to the numerical solution of 2-phase immiscible flow, implicit means fully implicit (pressure and saturation equations are solved implicitly) while explicit means IMPES discretisation (implicit pressure and explicit saturation) (Fanchi, 2006).

The numerical dispersion generated for single-phase (non-reactive) transport has the same form of equation (4.20) (Herzer and Kinzelbach, 1989):

$$\alpha_{num,non-reactive} = \frac{\Delta x}{2} \pm \frac{v \cdot \Delta t}{2} \tag{4.20}$$

For reactive flows, one must include the retardation factor (R) associated to heterogeneous reactions (sorption, precipitation, dissolution, etc.) (Appelo and Postma, 2013):

$$R = \frac{C_{new} - C_{old}}{C_{new+react} - C_{old}} \tag{4.21}$$

where C_{old} is the old concentration in a cell, C_{new} is the concentration after the transport step, and $C_{new+react}$ is the concentration after reactions.

Herzer and Kinzelbach (1989) calculated the numerical dispersion for the two sets of numerical procedure used to solve reactive transport: global-step schemes (transport and reactions are calculated simultaneously in the same integration step) and operator-splitting schemes (transport and reactions are calculated sequentially, thus there is one

integration step for transport calculations followed by the calculation of reactions). They concluded that for operator-splitting schemes (also called two-step procedure) the additional numerical dispersion caused by retardation is independent of the discretisation scheme (i.e. forward, backward or centred). The numerical dispersivity for reactive transport can be written as

$$\alpha_{num,reactive} = \frac{\Delta x}{2} \pm \frac{v \cdot \Delta t}{2R} \tag{4.22}$$

The impact of retardation for global step schemes (also called one-step procedures) is either null or negative (dispersion becomes lower). However, the retardation factor is dependent on the conditions of the flow and porous media.

4.2. PHREEQC simulations

Now, we proceed to numerical simulation of reactive transport. First, we simulate single-phase flow using PHREEQC, while more complex flows are presented in the next section using GEM.

A unidimensional model was constructed using 15 blocks (grid cells) of 66 m of length, with fluids propagating from block 1 (injector) to block 15 (producer). All blocks contain 1 L of water (default) and calcite. The water in all blocks is initially in equilibrium with calcite and the volume of this mineral is the same everywhere. All reactions were modelled using equilibrium relations (no kinetic laws were used). The model is kept at 60 ℃ and 500 bar.

Boundary conditions of constant flux were assigned to blocks 1 and 15. PHREEQC transport calculations are performed by shifting all the water from one block (1 L) to its neighbour. In this sense, Darcy's Law is not used and therefore porosity, permeability and pressure gradient are not defined. However, dispersion can be part of the calculation and here dispersivity was set 33 m (half of the block length).

To make the simulation results comparable to GEM and other reservoir simulators, we calculated what would be the porosity change in a reservoir of 22% porosity based on the increase or decrease of moles of mineral due to dissolution or precipitation. This is a rather simple calculation because the porous volume in a block corresponds to the volume of water (1L) in PHREEQC and the volume change is the change in moles of calcite divided by its molar density (27 mol/L):

$$\emptyset_{PHREEQC} = 0.22 \cdot (1 \pm change\ in\ liters\ of\ calcite) \quad (4.23a)$$

$$\emptyset_{PHREEQC} = 0.22 \cdot \left(1 \pm \frac{change\ in\ moles\ of\ calcite}{27}\right) \quad (4.23b)$$

In addition to this pseudo porosity, we can calculate how an associated permeability would increase during dissolution of calcite, by using the standard Carman-Kozeny relation from GEM (GEM Manual, 2014):

$$\frac{\mathrm{k}_{current}}{\mathrm{k}_{initial}} = \left(\frac{\emptyset_{current}}{\emptyset_{initial}}\right)^3 \left(\frac{1-\emptyset_{initial}}{1-\emptyset_{current}}\right)^2 \quad (4.24)$$

Scenarios were configured to simulate injection of carbonated water in sandstone (initial calcite is limited) and carbonate formations (calcite is the dominant mineral). The injected water was either pure water or seawater saturated with CO_2 to match 0.423 mol/kgw of $CO_{2(aq)}$ in all cases (Tables 4.1 - 4.3).

Table 4.1. Simulated scenarios using PHREEQC transport model.

Scenario 1	**Scenario 2**	**Scenario 3**	**Scenario 4**
Reservoir 1 (Sandstone)	Reservoir 1 (Sandstone)	Reservoir 2 (Carbonate)	Reservoir 2 (Carbonate)
Pure water + CO_2 dissolved injected	Seawater + CO_2 dissolved injected	Pure water + CO_2 dissolved injected	Seawater + CO_2 dissolved injected

Table 4.2. Reservoir mineralogy used in simulated scenarios.

	Calcite (%)	**Quartz (%)**
Reservoir 1 (Sandstone)	0.5	99.5
Reservoir 2 (Carbonate)	78.0	22.0

Table 4.3. Composition of formation water and injected fluids for simulated scenarios.

	Formation Water	Pure Water + CO_2	Seawater + CO_2
Ca	0.526 M	0	0.010 M
HCO_3	0.002 M	0.0004 M	0.011 M
Mg	0.025 M	0	0.040 M
K	0.044 M	0	0.010 M
SO_4	0.004 M	0	0.030 M
Na	2.270 M	0	0.500 M
Cl	3.406 M	0	0.539 M

In scenario 1, calcite dissolves in the injector block before 1 pore volume (PV) is injected, while precipitation occurs in all other blocks. After that time, calcite is completely dissolved in the first block and the dissolution moves to subsequent blocks, one by one. The change of porosity is very small because it is limited to the initial volume of calcite. After 20 PV the water composition in the reservoir converges to the injected water, as shown in Figure 4.1, and there are no further changes in porosity. We also observed that before dissolution starts in each block, calcite precipitates slightly (Figure 4.2). We will see later on that the cause of this precipitation is the brine mixing which arises from the dispersion of the concentration fronts.

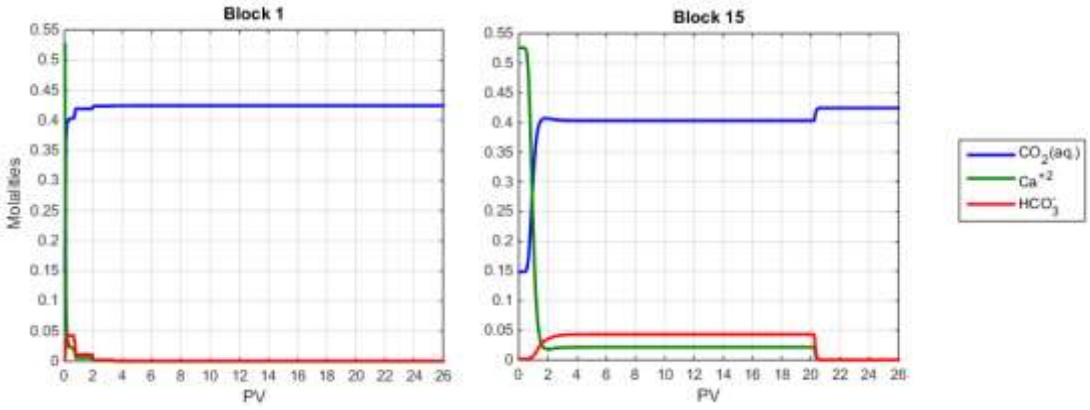

Figure 4.1. Water composition history of blocks 1 (left) and 15 (right) for scenario 1.

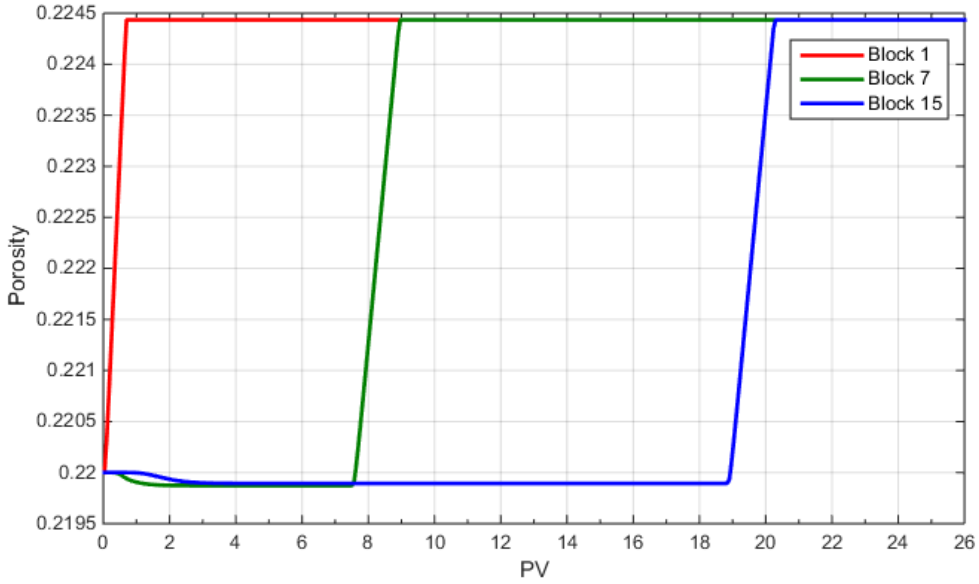

Figure 4.2. Porosity calculated from calcite volume change for scenario 1.

When brine is injected instead of water in the same type of reservoir (scenario 2), calcite is completely removed (by dissolution) from the system 3 PV earlier (see Figures 4.3 and 4.4). This is a consequence of the impact of charge balance between inert species in seawater (discussed in Chapter 2), which is lower than pure water (see Table 4.3).

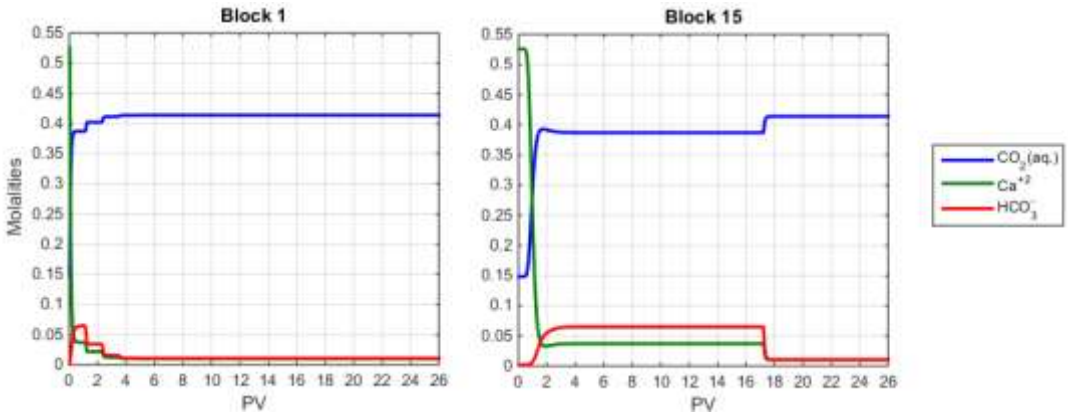

Figure 4.3. Water composition history of blocks 1 (left) and 15 (right) for scenario 2.

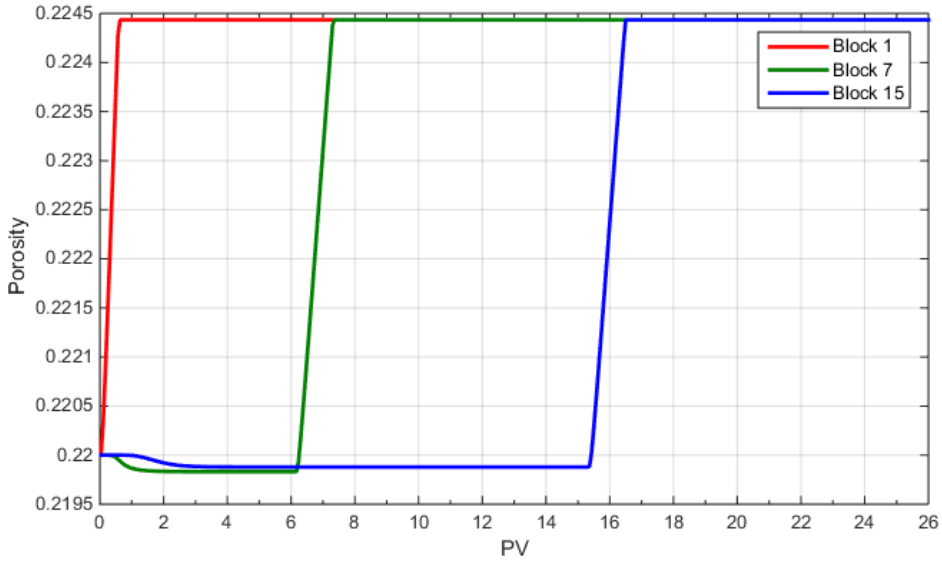

Figure 4.4. Porosity calculated from calcite volume change for scenario 2.

In scenario 3, the initial calcite was high enough and complete dissolution of it was not observed in any block. Therefore, dissolution only happens in the injector block, while calcite precipitates in other blocks (Figures 4.5 and 4.6). The dissolution is strong, continuous and localised, which yields a significant increase in porosity in the first block only.

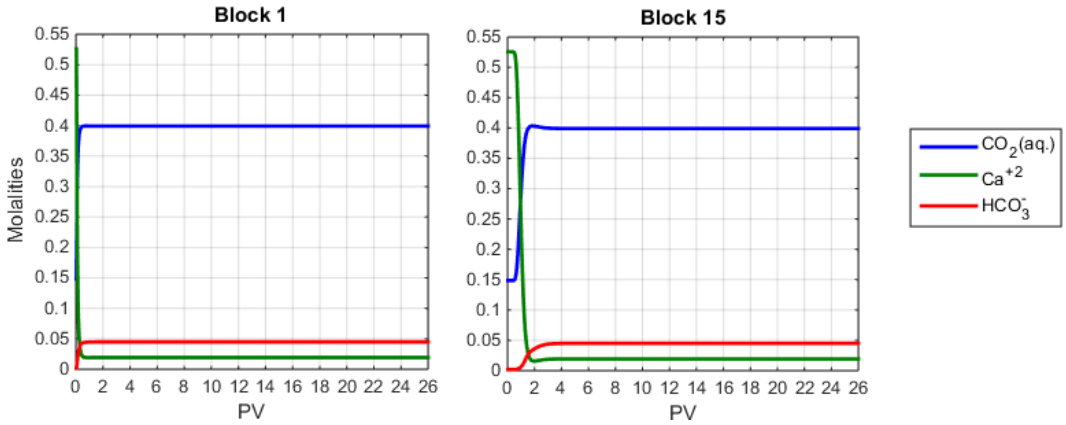

Figure 4.5. Water composition history of blocks 1 (left) and 15 (right) for scenario 3.

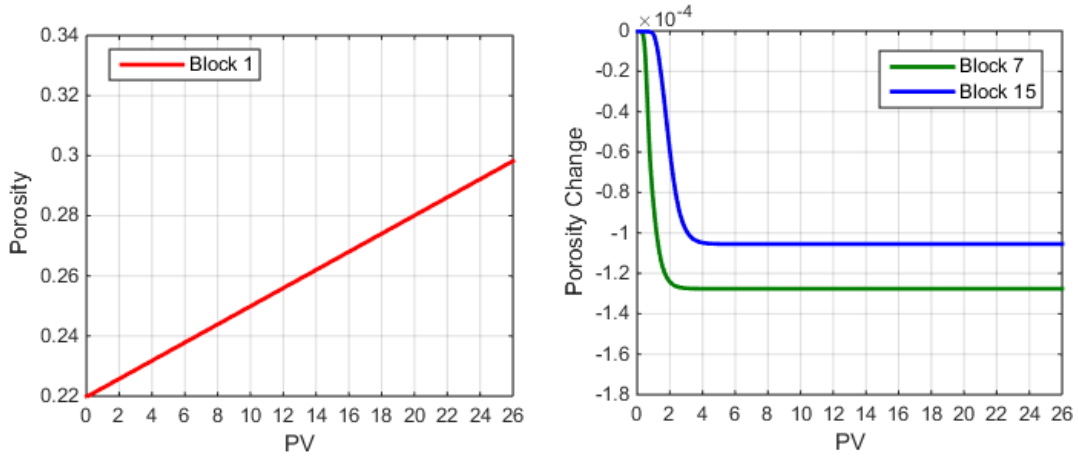

Figure 4.6. Porosity and porosity change (delta porosity) calculated from calcite volume change for scenario 3.

We can see that the precipitation is limited in time and decreases as the water propagates further. This precipitation is characteristic of scale formation caused by brine mixing, and it is usually observed for sulphate scales like $BaSO_4$. To show this, we run this simulation again with a pure advective transport (dispersion was disabled). The piston-like displacement of the formation water by the injected water can be observed in Figure 4.7. One can see that the concentrations in block 1 are constant from the start of the injection (that is the equilibrium between injected water and calcite). Moreover, in block 15 concentrations jump from the initial composition to equilibrium at exactly 1 PV.

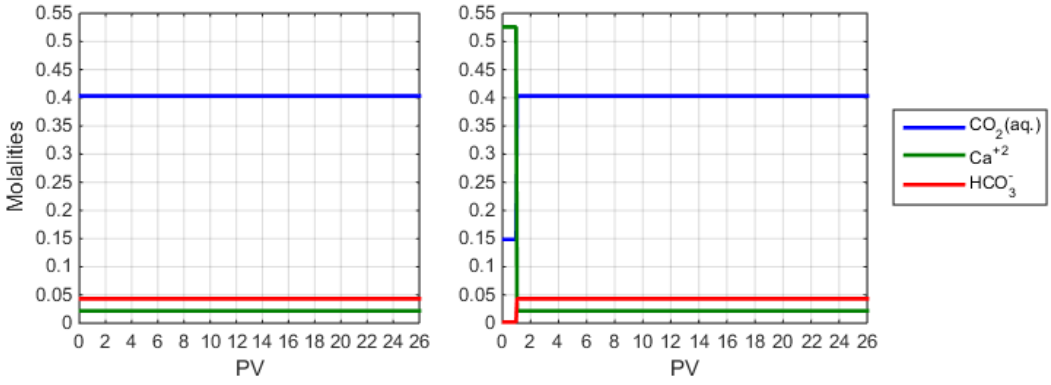

Figure 4.7. Water composition history of blocks 1 (left) and 15 (right) for scenario 3 without dispersion (pure advective transport or piston-like displacement).

The immediate convergence to equilibrium in block 1 still causes a continuous dissolution of calcite since the injected water is undersaturated. On the other hand, the equilibrated water that propagates to subsequent blocks does not trigger further reactions and therefore precipitation does not occur (Figure 4.8).

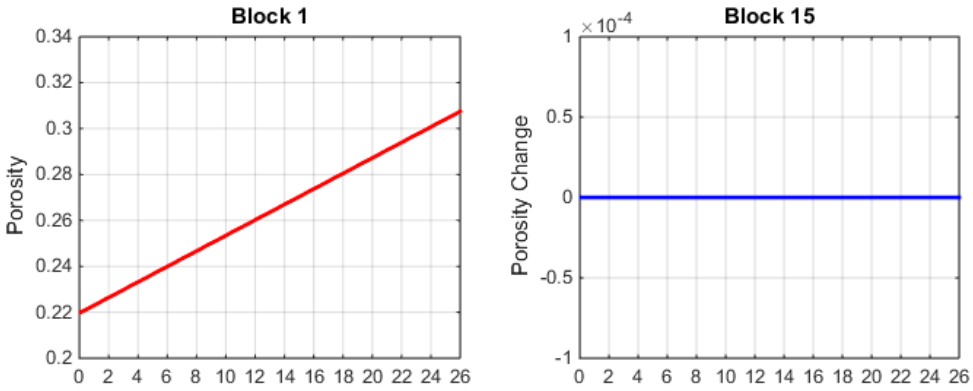

Figure 4.8. Porosity and porosity change (delta porosity) calculated from calcite volume change for scenario 3 without dispersion (pure advective transport or piston-like displacement).

In scenario 4, the injected seawater saturated with CO2 stimulates more dissolution in the first block and the additional Ca produced leads to more precipitation in downstream blocks as this brine mixes with the original HCO3 containing formation water (Figures 4.9 and 4.10).

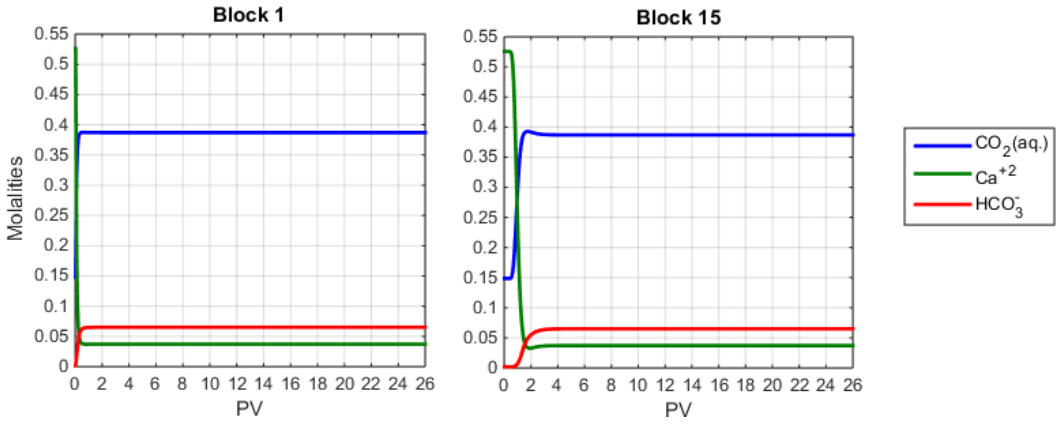

Figure 4.9. Water composition history of blocks 1 (left) and 15 (right) for scenario 4.

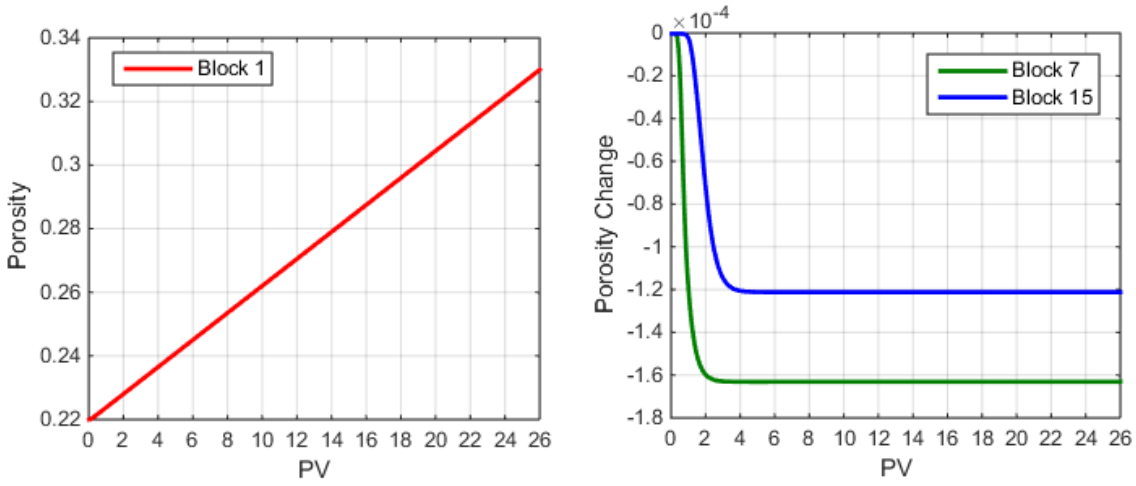

Figure 4.10. Porosity and porosity change (delta porosity) calculated from calcite volume change for scenario 4.

Finally, we show in Figure 4.11 the growth of permeability against the porosity increase. One can see that permeability (and also porosity) are significant only when there is enough calcite to be dissolved. Moreover, an increase in porosity from 22% to 32% leads to permeability four times larger.

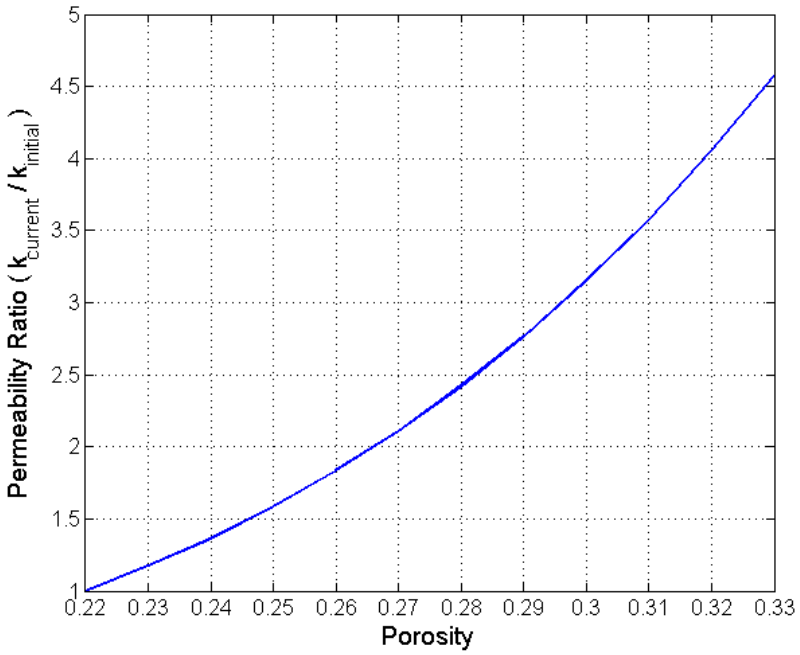

Figure 4.11. Permeability growth during scenarios according to Carman-Kozeny relation. The stronger dissolution observed in scenario 4 is responsible to increase the permeability by 4.5 times, while the permeability in scenario 3 becomes just 3 times larger.

The importance of these results is that the strength of the dissolution is dependent on the composition of injected water (charge balance between non-reactive ions) and precipitation downstream is triggered because of mixing between injected water (high in HCO_3 from dissolution of CO_2 and calcite in it) and formation water (high in Ca). Moreover, for stronger dissolution in the inlet the precipitation is also stronger.

These conclusions is our starting point in the understanding of the reactions during injection of CO_2 WAG where the pressure changes will alter the equilibrium concentrations as the water propagates.

4.3. GEM

4.3.1. Damköhler analysis

In GEM, equilibrium calculations are performed for all aqueous (homogeneous) reactions and also for vapour-liquid mass exchange (e.g. dissolution of gas in water). On the other hand, mineral dissolution and precipitation reactions are modelled by the kinetic law of Bethke (1996):

$$r_\beta = A_\beta k_\beta \left(1 - \frac{Q_\beta}{K_{eq,\beta}}\right) \tag{4.25}$$

where r_β is the rate (mol/m^3/sec), A_β is the reactive surface area (m^2/m^3) for mineral β, k_β is the rate constant (mol/m^2/sec) of mineral reaction β, $K_{eq,\beta}$ is the chemical equilibrium constant for mineral reaction β and Q_β is the activity product of mineral reaction β.

Since we are interested in modelling calcite dissolution and precipitation we need to specify A_β and k_β. A_β for calcite varies from 10^2 to 10^5 m^2/m^3 (Walter and Morse, 1984; Chou et al., 1989; Brosse et al., 2005; Finneran and Morse, 2009), while k_β is more accurate and has been determined experimentally to be equal or higher than 10^{-5} mol/m^2/sec for $pH \leq 5$ and temperatures between 25 and 100 ℃ (Plummer et al. 1978; Pokrovsky et al., 2009). We have simulated calcite dissolution during injection of carbonated water (seawater plus CO2) in a 1D limestone (100% calcite) reservoir to calculate the Damköhler number (Da_I) under different flow regimes. Water composition is the same as in Table 4.3, while the parameters of the simulation are displayed in Table 4.4.

Table 4.4. Grid properties, initial and boundary conditions for Damköhler study

Model Dimensions	100 x 10 x 10 m
Grid Resolution	1 x 10 x 10 m
Porosity	0.22
Permeability (homogenous)	400 mD
Reservoir Temperature	60℃
Reservoir Pressure	500 bar
Water Saturation	100%
Calcite Kinetic Rate	10^{-5} mol/m^2.s
Calcite Reactive Surface Area	Case dependent
Maximum Bottom-hole Fluid Rate in injector well	Case dependent
Minimum Bottom-hole Pressure in producer well	500 bar

The first set of simulations consisted in setting A_β to 1 m^2/m^3 and increasing the injection flow rate from 1 to 200 m^3/d. Figure 4.12 shows that increasing the injection rate causes an increase in the calcite dissolution rate. However, after the injection rate increases by more the two orders of magnitude the dissolution rate does not increase as much and remains one order lower. As the injection rate increases, the residence time becomes lower than the reaction time and the reaction is incomplete and does not reach equilibrium (low Da_I). This can be observed by looking at the equilibrium length ($\lambda_{\text{advection}}$), which becomes larger than the block length (see Figure 4.13).

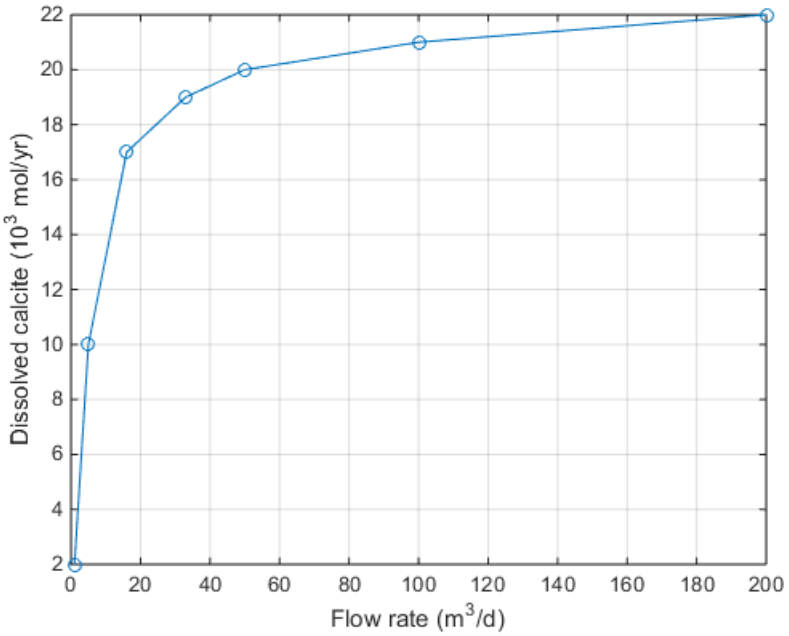

Figure 4.12. Calcite dissolution rate in the first block for increasing flow rate. Equilibrium is reached only for low injection rates.

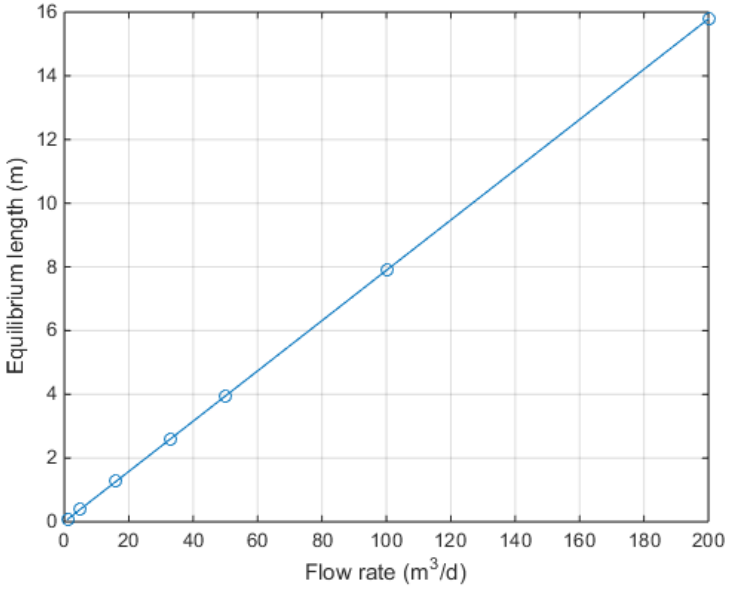

Figure 4.13. Calculated equilibrium length (advective transport) for increasing flow rate.

A second set of simulation was performed. This time we set the flow rate to 100 m^3/d and varied A_β from 0.1 to 10^4 m^2/m^3. As A_β increases the dissolution rate increases by the same order of magnitude until 10 m^2/m^3. This shows the transition from a kinetic controlled regime, where the kinetic rate controls the dissolution rate of calcite

since equilibrium is not reached, to a transport controlled regime, where dissolution rate is determined by the flow rate since the residence time becomes larger than the time to reach equilibrium (see Figure 4.14).

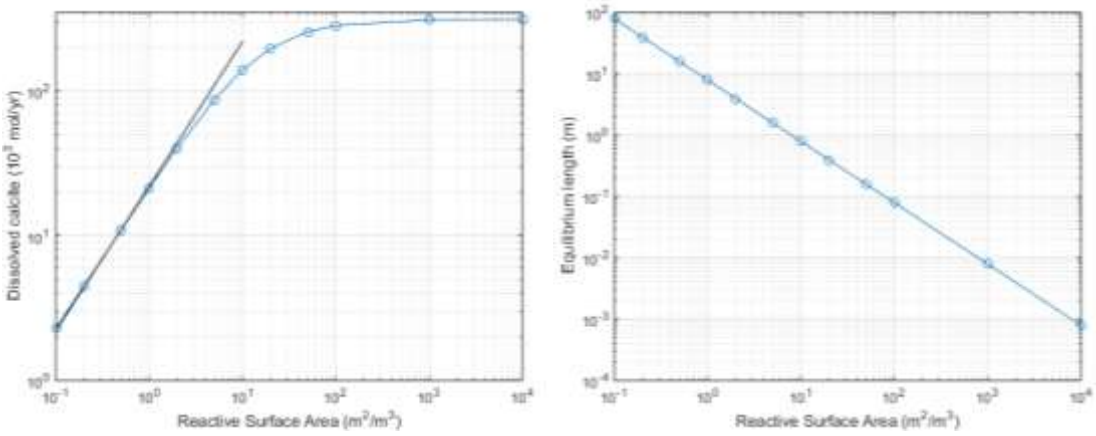

Figure 4.14. Calcite dissolution rate in the first block (left) and calculated equilibrium length (advective transport) (right) for increasing flow rate.

It is clear that the equilibrium length and its reciprocal (Da_I) are useful to identify if kinetic laws are needed for a given configuration of simulation run (grid dimensions, flow rate and kinetic parameters). Therefore, to complete this analysis, we calculated Da_I for different configurations to determine in which conditions we have $0.01 < Da_I$ (kinetic controlled) and $Da_I < 100$ (transport controlled). In Figure 4.15, we show a Damköhler mapping which shows that kinetic laws must be used for kinetic rates lower than 0.001 mM/sec ($A_\beta < 10$ m^2/m^3). If a more restrictive criterion for kinetic-limited regime is used, such as $1 < Da_I$, then kinetic rates lower than 0.1 mM/sec ($A_\beta < 1000$ m^2/m^3) are not enough for the transported water to reach equilibrium in grid blocks of 1 m^3.

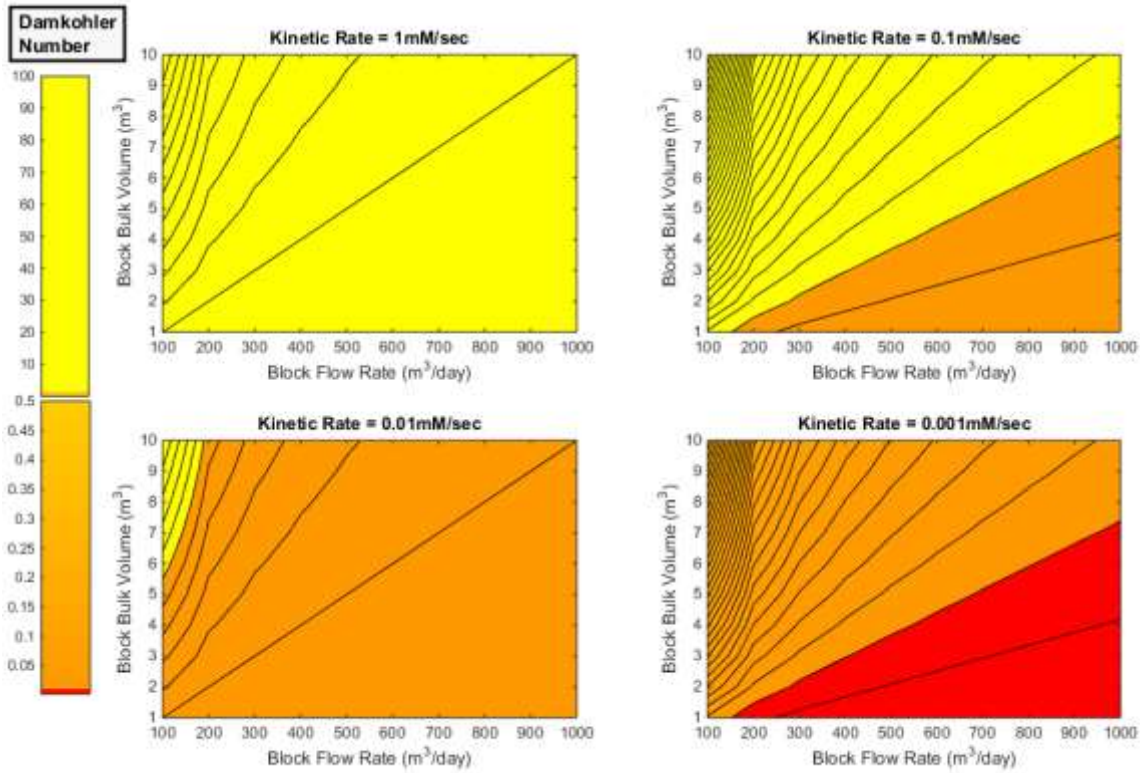

Figure 4.15. Calculated Damköhler mapping. Yellow coloured regions indicate configurations that equilibrium assumption is valid (transport-limited regime), while red coloured regions require kinetic laws modelling (kinetic-limited regime) and orange are transition regime.

These are very important results for reservoir simulation at reservoir scale (i.e. grid block dimensions in the order of a few meters). When the reservoir mineralogy is almost completely calcite, A_β is high enough (since the internal surface of the pores is formed of reactive material). On the other hand, in multi-mineral systems which exhibit other less reactive minerals (e.g. clays, silica, etc.), calcite can get shielded from dissolution (A_β will be lower) and therefore the reactive transport may be kinetic controlled. In addition, the wetting state of the reservoir rock may reduce the contact between water and the pore surface (formation of oil films in oil-wet or mixed-wet pores). This decrease in A_β due to impurities and oil films in the pores of limestone rocks will be more severe when the simulation is at the core scale and even worse at the pore scale. For the purpose of this thesis, we do not include this detrimental effect on A_β since our grid blocks are large enough (block volume > 100 m^3) and we assume all models to be a limestone reservoir (100% calcite). However, this is a relevant issue and the impact of impurities in A_β should be investigated to validate the transport controlled regime for calcite in more complex carbonate rocks.

4.3.2. Simulation of single-phase reactive transport

In GEM, we simulated the injection of seawater, carbonated water (seawater saturated with 1 bar CO_2) and CO_2 Gas, in a 1D model of limestone reservoir. Although in reality the injected CO_2 may have the properties of a gaseous or of a supercritical dense phase, in the model it is treated as being injected in the gas phase, and so hereafter we refer to gas injection as synonymous to CO_2 injection.

An inter-well distance of 2000 m was divided in 20 blocks of equal length and bulk cross-section area of 225 m^2. The injector well was placed in block 1 with maximum bottom-hole fluid rate of 50 m^3/d (~1 m/d in porous media), while the producer was located in block 20 with minimum bottom-hole pressure of 500 bar.

The numerical scheme adopted was implicit for the injector and producer blocks, and explicit for all other blocks, while a maximum time step (Δt) of 1 day was chosen to honour the CFL limit (i.e. $\Delta t \leq \Delta x/v$). This made the numerical dispersivity dependent on the grid block size (Δx), as $\Delta x \gg v \cdot \Delta t$.

All simulations were isothermal with temperature equal to 60℃, while the initial reservoir pressure was 545 bar. The rate constant of calcite dissolution/precipitation was set to 10^{-5} $mol/m^2/sec$ while A_β was 10 000 m^2/m^3, which translates to a kinetic rate of approximately 0.1 mM/sec. During porosity changes, permeability is updated using Carman-Kozeny formula (Equation 4.24). Since our focus is on assessing the mineral reactions that happen when the aqueous phase interacts with rock matrix, the model is initially saturated with water. The concentrations of injected waters as well as formation water were adapted from Mackay and Souza (2014) and are displayed in Table 4.5.

Table 4.5. Composition of injected and formation waters in milimoles per kilogram of water (mmol/kgw) and parts per million (ppm).

	Carbonated water		**Seawater**		**Formation water**	
pH	4.63		7.81		4.68	
Conc.	mmol/kgw	ppm	mmol/kgw	ppm	mmol/kgw	Ppm
CO_2	31	1314	0.02	0.8	113	4118
Ca	10	385	10	386	554	18356
HCO_3	1.1	64	0.98	64	11	556
Mg	49	1133	49	1134	26	515
K	10	376	10	376	45	1454
SO_4	29	2682	29	2686	4	318
Na	500	11080	500	11094	2267	43191
Cl	570	19496	570	19521	3506	103129

It was observed that if seawater is injected calcite dissolution occurs when the injected fluid (which contains lower concentration of Ca and HCO_3) reaches each block. However, with the exception of block 1 (injector), the dissolution is limited and stops after the mixing front propagates through the block (see Figure 4.16). Calcite is continuously dissolved only in the injector block because the injected water is not equilibrated with the mineral. Moreover, after the mixing front leaves the first block, the water that goes to the next block is already equilibrated and does not trigger mineral reactions.

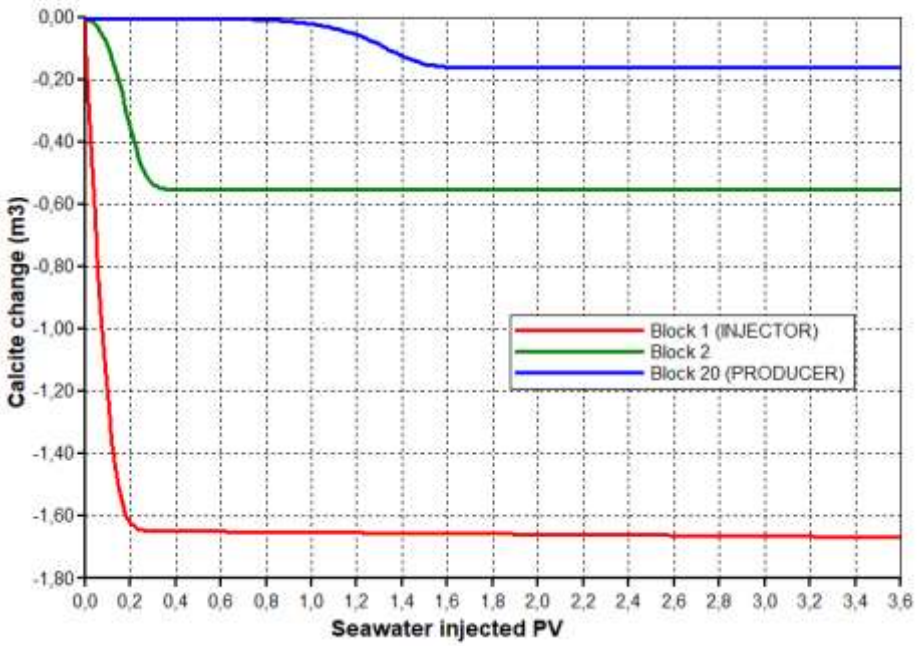

Figure 4.16. Calcite change in m^3 at blocks 1 (injector), 2 and 20 (producer) during seawater injection. Mineral dissolution at the producer stops after 1.60 injected PV.

The dissolution rate in block 1 decreased by more than 50 times after 0.20 PV. To address this issue, we observed that the saturation ratio of calcite depends on H^+ concentration and that increases with CO_2 concentration because they are linked by an equilibrium relation (Equation 2.5). In addition, it was found that the initial dissolved CO_2 takes the same time to be flushed out (see Figure 4.17) and thus the (kinetic) dissolution rate for calcite is reduced.

Moreover, calcite dissolution at the producer started when the formation water has been displaced almost completely, and stops shortly when the initial dissolved CO_2 has been produced. This is an important result because it shows that the presence of CO_2 in formation water must be considered to better estimate calcite dissolution during waterflooding (neglecting the initial CO_2 leads to predictions of lower mineral

dissolution). Limestones at similar conditions of temperature and pressure will show higher mineral changes for higher amount of CO_2 either dissolved or in the gas phase.

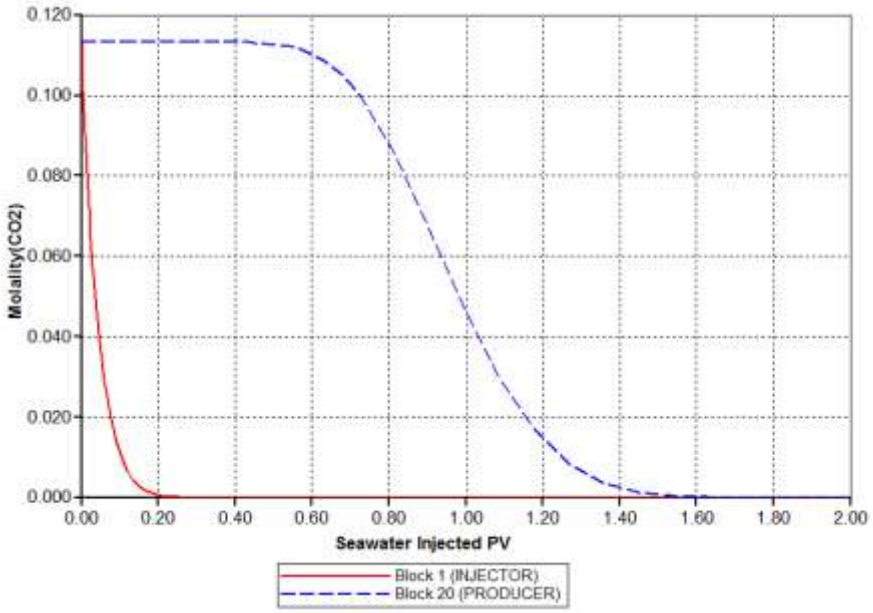

Figure 4.17. CO_2 concentration in molality at blocks 1 (injector) and 20 (producer) during seawater injection.

On the other hand, CO_2 can be previously dissolved in seawater (to form carbonated water) and then injected. In this scenario, calcite dissolves in the injector block and precipitates downstream. This time the mineral dissolution in injector is faster because of higher concentration of CO_2 in the injected water. However, the water also contains a higher amount of HCO_3 (produced by calcite dissolution and CO_2 speciation in water) which interacts with the high Ca formation water and cause (limited) precipitation during the propagation of the mixing front in each block, but with intensity decreasing with distance (see Figure 4.18). This physical alteration of higher calcite dissolution combined with precipitation in adjacent regions of the reservoir was previously observed in reactive transport simulations of carbonated water injection (André et al., 2007; Qiao et al, 2016). However, our simulations are different because the injected water was saturated at surface conditions, while it is usually saturated at reservoir conditions. Therefore, in our case, the dissolution rate is lower but still high enough to trigger the precipitation due to brine mixing. Nevertheless, for reservoirs with lower initial concentrations of Ca and HCO_3, saturating the water with CO_2 at lower pressures may not be enough for the precipitation to occur.

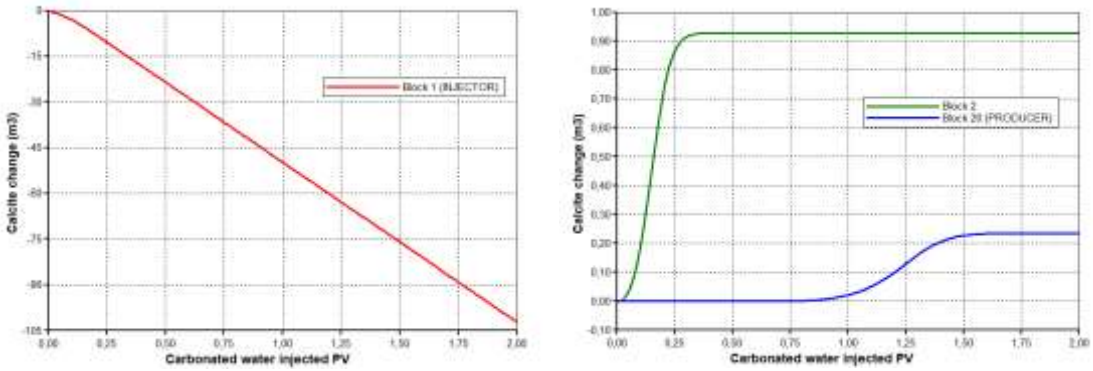

Figure 4.18. Calcite change in m^3 at blocks 1 (left), 2 and 20 (right) during carbonated water injection. Mineral dissolution in injector is faster than the seawater injection scenario.

A different behaviour was observed during CO_2 gas injection. For this scenario calcite was dissolved across the entire reservoir. The mineral dissolution was much faster than the other two cases. Because in the simulator dissolution of gaseous CO_2 in water is instantaneous (as well as the convergence of aqueous reaction to equilibrium), the mineral dissolution rate is high from the start. However, after the water is equilibrated with both the mineral and gas phases, the additional CO_2 gas, that is continuously injected, does not dissolve anymore in water and calcite dissolution stops (see Figure 4.19). Since the mineral dissolution is limited by the availability of water, the porosity alterations during continuous CO_2 gas injection are much smaller than the previous scenarios (André et al., 2007; Tutolo et al., 2015; Qiao et al, 2016).

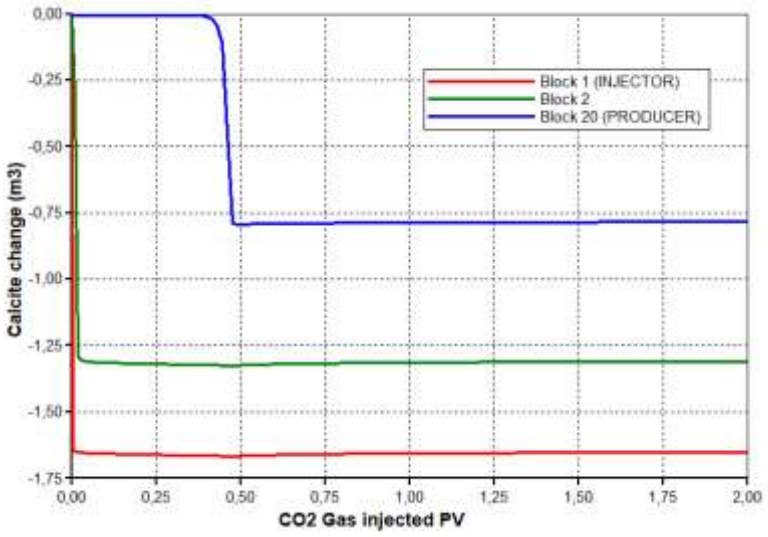

Figure 4.19. Calcite change in m^3 at blocks 1 (injector), 2 and 20 (producer) during CO_2 gas injection. Mineral dissolution is limited everywhere and the dissolution front reaches the producer earlier than the water injection scenarios.

In addition, as soon as CO_2 is injected, water is produced and the average gas saturation grows linearly with injected PV until about half of the total reservoir pore volume. From this point and forward the injected gas breaks through and the gas saturation increase is slower (Figure 4.20). This means that the gas phase occupies around 0.50 of the total reservoir pore volume just after reaching the producer and therefore calcite reaction in the last block happens earlier when compared to water (carbonated or sea water) injection which needs 1 injected PV.

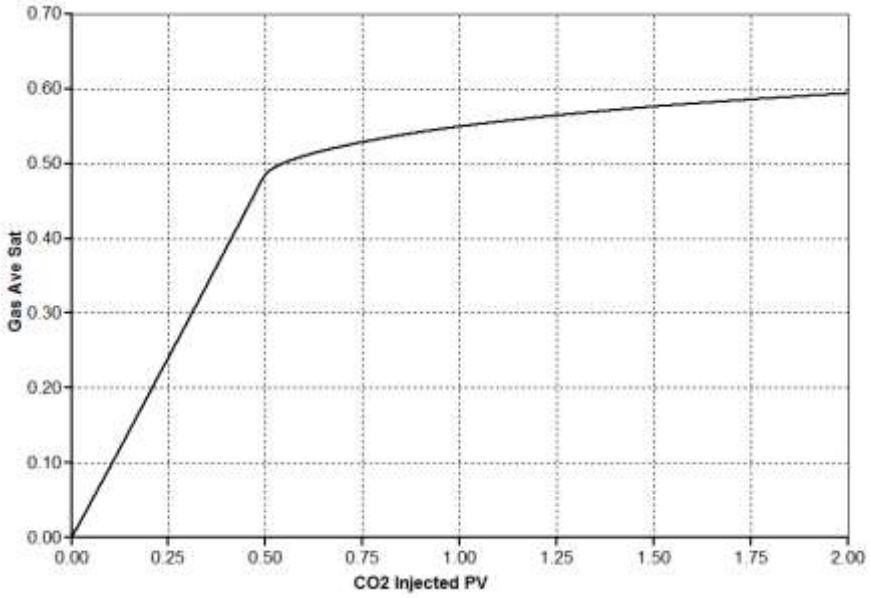

Figure 4.20. CO_2 gas average saturation during CO_2 gas injection. The gas saturation increases linearly with time until the CO_2 reaches the last block.

4.3.3. Simulation of 2-phase reactive transport: CO_2 WAG & CO_2 SWAG

After analysing the calcite dissolution and precipitation during the injection of single-phase fluids we are ready to understand some phenomena that occurs during CO_2 WAG.

For CO_2 WAG we started with the sea water injection and then we alternate for CO_2 gas injection, which completes a WAG cycle of 120 days. The duration of gas (T_G) and water (T_W) injections were set in terms of the WAG ratio:

$$T_G = 120\ days/(WAG\ ratio + 1) \tag{4.26}$$

$$T_W = T_G \times WAG\ ratio \tag{4.27}$$

We also simulate, for comparison, one important EOR method called CO_2 SWAG (simultaneous water and gas injection), which is a special case of WAG. In our simulations for CO_2 SWAG, we injected sea water and CO_2 simultaneously, each with half of the bottom-hole fluid rate used in WAG.

We observed that for both processes, calcite was continuously dissolved in the injector block, although for CO_2 WAG most part of the dissolution occurred when the water was being injected (Figure 4.21). This is in agreement with the CO_2 gas simulation when mineral dissolution was limited.

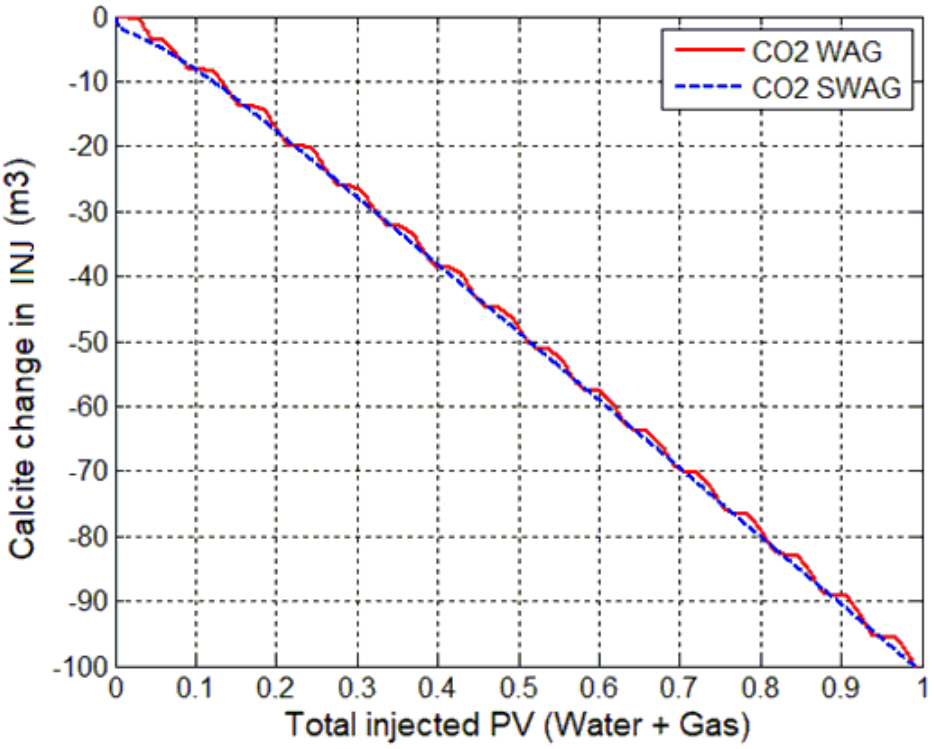

Figure 4.21. Calcite change in m^3 at block 1 (injector) during CO_2 WAG or CO_2 SWAG injection. Dissolution is (globally) continuous and faster than the dissolution observed in the Carbonated Water scenario.

The rate of calcite dissolution for CO_2 WAG and CO_2 SWAG was higher than the rate found for carbonated water (see Table 4.6), which is explained by the higher CO_2 molalities obtained during the gas injection at reservoir pressure. This higher dissolution may put the wellbore integrity into a higher risk of collapsing.

Table 4.6. Dissolved calcite and porosity in the injector block after 1.5 PV (=148 500 m^3) of injected water.

	seawater	carbonated water	CO_2 WAG or CO_2 SWAG
Calcite Dissolved after 1.5 PV (m^3)	1.6	76.4	157.0
Porosity in Injector block after 1.5 PV	22.00%	22.34%	22.69%
Dissolution Rate (m^3/ PV)	8.1*	50.9	104.6
Porosity increase per injected PV	<0.01%	0.23%	0.46%

*Initial dissolution rate (before 0.2 PV)

In addition in Figure 4.22, we can see that, due to the higher reaction rate, a non-limited precipitation occurs in both blocks 2 and 20 (producer). An interesting fact is also observed: before the precipitation starts (at 0.70 PV), calcite is dissolved during the earlier arrival of the injected CO_2 (at 0.50 PV), similar to the CO_2 gas simulation. The dissolution in block 2 during CO_2 SWAG injection is weaker if compared to CO_2 WAG because at each WAG cycle the water becomes saturated in block 1 during the injection of the CO_2 slug and then the gas dissolves in subsequent blocks, while for SWAG there is more water available for CO_2 to be dissolved in. However, as the gas phase travels through the reservoir both recovery processes converge and similar values of dissolution are achieved.

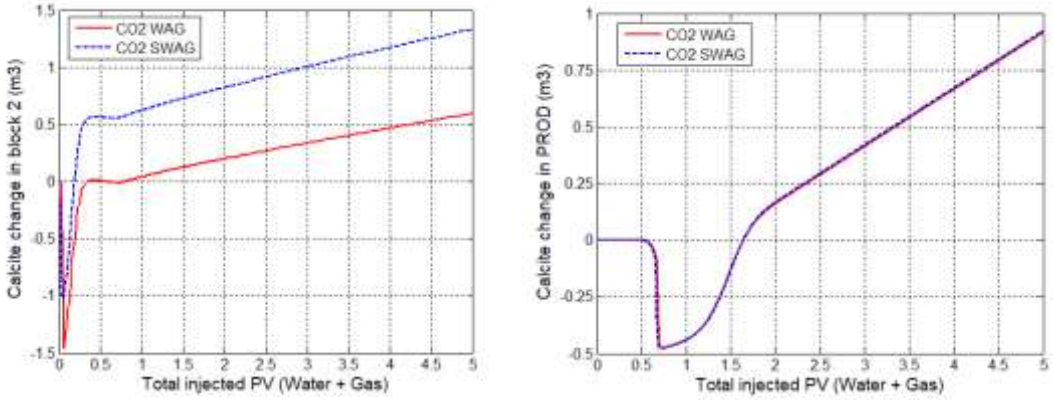

Figure 4.22. Calcite change in m^3 in block 2 (left) and 20 (right) during injection of CO_2 WAG or CO_2 SWAG. Mineral dissolution is caused by earlier arrival of the injected gas

Moreover, the amount of re-precipitated calcite at the producer overcomes the initial dissolution after 1.5 PV and thus scale deposition may pass undetected by operators during the first years of production. This re-precipitation initiates around 3%

injected water fraction, when CO_2 gas breaks through and local pressure starts to decrease. Both CO_2 and HCO_3 molalities increase as the injected water fraction approaches unity, however when CO_2 free-gas starts to be produced the increase in CO_2 concentration becomes slower relative to HCO_3 (see Figure 4.23). In addition, the mixing between high HCO_3 brine and high Ca formation water (as occurred in the carbonated water simulation) speeds up the precipitation rate. After all formation water has been produced, the rate of precipitation becomes lower but constant. Therefore, mineral scale problems around the producer wellbore will definitely occur because the precipitation is continuous.

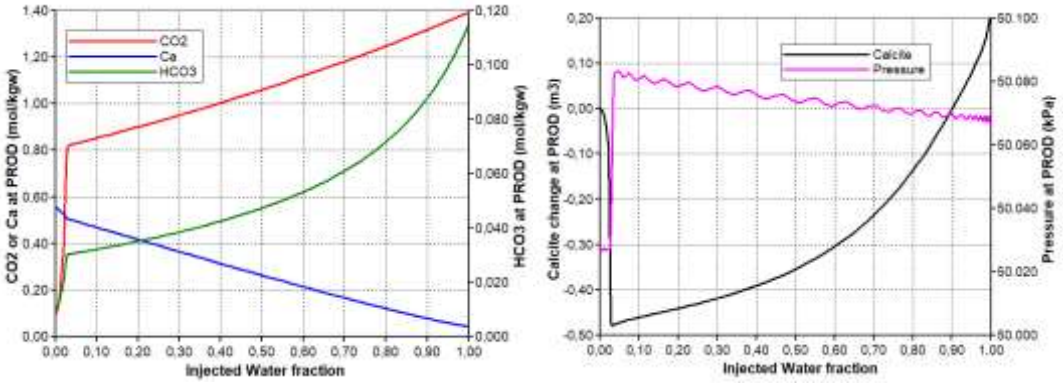

Figure 4.23. Molal concentration of relevant species (left) compared to calcite change and pressure (right) in block 20 (producer) during production of formation water.

4.3.4. Impact of grid refinement

We evaluate the impact of grid refinement on dissolution near the injector and on precipitation near the producer. We have increased the resolution of the entire inter-well distance by increasing the total number of blocks and re-run selected scenarios.

We found that the total volume of dissolved calcite around the injector well is independent of block size. However, for CO_2 WAG simulation with finer grids, significant portions of the dissolution happen in more than one block (not only the injector block), while for SWAG injection continuous dissolution remained restricted to the injector block and led to complete dissolution of rock matrix in some cases (ultimate porosity in injector block reached 100%). In addition, since the total dissolved volume was invariant, simulations performed with smaller blocks showed larger porosity increase and could yield larger increase in permeability and injectivity (see Table 4.7).

Table 4.7. Calculated calcite dissolved volume and final porosity near injector wellbore after 27 years of CO_2 WAG injection (with slug sizes of 60 days) for different grid resolutions.

Block Length (m)	**100**	**50**	**25**	**10**	**5**	**2.5**
Dissolved Volume in block 1 (m^3)	515	516	516	**501**	400	236
Dissolved Volume in block 2 (m^3)	<1	<1	<1	14	73	57
Dissolved Volume in block 3 (m^3)	<1	<1	<1	<1	33	54
Final Porosity in block 1	**0.24**	**0.26**	**0.31**	**0.44**	**0.57**	**0.64**
Final Porosity in block 2	0.22	0.22	0.22	0.22	0.28	0.32
Final Porosity in block 3	0.22	0.22	0.22	0.22	0.25	0.32
Final Permeability in block 1 (mD)	**547**	**733**	**1430**	**6208**	**22 891**	**46 229**
Final Permeability in block 2 (mD)	400	400	400	400	967	1 619
Final Permeability in block 3 (mD)	400	400	400	400	634	1 619

At higher resolution one can observe the dissolution zone dependency on the WAG scheme. Figure 4.24 reveals that when the WAG ratio is reduced from 1 to 0.5 the dissolution around the injector becomes smaller and closer to the injector well. Moreover, by increasing the WAG cycle length from 120 days to 240 days the dissolution zone is enlarged from 15 to 45 m, although the total dissolved volume in both zones are similar (difference is less than 1%). In addition to this, the dissolution zone for WAG ratio 2 with WAG cycle length of 180 days is also 45 m. Thus, we can conclude that the volume of the water slug dictates the size of the dissolution zone. This means that larger water slugs distribute the mineral dissolution into a broader area.

Shorter WAG cycles or SWAG will dissolve calcite in smaller regions close to the injector well.

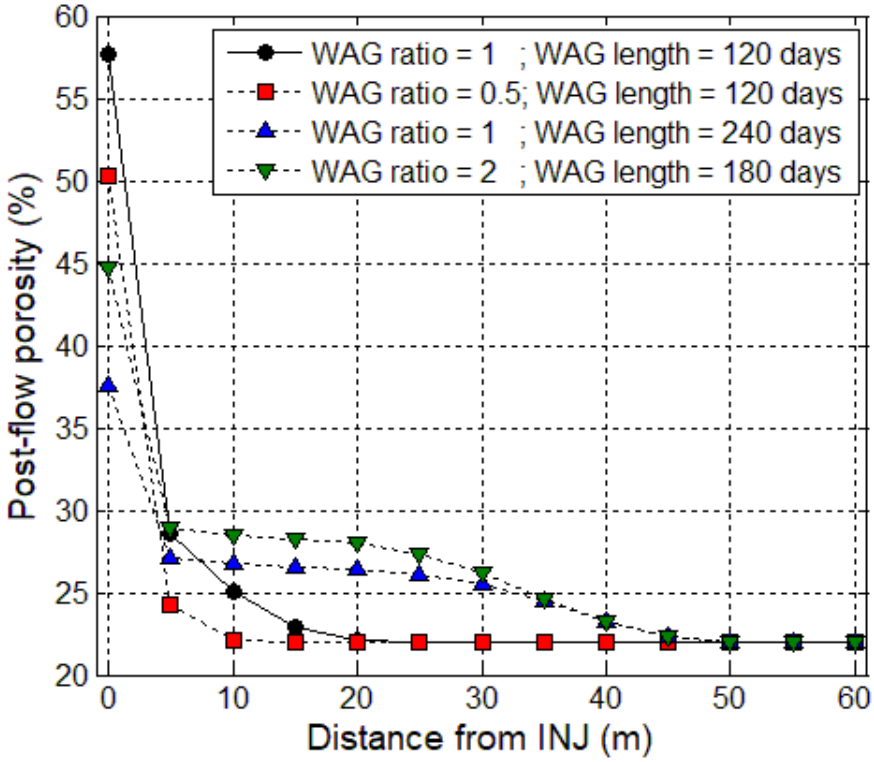

Figure 4.24. Porosity around the wellbore (resolution of 5m) after 27 years of CO_2 WAG injection for different WAG schemes. Larger water slugs cause larger dissolution zones but total dissolution depends on WAG ratio only.

Qiao et al. (2016) have run simulations to evaluate the calcite dissolution during CO_2 SWAG injection with a low k_β ($10^{-8.19}$ mol/m^2/sec). In their scenarios, dissolution happened up to a few meters away from the injector wellbore and the dissolution zone decreased when A_β was increased (from 10^2 to 10^4 m^2/m^3), while the total dissolution remained constant. Since their kinetic rate was not high enough compared to their flow rate, the actual reaction rate became limited by the kinetic law parameters ($Da_I < 1$) and the water is transported through more than one block before equilibrium was reached. Our result shows that even with a high kinetic rate, which enables immediate equilibration of components in all phases, dissolution far from the injector wellbore may happen during CO_2 WAG with larger water slugs. These results highlight the importance of planning the WAG scheme considering the mineral dissolution since the spreading of the dissolution zone will affect the injectivity increase.

Grid refinement caused different effects around the producer well. We have seen that dissolution and precipitation rates are proportional to block length, if the resolution

is high enough. The threshold for this behaviour is the same that was required to observe the dissolution zone around the injector (grid block length ≤ 10 m). Therefore, when applying grid refinement the total precipitation within a certain distance from the producer remains constant, independent of the grid. However, we did observed slightly less dissolution during CO_2 breakthrough and slightly less precipitation during a shorter mixing between injected and formation waters. What happened is that finer grids have lower numerical dispersion (from equation 4.22), which decreases the contact between displacing and displaced fluids. These differences are within 5% between grids, and hence the convergence.

In Figure 4.25, we show the mineral change in the producer block for two different grids. The vertical axis scale was chosen to be proportional to the grid block size and show constant precipitation rates with similar inclinations. One can see that reducing the block length by a given factor does reduce by a similar factor the dissolution caused by CO_2-saturated brine front.

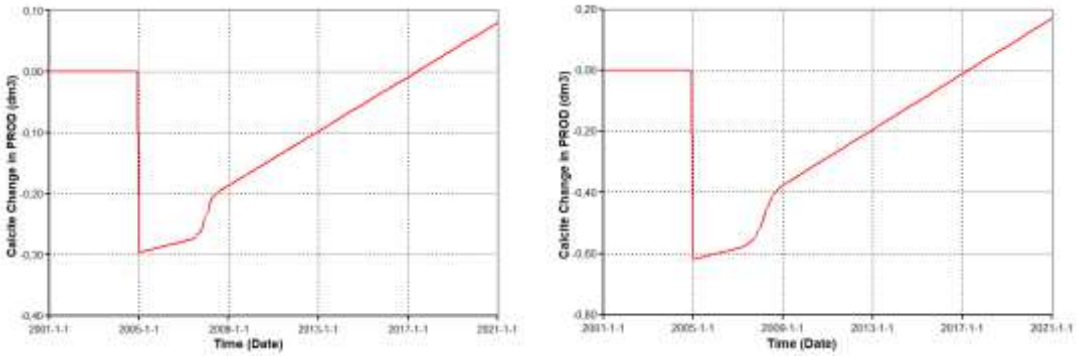

Figure 4.25. Calcite change in the producer well block during CO_2 WAG injection with grid block size of 5 (left) and 10 m (right). For the coarser grid, the vertical axis scale is 2 times larger than the finer grid. Precipitation rates are proportional to the grid resolution.

On the other hand, when the grid resolution is too low, such as our base case (100 m), the numerical dispersion is too much and the precipitation by mixing may be overestimated, while the ultimate precipitation rate (due to degassing after formation water is totally displaced) remains proportional to the grid length. However, the physical dispersion in real fields will have a major impact on precipitation because of mixing and should be estimated (e.g. through coreflooding experiments) and modelled through numerical dispersion.

To conclude the grid sensitivity analysis, we can say that finer grids are required to capture the information regarding the dissolution around the injector block. It is clear that the size of the water slug determine the size of the dissolution zone and thus the

length of the grid blocks must be smaller than the distance travelled by the slugs during each WAG cycle. However, our simulations revealed that the grid resolution should be even higher, as grid blocks smaller or equal to 10 m were required to observe the dissolution zone, while the slugs are estimated to travel 60 m (= 60 days x 1 m/day). It seems that the calcite dissolution enlarges the first blocks significantly and causes an accumulation of the injected slugs close to the point of injection, therefore reducing the length of penetration of slugs between cycles.

Nevertheless, the total volume of dissolved calcite is independent of the grid block size. Then, if the purpose of simulation is to calculate the mass of calcite that reaches the producer wellbore and can potentially precipitate in the production tubing and surface equipment, a lower resolution may suffice, provided the numerical dispersion is controlled. Moreover, the grid does not impact the rate of precipitation after formation water has been displaced.

4.3.5. Impact of WAG ratio

With potential threats in mind (collapse of the injector well and clogging of the producer wellbore), which are caused by a higher dissolution rate near the injector, it is interesting to evaluate the calcite change during CO_2 WAG with other WAG cycle lengths and WAG ratios. In this subsection we simulate WAG scenarios with a low grid resolution (grid blocks of 100 m) with the same parameters, boundary and initial conditions used previously. The main objective here is to investigate the influence of the WAG scheme in the dissolution and precipitation around the wells. In Table 4.8, we show the dissolution and precipitation caused by different WAG configurations.

Table 4.8. Calcite change in injector and producer blocks after 27 years (~5 PV) of CO_2 SWAG and of CO_2 WAG injection for different configurations.

WAG ratio	WAG Cycle Length (in days)	Dissolved Calcite in INJ after 27 years (in m^3)	Porosity in INJ after 27 years (%)	Precipitated Calcite in PROD after 27 years (in m^3)
SWAG	-	516.7	24.3	0.92
1.0	60	517.5	24.3	0.92
2.0	60	691.0	25.1	1.65
0.5	120	342.5	23.5	0.27
1.0	120	515.2	24.3	0.91
2.0	120	686.3	25.0	1.63
3.0	120	769.5	25.4	2.05
1.0	180	514.0	24.3	0.91
2.0	180	686.2	25.0	1.63
1.0	240	511.8	24.3	0.90
2.0	240	681.2	25.0	1.62

When the WAG cycle length was varied no strong trend was detected. However, we observed slightly higher dissolution and precipitation for shorter WAG cycles. This is in accordance with previous research from other authors, where reactivity decreased for increasing gas slug sizes (Mackay and Souza, 2014), but up to a certain limit (Qiao et al, 2016).

Without considering mineral reactions, some author have found that the choice of WAG ratio has an impact on oil productivity and CO_2 storage (Elwy et al., 2012; Ettehadtavakkol et al., 2014; Agada et al., 2016). On the other hand, our simulation results in Table 4.8 show that higher WAG ratios yield higher rates of calcite dissolution in injector and precipitation in producer. This is a relevant finding because it suggests that the rate which injectivity increases is affected by WAG ratio and may be an explanation for the different findings obtained via core-flooding experiments by Elwy et al. (2012), which observed that WAG ratio 1 had a faster recovery than WAG ratio 0.5 (the injected water may block oil droplets and for lower WAG ratios the enlargement of the pores may be insufficiently fast to free the oil and enable its

interaction with the injected CO_2). We also noted that since an increase of the WAG ratio delays the CO_2 breakthrough, a high HCO_3 water (which has a high scale tendency) may arrive at the producer before the CO_2-saturated brine if the WAG ratio is too high. In such conditions, initial calcite dissolution around the producer may be weak or not happen (see Figure 4.26) and scale formation will start earlier. Therefore, WAG ratio not only controls the rate of oil production and CO_2 storage, but also the critical time for intervention on producer wells before the wellbore is clogged by calcite scale.

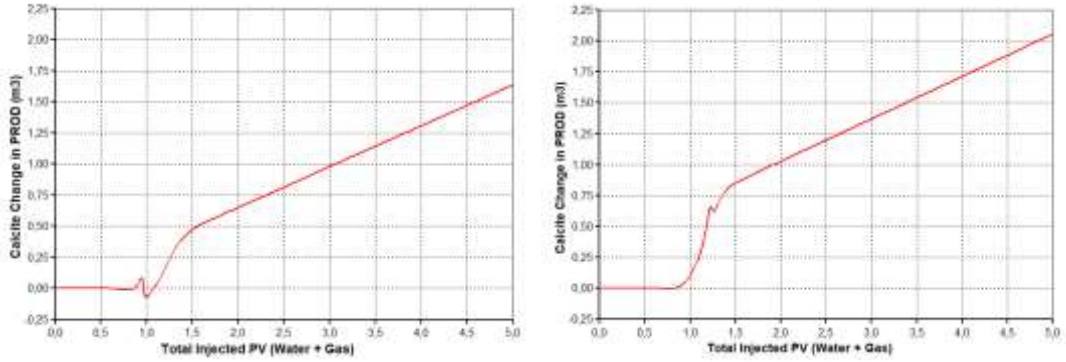

Figure 4.26. Calcite change in m^3 in block 20 (PROD) during CO_2 WAG with WAG ratios of 2 (left) and 3 (right). Mineral Dissolution caused by the arrival of the CO_2-saturated front is identified by the peak/valley pattern and happens after seawater breakthrough.

To clarify the role of the WAG ratio we analysed the relationship between the calcite dissolution and the injected volumes of water and gas. We found that the volume of dissolved calcite grows with WAG ratio but not proportionally. In Figure 4.27, we show that the obtained data from Table 4.8 can be explained by simple functions with good match.

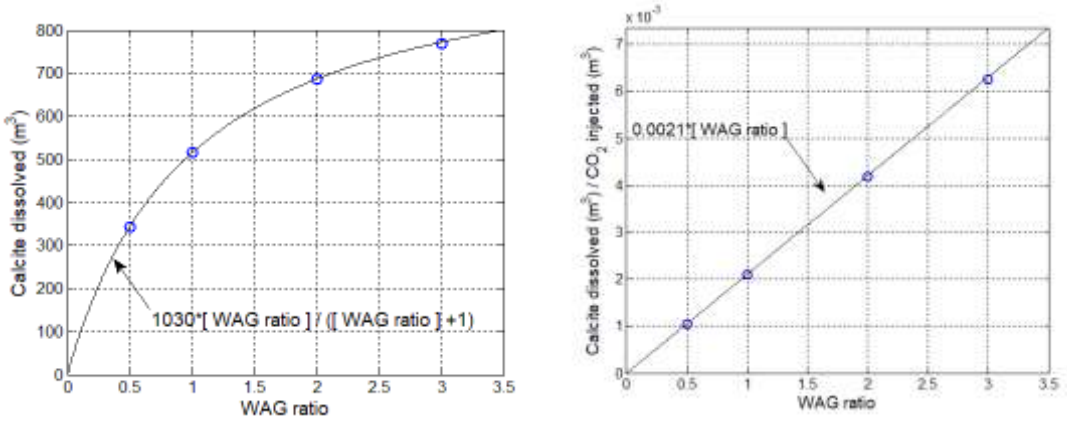

Figure 4.27. Calcite dissolution in m^3 after 27 years (~5 PV) of CO_2 WAG injection with WAG cycles of 120 days and different WAG ratios.

Considering the two obtained functions, we noted that the ratio between both coefficients is very similar to the total volume of injected fluids during 27 years (492 750 m^3), for any WAG ratio. Thus, by the definition of WAG ratio as the ratio between injected volumes of water (V_W) and gas slugs (V_G), the dissolved calcite can be written as a linear function of the injected volume of water:

$$Calcite\ dissolution\ (m^3) = 0.0021 * (V_W + V_G) * \frac{V_W}{V_W + V_G} \tag{4.28}$$
$$= 0.0021 * Injected\ Water(m^3)$$

or a linear function of both injected volume of gas and WAG ratio:

$$Calcite\ dissolution\ (m^3) = 0.0021 * Injected\ CO_2(m^3) * WAG\ ratio \tag{4.29}$$

Equations 4.28 and 4.29 are useful in calculating the calcite dissolution caused by CO_2 WAG. The value of the coefficient is related to the chemical composition of the injected water and the physical conditions near the injector wellbore (temperature and pressure), which set the state of chemical equilibrium. The validity of these equations is lost for higher WAG ratios (> 20) because the injected gas will dissolve completely in smaller portion of the water slug and the porosity alterations become more similar to the carbonated water scenario. However, such conditions are impractical and the usual WAG ratios applied in oilfields are rather small (up to 4) (Christensen et al, 1998).

We also checked the dissolution dependency on flow rate to test the validity of expressions above. It is shown in Figure 4.28, that the dissolution grows linearly with water injection rate as expected because the reaction is fast compared to flow rate

($Da_I > 1$). Therefore, during a CO_2 WAG the porosity around the injector increases faster when the water is injected faster (i.e. higher WAG ratio or higher injection rate).

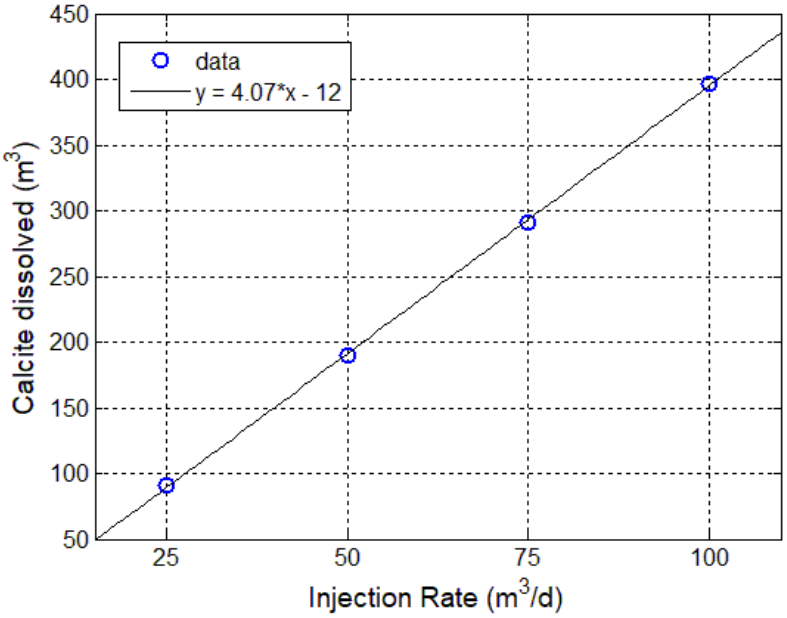

Figure 4.28. Calcite dissolution in m^3 after 10 years of CO_2 WAG injection for different water injection rates. WAG ratio and WAG cycle are 1 and 120 days, respectively.

Chapter 5:
Reactive Transport in 2D with oil

In the previous Chapter, we have studied the calcite dissolution and precipitation in a simple linear flow path. The feature of 2-phase flow included in the simulation (CO_2 WAG and CO_2 SWAG scenarios) was required to observe calcite dissolution and precipitation around the producer wellbore, and not only dissolution (as in the CO_2 gas scenario) or only precipitation (as in the carbonated water scenario). Moreover, we have seen that under the assumption of calcite reactions being transport controlled ($Da_I > 1$) for simulations at reservoir scale, total calcite dissolution during CO_2 WAG grows linearly with the volume of water injected or $Q * W_R/(W_R + 1)$, where Q is the constant injection flow rate of water or gas and W_R is the WAG ratio (i.e. the volumetric ratio between water and gas injected, at reservoir conditions, over a WAG cycle).

One key difference from SWAG, is that CO_2 WAG allows the EOR operator to control the size of the dissolution zone and the porosity increase around the injector, by setting appropriate WAG configurations. The dissolution zone was observed to be larger for larger water slugs, which depended on W_R and WAG cycle, since flow velocity was constant everywhere.

In this Chapter, we move a step further in the complexity of the flow by including an oil phase and upgrading the model geometry to 2D areal. In this sense, we simulate the reactive transport during multiphase flow in a calcite porous medium that exhibits larger flow velocities closer to injector and producer wells. The addition of the oil phase will enable the observation of mechanisms of CO_2 EOR (condensing gas and vapourising oil drives, or a combination of both) (see Zick, 1986), which reduce the residual oil saturation and therefore increase the fraction of water in contact with the calcite in the pores.

To make the simulations even more realistic we also enabled heat exchange and studied its impact on calcite reactions around the wells and in the full model. This makes our simulation part of a larger group of flow simulations that involves multi-physics: THMC (Thermo-Hydro-Mechanical and Chemical) coupled transport

(Lichtner, 1985; Steefel and Lasaga, 1994; Guimarães et al., 2007; Lichtner et al., 2013; Tutolo et al., 2015). Thus, here we have a THC transport with three fluid phases in two dimensions.

5.1. Model description

We have performed reservoir simulations with the following parameters to investigate calcite reactions during multiphase flow in 2D models of limestone reservoirs (Table 5.1):

Table 5.1. Model parameters used for reservoir simulation.

Model Dimensions	600 x 600 x 20 m
Grid Resolution	20 x 20 x 20 m
Porosity	0.22
Permeability (homogenous)	400 mD
Reservoir Temperature	60℃
Temperature of injected fluids	25℃
Reservoir Pressure	500 bar
Initial Water Saturation	21%
Irreducible Water Saturation	21%
Residual Oil Saturation	31%
Residual Gas Saturation	20%
Calcite Kinetic Rate	10^{-5} mol/m^2.s
Calcite Reactive Surface Area	10 000 m^2/m^3
Rock Heat Capacity	1046.7 J/kg.K
Rock Thermal Conductivity	3.46 W/m.K
Well Position Pattern	$^1/_4$ five-spot
Maximum Bottom-hole Fluid Rate in injector well	500 m^3/day
Minimum Bottom-hole Pressure in producer well	500 bar

We have set an oil phase with eight pseudo-components and dissolved CO_2 using CMG WINPROP (Table 5.2). Heat is exchanged between the transported phases (oil, water and gas) and the rock matrix. Parameters associated to heat exchange for oil components were set using WINPROP.

Table 5.2. Mole fractions of oil components (viscosity = 4.05 cP)

	N2 to C1	CO2	C2 to C3	IC4 to NC5	C6 to C9	C10 to C19	C20 to C29	C30A+	C30B+
Moles (%)	4.8	0.3	8.6	11.2	26.3	25.3	20.6	1.7	1.3

Water compositions are the same as previously (see Table 4.4), except for initial CO_2 and HCO_3 which were 10 and 0.1 mM, respectively (after CO_2 equilibrated between formation water and oil phase). In addition, permeability is updated during dissolution of calcite via Carman-Kozeny formula (Equation 4.24).

Finally, the WAG cycles were set to 120 days and W_R was equal to unity (water and gas injections are alternated every two months, approximately).

5.2. Simulation Results

Our analysis of THC simulation revealed three distinct zones of calcite dissolution and precipitation, which emerged from the propagation of different fluids. As in previous simulations, the injected CO_2 dissolves in injected and formation waters and triggers calcite dissolution. This time however, the injected CO_2 goes primarily to the oil phase (reducing its viscosity) and then to water phase. In this sense, as the oil phase is being displaced, formation water moves toward the produced and hence an oil/FW saturation front propagates (see Figure 5.1).

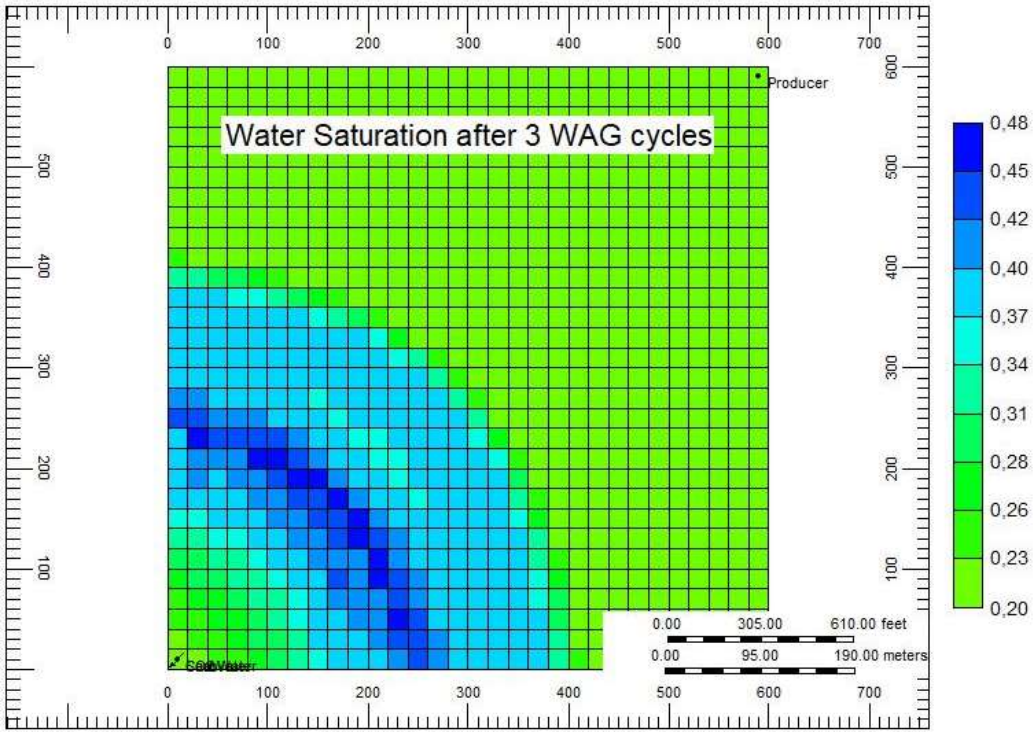

Figure 5.1. Water saturation after 360 days of injection (0.113 PV). An oil/formation water front was developed and is currently at 400 meters away from the injector.

The formation water is then displaced by the injected seawater, which carries a higher amount of the injected CO_2, because of lower salinity. Therefore, a group of aqueous concentration fronts propagate together: CO_2, Na, Cl, etc. (see Figure 5.2 and 5.3). Moreover, the injected CO_2 interacts with the oil phase and reduce the residual oil saturation (by increasing the mobility of the oil phase and by vapourising light components). Therefore, fronts of higher water saturation are constantly created during water injection periods that follow each gas injection (Figure 5.1 shows one front around 270 m) and CO_2 EOR increases the interaction of water with the rock because oil films are reduced (only the immiscible oil remains in the pores). In fact, Henry et al. (1981) have observed that during CO_2 WAG the produced water salinity may rise, while their explanation for this phenomenon is that high salinity connate water is exposed to flow channels due to enlargement of the pores and extraction of the oil films.

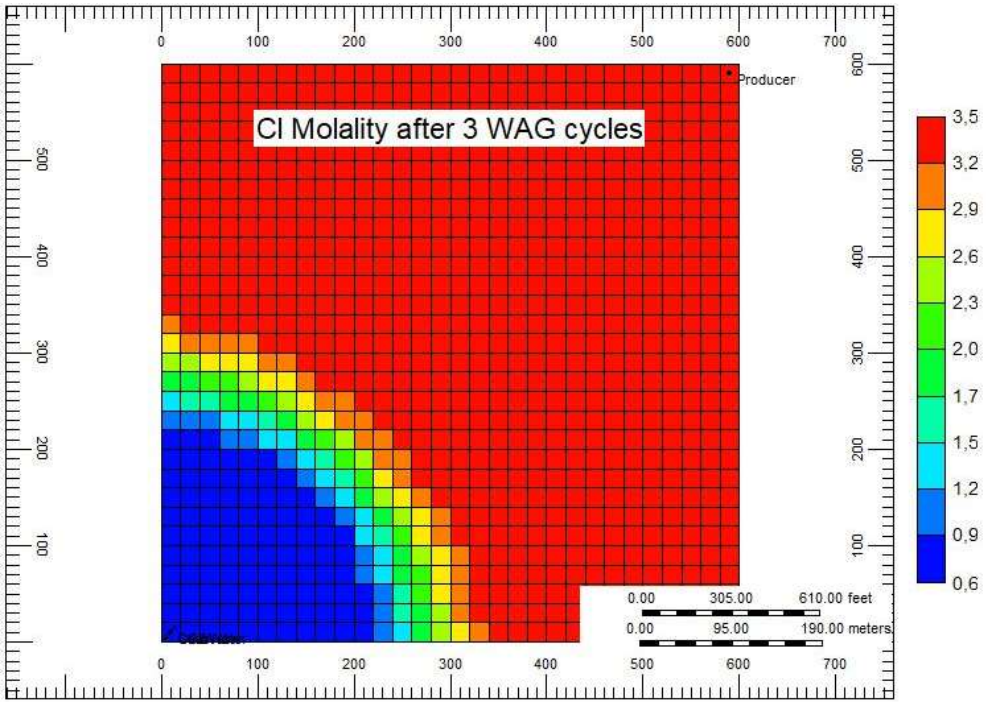

Figure 5.2. Cl molality after 360 days of injection (0.113 PV). The advancing front of injected fluids is currently at 300 meters away from the injector, just behind the oil/formation water front.

As these fronts propagate, calcite is first dissolved and then precipitated through the model. For this WAG configuration, the injector block is the only location where calcite dissolves at a constant rate. Moreover, the injection of cooler fluids creates an additional zone with CO_2-rich water around the injector wellbore (see Figure 5.3). The heat exchange in the entry point of the reservoir will force more and faster dissolution, since calcite solubility decreases with temperature (see Chapter 2) and thus more calcium will propagate toward the producer.

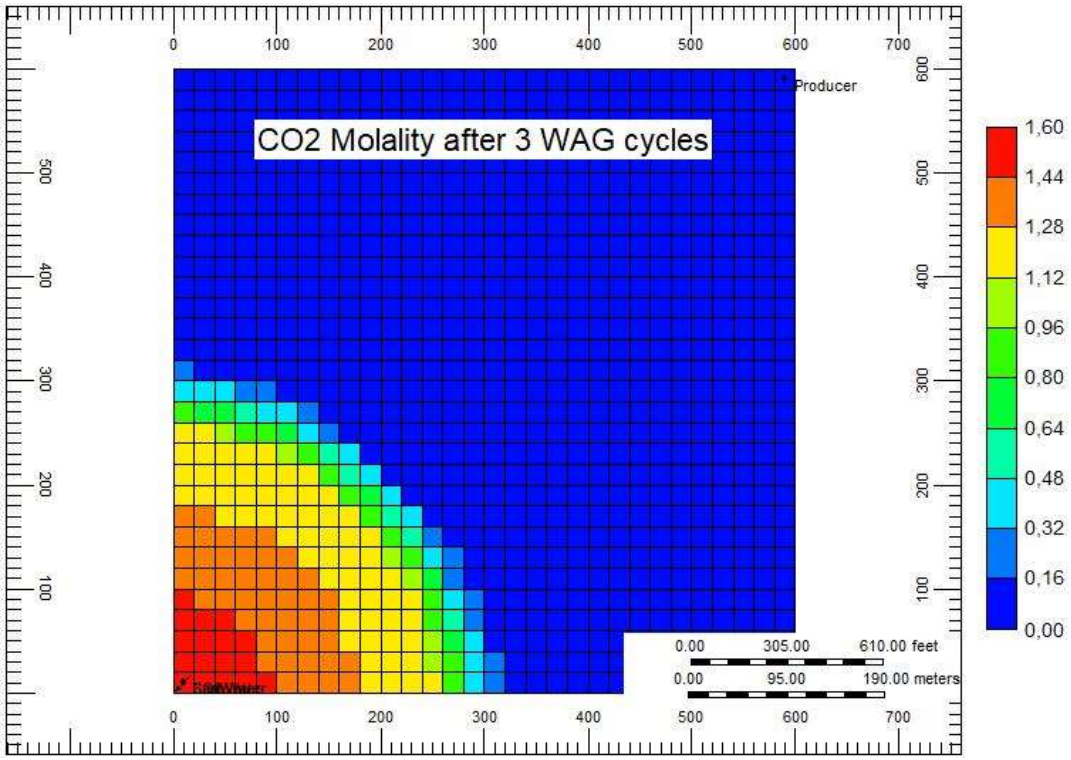

Figure 5.3. CO_2 molality after 360 days of THC CO_2 WAG injection. Cooler zone (<100m) keeps the CO_2 molality high despite the pressure decrease.

5.3. Impact of Heat Exchange

To address the impact of heat exchange in calcite reactions, we have re-run the simulation in isothermal mode, i.e. temperature of injecting fluids are equal to the reservoir temperature, and compared the results. We have found that during non-isothermal flow calcite dissolution in the near injector wellbore (<20m) is stronger, which is due to higher solubility at lower temperature. On the other hand, deeper in the reservoir, dissolution is suppressed as the injected fluids move from cooler to warmer zones. Thus, although the reservoir becomes cooler, scale deposition around the producer is higher when compared to isothermal calculation. In fact, after 26 years of injection (3 PV) of cooler fluids, 4.7 m^3 of calcite precipitated within 20 meters from the producer wellbore, while under isothermal assumption 4.4 m^3 of precipitate was calculated. On the other hand, the ultimate precipitation rate (i.e. after formation water is displaced completely) for non-isothermal flow is $^2/_3$ of the isothermal simulation, although most of the precipitation happens during mixing of injected water and formation water (as we have seen in Chapter 4). Therefore, the biggest impact of heat exchange is after breakthrough of injected water and before the displacement of formation water is complete, when the scale formation is the fastest.

A deeper analysis of the consequences of heat exchange reveals that they are dependent on the amount of dispersion involved, which can be controlled by the size of time step. Table 5.3 shows that for smaller time steps (less numerical dispersion), the ratio between calcite dissolution with and without heat exchange in the full field is smaller. At each time step, GEM is instructed to solve the transport equations implicitly whenever the CFL condition is violated or the explicit solution showed instabilities in either the water saturation or hydrocarbon mole fractions (including CO_2 mole fractions in water, gas and oil phases). This is called adaptive-implicit method or AIM (GEM Manual, 2014). However, as seen in Chapter 4, implicit solutions of the transport equation have more dispersion.

Table 5.3. Total calcite dissolution after 3 PV for different simulations

Maximum Time Step (day)	**Isothermal**		**Non-isothermal**		**Heat Impact on Dissolution relative to Isothermal sim (%)**
	Field Dissolution (10^3 m^3)	Steps solved implicitly (%)	Field Dissolution (10^3 m^3)	Steps solved implicitly (%)	
1.6	16.7	16	10.5	19	**-37**
1.4	16.4	15	12.1	18	**-26**
1.2	15.0	13	11.6	12	**-23**
1.0	13.0	10	11.1	10	**-15**
0.1	3.14	1	3.01	1	**-4**

The fact that the total field dissolution increased with dispersion (or degree of implicitness) it's a consequence of more mixing, hence more contact between injected water and gas with formation water and more interaction of the mixing front with porous medium. Therefore, the porosity alterations due to CO_2 WAG are expected to be higher in more heterogeneous reservoirs. Moreover, the heat impact on dissolution also grows with the dispersion, and then it should be increasingly important with higher degree of heterogeneity of carbonate formations (see Figure 5.4).

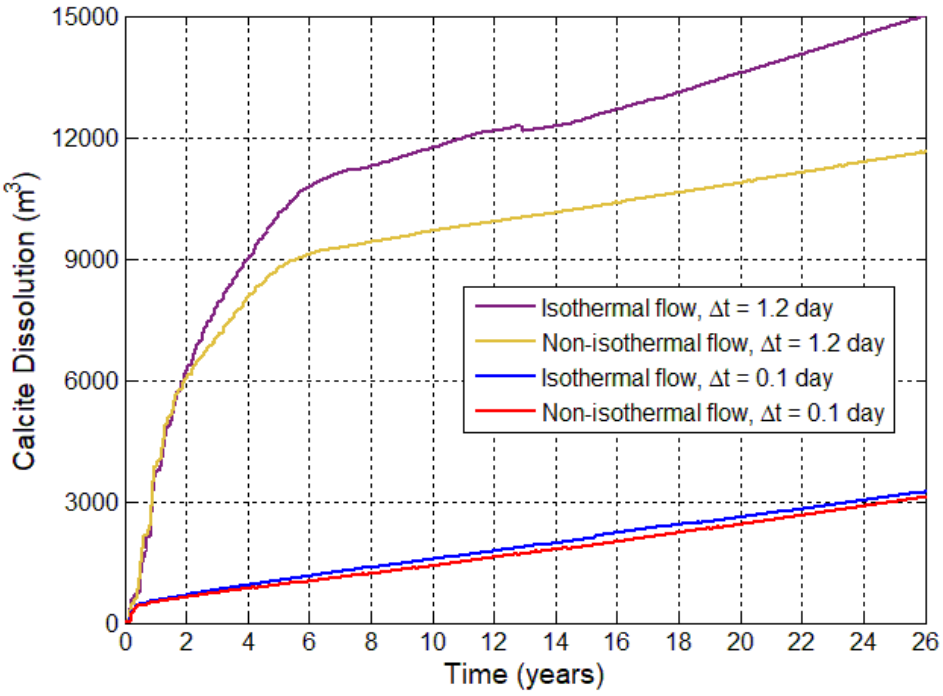

Figure 5.4. Calcite dissolution in the full model with or without heat exchange for two different time step sizes. Impact of heat exchange on dissolution is stronger during more dispersive flow conditions (longer time steps and before breakthrough).

Finally, the computational time required to run these simulations varies between 0.7 and 5.5 hours, using a PC with Intel i5 processor of 3.0 GHz and 8GB of RAM (Figure 5.5). Including heat exchange in the calculations adds more time to the simulation run to be complete (up to 1 hour more). However, the ratio between this additional computational time during non-isothermal calculations and the time for isothermal calculations tends to decrease with decreasing time step sizes, going from 49% (1.6 days) to 22% (0.1 day). This shows that implicit solution of the flow equations (as opposed to explicit) takes even more time to run if heat propagation is calculated. In conclusion we can say that when using very short time steps, numerical dispersion is controlled, the additional computational time associated to heat exchange is proportionally smaller, and the impact of heat in calcite dissolution is negligible. The cost of this is a time of simulation that may exceeds 5 hours. Then, we decided to run the simulations for the rest of this chapter with maximum time step of 1.2 days, but keeping in mind that shorter time steps may be required if the numerical dispersion is inconsistent with the physical dispersion.

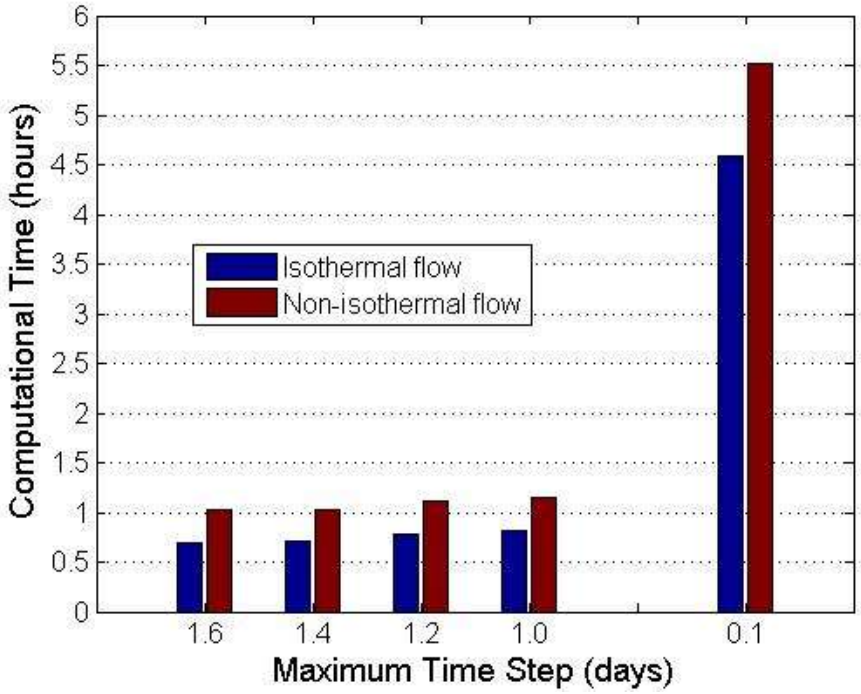

Figure 5.5. Computational time required to run isothermal and non-isothermal reactive flow in 2D areal model. The additional time for heat exchange calculations decreases in proportion when compared to the isothermal flow simulations.

5.4. Scenarios of CO_2 WAG

5.4.1. Injector Wellbore

In Chapter 4, we have seen in 1D simulations that higher W_R's yield faster porosity increase around the injector, while larger water slugs lead to larger dissolution zones. Here, we investigate if these rules are extended to 2D geometry and non-isothermal 3-phase flow. We simulate nine scenarios of 26 years (3 PV) of CO_2 WAG injection (see Table 5.4), with water slugs of 60, 120 and 180 days (equivalent 3 000, 6 000 and 9 000 m^3).

Table 5.4. Simulated scenarios of CO_2 WAG

Scenario Code	W_R	WAG Cycle (days)	Water Slug (days)	Gas Slug (days)	Total Volume of Water Injected (m^3)
A1	0.5	180	60	120	1 581 666
A2	1	120	60	60	2 372 500
A3	2	90	60	30	3 163 333
B1	0.5	360	120	240	1 581 666
B2	1	240	120	120	2 372 500
B3	2	180	120	60	3 163 333
C1	0.5	540	180	360	1 581 666
C2	1	360	180	180	2 372 500
C3	2	270	180	90	3 163 333

It is shown in Figure 5.6 that for each water slug size there is a strong linear relationship between injected volume of water and calcite dissolution around the injector wellbore. On the other hand, shorter WAG slugs cause slightly more calcite dissolution because of more contacts occurring between water and gas phases (which cause more dissolution of gaseous CO_2 into water). However, for very short WAG cycles with high W_R (scenarios A2 and A3), the gas slug may be not large enough to support gaseous dissolution and therefore the total dissolved calcite will be less.

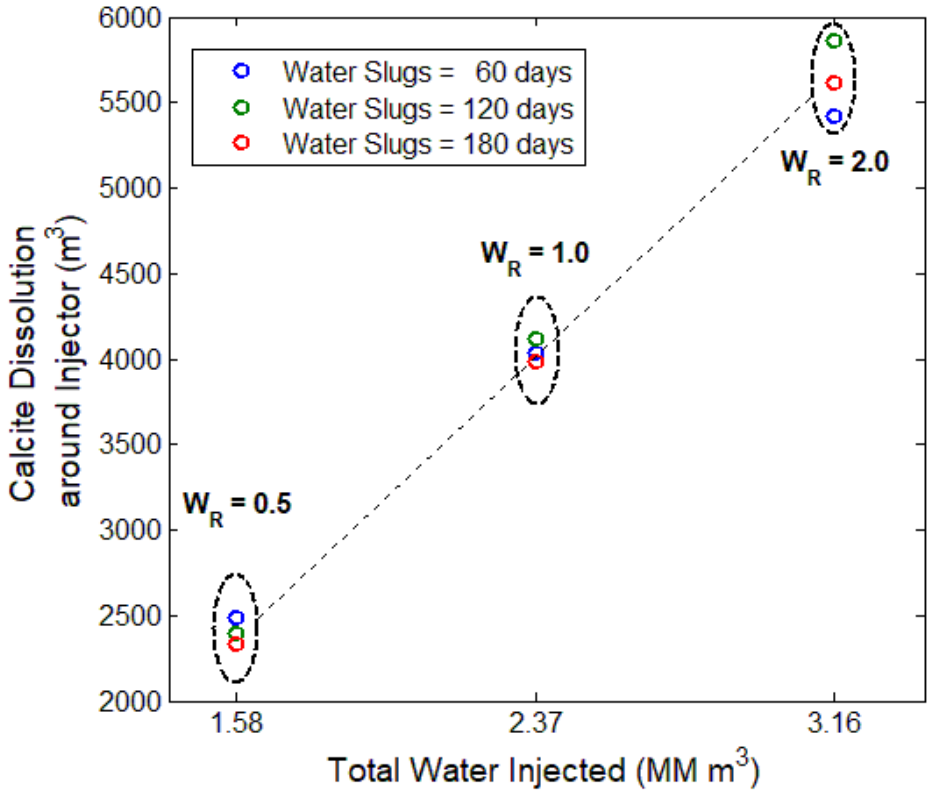

Figure 5.6. Dissolved calcite around injector for different WAG schemes. Scenarios A1, A2 and A3 (blue circles) deviate from the linear trend because the gas slug is insufficient to support the dissolution at higher W_R.

It is interesting to see that the slope of the linear trend in Figure 5.6 (~0.002 m^3/m^3) is very similar to that found in Chapter 4 (Figure 4.24 and Equation 4.29), although here there is flow of oil and heat exchange in 2D (i.e. front velocity changes spatially). Thus, the ratio between dissolved calcite and injected water is predominantly dependent on the composition of the injected water after equilibrated with CO_2.

The W_R is a key operational parameter to control calcite dissolution during CO_2 WAG injection and it is preferred over water slug size because of its higher impact and also because of operational constraints on the slug size.

However, the size of the water slug has been found to control the size of the dissolution zone around the injector wellbore independently of W_R. Figure 5.7, 5.8 and 5.9 show that higher W_R yield more dissolution close to the well. On the other hand, the maximum range for which porosity changes are relevant grows linearly with the duration of the water flood per WAG cycle. Moreover, as seen in Figure 5.6, the volume

of dissolved calcite for fixed W_R changes very little with water slug size. This is a very important result since the spatial distribution of the mineral dissolution impacts the increase of injectivity. While tight dissolution zones have faster increase of porosity, a deeper penetration of the dissolution into the reservoir will be more beneficial for fluid displacement and, in addition, contributes to a lower risk of wellbore collapse.

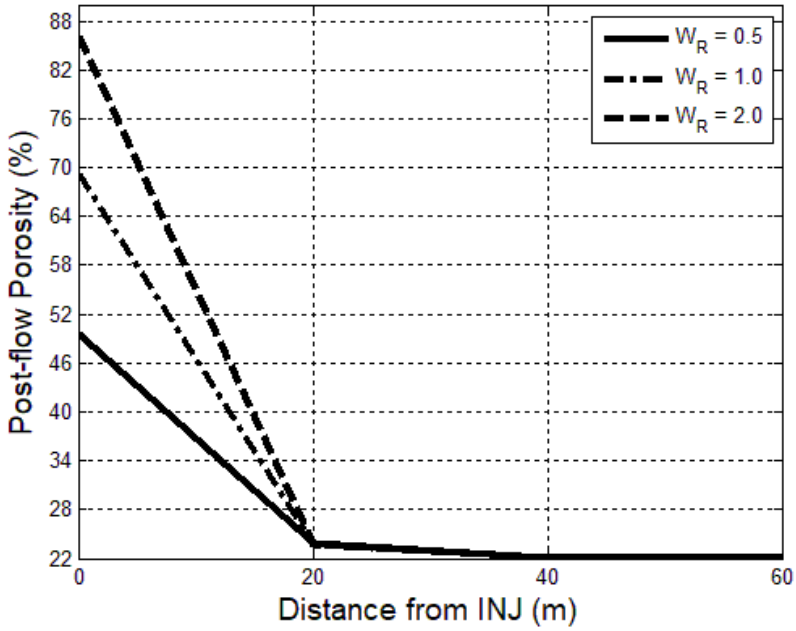

Figure 5.7. Post-flow porosity around injector for scenarios A1, A2 and A3.

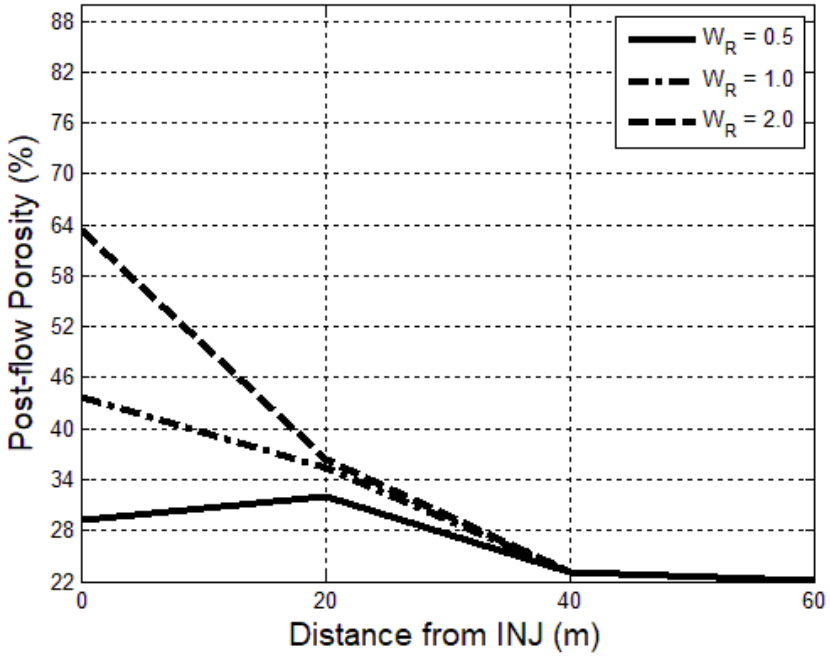

Figure 5.8. Post-flow porosity around injector for scenarios B1, B2 and B3.

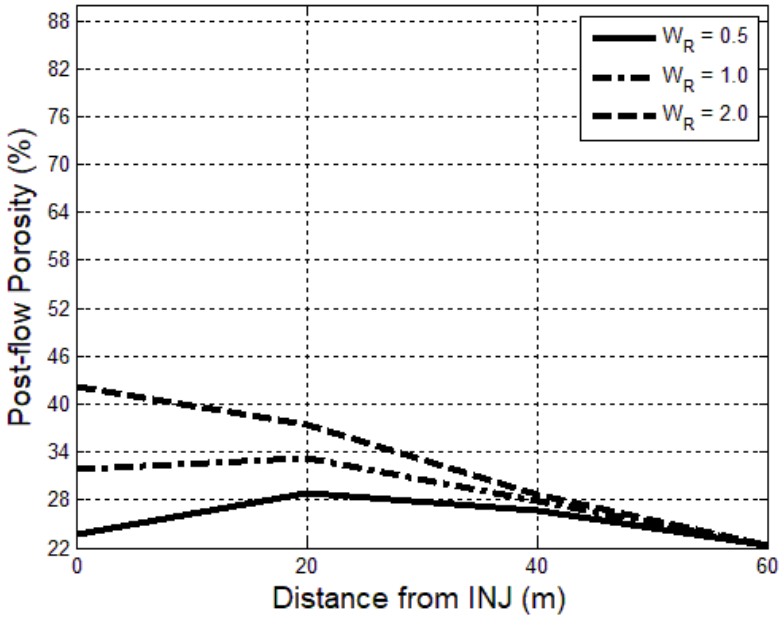

Figure 5.9. Post-flow porosity around injector for scenarios C1, C2 and C3.

Scenario C1, which has the largest gas slug, showed the smallest increase in porosity in the injector block (1.7%). By investigating scenario C1, we have observed precipitation very close to the injector well during each WAG cycles which reduced the ultimate porosity increase. This phenomenon has occurred because of pressure oscillations during the injection of the gas slugs. First, in the beginning of the gas flood, pressure sharply increases to force the entry of the injected gas into water saturated pores (which correspond to rock with low gas and oil relative permeabilities). During this phase, the HCO_3 and CO_2 concentrations in water increase due to the contact between gas and water, and also the Ca concentration rises because of calcite dissolution in the more acidic environment. However, after the water saturation has decreased, pressure drops slightly and a small portion of the CO_2 evolves. Then, to maintain the chemical equilibrium between carbon species, HCO_3 and pH increase, which leads to calcite precipitation. We have observed that this process is strong and robust since higher pressure values will force more dissolution of CO_2 into the water and its subsequent dissociation will also raise the HCO_3 concentration (see Figure 5.10 and 5.11). This precipitation happens close to the well, where changes in pressure and concentration are more significant. Moreover, although the reaction occurred in all scenarios, it is stronger for longer gas floods since it proceeds continuously until the injection is alternated to water. Therefore, to avoid formation damage it is

recommended to either reduce the period of gas injection (making this gas-driven precipitation lower compared to the dissolution during water injection) or decrease the gas injection rate (eliminating the pressure jump in the start of the gas flood).

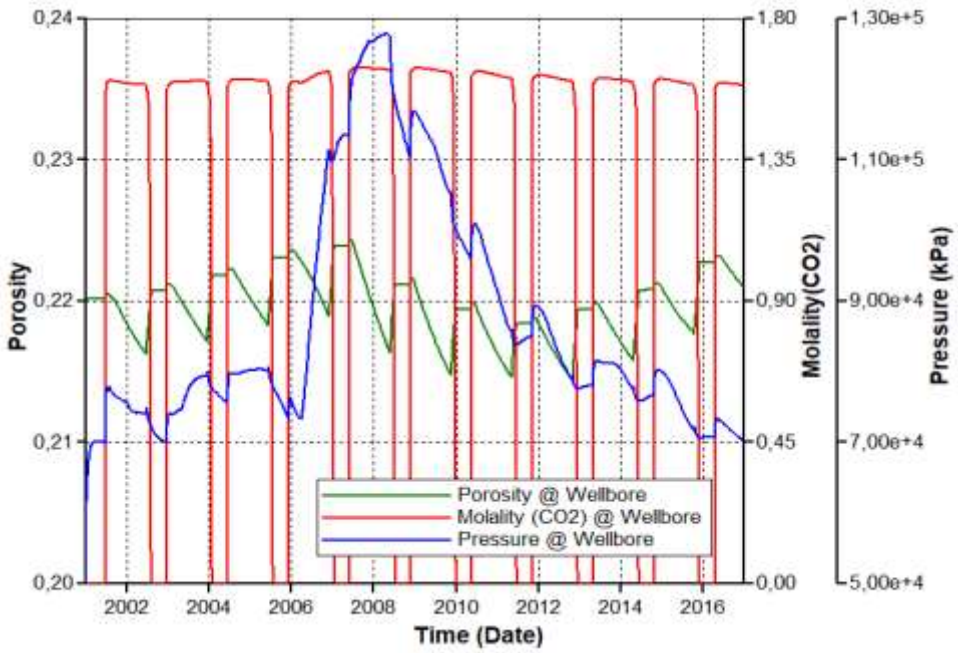

Figure 5.10. Temporary formation damage in injector block during simulation of scenario C1 (largest gas slug).

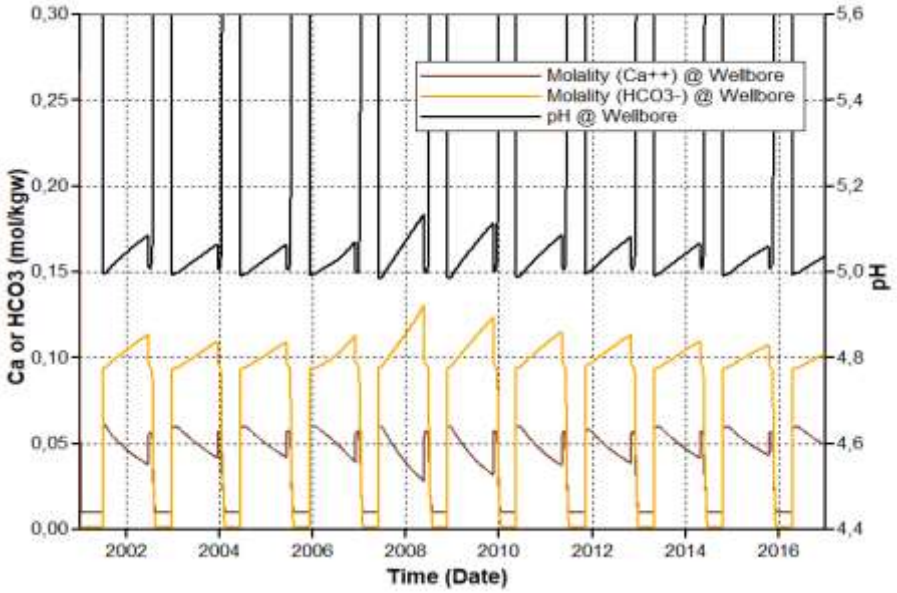

Figure 5.11. Behaviour of relevant ions in injector block during simulation of scenario C1 (largest gas slug).

Formation damage in the near wellbore area may not be detected by reservoir simulation if the grid resolution is low. In Figure 5.12, we show a strong precipitation

close to the injector by running scenario C2 with four times as many grid blocks. An average porosity was calculated in the region equivalent to one block of the original grid. It can be seen that this average porosity is slightly smaller than the porosity calculated via the unrefined grid (see Figure 5.9). However, the porosity in the injector block decreased to 19% after 27 years.

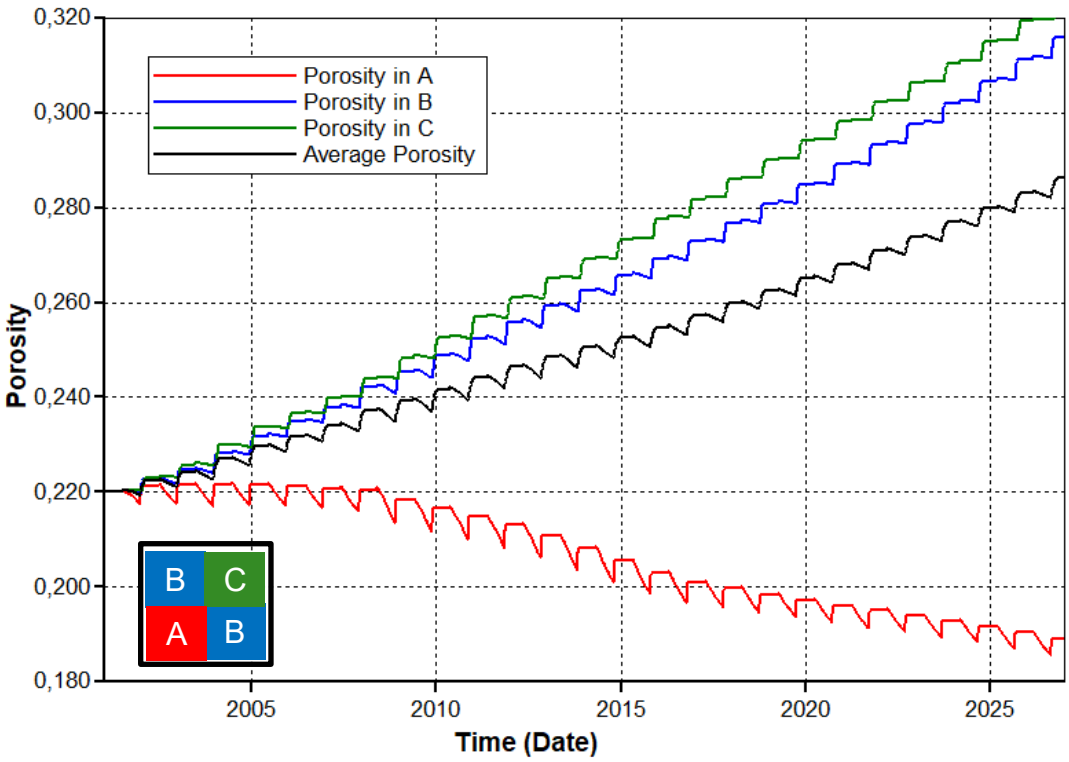

Figure 5.12. Porosity changes in the near injector wellbore zone during simulation of scenario C2 with grid refinement.

5.4.2. Producer Wellbore

Calcite changes at the producer wellbore occur in three steps. First, calcite dissolves during the arrival of the injected CO_2 at the wellbore, which dissolves into formation water and reduces pH close to the well. Then, the injected water mixes with the formation water and strong precipitation begins. After that, when most of the formation water has been produced, the precipitation rate decreases but remains constant because of degassing.

For fixed W_R, calcite dissolution around the producer is greater for larger water slugs; this is because larger slugs delay the dissolution of injected CO_2 into the injected water, and thus reduces the degree of interaction around the injector, delaying this

interaction such that it increasingly occurs around the producer. Effectively, although there will be dissolution along the entire flow path, the point at which most dissolution occurs moves gradually away from the injector and towards the producer as the sizes of the injected slugs increase. Moreover, higher W_R yields greater precipitation and at faster rates, since high HCO_3 concentration water propagates faster through the reservoir (see Figure 5.13, 5.14 and 5.15)

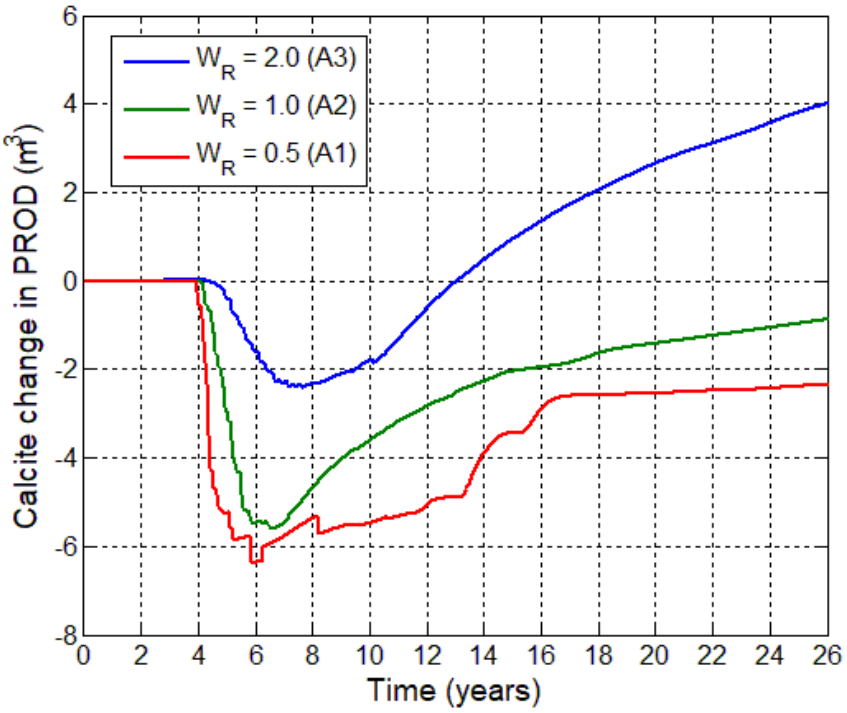

Figure 5.13. Calcite change in producer wellbore during simulation of scenarios A1, A2 and A3.

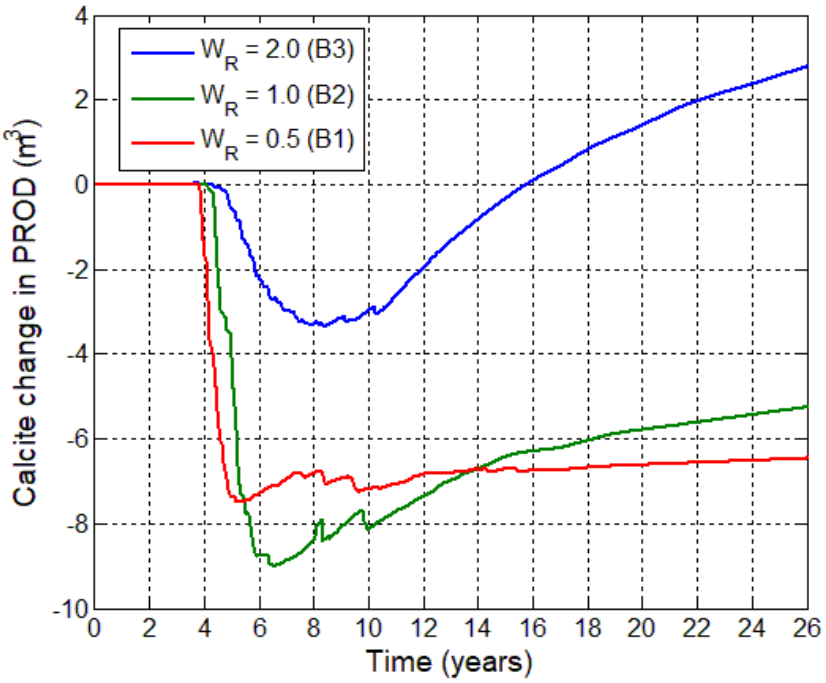

Figure 5.14. Calcite change in producer wellbore during simulation of scenarios B1, B2 and B3.

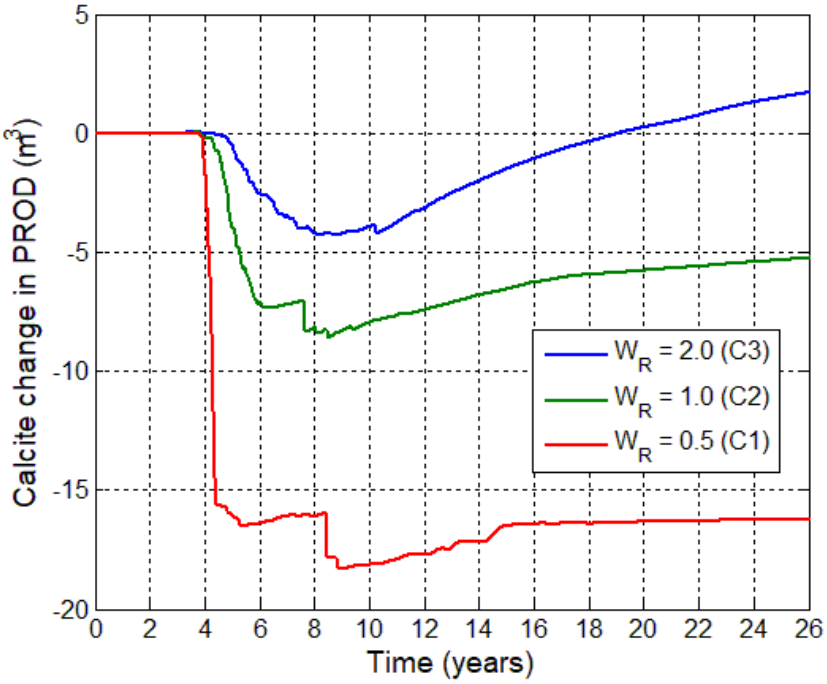

Figure 5.15. Calcite change in producer wellbore during simulation of scenarios C1, C2 and C3.

We have confirmed that an increase in W_R causes earlier breakthrough of seawater and a longer time elapses before the injected CO_2 starts to be produced (see Figure 5.16). The moment when the gas production rate first increases is an indication of the start of the precipitation caused by CO_2 evolution. On the other hand, when the injected

water fraction approaches unity and the gas rate approaches zero, the precipitation caused by mixing of incompatible waters terminates and the mechanism of precipitation is restricted to depressurisation/degassing along the flow path (self-scaling).

We have noted that lower W_R cause higher gas rates at breakthrough. Moreover, more oscillations and instabilities were observed (in saturations, calcite dissolution and precipitation rates and injected water fraction). These instabilities are due to more periods of 3-phase flow in lower W_R (as opposed to 2-phase flow in higher W_R).

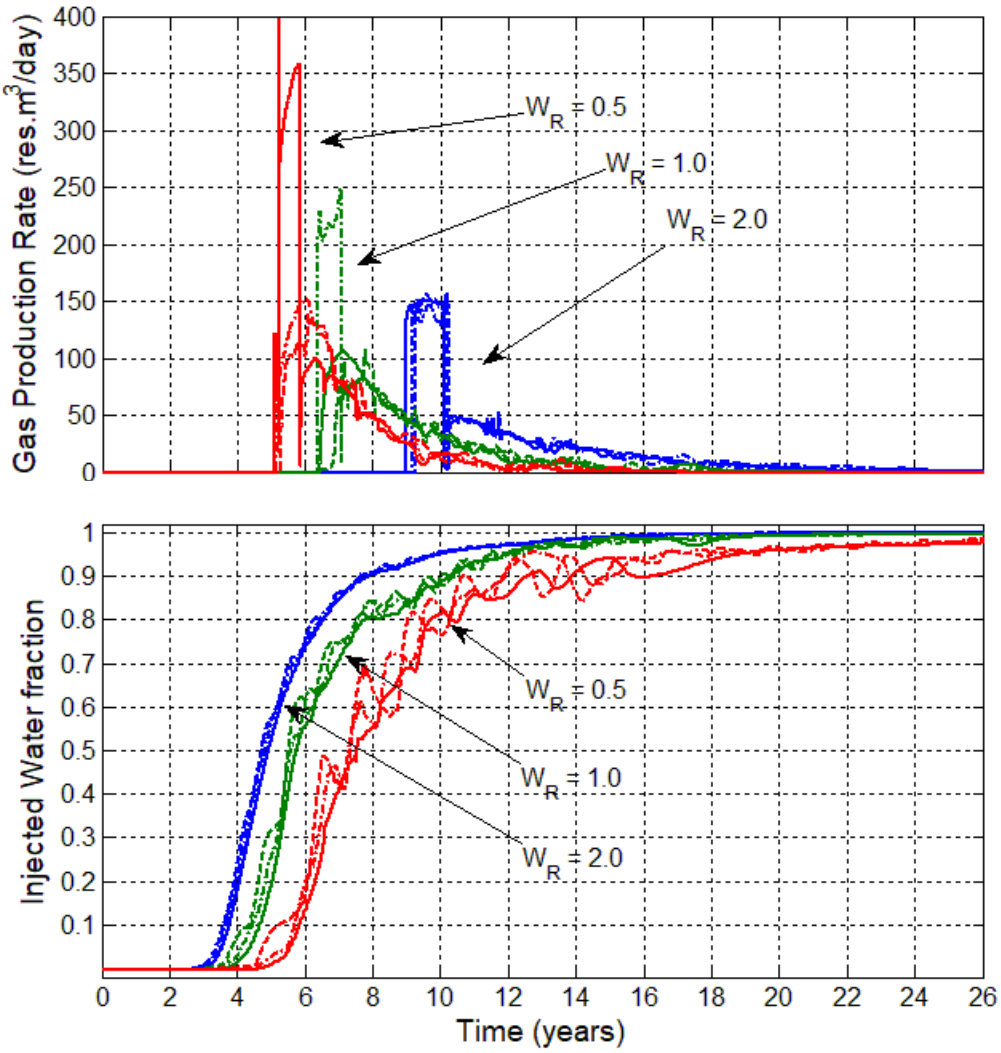

Figure 5.16 Gas breakthrough (top) and seawater breakthrough (bottom) for different scenarios. Solid lines represent smaller gas slugs while dash-dot lines are for larger slugs. Gas production rate here is at reservoir conditions.

We have also analysed the area around the producer wellbore to evaluate water composition changes and calcite precipitation. In Figure 5.17, we show that due to the

nature of the flow in a 5-spot well pattern, displacement fronts are concentric near the injector. However, since the straight line connecting the wells is the shortest flow path, the displacement front is deformed as it approaches the producer and more contact between injected and formation fluids occurs. Therefore, we could observe that regions that are closer or within the shortest flow path are subjected to less mixing between incompatible waters (i.e. high Ca and high HCO_3 waters). On the other hand, regions that are closer to the top and right boundaries of the reservoir model show higher precipitation due to greater extent of fluid-fluid interactions.

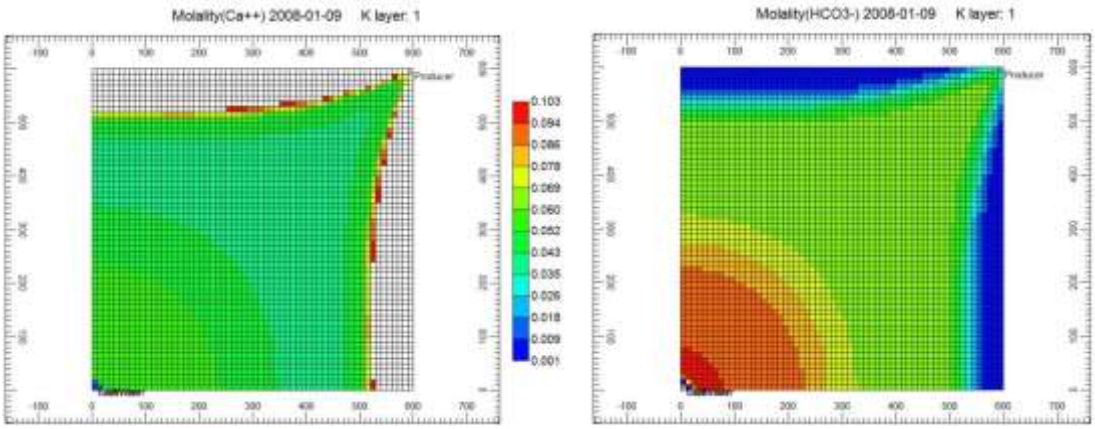

Figure 5.17. Ca (left) and HCO_3 (right) concentration during simulation of scenario C2 with refined grid. White blocks represent concentrations higher than included in the colour scale.

Although the flow field in the near wellbore area points toward the producer well, in the standard numerical solution there is only flux through the grid block boundaries in perpendicular directions. This is the 5-point discretisation scheme, where the numerical solution is obtained using input from a given grid block and four of its neighbours (the ones in perpendicular directions). In this way fluid components move in a zig-zag pattern around the diagonal of the grid to follow the shortest path. This may yield non-realistic behaviour on the mixing zone and therefore mineral precipitation, but the effect is mitigated by having a fine scale resolution grid.

An advanced numerical technique called 9-point grid discretisation is included in CMG GEM. The method works with input of a grid block and all of its eight neighbours and therefore has a more realistic calculation of the pressure gradient. This option, however, cannot be used with heat exchange calculations. Therefore we have compared two isothermal calculations using these two approaches. Results in Figure 5.18 show

that with the more accurate calculation, mineral precipitation along the diagonal is stronger.

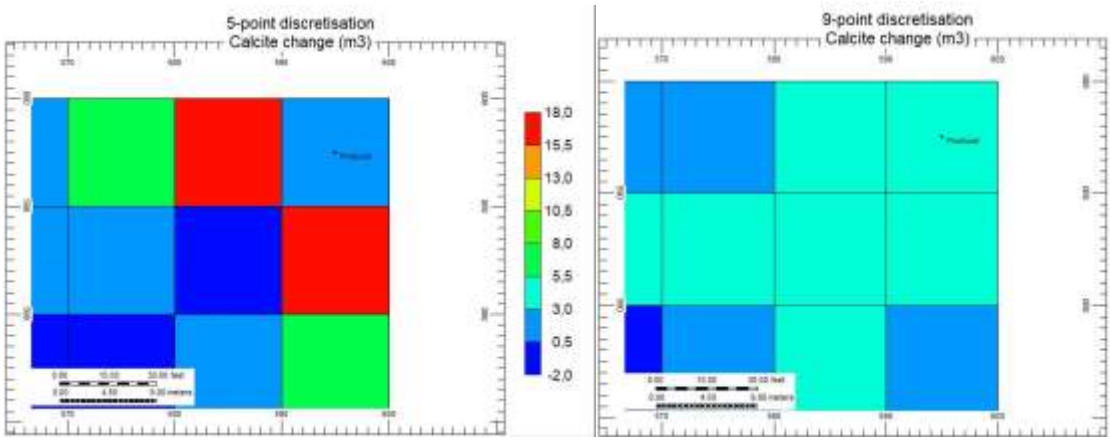

Figure 5.18. Calcite change (scenario C2 with refined grid) after 2PV using 5-point (left) and 9-point (right) discretisation schemes.

Therefore, the prediction of scale deposition in the producer wellbore is dependent on the discretization scheme used for solving the transport equations. If the 9-point approach is a better representation of reality, the volume of calcite scale may be underestimated by more than three times, when using the standard 5-point discretization (see Figure 5.19). However, this formulation must be validated against 2D experiments and compared to other methods such as streamlines and finite-element discretisation schemes.

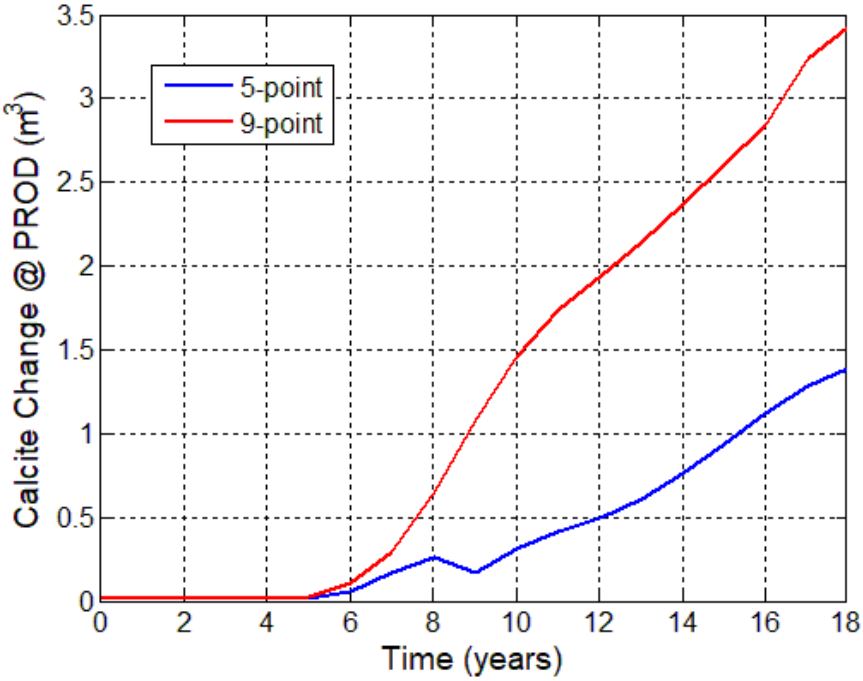

Figure 5.19. Calcite precipitation in the producer well block during simulation of scenario C2 with refined grid using 5-point and 9-point discretisation schemes.

5.5. Discussions regarding 2D Modelling

In this Chapter, we extended the 1D model from Chapter 4 by including three different features: 2D areal geometry, transport of oil phase and heat exchange between fluid components and the porous medium.

All conclusions from 1D two-phase isothermal transport are still applicable, in despite of a more complex flow. Namely, we still have a dissolution zone around the injector that is dependent of water slug size, the dissolved volume of calcite is determined by the volume of water injected (Equation 4.29) and a higher W_R causes a faster dissolution rate and leads to severe scale risk at earlier times.

On the other hand, in this more realistic simulation we observed some deviations from the characteristic behaviour of calcite reactions during CO2 WAG. First, although some of the shortest WAG cycles produce the highest dissolution around the injector when comparing WAG schemes of same W_R (as seen in Chapter 4), slugs that are too small may yield slightly less dissolution. This was the case for water slugs of 60 days (scenario A2 and A3) and indicates insufficient supply of CO_2 during gas injection.

Second, grid refinement of the 2D model revealed that formation damage (calcite precipitation) may happen close to the injector wellbore due to local pressure oscillations and therefore the profile of porosity increase around the injector is not monotonically decreasing with distance (as opposed to the profiles of Figure 4.24 in Chapter 4). This effect is strong for larger gas slugs (>180 days) and may not be detected at lower grid resolutions (see Figure 5.11).

Inclusion of heat exchange showed that calcite dissolution in the field may be overestimated during isothermal calculations. The suppression of dissolution (or precipitation) happens in the mixing zone and the difference between the two types of simulations decreases with decreasing time step sizes, where the numerical dissolution is smaller. This shows that carbonate fields with larger physical dispersion may be susceptible to stronger calcite precipitation in transition zones from cooler to warmer waters.

When looking at reactions around the producer we have seen that the calcite change curves are not as smooth as the curves from Chapter 4. The observed instability is a consequence of calculations during 3-phase flow, and is more pronounced for smaller W_R, which exhibit larger gas slugs. Moreover, this difficulty may be resolved by using oil phases with viscosities low enough to allow a less viscous flow (near piston-like displacement).

Finally, the numerical scheme of solution for the flow equations is important for the calculation of calcite precipitation around the producer. Comparison between a 5-point and 9-point scheme shows large discrepancies in calcite precipitation that are both qualitative and quantitative. The 9-point scheme seems to be more sensible to use since it uses more input from neighbouring grid blocks, but it lacks validation against experiments.

Chapter 6:
Reactive Transport in 3D with oil

An important part of reservoir modelling of CO_2 EOR is the impact of gravity segregation on the flow of different fluids. Particularly, one of the strengths of CO_2 WAG, as opposed to continuous CO_2 injection, is the improvement in sweep efficiency and retardation of gas breakthrough. The appropriate selection of the slug sizes can limit the upward movement of injected gas as well as the downward migration of the injected water.

In addition to that, the heterogeneity of the reservoir plays a role in the gravity segregation impact. When the permeability increases with depth, injected water flows faster in the deeper layers, while the opposite trend in permeability favours the flow of injected gas. The impact of this cross-flow between layers is higher for larger density differences, therefore the initial reservoir conditions (temperature and pressure) should also be considered.

In this final Chapter, we extend our reservoir model to 3D geometry by including layers with different properties. We simulate a base case to analyse how calcite dissolution and precipitation are different at each depth. Moreover, three types of scenario are shown to assess how geology, operation and initial conditions affect the results.

6.1. Model description

We have built a three phase (oil/water/gas) 3D model of a limestone reservoir that contains five layers of grid blocks of different thicknesses, porosities and permeabilities. These properties are constant within each layer and were obtained by averaging (thickness weighted) the properties of a single column of a carbonate reservoir divided in 20 layers.

Thus, we extended the model of Chapter 5 by adding layers to the 2D areal grid. Model parameters and initial and boundary conditions are from Table 5.1, with initial

pressure assigned to the top of the reservoir and saturations and temperature being equal for all layers. The layers properties, including porosity and permeability are shown in Table 6.1.

Table 6.1. Model layers properties from top (L1) to bottom (L5)

Layer	Thickness	Porosity	Horizontal Permeability*	Flow Capacity	Front Velocity
Code	T (m)	$\emptyset$	K_H (mD)	$K.T$	$K/\emptyset$
L1	22	6%	121	20%	12%
L2	15.4	7%	320	38%	27%
L3	11.1	4%	79	7%	12%
L4	18.8	3%	52	8%	10%
L5	26.4	2%	135	27%	40%
Full	93.7	4%	138	100%	100%

*$K_V/K_H = 0.1$

The oil phase was modelled with CO_2 and four light-to-intermediate oil components (3.5% CH4, 5% CO2, 5.5% C3, 6% FC9 and 80% FC30), and because the oil viscosity was 0.16 cP, a piston-like displacement is predicted (according to the classical Buckley-Leverett theory of water displacing oil). Thus, it is expected that the time for injected water and gas to break through should be around half of injected PV (PV*(1-Sor-Swi)). However, as the layers are heterogeneous, the velocity of the advancing fronts will also be different and will be proportional to the ratio between permeability and porosity. Moreover, the injected volume of fluids that enters in each layer is a fraction of the layer flow capacity and the total flow capacity (i.e. permeability x thickness) and will be important to predict the rate of dissolution and precipitation of calcite per layer.

Water vapourisation as well as heat exchange between components and the rock were allowed in the simulation. Aqueous components were restricted to the carbonic acid system supplemented by calcite and halite mineral reactions. This decision was made to run simulations faster without compromising the modelling of calcite reactions in the presence of heat exchange and water vapourisation (during gas injection water evaporates near the injector and all aqueous concentrations increase, including Na and Cl). Water composition is listed in Table 6.2.

Table 6.2. Water composition for Formation Water (FW) and Injected Water (IW).

	pH	CO_2	HCO_3	Ca	HCO_3	Ca	Na	Cl	TDS
	-	mol/kgw			Ppm				
FW	4.9	0.076	0.004	0.558	192	19 114	44 876	103 118	170 076
IW	7.8	<0.0001	0.002	0.010	118	387	12 285	19 580	32 371

6.2. Representivity of layer properties

A comparison of porosity and permeability cases selected for this thesis with a broader database of core plug data from real carbonates (Fig. 6.1) can be used to judge the representivity. The Carbonate 1 case represents a location in the middle of the plot – equivalent to a good permeability Middle Eastern reservoir. Our 5-layer limestone model might be representative of higher permeability pre-Salt material. The data used in this thesis (including Chapter 4 and 5), albeit necessarily higher permeability than average – as required for simulation – is representative of some carbonates – but carbonates have a wide spread of porosity-permeability characteristics.

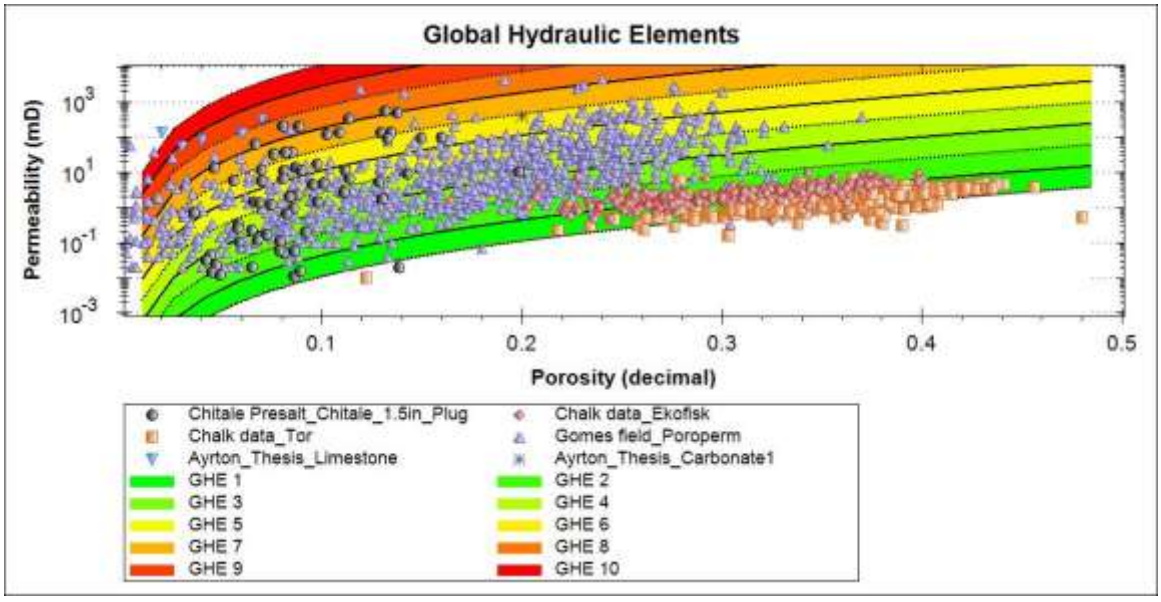

Figure 6.1. Comparison of porosity and permeability data from this work with real filed data using a Global Hydraulic Element Basemap (Corbett and Potter, 2004). Data sources: Chalk data from Peter Frykman; Middle East "Gomes Field" data (Corbett and Gomes, 2000); Pre-Salt data from Campos Basin from Chitale (Chitale et al., 2015).

It can also be seen that the variability of the layers in our 3D model is rather low and should be borne in mind when considering the results of this work (see Figure 6.2).

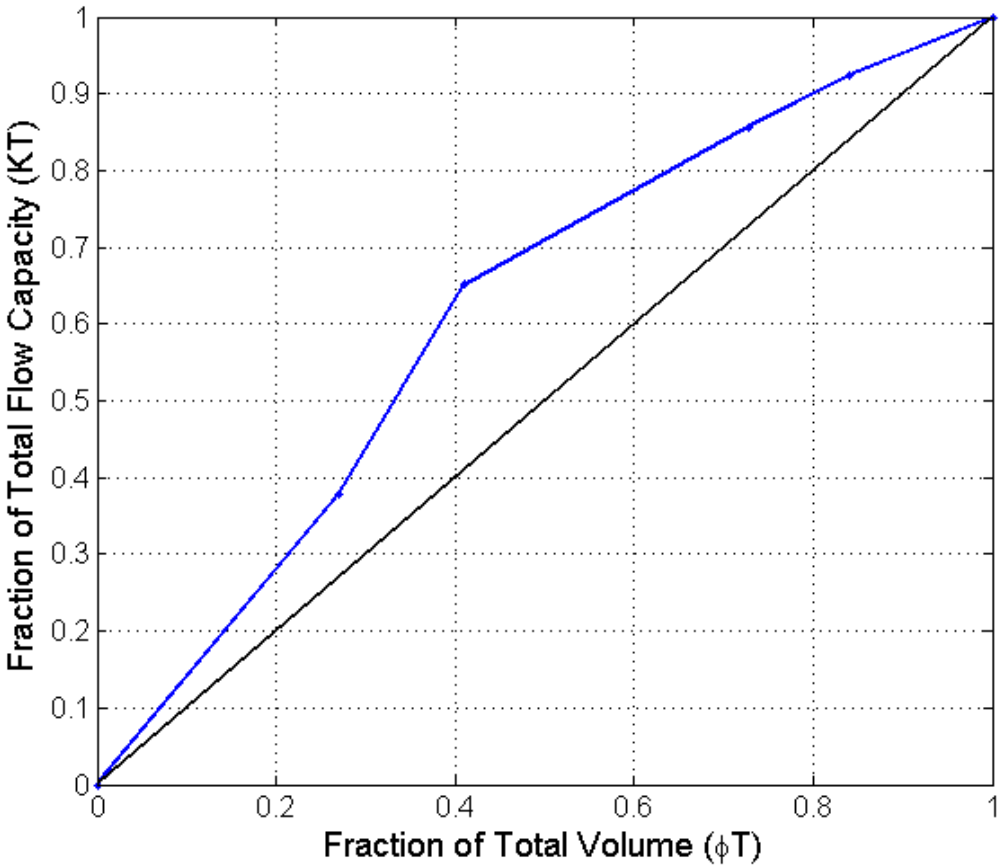

Figure 6.2. Cumulative flow capacity versus cumulative volume (Lorenz plot). The area between the blue and black curves, when divided by 0.5 (Lorenz coefficient) is equal to 0.22; Values closer to unity identify more heterogeneous distributions.

The reduced heterogeneity of the model makes the reactive flow calculations simpler, while GEM could not reach convergence when running a model with the full original data. It seems that GEM is incapable of handling multiphase reactive flow and porosity (and permeability) alterations in a heterogeneous environment, or at least it is very difficult to find a stable solution. To investigate this we tried to run two models with the original 20 layers without (a) calcite reactions and (b) without any chemical reactions. Using the same parameters and conditions of Chapter 5, convergence was obtained for maximum time steps of 0.5 days. The computational time for simulating 24 years of injection using these two models were 80.3 hours (without calcite) and 13.8 hours (without chemical reactions), which shows the increasing difficulty when adding mineral changes (including porosity and permeability alterations).

6.3. Simulation of Base Case

We have simulated the injection of CO_2 WAG with half-cycle of 180 days (unit WAG ratio) in the described reservoir model. As expected, water penetration in each layer is proportional to its flow velocity, with deeper layers exhibiting sharper advancing fronts because of both heterogeneity and buoyancy forces. However, for the gas saturation front, layer 4 shows the second fastest propagation, which is a consequence of the upward migration of the gas phase from L5 (see Figure 6.3).

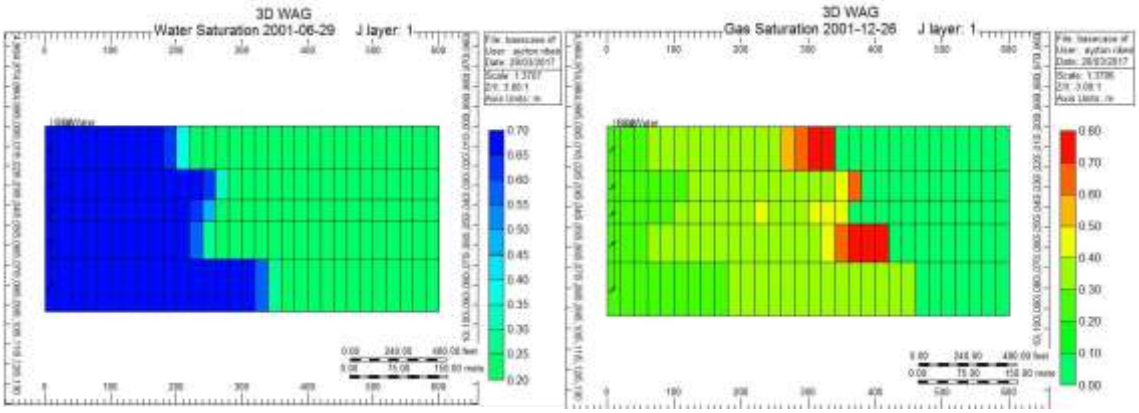

Figure 6.3. Displacement of oil in the x-z plane by injected water (left) and gas (right) during WAG.

Buoyancy forces act more strongly in regions far from both wells, where the system cross sectional area perpendicular to flow is greatest, and hence the flow velocity is the lowest. In Figure 6.4 one can see that gas permeates in front of the injected water in L4, while for L5 water travels faster.

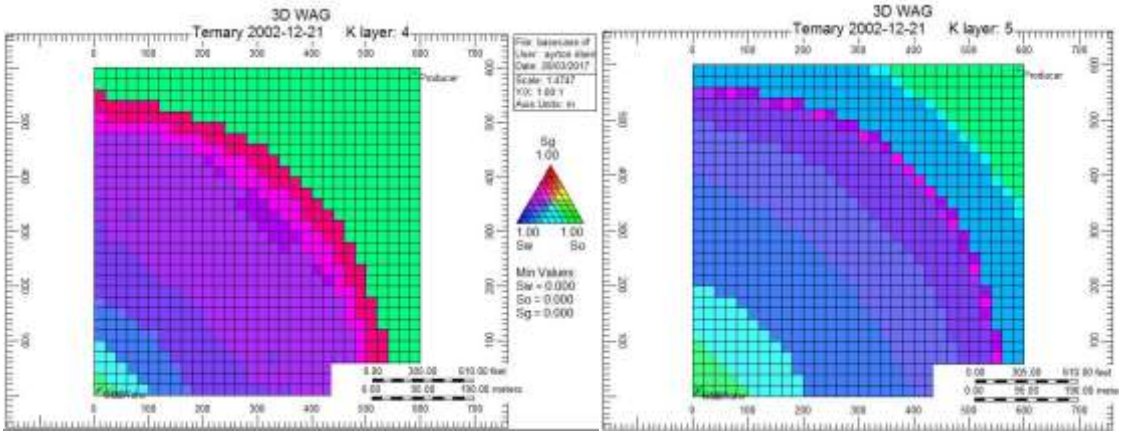

Figure 6.4. Ternary plots during water flooding in L4 (left) and L5 (right).

The EOR mechanism was observed to be condensing/vapourising drive. The injected CO_2 gas phase condenses into the oil phase because of very miscible conditions. Immediately afterwards, the trailing edge of CO_2 gas (which did not

condense) completely vapourises the heavier (still soluble) oil components (FC9 and FC30) and almost all of the lighter components (CH4 and C3). After the displacement front passes, traces of the light components are left in the oil phase, along with a CO_2 concentration of more than 98%, while the gas phase is shared between CO_2, FC9 and FC30.

Near the injector wellbore, during water flooding CO_2 is extracted from the oil and gas phases since the water is undersaturated with respect to CO_2. On the other hand, during gas flooding CO_2 condenses into the oil phase again and the remainder goes to both water and gas phases (Figure 6.5 and 6.6). This process is constantly repeated during each WAG cycle and oil and gas phases (carrying oil components) are displaced continuously.

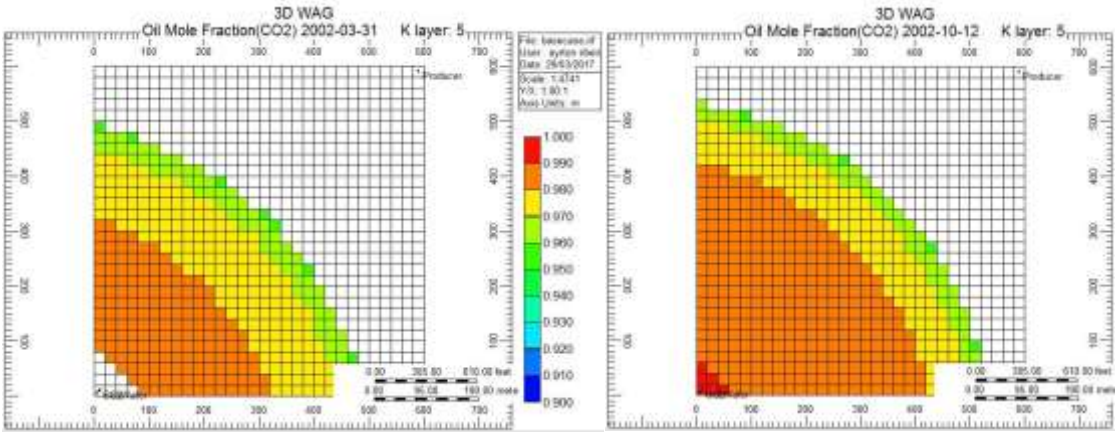

Figure 6.5. CO_2 mole fraction in the oil phase in L5 during water flooding (left) and during gas flooding (right). Major changes are limited to the near injector wellbore zone.

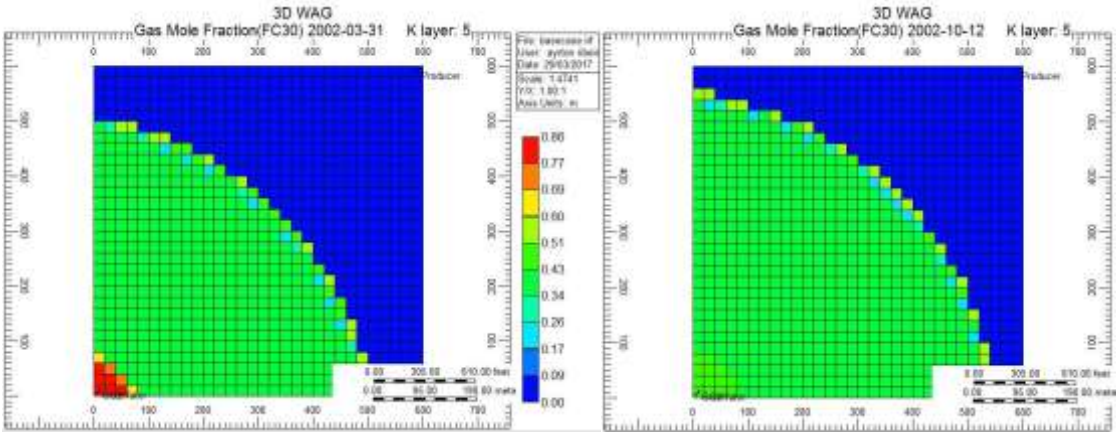

Figure 6.6. FC30 mole fraction in the gas phase in L5 during water flooding (left) and during gas flooding (right). FC30 is the dominant species during water flooding because the injected water extracts CO_2 from the gas phase, which is then replenished during gas flooding.

One important thing to understand is that after an initial displacement of oil and gas phases by injected water, there is no supply of CO_2 to be dissolved into water. Therefore, dissolution of CO_2 into water (and hence calcite dissolution) happens at the displacement front while water is propagating. The gas flooding, as part of the WAG cycle, does not trigger significant calcite dissolution near the injector wellbore since the water is already in equilibrium (or at least near equilibrium if we consider the cross-flow between layers). The role of the gas flooding in calcite dissolution mechanism is to build a supply of CO_2, for the ensuing water displacement, by increasing the saturations in oil and gas phases, which can then subsequently partition into the advancing water flood.

In this sense, the dissolution of CO_2 and calcite into the water around the injector wellbore occurs in a zone correspondent to the penetration of injected water into each layer. Since we have simulated with a fixed injection rate and the water cycles have all the same duration, the dissolved zone is controlled by the flow velocity described in Table 6.1. Moreover, the total dissolution in each layer is obtained by considering the total volume of injected water, which is proportional to the flow capacity. Therefore, L2 and L5 have the highest dissolved volume and the largest dissolution zone. A second order effect was also detected: the reaction rate in these more permeable layers increases with time since during mineral dissolution permeability increases as a monotonic function of itself (higher permeability, higher volume throughput, therefore more dissolution and greater permeability increase). However, because the dissolution is spread over a given area, some layers may show a limited porosity increase closer to the injector (similar to WAG scenarios in Chapters 4 and 5). This is the case for L5, which has the longest penetration but the porosity increase near the injector is similar to L1 and L3 (see Figure 6.7). This result is important because it suggests that changing the water slug size can have different impacts on the injectivity increase of different layers. As CO_2 WAG may reduce the injectivity during water injection (Brannan and Whittington, 1977; Henry et al., 1981), water slug sizes should be adjusted based on the properties of the layers to improve performance.

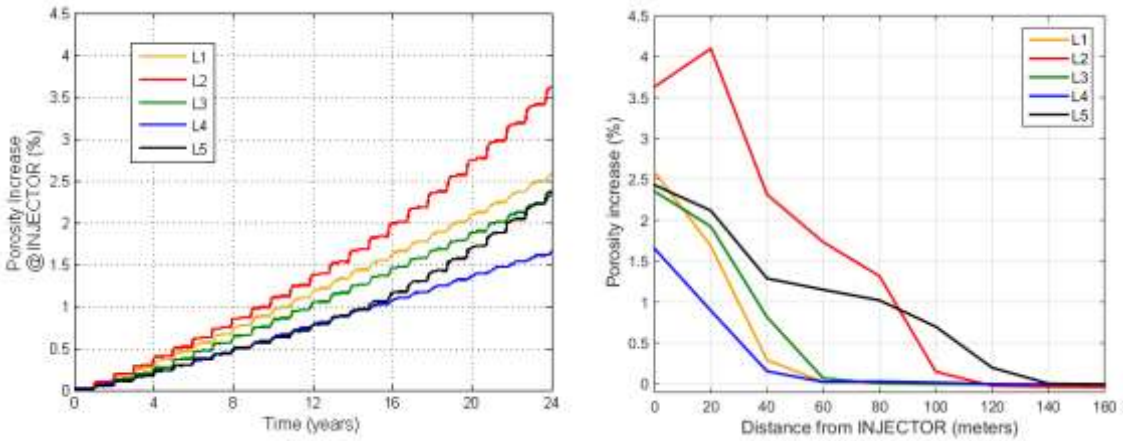

Figure 6.7. Porosity increase (delta porosity) at injector block against time (left) and ultimate porosity increase against distance from the injector (right) for all five layers.

The permeability increase is even more dependent on layer properties given that Carman-Kozeny formula has a non-linear dependence on initial porosity and permeability. In Figure 6.8, we show that the permeability of L2 and L5 grow faster than the others, and L5 becomes the more permeable layer after 21 years of injection.

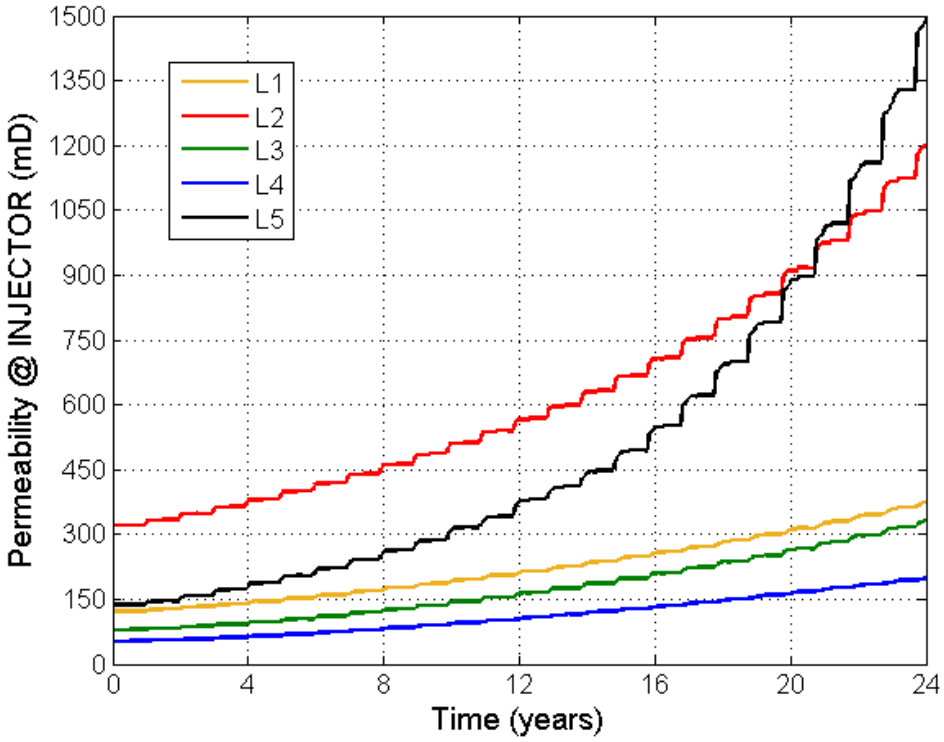

Figure 6.8. Evolution of permeability at injector block for all five layers. L2 and L5 have the largest growths.

Thus, calcite dissolution increases the porosity and permeability of larger and more permeable pore spaces. On the other hand, layers of lower quality still exhibit an enlargement of pores but in a weaker manner. This can increase the vertical heterogeneity near the injector wellbore (see Figure 6.9), as thief zones become stronger, and also build a small areal heterogeneity since different dissolution zones are obtained in each layer.

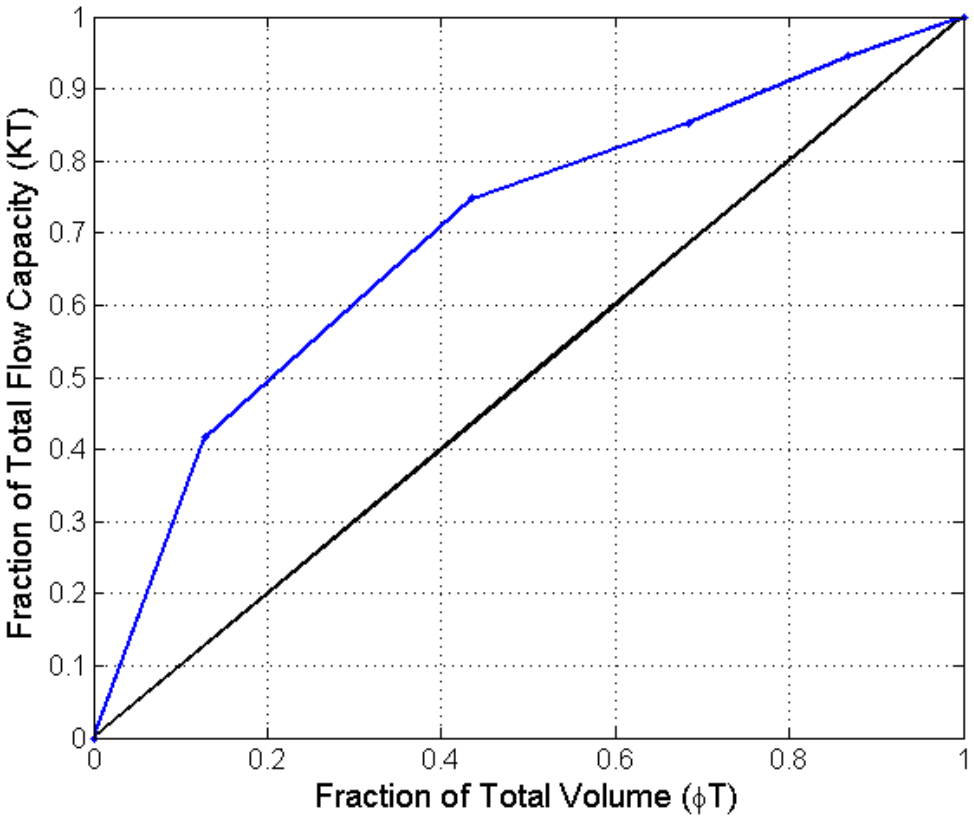

Figure 6.9. Lorenz plot of the injector blocks after 24 years of injection. The Lorenz coefficient has increased to 0.40 (compare with Figure 6.2).

The behaviour of the local calcite reactions changes gradually as the injected water propagates further away from the injector and closer to the producer. Immediately beyond the dissolution zone around the injector, calcite is dissolved only for a limited time and the impact on porosity and permeability is not significant. Just one step further away along the flow path and a limited calcite precipitation is observed after an initial dissolution. This precipitation is limited because it is caused by the mixing front between the HCO_3-rich displacing water (seawater saturated with CO_2 at local pressure) and the Ca-rich displaced water (formation water initially saturated with calcite). As the

injected water propagates toward the producer, its ability to dissolve calcite is continually reduced because of lower solubility of CO_2 at decreasing pressures. In addition to that, calcite precipitation becomes stronger because CO_2 evolution leads to an increase in HCO_3 (see analysis of the mixing front in Chapter 4). In Figure 6.10 one can see how the displacing fluid changes the profile of HCO_3 concentrations in L2 at different times.

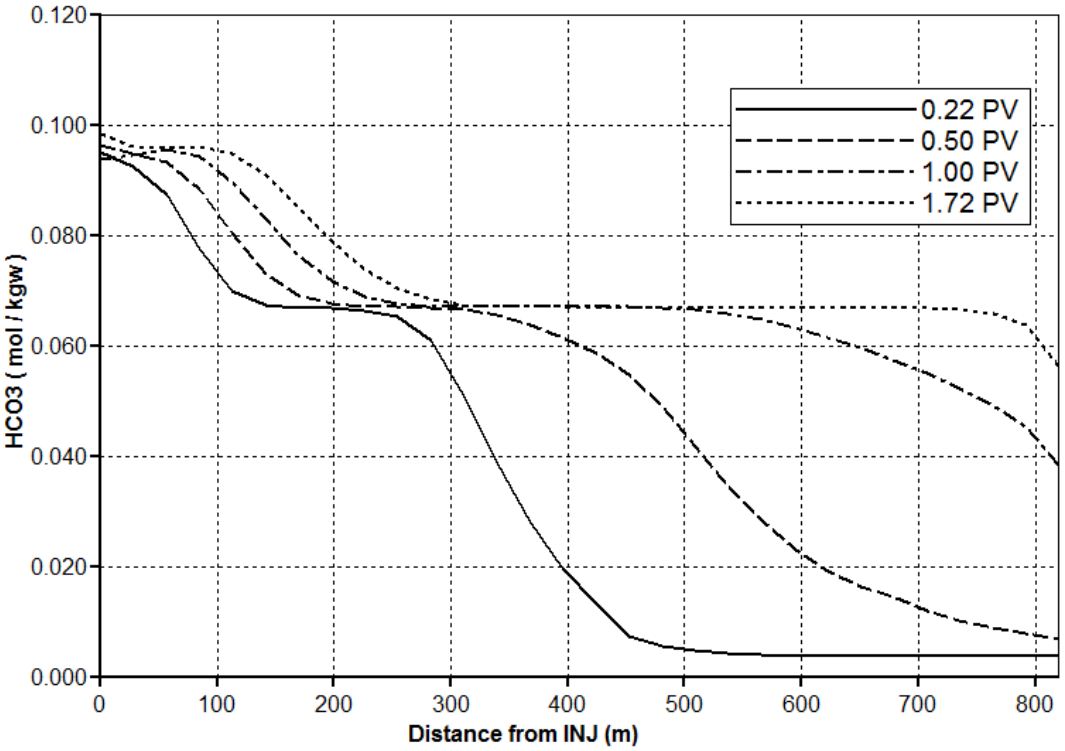

Figure 6.10. HCO_3 concentration profile for L2 at different times (in injected pore volumes).

The two mechanisms of calcite precipitation (i.e. brine mixing and self-scaling) act together to cause a faster calcite change everywhere except in the dissolution zones around the injector. The calcite change in regions of precipitation is much lower than the dissolution near the injector (up to two orders of magnitude). However, around the producer wellbore calcite precipitation can lead to scale deposition that can clog the perforations.

The calcite reaction rate around the perforations in each layer changes constantly because of oscillations in pressure and water production rate; however, the overall behaviour of calcite can be described as occurring in three distinct stages, each of which poses different challenges to scale management. First, calcite is rapidly dissolved during the breakthrough of the injected water (which carries more dissolved CO_2 than the

formation water). In this stage, high Ca water is produced and can lead to severe scale risk in the production tubing and surface equipment.

Then, after breakthrough of the CO_2 free gas at reservoir conditions, calcite precipitates by the combined mechanism of brine mixing and self-scaling, since the CO_2 concentration does not increase anymore, but HCO_3 and Ca concentrations are still high. At this moment, the scale risk moves down to the perforations and is dependent on water volume throughput. In our simulation, L2 and L4 have the highest risk during this stage, while L1 has the lowest risk (see Figure 6.11). The reason for the lower risk at L1 and L5, in despite of the higher flow capacity, is that the top layer has the highest gas saturation and the lowest water flow rate (because of gravity segregation of injected fluids), while the water that reaches the deepest perforation has less HCO_3 because that layer loses the supply of CO_2 gas to the upper layer faster and CO_2 dissolution in injected water upstream becomes reduced.

Finally, after the produced water is 95% injected water, calcite precipitation is caused only by depressurisation, since Ca concentrations are low. Although this stage poses the overall lowest scaling risk, it still deserves some attention since precipitation is occurring continually at the perforations.

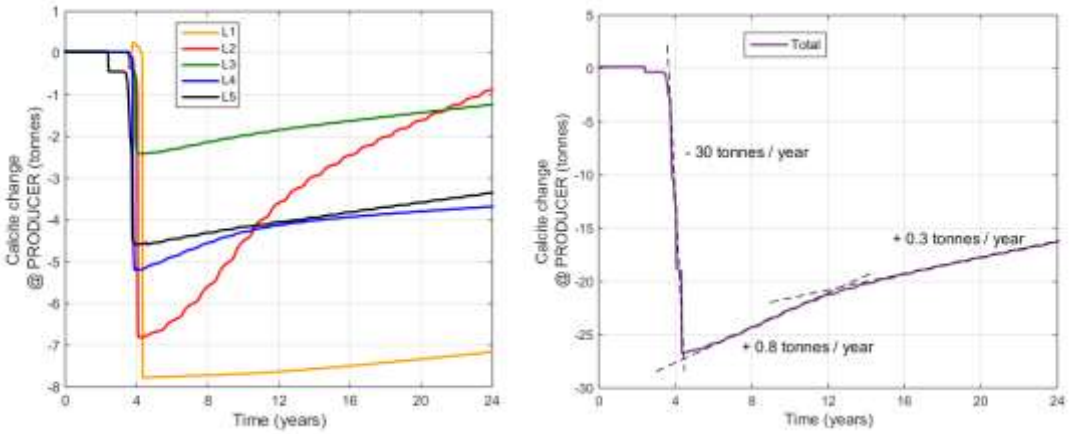

Figure 6.11. Calcite change around producer for each individual layer (left) and well total (right). Breakthrough occurs around 4 years of production (0.5 PV). In L5, water displaces oil faster due to gravity segregation.

6.3.1. Impact of grid refinement

To check the impact of the grid resolution, we have refined the model in the vertical direction to include twice as many blocks per layer in a simple geological model. In Figure 6.12, one can see that during water flooding water saturations are larger in the bottom of all original layers except for L3 (now model layers 5 and 6) where the higher permeability of L2 causes a water flow from that layer into the upper part of L3 where the permeability is lower and therefore water takes longer to move downward. Since vertical migration depends on the difference between phase densities, the gas phase is more affected than the water phase. As seen for water, gas moves faster from layers of greater permeability, but in this case the movement is upward. Therefore, a layer which has permeability lower than its lower neighbour will retain the gas phase for a longer period before it migrates to a shallower layer (e.g. L4 and L5). Moreover, in more permeable layers the gas front will be sharper, since the spreading of the front is counteracted by the vertical migration to other layers (e.g. L2 and L5).

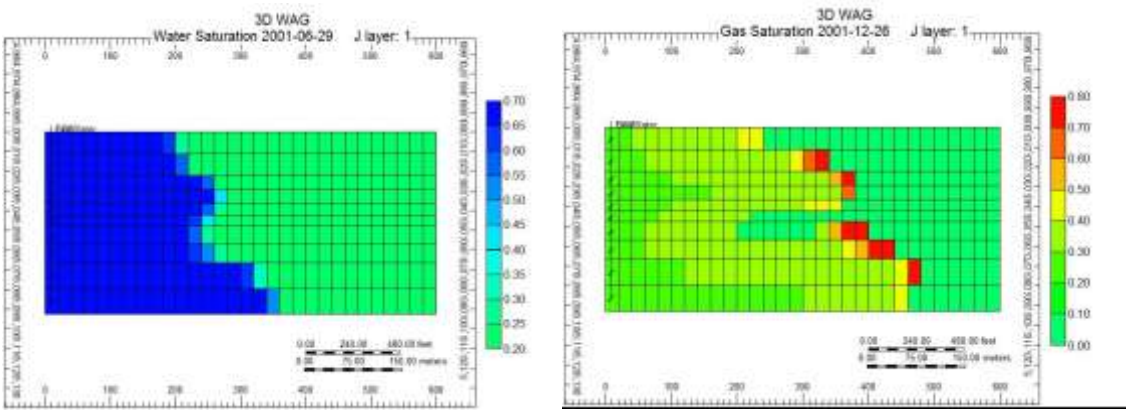

Figure 6.12 – Displacement and gravity segregation (x-z plane) in refined model: water saturation during water flooding (left) and gas saturation during gas flooding (right).

No major changes occur in respect of the calcite dissolution around the injector wellbore. However, the refinement revealed that the vertical segregation decreases the dissolution around the producer wellbore during breakthrough of injected water (as was previously suggested by looking at the reaction rate of L5 in the base case), and the most affected are model layers 1 to 4 (originally L1 and L2). On the other hand, the calcite scale deposited at the perforations (i.e. local calcite change after initial dissolution) remains very similar after grid refinement (see Figure 6.13).

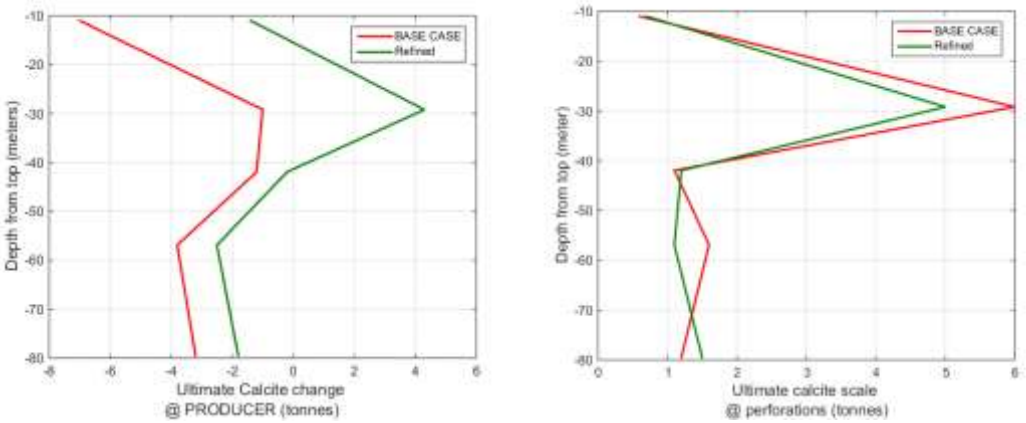

Figure 6.13. Total calcite change (left) and scale deposited (right) at each perforation. Results for base case (red) and refined model (green).

6.4. Scenarios

We have simulated different scenarios by changing variables related to geology, operations and initial physical/chemical conditions.

6.4.1. Geological scenarios: Layer properties

In the last sub-section, it was shown that gravity segregation impacts scale deposition, especially at the boundary layers. Moreover, the most severe scaling risk was located at L2, which is the most permeable and has the second highest front velocity. However, since the injected water sinks to the deepest layers, L2 is the second latest layer to start producing the injected fluids and to precipitate calcite.

The impact of cross-flow between layers is important to investigate since successful WAG field projects in the Permian Basin have limited vertical permeability (Brannan and Whitington, 1977; Henry et al., 1981; Tanner and Baxley, 1992). The Permian Basin (west Texas and eastern New Mexico, USA) concentrates the majority of the CO_2 WAG field experience and some projects have reported dissolution of carbonates (Henry et al., 1981) but not scale deposition. It is unclear if the scale existed or simply were not reported. Moreover, recent developments do pose challenges for scale management and their vertical communication may be higher.

Therefore we have simulated three scenarios to investigate the impact of the location of the most permeable layer and vertical segregation. In Table 6.3, we show that by turning the vertical permeability off (no cross-flow), precipitation in L2 to L4 decreases while more calcite precipitates in L5 and no changes occurred in L1.

Therefore, vertical communication increases the overall calcite scale at perforations because convective currents increase the mixing between fluids.

Swapping L2 to either L3 or L4 to change the relative position of the layer with the highest flow to the others has also produced interesting results. When L2 is located in the middle of the reservoir model and between the lower permeable layers the effect is similar to the previous scenario since the vertical communication is reduced and injected fluids are retained longer in L2 and L4. On the other hand, when the two bottom layers are the most permeable more convective currents are generated involving L3 and L4, which then exchange more fluids during cross-flow. This scenario compared to the base case has a similar cumulative scale risk at the perforations. However, this time the risk is shared between two layers instead of one and they are located deeper in the well. Overall, this first set of scenarios shows that the scale risk at perforations is higher where there is vertical communication between highly permeable layers.

Table 6.3. Scale deposition for scenarios with different layer property.

	L2 with highest flow (BASE CASE)	**No Cross-flow**	**L3 with highest flow**	**L4 with highest flow**
L1	0.6	0.6	0.5	0.5
L2	**6.0**	**3.8**	1.9	0.4
L3	1.1	0.3	**3.6**	**3.1**
L4	1.6	0.2	1.3	**4.8**
L5	1.2	**2.1**	1.1	1.2
Perforations Total	10.5	7	8.4	10
Production Line	26.5	31.3	25.8	19.7

6.4.2. Operations constraints: Injection rate and WAG scheme

The parameters chosen to operate injector and producer wells are the responsibility of the reservoir engineer. The choice of injection rate and WAG ratio will impact the performance and productivity of the selected well pattern and can be optimised to maximise recovery, cash-flow, CO_2 storage, etc. It is interesting for scale management to know how different well controls will impact the calcite scale risk.

The first scenario tested was injection with a lower injection rate (and also lower injection pressure). As reactions are a function of injected volume of water, to compare with the base case we have calculated the calcite scale risk after 48 years of injection with a rate of 250 m^3/day. In Figure 6.14, one can see that injecting at half of original injection rate leads to a less severe scaling risk even if the life of the project is doubled. Thus, calcite precipitation rate around the producer is not a linear function of the injection rate (as opposed to the results in Chapter 4).

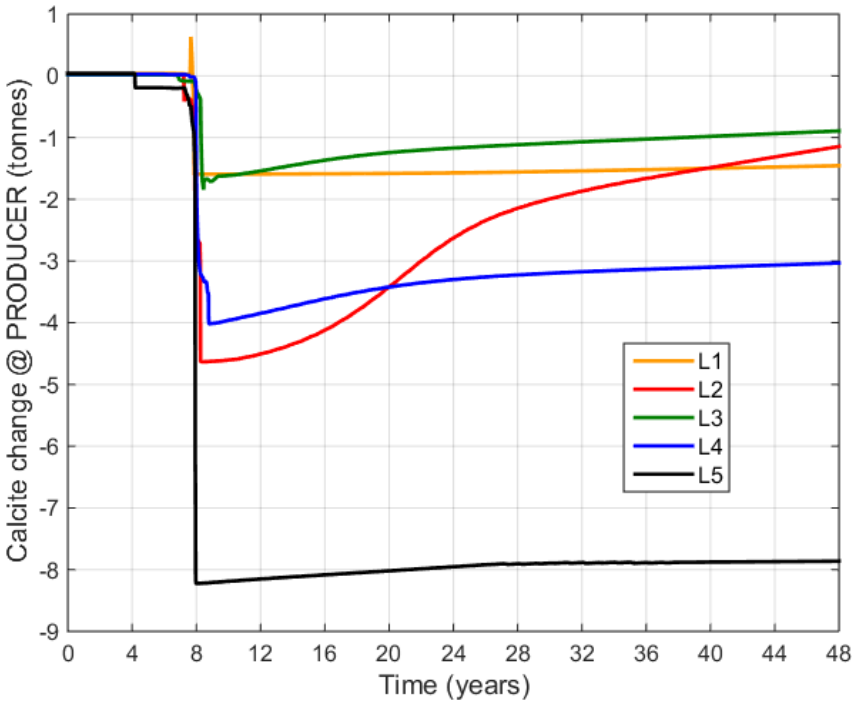

Figure 6.14. Calcite change around producer (during injection at 250 m^3/day) for each individual layer. Breakthrough occurs after around 8 years (0.5 PV) of production.

This occurs because of two reasons. First, injection at a lower rate allows more time for the gravity segregation to act and less precipitation is triggered in the boundary layers. Second, the lower pressure at the injector causes less dissolution upstream (see Figure 6.15) and thus lower concentrations of Ca, and HCO_3 ions are transported and precipitated around the producer. Overall, we conclude that raising the injection rate to achieve higher productivity or faster oil recovery will make the calcite deposition problem worse and earlier.

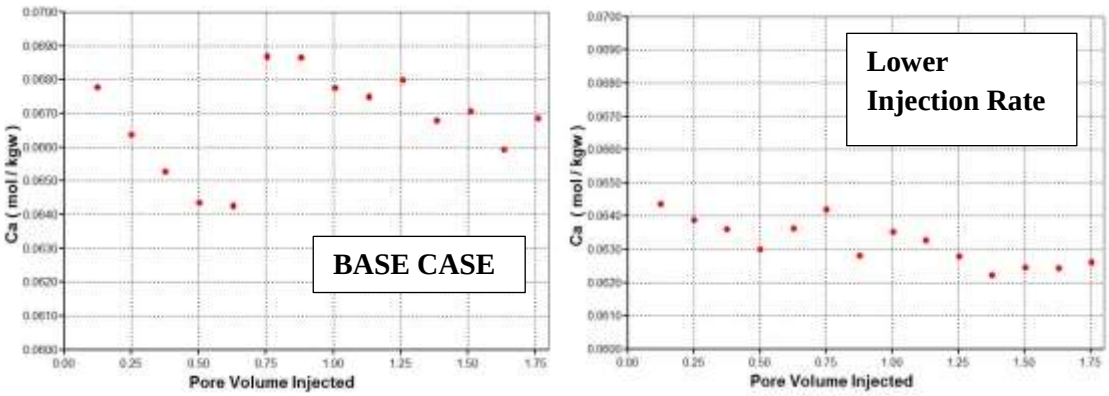

Figure 6.15. Ca concentration around injector for the base case (left) and lower injection rate (right).

Another parameter that can be changed to increase performance is the WAG ratio, which as we have seen, controls the rate of precipitation (Chapter 4) and affects water breakthrough time and oil recovery (Chapter 5). The WAG ratio determines the injected volume of water and therefore the mass of calcite scale deposited at the perforations. Lower WAG ratios will give a faster response in incremental oil recovery but an earlier gas breakthrough, while a higher WAG ratio may be beneficial to control the gas production rate and improve sweep efficiency (Green and Willhite, 1998; Kane, 1979; Tanner and Baxley, 1992; Ettehadtavakkol et al., 2014; Agada et al, 2016).

To obtain the best performance, a variable WAG scheme is used to obtain fast response to gas injection and increase the gas utilisation factor (volume of injected gas per volume of incremented oil recovered). The so called Tapered WAG (or Hybrid WAG) is referred as the optimum WAG scheme in the Permian Basin in West Texas and consists in the implementation of WAG process with decreasing gas slug sizes between cycles (Kane, 1979; Green and Willhite, 1998). Special cases of this strategy have been reported, such as continuous gas injection followed by CO_2 WAG implemented in the Denver Unit of the Wasson Field (Tanner and Baxley, 1992), pre-solvent water followed by buffer slug enriched gas and then WAG, implemented in the Levelland Unit of the Levelland Field (Brannan and Whittington, 1977) or CO_2 WAG chased by continuous water injection, also in Levelland Field (Henry et al., 1981).

We have simulated the WAG injection with constant WAG ratios of 0.5, 1 and 2, as well as a Tapered WAG that combines them. For the Tapered WAG, we kept the

water slug cycles fixed in 180 days, while the gas slugs were 360, followed by 180 and then a constant cycle length of 90.

In Figure 6.16, it is shown that although the Tapered WAG caused less dissolution around the producer compared to all but the lower-limit WAG ratio (less scaling risk during breakthrough), the precipitation by mixing is even stronger than the precipitation given by a WAG process with a constant and high WAG ratio. On the other hand, the ultimate precipitation rate (given by self-scaling) is of similar value of the upper-limit WAG ratio, since the water volume throughout of the former converges to the later (see Table 6.5).

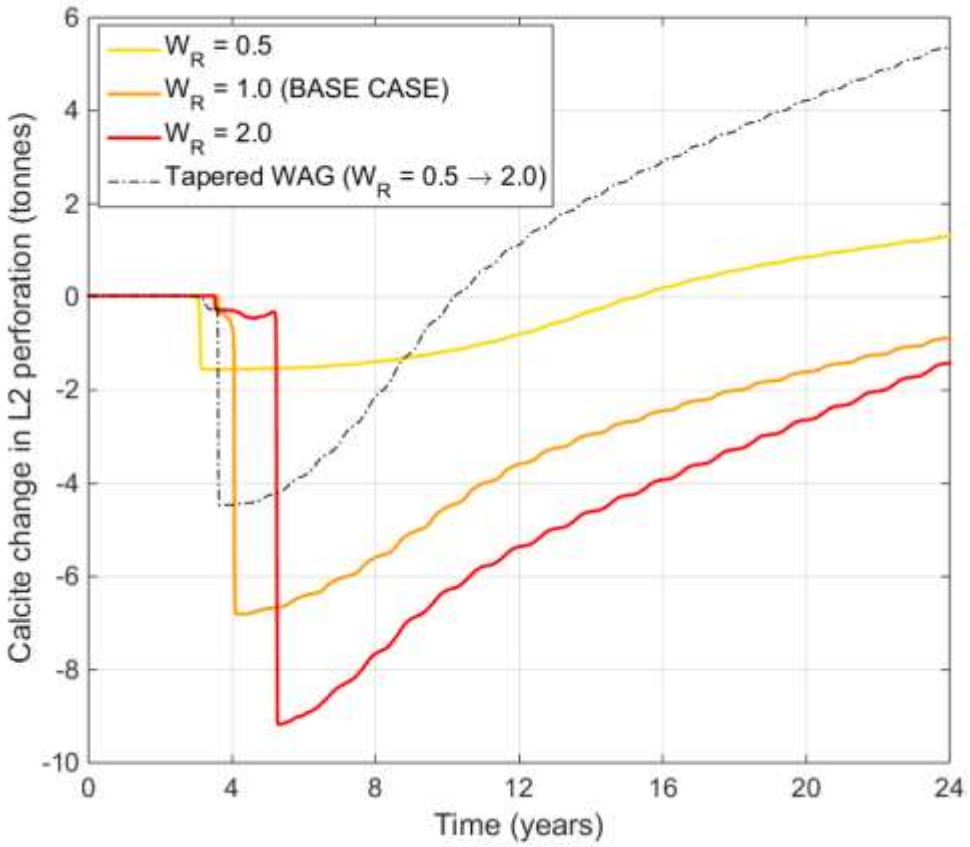

Figure 6.16. Calcite change around the second perforation for different WAG schemes.

Table 6.5. Scale deposition for different WAG scheme scenarios.

WAG ratio	0.5	1.0	2.0	0.5 → 2.0
Injected Pore Volume of Water	1	1.5	2	2
Total Scale @ Perforations (tonnes)	5.2	10.5	15.2	17.8
Ultimate precipitation rate @ L2 (tonnes per year)	0.14	0.22	0.37	0.36

In conclusion, Tapered WAG may be a useful tool to optimise both oil recovery and scale risk management if the early precipitation risk is suitably addressed. In addition, if the gas production rate decreases excessively, the operator can decrease the WAG ratio to re-establish a desired gas rate (Kane, 1979). This would also be beneficial for limiting the scale deposition rate.

6.4.3. Reservoir initial conditions: T, P and Formation Water

The last set of the modelled scenarios consists of changing the reservoir initial conditions (temperature, pressure and formation water). We have selected two reservoir conditions to use, assuming the same geological properties and well constraints as the base case. The first type of reservoir conditions is based on Ekofisk (a chalk reservoir located in the North Sea), which has a higher temperature of 135 ℃ and the same pressure as the base case. The second set of reservoir conditions is called Reservoir F and has a temperature of 95 ℃ and a lower pressure of 150 bar (2200 psi). Simplified formation water composition were used and calcite was equilibrated with each (see Table 6.6).

Table 6.6. Formation Water composition for Ekofisk (E) and Reservoir F (F).

	pH	CO_2	HCO_3	Ca	HCO_3	Ca	Na	Cl	TDS
	-	mol/kgw			ppm				
E	4.6	0.063	0.001	0.741	38	23 595	53 555	124 542	203 938
F	5.6	0.082	0.02	0.011	1 091	392	59 830	45 225	109 750

Before running simulations, we have assessed the impact of temperature in the solubility of calcite in the presence of CO_2 (i.e. Ksp = [Ca] $[HCO_3]^2$ / $[CO_2]$). Figure

6.17 shows the decrease of the equilibrium constant with increasing temperature. We recall that all simulations performed are non-isothermal and as the injected water is warmed to reservoir temperature, calcite solubility will decrease and precipitation will occur at the temperature front. The location of this precipitation is very stable since the propagation of the temperature front is a very slow process compared to fluid displacements.

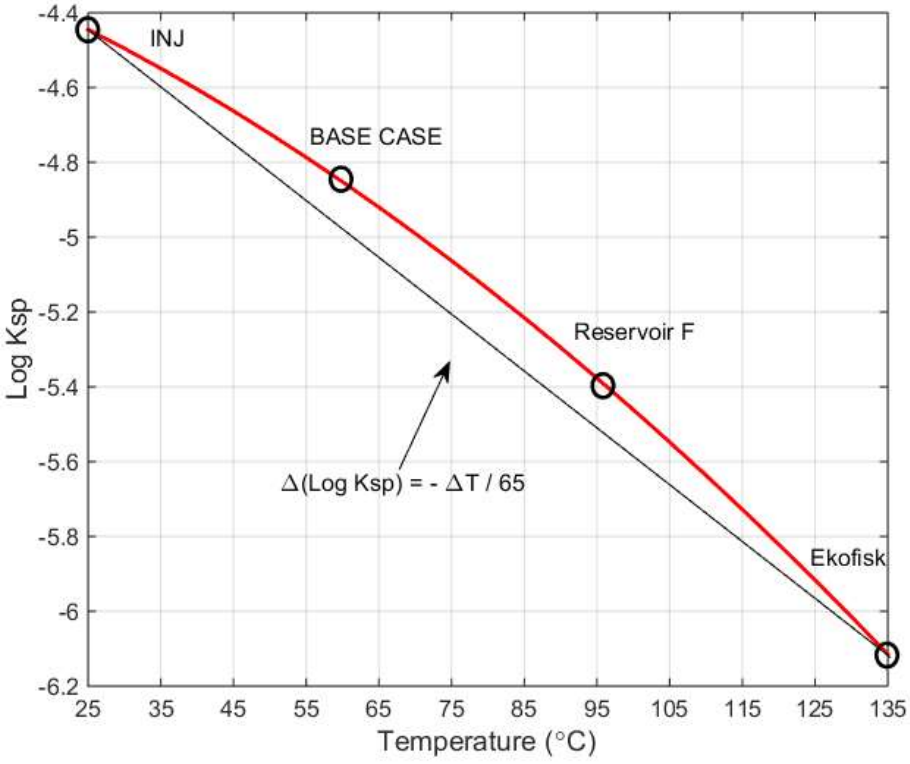

Figure 6.17. Equilibrium constant for calcite in the presence of CO_2 with varying temperature.

Simulation with Ekofisk reservoir conditions produced a similar mass of dissolved calcite around the producer (28 tonnes dissolved), but only a relatively low scale risk at the second perforation (see Figure 6.18). By the end of the simulation run, only 2.5 tonnes of calcite precipitated in the perforations (half of it in L2). Moreover, the higher reservoir temperature protects the producer wellbore against calcite scale deposition because calcite precipitates in the temperature transition front, as mentioned above, and thus the water that arrives at the producer has less HCO_3 (see Figure 6.19). This is an important result since it shows the relevance of considering heat exchange to evaluate the calcite reactions in hotter reservoirs.

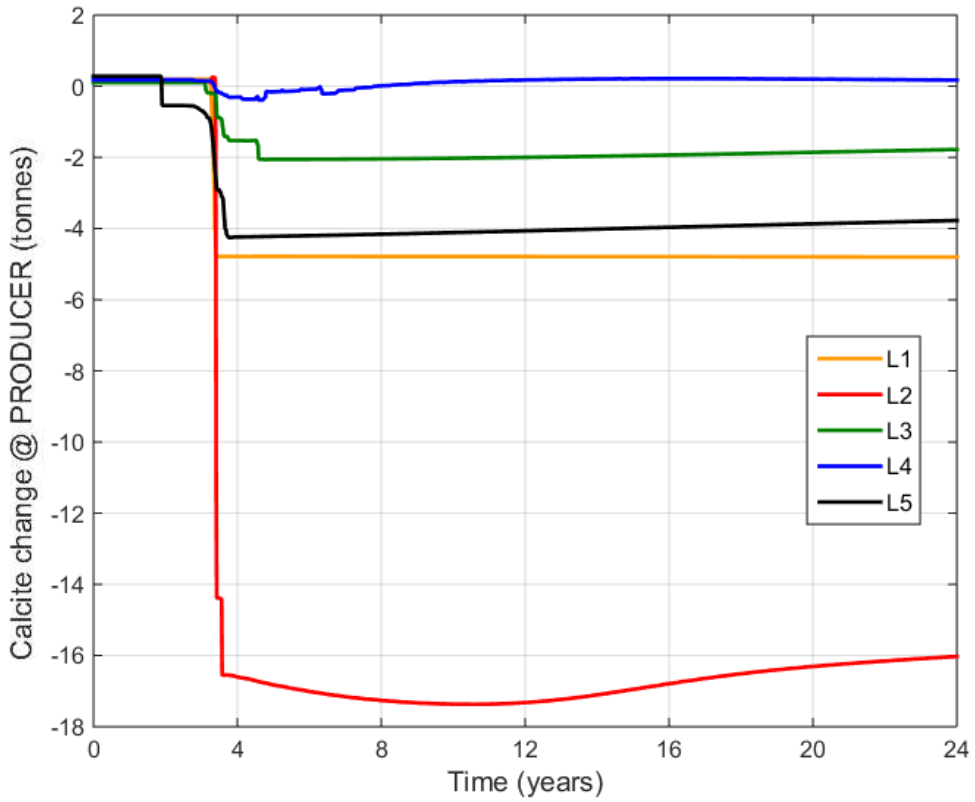

Figure 6.18. Calcite change around the producer for Ekofisk reservoir conditions.

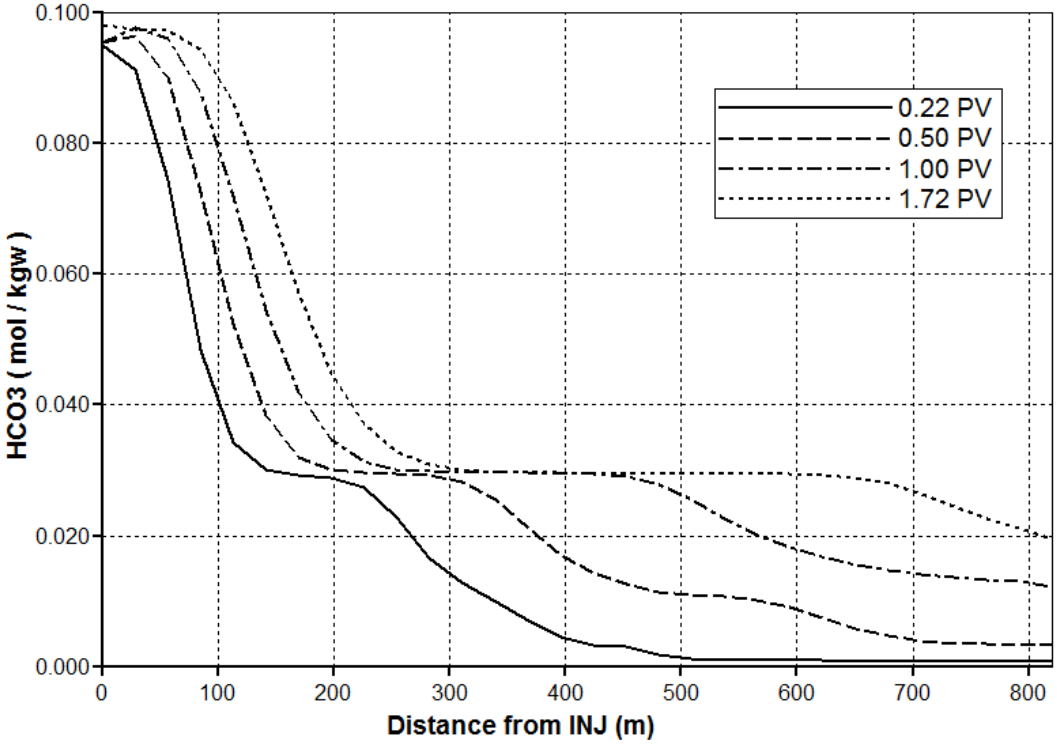

Figure 6.19. HCO3 concentration profile for L2 at different times (measured in pore volumes).

For Reservoir F, the lower reservoir pressure leads to a lower production of Ca during calcite dissolution around the injector wellbore (similar to the lower injection rate scenario). Vertical migration between layers is stronger because the density of the gas phase is lower at the given reservoir pressure (369 kg/m3, while it was around 700 kg/m^3 for other scenarios). The migration of CO_2 to shallower layers occurs constantly and faster than in the base case. Scale deposition at the perforations is then stronger in deeper layers (L3 to L5) where gravity keeps the water volume throughput higher and also drags saturated water from shallower layers (see Figure 6.20). Nevertheless, the total scale risk at perforations (6.6 tonnes) is less severe than the base case.

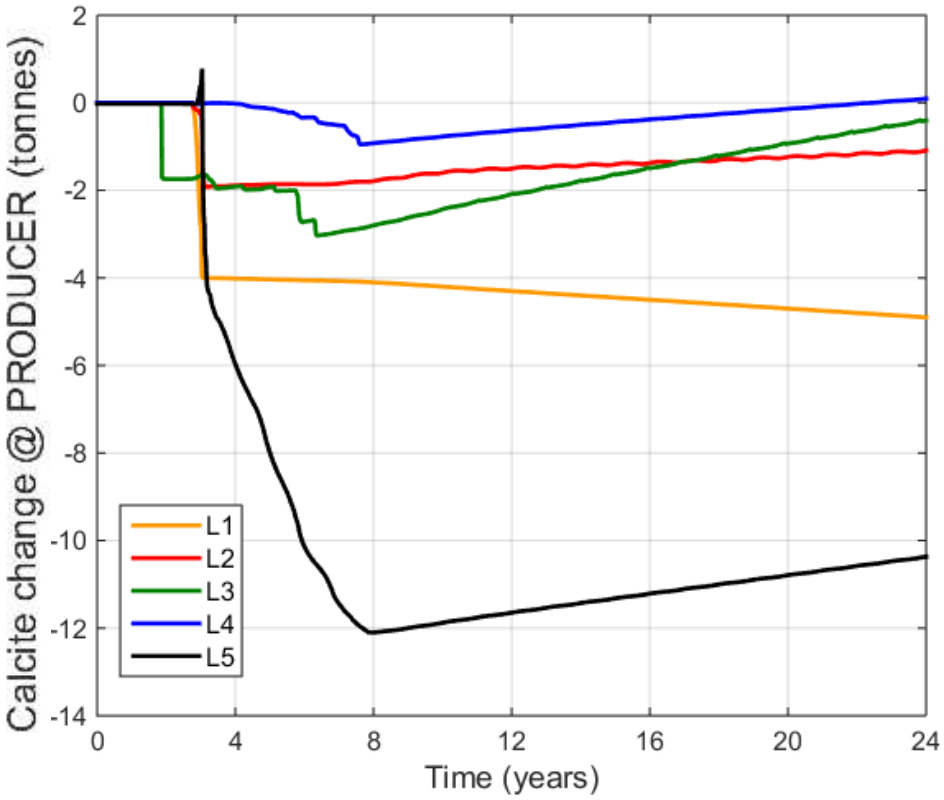

Figure 6.20. Calcite change around the producer for Reservoir F conditions.

6.5. Discussions regarding 3D Modelling

In this Chapter, we have modelled calcite reactions in a layered model of limestone reservoir. We investigated the impact of having layers with different storage and flow properties, which are subjected to vertical cross-flow. We identified the importance of calculating flow capacities and front velocities, for they will determine the calcite dissolution rate and the size of the dissolution zone around the injector.

Moreover, we saw that calcite dissolution increases the heterogeneity near the injector wellbore by dissolving more permeable zones faster.

The strength of reactions around the producer is also influenced by the layer properties, but vertical cross-flow plays a role. We noted that the layers in the boundaries are subjected to gravity segregation and therefore exhibit lower precipitation rates due to limited flow of water (L1) or limited supply of gas (L5).

On the other hand, vertical cross-flow increases the mixing of fluids between layers, which leads to stronger scale deposition. The ordering of the layers is important and higher precipitation was found in scenarios which high permeable layers are in contact.

We observed that calcite scale deposition is not a linear function of the injection rate (as it was for 1D simulations in Chapter 4). Increasing the injection rate will cause a scale risk that is more severe (even at reduced time of injection) because of less gravity segregation in the boundary layers and higher pressure of injection, which increases the dissolution upstream.

Another way to improve the performance of a field is by changing the WAG ratio, and the same conclusions of Chapter 4 and 5 were also true in 3D simulation. In addition, we showed that the Tapered WAG could be used to optimise oil productivity and minimise the scale risk. When varying the WAG ratio from 0.5 to 2, instead of using a constant WAG ratio of 2, we obtained the same ultimate rate of precipitation of the upper limit, while dissolution during gas breakthrough was weaker (but still above the dissolution of WAG ratio 0.5. However, the precipitation during mixing was stronger and caused more scale deposition at the perforations. Nevertheless, the Tapered WAG scheme could decrease the scale risk at surface equipment and production tubing, which happen at early times, but the precipitation at perforations will be stronger.

Finally, the reservoir initial conditions have some impact on the scale deposition. Hotter reservoirs have more precipitation in the temperature front and therefore scale formation is reduced. Lower pressure reservoirs also exhibit less severe scale risk, since gravity segregation is stronger and limits the mixing between layers. The reservoirs with the most severe calcite scale risk are cooler and deeper (higher pressure), such as the Lula field (Cruz et al., 2016).

Conclusions and Recommendations

Final Discussion

In this work, we investigated the calcite dissolution and precipitation during different conditions of flow in carbonates. The analysis started in a static environment without a gas or oil phase, and was completed with a non-isothermal 3-phase flow in 3D model of limestone reservoir. Now, we recall the main aspects of each step of investigation.

In Chapter 2, we studied the carbonic acid system and showed that for pH is between 4.3 and 8.3, HCO_3 and CO_2 are the relevant species, with later being dominant at lower pH and the former being dominant for higher pH values. The equilibrium concentrations, determined by equilibrium constants, are very stable under variations of temperature and pressure of a liquid solution (i.e. limited or no contact with a gas phase). On the other hand, when calcite is added to the system, a temperature and pressure dependency emerge due to the solubility of the mineral. Calcite dissolution is favoured by increase in pressure and total carbon dissolved, while precipitation happens when the Ca or HCO_3 concentrations increase, or the solution is heated. We built an analytical formulation centered in a cubic polynomial, which shows that the charge balance between foreign species, such as Na or Cl, has an impact on the equilibrium Ca concentration (lower charge yields higher Ca).

In Chapter 3, we presented four different models for calculating the CO_2 solubility in aqueous solutions (GEM, PHREEQC, Duan & Sun and Diamond & Akinfiev) based on thermodynamic principles. We compared the models with experimental data from the literature and concluded they all are accurate for solubility in pure water (rel. err. < 5%). For high salinity brine, however, all models exhibit difficulties in representing the data with the same accuracy especially GEM and PHREEQC (which use Peng-Robinson EOS) at lower pressure (<100 bar) or higher salinity (>4 M NaCl). In addition to this, we showed that based on the properties of isobaric CO_2 solubility curve one can incorporate the gas phase into the model of Chapter 2. The main feature of equilibrating calcite with gaseous CO_2 in a solution of NaCl is that the Ca equilibrium concentrations can be higher at higher salinity, as seen in Chapter 2, and also at higher pressure.

In Chapter 4, we performed reactive transport simulation of carbonate water injection in a limestone formation using PHREEQC. Dissolution of calcite happens in the injector block, while precipitation occurs in the producer and all other blocks. The dissolution occurs because the carbonated water is undersaturated with respect to calcite when entering the system, and convergence to equilibrium is within the first block. The cause of precipitation was identified as mixing of incompatible waters (between high HCO_3-displacing water and high Ca-displaced water), since PHREEQC does not consider a pressure gradient in the model (i.e. flow velocity is not calculated by Darcy`s Law). Moreover, we observed that when injecting waters of a lower charge balance between inert species, dissolution and precipitation are stronger.

By simulating reactive transport using GEM, we obtained similar results for the case of carbonated water (limited precipitation in the producer caused by brine mixing). Moreover, we simulated the injection of seawater and gaseous CO_2 to see the main differences between the two types of single-phase (continuous) injection. Results showed that seawater dissolves the calcite rock everywhere but at the injection point the dissolution rate decreases as the initial CO_2 concentration is displaced. Nevertheless, the dissolution becomes slow but continuous. On the other hand, CO_2 injection causes a faster dissolution everywhere, which is not continuous because the formation water becomes saturated with calcite.

When we combined the scenarios to simulate CO_2 WAG and CO_2 SWAG, we observed that calcite dissolution in the injector happens during water injection, since it dissolves the free-gas that was injected before (in WAG) or that is injected simultaneously (in SWAG). Provided the volume of injected water over a period is equivalent, both WAG and SWAG dissolve the rock with the same rate, and also causes similar effects in the producer. The simulation of 2-phase reactive flow revealed that in the producer calcite can be dissolved and precipitated (as opposed to just precipitation during carbonated water injection). The reactions are more complex and are affected by the time for breakthrough of injected gas and water. We saw that when the injected CO_2 reaches the producer, a fast but limited dissolution occurs (like the CO_2 injection scenario), while when the injected water breaks through, a strong precipitation starts (like the carbonated water scenario), which is followed by a continuous precipitation (not observed in other scenarios) caused by degassing along the flowpath. Thus, the implementation of CO_2 WAG in carbonates causes scale deposition by a combined

mechanism of brine mixing and self-scaling. This is different from what was expected, for carbonate scale are usually understood to be self-scaling by the scale management community.

The impact of the WAG scheme on the reactions was investigated. The WAG ratio, which has been identified as an important parameter for controlling the EOR performance, is also what dictates the rate of the porosity increase around the injector and the growth of the scale risk around the producer. Higher WAG ratios yield higher volumes of water flowing through the reservoir and hence higher volumes of calcite dissolved upstream and precipitated downstream. Regarding the producer, severe scale risk occurs earlier because with higher WAG ratios more mixing occurs between injected and formation waters.

The reactions are faster than the residence time when the simulation is at the reservoir scale (as opposed to core scale). This allowed the calcite dissolution to be calculated as a linear function of the volume of water injected. The relationship is invariant under grid refinement, however the porosity increases faster for higher grid resolution. Moreover, for grid blocks that are sufficiently small, CO_2 WAG causes a dissolution zone that goes beyond the injector block, while CO_2 SWAG dissolves only the calcite in the first block. The dissolution zone was observed to be larger for larger water slugs. This points out an advantage for operators performing CO_2 WAG in carbonates: the water slug size may be selected to maximise the injectivity increase by forcing a significant increase in porosity and permeability up to a target distance from the injector wellbore, for the total volume of dissolved rock is predominantly determined by the WAG ratio.

In Chapter 5, these results were tested in more complex flow conditions by considering non-isothermal 3-phase flow in 2D. All conclusions are still applicable when adding the transport of an oil phase. However, around the producer the calcite change is subjected to oscillations that lead to variable precipitation rate. The cause of oscillations is the irregular alternation between periods of multiphase flow, which limits the flow of water, and 2-phase flow. This instability in the reaction rate is stronger for lower WAG ratios because more injected gas competes for pore space that was previously occupied by water and oil phases. Whether these instabilities occur in field applications or not will depend on the heterogeneity of the formation and higher mobility ratio between displacing and displaced fluids, which may cause a more

dispersive and viscous flow that favours multiphase flow and hence challenges in the predictions of scale deposition.

Regarding heterogeneity, we analysed the impact of heat exchange on the dissolution of calcite in the full model by running isothermal and non-isothermal simulations with different time step sizes. We observed that for shorter time steps, less numerical dispersion is generated and less dissolution occurs in both types of simulations. Non-isothermal flow dissolves less calcite than isothermal flow, but the relative difference between than decreases with decreasing numerical dispersion. This happens because under non-isothermal flow calcite is constantly dissolved around the injector (which is cooler) and precipitated as Ca and HCO_3-rich waters propagate to warmer regions, and a more dispersive advancing front increases the interaction of fluids as said in the last paragraph. Thus the mixing between waters cause precipitation and if there is a temperature difference the precipitation is stronger.

In Chapter 6, we investigated the system in a reservoir with five layers of different porosity, permeability and thickness. We demonstrated that by calculating the flow capacities of the layers one could determine at which depth the calcite dissolution will be stronger, and by calculating the front velocities one could rank the size of the dissolution zone by layer. Therefore operators have one more tool to increase the injectivity during CO_2 WAG and improve the EOR performance of an oilfield, as WAG parameters can be set to control the size and strength of the dissolution zone.

The prediction of where the scale risk will be more severe is more challenging since there is cross-flow between layers that can segregate the injected gas and the injected water and limit their interaction. In the simulation of the base case, gravity plays a role and promotes an escape of the injected gas from the bottom layer, reducing the calcite reactivity around the deepest perforation, hence lower scale risk although the dissolution in the injector was the highest. A lower scale risk was also observed for the top layer, where CO_2 accumulates and limits the water production rate. Moreover, we simulated scenarios of vertical permeability and observed the direct relationship between dissolution upstream and precipitation downstream is restored when there is no vertical communication. By comparing scenarios, we conclude that the scale risk is higher when there is cross-flow, especially when the most permeable layers are in direct contact with each other.

Simulation of additional scenarios related to well operations revealed that reducing the injector rate makes the gravity segregation stronger and the total scale risk

less severe. In addition to that, the implementation of a Tapered WAG can delay the gas breakthrough, hence the start of scale deposition. However, the scale risk grows faster by enhancing brine mixing. Perhaps, the optimum strategy for Tapered WAG in terms of reduced scale risk is to start decreasing the gas injection after the rise of the gas-oil ratio, reducing the brine mixing. If this strategy would be economically feasible is outside the scope of this thesis.

The final set of scenarios showed that higher temperature reservoirs act like a shield against scale deposition: calcite dissolves around the injector but precipitates in the temperature front before reaching the producer. Moreover, injecting CO_2 WAG in lower pressure reservoirs yields a lower scale risk because gravity segregation is stronger due to higher density difference between injected fluids. Thus, there is a tendency for reservoirs with higher pressure and lower temperature to exhibit a more severe scale risk, like the Lula field in the Brazilian pre-salt. However, gravity segregation may be difficult to estimate since it depends on the uncertainty associated to vertical permeability measurements.

Conclusions

To summarise the main findings we answer the two Questions that were posed in the introduction.

Answer to Question 1 (What impacts scale deposition during CO_2 WAG?):

During CO_2 WAG scale deposition is impacted by three types of factors (and also interactions between them): Initial conditions, well operations and permeability distribution.

- The scale risk is generally more severe for higher pressure (either initial or applied) and lower reservoir temperature, since more calcite can be dissolved and high Ca waters can reach the producer. We note that pre-salt reservoirs have at least one of these conditions (higher pressure) and some have both (such as Lula field). Then they tend to pose more challenges when compared to shallower reservoirs.
- The WAG ratio is a key operational parameter, as it controls the rate of dissolution and precipitation of calcite, provided there is enough injected gas to saturate the water.

- One important contribution of this thesis was Equation 4.28, which relates the volume of calcite dissolved with the volume of water injected for a given injected water composition. The equation was valid for isothermal or non-isothermal flow, with or without an oil phase.
- The size of the water slugs is also important to keep in mind, since they determine the size of the dissolution zone around the injector wellbore.
- Calcite scale has been found to form by a combination of two mechanisms: depressurisation (or self-scaling) and mixing of incompatible waters (or brine mixing). Dispersion across the field increases brine mixing whenever the formation water is high in Ca and the displacing fluid is HCO3-rich. Heat exchange causes an additional precipitation in the transition zone between cooler and warmer regions, which is larger for higher fields with higher dispersion.
- Vertical communication between highly permeable layers increases the scale deposition due to more mixing between fluids. While gravity segregation inhibits precipitation in the boundary layers due to low water flow rate (top layer) or low gas supply (bottom layer).
- Higher injection rate increases the precipitation rate because it forces more CO_2 and calcite dissolution upstream and decrease gravity segregation in the boundary layers.

Answer to Question 2 (How to model calcite reactions in 3D models of carbonate oil reservoirs?):

To model calcite reactions in 3D models of carbonate oil reservoirs one needs a multiphase and multicomponent flow simulator that updates porosity and permeability when calculating chemical equilibrium states.

- The correct calculation of multiphase flow is very important since time for breakthrough of injected gas and water determine the start of the dissolution and precipitation around the producer. In addition to that, variations in water flow rate during transitions between 2-phase and 3-phase flow exhibit some instabilities that must be resolved otherwise the calculations of calcite reactions may be compromised.

- Changes in viscosity and density of components with temperature and pressure are important to determine if the displacement of fluids are dominated by gravity, viscous flow or piston-like displacement.
- Formation water composition is required for assessing CO_2 solubility and precipitation during mixing of waters, especially the concentrations of Na, Cl, Ca, HCO3 and pH.
- Simple equilibrium reactions (carbonic acid system and calcite dissolution) are enough; Kinetic modelling is required only for simulations at the core scale since calcite reactions are faster than the flow through large grid blocks (>10m^3).
- Heat exchange should be included in the simulation for calculating the additional precipitation in the temperature front, which is higher for more heterogeneous models.
- Water vapourisation and halite precipitation are optional and they are recommended only for longer gas injection periods, where formation damage around the injector can occur.
- Good description for the vertical permeability is essential for calculating cross-flow and gravity segregation, while storage and flow capacities around the injectors are required to determine the size of the dissolution zone. Permeability distribution within each layer would be beneficial for more realistic estimates of the precipitation by brine mixing, but could be substituted by appropriate selection of the numerical scheme and its associated numerical dispersion.

Future work

There are a few lines of research that could be done in the future.

1) Distribution of rock types:

   More heterogeneous distributions of rock types could be linked to loss of injectivity and also to oil trapping between WAG cycles when hysteresis is modelled. It would be interesting to see if calcite dissolution and precipitation mitigate these problems or make them stronger. Moreover, it would be beneficial to see how a CO_2 WAG changes the porosity and permeability of a realistic heterogeneous field: is the post-flow distribution less heterogeneous?

2) Inclusion of other minerals:

Anhydrite ($CaSO_4$) and dolomite ($CaMg(CO_3)$) may compete with calcite for the available Ca and the dissolution and precipitation reactions may change across the reservoir especially during non-isothermal flow. The injection of low salinity water, a common practice to prevent $BaSO_4$ scale deposition, should be investigated in such a system to see if it is still beneficial: Is the low salinity injection going to promote precipitation of sulphates or carbonates?

3) Couple with geomechanics:

The enlargement of the pores by dissolution may cause a subsequent closure of pore throats that are subjected to higher mechanical stresses (water weakening). Such phenomenon should be addressed to improve the risk assessment of collapsing the wells.

4) Optimisation of CO_2 WAG considering calcite:

Since the WAG ratio controls both EOR performance and mineral reactions, it should be investigated how the dissolution and precipitation of calcite alters the economics of a project. In this sense, Tapered WAG looks promising to achieve optimum economic performance. What is the optimum Tapered WAG scheme to achieve lowest scale risk subjected to economic constraints?

Appendix A1

Report for CMG: Geochemical Modelling in GEM – Activity Model

A1.1 Overview:

In chemical equilibrium calculations the interactions between charges contribute to move the system away from an ideal (diluted) case. These interactions are stronger in concentrated solutions, especially high salinity waters, and therefore require calculation of activity coefficient in these conditions which are performed by an activity model.

Currently, GEM allows the user to choose between IDEAL, DEBYE-HUCKEL and B-DOT activity model. However, these models consider only the interaction of the species with the solution medium and therefore have limited accuracy in high saline solutions. B-DOT for example, provides reasonable results for ionic strength smaller than 2 mol/kgw in dominantly chlorine solutions (Parkhurst, 1990). On the other hand, the so-called PITZER model calculates activity coefficients by incorporating short-range interactions between ion pairs and triples. These type of interactions become relevant in solution with high ionic strength (above 2 to 3.5 mol/kgw) (Langmuir, 1997) and it is proved that PITZER model can accurately model them in solutions up to 6 mol/kgw (Pitzer, 1987). In addition, PITZER model uses a multi parameter approach that can be used to fit the model to experimental data and provide accurate results in high salinity, high pressure and high temperature solutions (Appelo et al., 2014; Appelo, 2015).

In this report, we compare experimental data related to barite, anhydrite and calcite solubility with the chemical equilibrium results using (1) GEM with the B-DOT model and (2) PHREEQC with the PITZER model.

A1.2 Modelling of $BaSO_4$ and $CaSO_4$ precipitation.

A1.2.1 Methodology

5-blocks reservoir model was developed using GEM. Initially, all aqueous species in the reservoir were set to 0 and no mineral was present. Saline water containing Ba+2

(or Ca+2), SO4-2, Na+ and Cl- was continuously injected into the first block since the start of simulation. Ba+2 (or Ca+2), SO4-2 were set to 0.5 mol/kgw, which is a high enough concentration to observe barite (or anhydrite) precipitation, while Na+ and Cl- varies from 0, 0.5, 1, 2, 3, 4, 5, 6 mol/kgw. The solubility of barite or anhydrite is determined by the concentration of barium (or calcium) which is dissolved in the brine when the injected water reaches equilibrium by the last block. The same mechanism model was also built in PHREEQC and run with PITZER database. The experimental data with regard to the solubility of barite and anhydrite were compared to GEM results with the B-DOT model and PHREEQC results with the PITZER model.

A1.3 Results and discussion

The GEM results with the B-DOT activity model underestimate the solubility of barite (and anhydrite) when compared to the experimental data available (Templeton, 1960; Uchameyshvili et al., 1966; Blount, 1977; Block and Waters, 1968; Blount and Dickson, 1969.). In contrast, the PHREEQC results calculated with the PITZER activity model match with the experimental data very well (Figures A1.1 and A1.2).

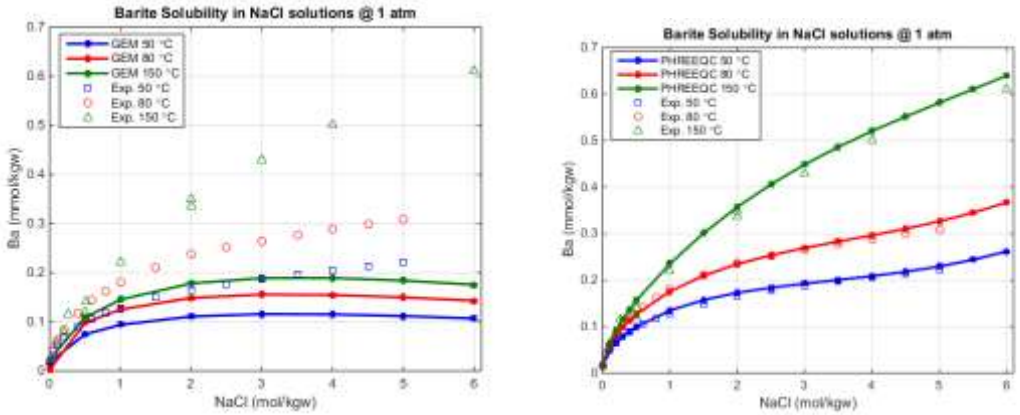

Figure A1.1. Barite solubility using GEM (left) and PHREEQC (right). Experimental data from Templeton, 1960; Uchameyshvili et al., 1966; Blount, 1977.

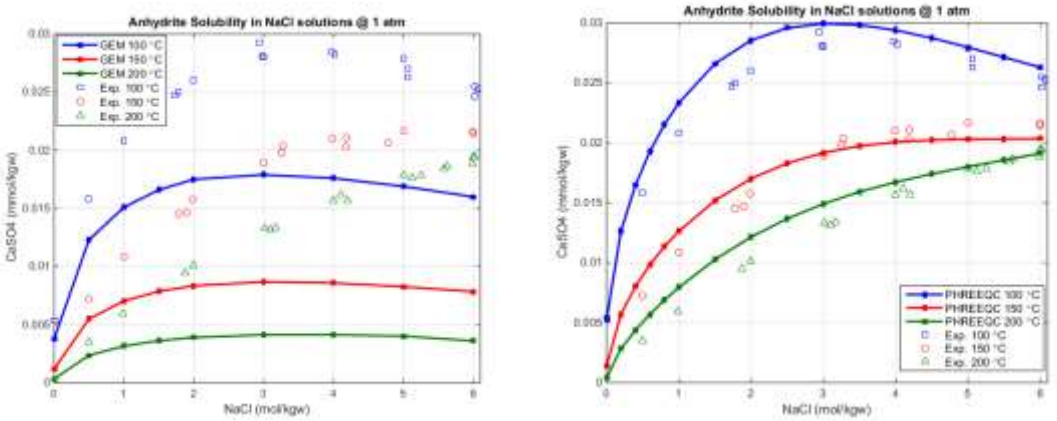

Figure A1.2. Anhydrite solubility using GEM (left) and PHREEQC (right). Experimental data from Block and Waters, 1968; Blount and Dickson, 1969.

For these geochemical systems the theoretical solubility are determined by

$$m_{Ba} = \sqrt{\frac{K_{Barite}}{\gamma_{Ba} \cdot \gamma_{SO_4}}} \; ; \qquad m_{Ca} = \sqrt{\frac{K_{Anhydrite}}{\gamma_{Ca} \cdot \gamma_{SO_4}}}$$

Thus, the sources of errors are (a) the equilibrium constants and (b) the activity coefficients, because the same molalities were defined in GEM and PHREEQC model. In Figure A1.3, we performed the simulation using GEM with the equilibrium constants extracted from the PITZER database of PHREEQC. There is a slight modification, but it is obviously not enough to cause the big discrepancy shown in Figures A1.1 and A1.2.

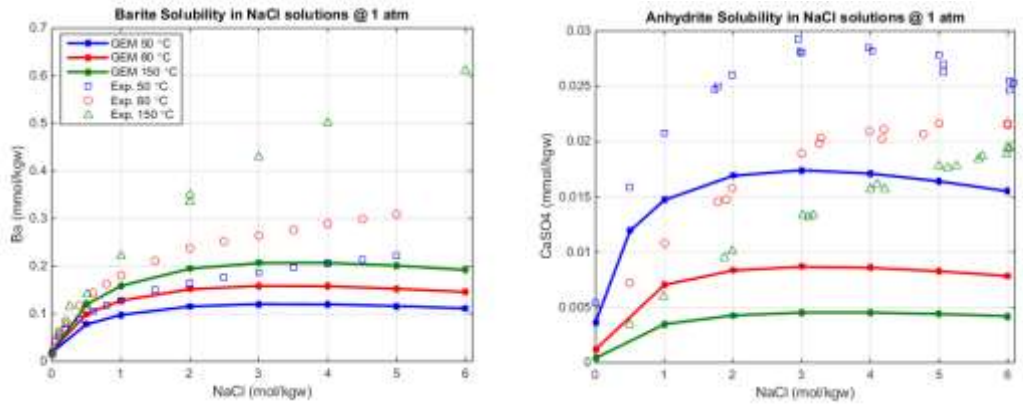

Figure A1.3 – Barite (left) and Anhydrite (right) solubility using GEM with equilibrium constants from PHREEQC. Experimental data from Templeton, 1960; Uchameyshvili et al., 1966; Blount, 1977 (Barite); Block and Waters, 1968; Blount and Dickson, 1969 (Anhydrite).

The inaccurate activity coefficients calculated by B-DOT activity model in GEM is the only one reasonable explanation for the errors highlighted in Figure 1.1. **Therefore,**

the introduction of PITZER activity model, as an option to be selected in systems where it is necessary, is believed to be helpful with more accurate modelling of chemical and mineral reactions.

A1.4 Modelling of $CaCO_3$ dissolution.

A1.4.1 Methodology

In GEM, we designed a 2-blocks reservoir model with calcite as a mineral, CO2 and CH4 as gas components and the following aqueous species: H+, OH-, Ca+2, HCO3-, CO3-2, Na+ and Cl-. Initially, H+ and OH- were set to 1.0E-07 M, while Na+ and Cl- were 0.01E+01, 0.05E+01 or 0.10E+01 mol/kgw, depending on the simulation. All other species were initially set to 0.

A1.4.2 Results and Discussion:

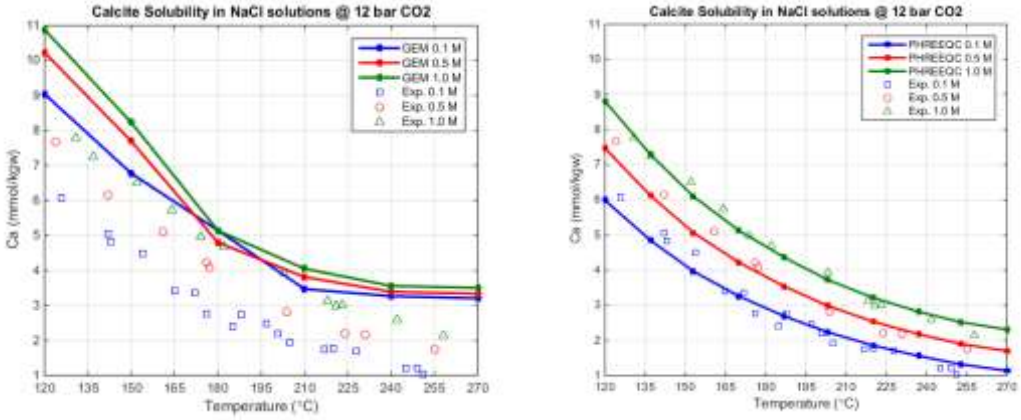

Figure A1.4. Calcite solubility using GEM (left) and PHREEQC (right). Experimental data from Ellis, 1963.

The GEM results using the B-DOT model overestimate the solubility of Calcite when compared to the experimental data available (Ellis, 1963), while PHREEQC with PITZER model fits nicely to data (Figure 2.1).

In projects with CO_2 injection in carbonate formations, the pH is usually between 4 and 7. In these conditions, Ca+2 and HCO3- are the dominant ions and we have:

$$m_{Ca} = \sqrt[3]{\frac{K_{Global}}{4} \cdot \frac{\gamma_{CO_2}}{\gamma_{Ca} \cdot {\gamma_{HCO_3}}^2} \cdot m_{CO_2}}$$

Therefore, the source of errors in calcite solubility is dependent on (a) CO_2 solubility in addition to (b) equilibrium constants and (c) activity coefficients. GEM can consider the salting out effect (which was done in our simulation) to correct the CO_2 solubility in brines. However, this was not enough to match with the experiments and although the user can change the values of the equilibrium constants and the CO_2 percentage to achieve a match, the modifications can lead to unrealistic results or to an unreliable in real reservoir systems where more reactions occur simultaneously. On the other hand, if the PITZER model becomes available, it can correct the activity coefficient and even determine reliable solubility of gases in saline solutions (Appelo, 2015).

SPE-179884-MS

Predicting Calcite Scaling Risk Due to Dissolution and Re-Precipitation in Carbonate Reservoirs During CO_2 Injection

Ayrton S. Ribeiro and Eric J. Mackay, Heriot-Watt University; Leonardo Guimarães, Universidade Federal de Pernambuco

This paper was prepared for presentation at the SPE International Oilfield Scale Conference and Exhibition held in Aberdeen, Scotland, UK, 11–12 May 2016.

Abstract

Carbonate reservoirs are more geochemically reactive than sandstones and can experience big changes in porosity and permeability because of mineral reactions. In this work, we analysed the calcite dissolution and precipitation in chalk reservoirs during injection of seawater and CO_2 bearing fluids.

We performed reactive transport simulations with injection of seawater, carbonated water, CO_2 gas, CO_2 SWAG and CO_2 WAG. We evaluated the mineral reactions that occur in the injector and producer blocks. Moreover, the calcite dissolution rate was calculated and its relationship with flow rate was investigated.

Simulation results showed that during injection of CO_2 gas alone, calcite dissolution was fast but limited, and occurred everywhere. On the other hand, for the other injected fluids the dissolution around the injector was continuous and, with the exception of the seawater scenario, precipitation was observed downstream. In addition, the calcite dissolution per injected water pore volumes for both CO_2 SWAG and CO_2 WAG was higher because of higher dissolution of gaseous CO_2 in injected and formation waters. Moreover, the dissolution rate was found to be proportional to the water flow rate which confirms the assumption that calcite kinetics are fast compared to reservoir flow.

This knowledge is valuable when planning CO_2 WAG projects in carbonate reservoirs. As dissolution rates increase with flow rates, high permeability zones will show faster porosity changes, which may compromise the injector wellbore integrity and may lead to a more severe and growing calcite scaling risk around the producer wellbore.

Introduction

Carbonate reservoirs retain porosity and permeability characteristics at great depths and therefore are of importance in the exploitation of deeper reservoirs. Consisting mainly of limestone and dolomite (calcium and magnesium carbonates), carbonate reservoirs are typically more geochemically reactive than sandstone reservoirs. Understanding the chemical interaction between carbonate rocks and carbon dioxide in the aqueous phase has been shown to be very important during CO_2 injection, carbonated water injection or CO_2 water alternating gas (CO_2 WAG) injection processes (Svec and Grigg, 2001). Another relevant recovery method is CO_2 SWAG, which consists of injecting both CO_2 and seawater simultaneously. In

regions with high concentrations of CO_2, calcite will dissolve, increasing the porosity and permeability of the rock. On the other hand, in regions of high Ca concentrations, calcium carbonate precipitates, plugging the pores (Smith et al., 2013). While mineral precipitation can reduce reservoir porosity and permeability and also severely block wellbores, high dissolution of the rock matrix can lead to formation damage and also CO_2 leakage.

Moreover, as the majority of oil industry knowledge relative to scale management was developed predominantly from sandstone data and applied to sandstone reservoirs, investigation must be carried out to address the specific phenomena related to carbonate reservoirs. Concerning WAG projects, literature review (Christensen et al., 1998) shows that from 1955 to 1996, out of 59 studies involving field data, only 11 were reported as either limestones or carbonates reservoirs, while only three of them had CO_2 as the injected gas.

The purpose of implementing CO_2 WAG instead of just CO_2 is to increase oil recovery with an improved sweep efficiency during the gas injection. However, even with the lower residual oil achieved in a CO_2 WAG process, the multiple fluid-fluid and fluid-rock interactions in carbonates can lead to serious issues, such as early breakthrough, reduced injectivity, corrosion and scale deposition (Christensen et al., 1998). Therefore, a reactive transport model is a valuable tool because it can predict the mineral reactions that occur due to flow propagation of different reservoir fluids.

In this work we tackle the problem of calcite precipitation during CO_2 WAG in carbonate reservoirs. We make use of 1D reactive transport simulations which were performed in CMG GEM to evaluate the calcite dissolution and precipitation during CO_2, seawater, carbonated water, CO_2 SWAG and CO_2 WAG injection in chalk reservoirs. One important aspect of our analysis is our recent finding on the mineral dissolution rate for the different injected fluids.

Geochemical Reactions Involving CO_2 and Calcite

When gaseous $C0_2$ is injected in a water flooded reservoir, part of it dissolves in the aqueous phase and becomes $C0_{2(aq.)}$. A small amount of this aqueous species can associate with water to form carbonic acid:

$$CO_{2(aq)} + H_2O \rightarrow H_2CO_3 \tag{1}$$

In fact, at standard conditions, $C0_{2(aq.)}$ concentration is about 600 times higher than its associated acid (Appelo and Postma, 2005). To facilitate calculations hereinafter we write $C0_{2(aq.)}$ as an approximation of itself plus the carbonic acid and neglect (eq. 1).

The carbonic acid system can be represented by the following chemical reactions involving ionized carbon species produced via acid dissociation:

$$CO_{2(aq)} + H_2O = H^+ + HCO_3^- \tag{2}$$

$$HCO_3^- = H^+ + CO_3^{-2} \tag{3}$$

For completeness, we can also include the dissociation of water:

$$H_2O = H^+ + OH^- \tag{4}$$

On the other hand, when calcite ($CaC0_{3(s)}$) is added to the system, calcium ions may be produced through mineral dissolution:

$$CaCO_{3(s)} = Ca^{+2} + CO_3^{-2} \tag{5}$$

The solubility of calcite decreases with temperature and increases with pressure (Langmuir, 1997), as shown in **Figure 1**.

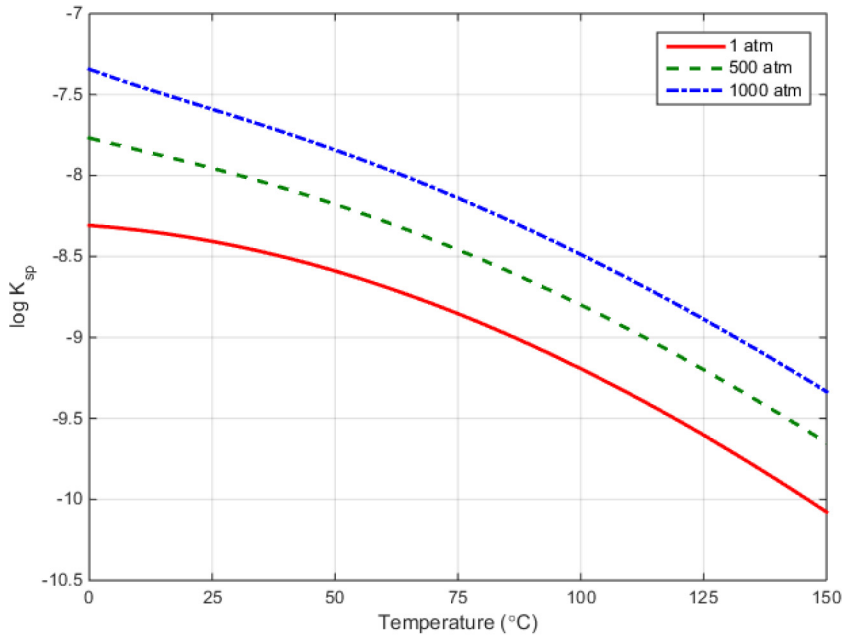

Figure 1—Equilibrium constant for calcite dissolution with varying temperatures and pressures calculated using the PHREEQC software.

In addition, because the mineral reaction changes the concentrations of carbonate species, all species belonging to the system are linked through equilibrium relations, charge and mass balances. Therefore, if one desires to know what would be the concentration of the species when equilibrium is reached, a certain number of equations must be solved simultaneously.

Reactive Transport Simulation

To determine the calcite dissolution and precipitation when different fluids are flowing through the rock pores, we performed reactive transport simulations using CMG GEM, which is a compositional reservoir simulator. In each time step, the simulator finds the chemical equilibrium state of the water phase regarding gaseous dissolution and aqueous (homogeneous) reactions. On the other hand, mineral reactions are simulated with kinetic laws that depend on the local saturation ratio of the mineral (CMG Manual, 2014). However, calcite reactions are fast and thus one time step may be sufficient to equilibrate the mineral.

In fact, calcite dissolution rate under laboratory conditions was found to be higher than 10^{-9} *mol/cm*^{2}. *sec* (~1 *mol/m*^{2}. *d*) for pH lower than 5.0 and temperatures between 25 and 100° (Plummer et al., 1978; Pokrovsky et al., 2009).

We have simulated the injection of seawater, carbonated water (seawater saturated with 1 bar CO_2), CO_2 Gas, CO_2 SWAG and CO_2 WAG in a 1D model of a chalk reservoir with 22% porosity and 400 mD permeability. An inter-well distance of 2000 m was divided in 20 blocks of equal length and cross-sectional area of 225 m^2. The injector well was placed in block 1 with maximum bottom-hole fluid rate of 50 m^3/d, while the producer was located in block 20 with minimum bottom-hole pressure of 500 bar.

All simulations were isothermal with temperature equal to 60°C, while the initial reservoir pressure was 545 bar. The calcite reactive surface area and rate constant were set to 10000 m^2/m^3 and 10^{-5} *mol/cm*^{2}. *sec*, respectively.

The concentrations of injected waters as well as formation water are displayed in Table 1.

Table 1—Composition of injected and formation waters. Units are millimole per kilogram of water (mmol/kgw) and parts per million (ppm)

	Carbonated water		Seawater		Formation water	
pH	4.63		7.81		4.68	
Conc.	mmol/kgw	ppm	mmol/kgw	ppm	mmol/kgw	ppm
CO_2	31	1314	0.02	0.8	113	4118
Ca	10	385	10	386	554	18356
HCO_3	1.1	64	0.98	64	11	556
Mg	49	1133	49	1134	25.9	515
K	10	376	10	376	45	1454
SO_4	29	2682	29	2686	4	318
Na	500	11080	500	11094	2267	43191
Cl	570	19496	570	19521	3507	103129

In our simulations for CO_2 SWAG, we injected seawater and CO_2 simultaneously with half of the previous bottom-hole fluid rate each.

For CO_2 WAG we started with the seawater injection and then we switch to CO_2 gas injection, which completes a WAG cycle of 120 days. The duration of gas (T_G) and water (T_W) injection periods were set in terms of the WAG Ratio, i.e. the ratio between injected water and injected gas during each cycle is:

$$T_G = 120\ days/(WAG\ Ratio + 1) \qquad T_W = T_G \times WAG\ Ratio$$

Simulation Results

Injection of single-phase fluids

It was observed that if seawater is injected then calcite dissolution occurs when the injected fluid reaches each block. However, with the exception of block 1 (injector), the dissolution is limited and stops after the mixing front propagates through the block (see Figure 2). Calcite is continuously dissolved only in the injector block because the injected water is not equilibrated with the mineral. Moreover, after the mixing front leaves the first block, the water that goes to the next block is already equilibrated and does not trigger mineral reactions.

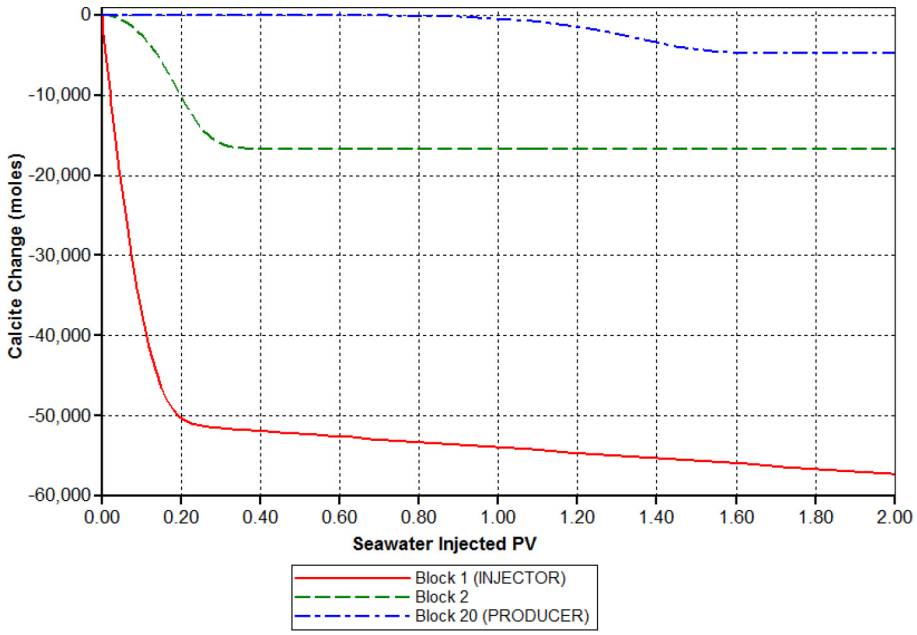

Figure 2—Calcite change in moles at blocks 1 (injector – red line), 2 (green line) and 20 (producer – blue line) during seawater injection in 1D calculation of a chalk reservoir. Mineral dissolution at the producer stops after 1.60 injected PV.

The dissolution rate in block 1 decreased by more than 50 times after 0.20 injected PV. To understand this issue, we observed that the calcite dissolution rate in CMG GEM is modelled by a kinetic law which depends on H^+ concentration and that it increases with CO_2 concentration because they are linked by an equilibrium relation. In addition, it was found that the initial dissolved CO_2 takes the same time to be flushed out (see Figure 3) and thus the (kinetic) dissolution rate for calcite is reduced.

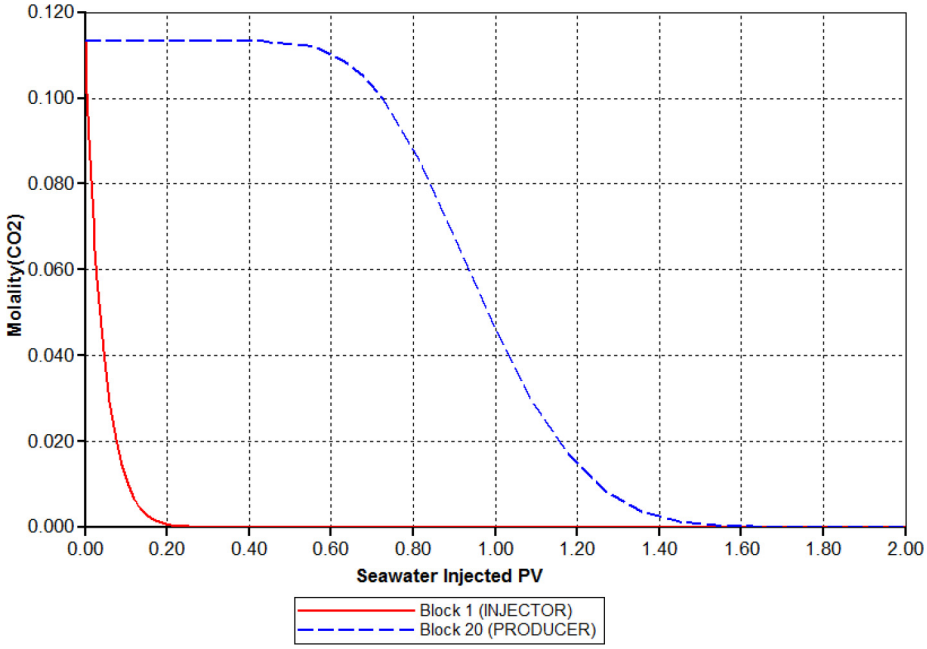

Figure 3—CO_2 concentration in molality at blocks 1 (injector) and 20 (producer) during seawater injection in 1D calculation of a chalk reservoir.

Moreover, calcite dissolution at the producer started when the reservoir was almost completely depleted of formation water, and stops shortly after (when the initial dissolved CO_2 has been produced).

On the other hand, if CO_2 is previously dissolved in seawater (carbonated water) and then injected, calcite dissolves in the injector block and precipitates downstream. This time the mineral dissolution in the injector is faster and produces more Ca ions which cause (limited) precipitation during the propagation of the mixing front in each block (see Figure 4).

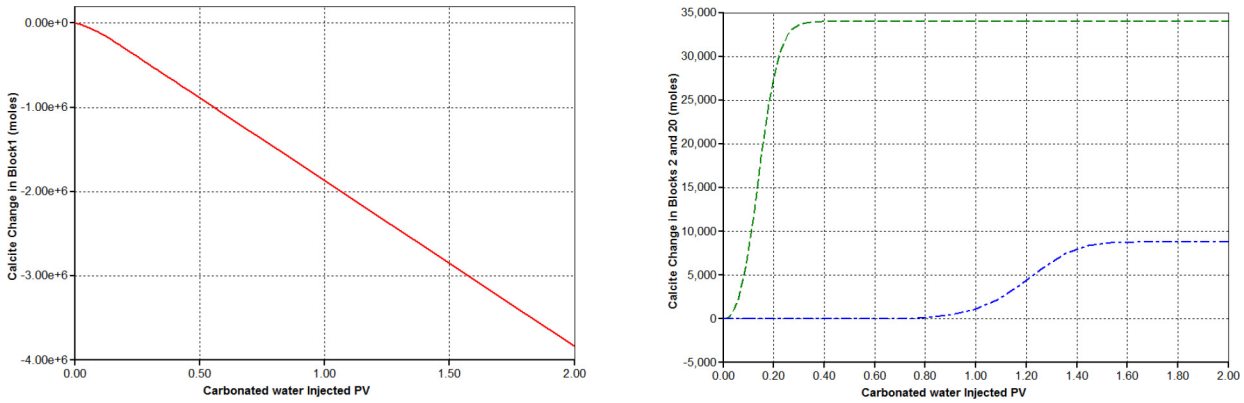

Figure 4—Calcite change in moles at blocks 1 (left – red line), 2 (right – green line) and 20 (right – blue line) during carbonated water injection in 1D calculation of a chalk reservoir. Mineral dissolution in injector is faster than the dissolution during seawater injection (shown in Figure 2).

A different behaviour was observed during CO_2 gas injection. For this scenario calcite was dissolved across the entire reservoir. The mineral dissolution was much faster than the other two cases. Because in CMG GEM the dissolution of gaseous CO_2 in water is instantaneous (as well as the convergence of aqueous reaction to equilibrium), the mineral dissolution rate is high from the start. However, after the water is equilibrated with both the mineral and gas phases, the additional CO_2 gas, that is continuously injected, does not dissolve any more in water and calcite dissolution stops (see Figure 5).

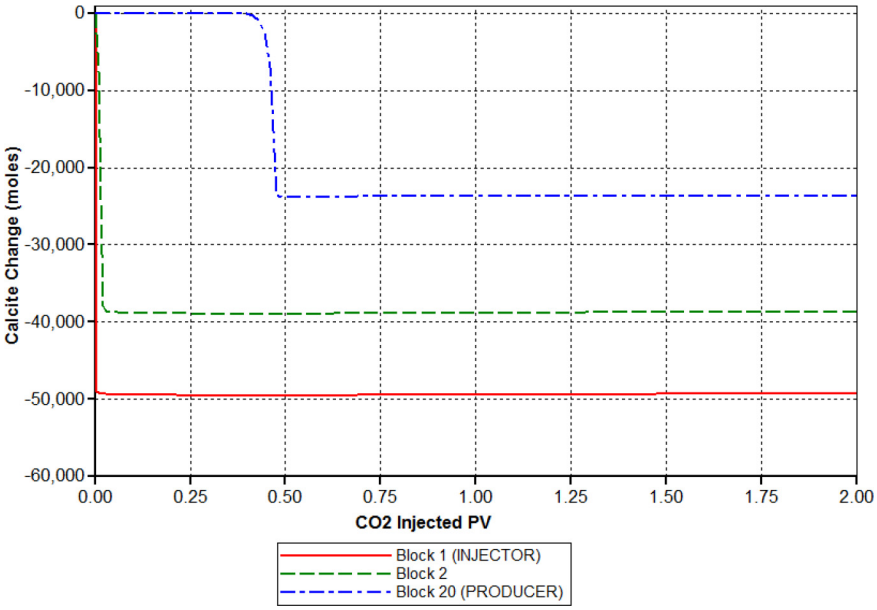

Figure 5—Calcite change in moles at blocks 1 (injector), 2 and 20 (producer) during CO_2 gas injection in 1D calculation of a chalk reservoir. Mineral dissolution is limited everywhere and starts earlier than the dissolution during water injection.

In addition, as soon as CO2 is injected, water is produced and the average gas saturation grows linearly with injected PV until about half of the total reservoir pore volume. From this point and forward the injected gas breaks through and the gas saturation increase is slower (Figure 6). This means that the gas phase occupies around 0.50 PV just after reaching the producer and therefore calcite reaction in the last block happens earlier when compared to water (carbonated or seawater) injection which needs 1 injected PV.

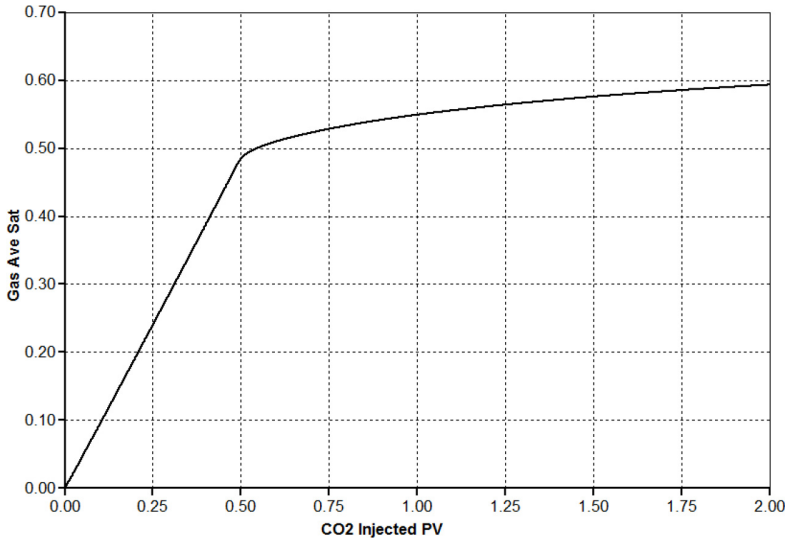

Figure 6—Average CO_2 gas saturation during CO_2 gas injection in 1D calculation of a chalk reservoir. The gas saturation increases linearly with time until the CO_2 reaches the last block.

CO_2 SWAG and CO_2 WAG injection

After analysing the calcite dissolution and precipitation during the injection of single type fluids we are ready to understand some phenomena that occurs during CO_2 SWAG and CO_2 WAG injection.

We observed (Figure 7) that for both processes, calcite was continuously dissolved in the injector block, although for CO_2 WAG most part of the dissolution occurred when the water was being injected. This is in agreement with the CO_2 gas simulation where mineral dissolution was limited. Moreover, the rate of calcite dissolution for CO_2 SWAG and CO_2 WAG was higher than the rate found for carbonated water (see Table 2), which is explained by the higher CO_2 molalities obtained during the gas injection at reservoir pressure. This higher dissolution may put the wellbore at higher risk of loss of integrity.

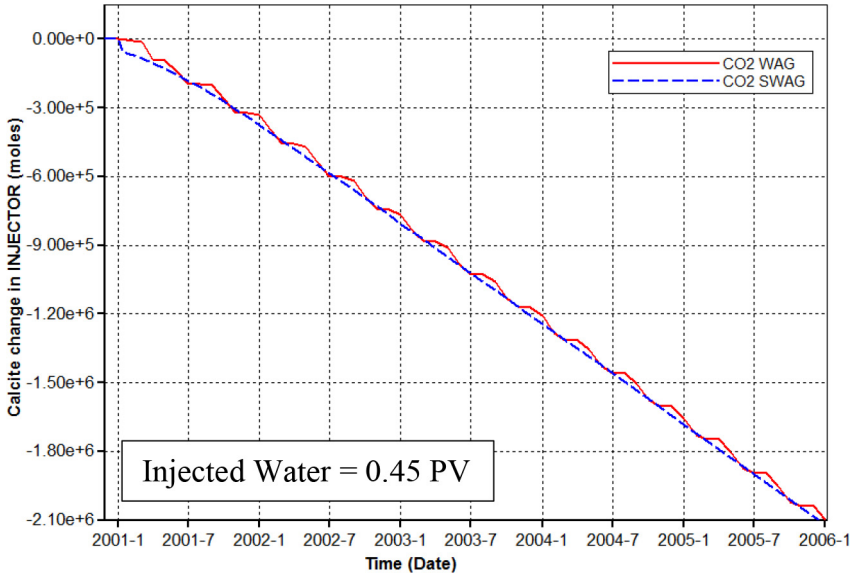

Figure 7—Calcite change in moles at block 1 (injector) during CO_2 WAG or CO_2 SWAG injection in 1D calculation of a chalk reservoir. Dissolution is (globally) continuous and faster than the dissolution observed in the Carbonated Water scenario.

Table 2—Dissolved calcite and porosity in the injector block after 1.5 PV of injected water.

	Seawater	Carbonated water	CO_2 SWAG	CO_2 WAG with WAG ratio =1
Calcite Dissolved after 1.5 PV (10^6 mol)	0.057	2.84	7.15	7.36
Porosity in Injector block after 1.5 PV	22.00%	22.46%	23.17%	23.20%
Dissolution Rate (10^6 mol / PV)	0.003	0.195	4.82	4.90
Porosity increase per injected PV	<0.01%	0.30%	0.78%	0.80%

In addition in Figure 8, we can see that, due to the higher reaction rate, a non-limited precipitation occurs in both blocks 2 and 20 (producer). An interesting effect is also observed: before the precipitation starts, calcite is dissolved during the earlier arrival of the CO_2 gas. The dissolution in block 2 during CO_2 SWAG injection is weaker if compared to CO_2 WAG because at each WAG cycle the water becomes saturated in block 1 during the injection of the CO_2 slug and then the gas dissolves in subsequent blocks, while for SWAG there is more water available for CO_2 to be dissolved in. However, as the gas phase travels through the reservoir both recovery processes converge and similar values of dissolution are observed.

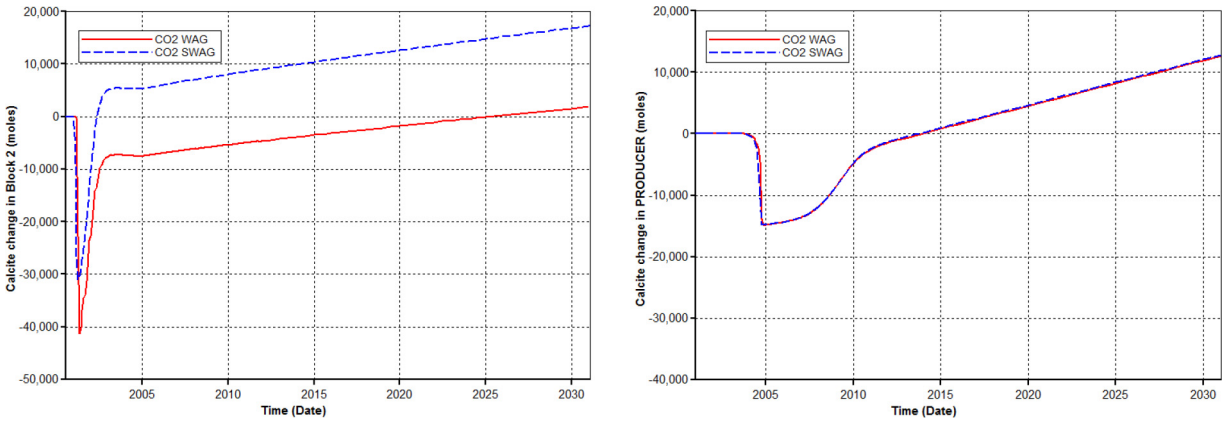

Figure 8—Calcite change in moles on block 2 (left) and 20 (right) during CO_2 WAG and CO_2 SWAG injection in 1D calculation of a chalk reservoir. Mineral dissolution is caused by earlier arrival of the injected gas.

Moreover, the amount of re-precipitated calcite at the producer matches the total dissolution only after 9 years of CO_2 production (year of 2005) and thus calcite precipitation may not be observed during the first years of production. This re-precipitation is caused by the arrival of seawater just before the gas phase and after the reservoir is depleted of formation water the reaction rate becomes constant (see Figure 9). Therefore, mineral scale problems around the producer wellbore will definitely occur because the precipitation is continuous.

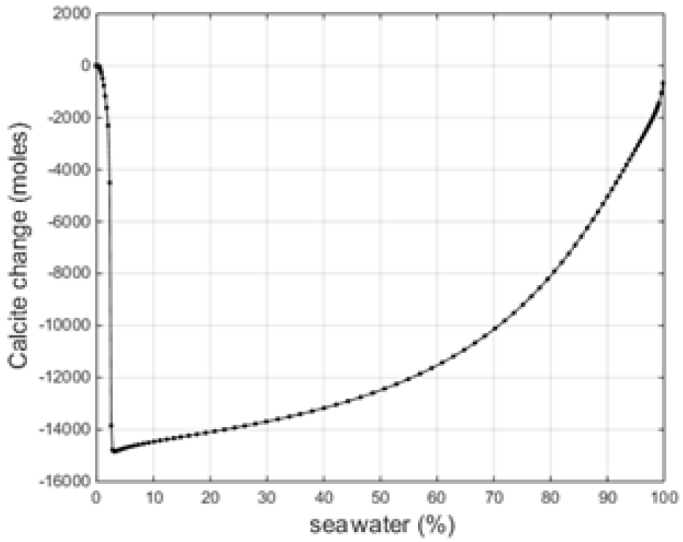

Figure 9—Calcite change in moles in block 20 (producer) with seawater breakthrough. After formation water is totally displaced, re-precipitation increases linearly with time.

With these potential threats in mind (collapse of the injector well and blocking of the producer wellbore), which are caused by a higher dissolution rate near the injector, it is interesting to evaluate the calcite change during CO_2 WAG with others WAG ratios and WAG cycle length.

Simulation results in Table 3 show that higher WAG ratios yield higher calcite dissolution in the injector and higher calcite precipitation in the producer. On the other hand, when the WAG cycle length was varied no strong trend was detected. However, we observed slightly greater precipitation for WAG cycles of 60 days with WAG ratio of 2.

Table 3—Calcite change in injector and producer blocks after 30 years of CO_2 SWAG and of CO_2 WAG injection for different configurations.

WAG Ratio	WAG Cycle Length (in days)	Dissolved Calcite after 30 years (in 10^6 mol)	Porosity in Injector Block after 30 years (%)	Precipitated Calcite after 30 years (in 10^3 mol)
SWAG	-	13.0	24.14	12.8
1.0	60	13.1	24.15	12.8
2.0	60	17.5	24.87	30.3
20.5	120	8.7	23.42	-1.1
1.0	120	13.0	24.14	12.6
2.0	120	17.4	24.86	29.8
3.0	120	19.5	25.21	41.4
1.0	180	13.0	24.14	12.6
2.0	180	17.4	24.86	29.7
1.0	240	13.0	24.14	12.1
2.0	240	15.2	24.50	19.9

To clarify the impact of the WAG ratio on calcite dissolution we show in Figure 10 the volume of mineral which is removed from the injector block that can be deposited elsewhere in the reservoir, production wellbore or tubing.

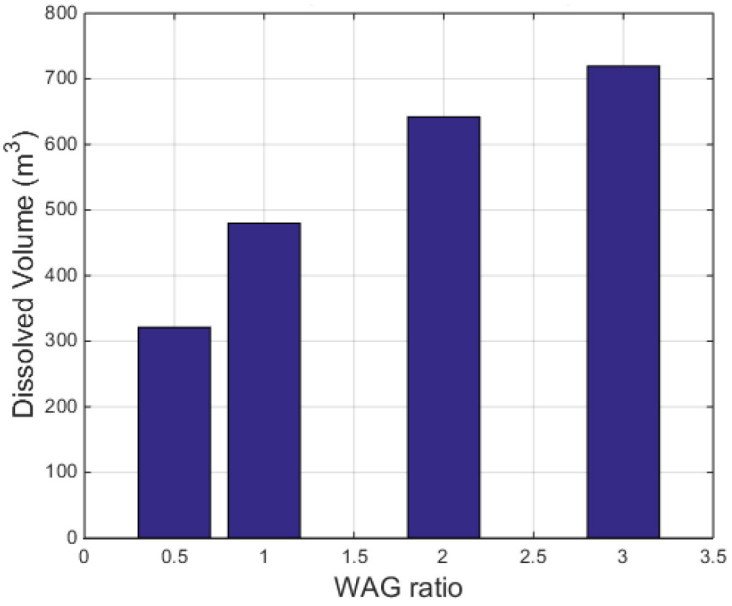

Figure 10—Calcite dissolution in m^3 after 30 years of CO_2 WAG injection with WAG cycles of 120 days and different WAG ratios.

The calcite dissolution grows with WAG ratio but not proportionally. In fact, it seems that the dissolution will converge at higher WAG ratios (as the slug size of injected CO_2 approaches zero). In this sense, a direct relationship should exist between the injected CO_2 and the dissolved calcite. Therefore, we developed a bar chart for the ratio between the dissolved calcite and injected CO_2, both in moles, against the WAG ratio, which is shown in Figure 11; the relationship can be approximated by a linear trend. The last two figures combined lead to the conclusion that gaseous CO_2 drives the mineral reaction but it needs sufficient water to be dissolved in and then trigger further reactions. This is also a confirmation of the role of aqueous CO_2 as the main component for the calcite dissolution mechanism.

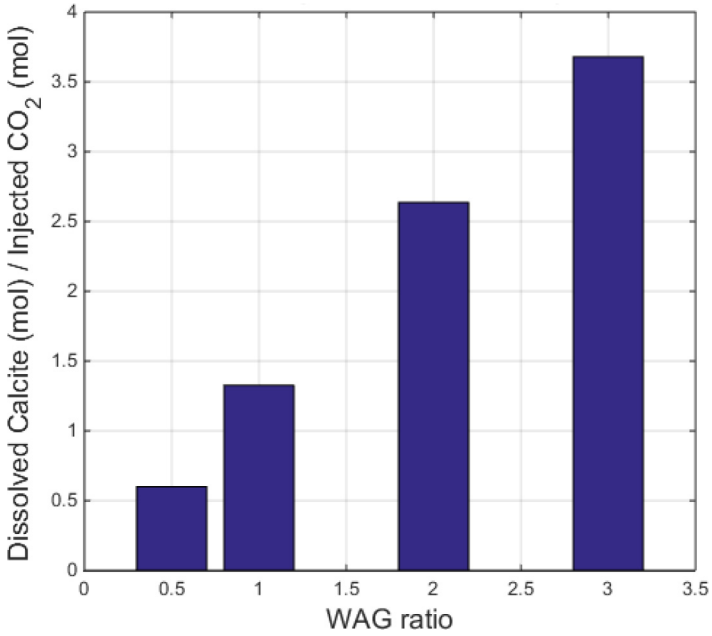

Figure 11—Calcite dissolution (mol) per injected moles of CO_2 after 30 years of CO_2 WAG injection with WAG cycles of 120 days and different WAG ratios.

Finally, we have investigated the calcite dissolution dependency on flow rate. This is shown in Figure 12, where the dissolution grows linearly with water injection rate, as expected because the reaction is fast. Therefore, during a CO_2 WAG process the porosity around the injector increases faster for higher WAG ratios and injection rate.

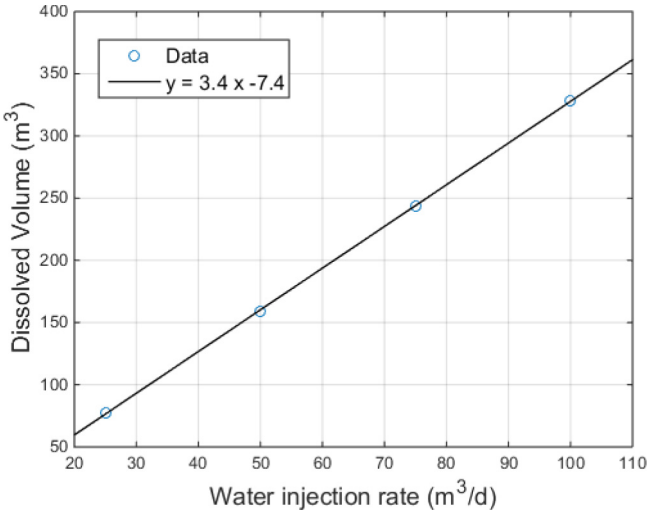

Figure 12—Calcite dissolution in m^3 after 10 years of CO_2 WAG injection for different water injection rates. WAG ratio and WAG cycle are 1 and 120 days, respectively.

Conclusions

In this work, we have performed reactive transport simulation using CMG GEM to evaluate the calcite dissolution and precipitation in chalk reservoirs subjected to continuous injection of different fluids. We have observed continuous dissolution in the injector block both when unsaturated seawater and when carbonated water were injected. On the other hand, limited dissolution occurred in other blocks when

unsaturated seawater was injected, while for carbonated water limited precipitation was observed because of a higher dissolution rate in the injector. In addition, during injection of CO_2 gas, fast but limited dissolution of calcite was observed everywhere.

The knowledge acquired after these first set of simulations helped us in understanding the mineral reactions during CO_2 WAG injections. For these processes, simulation results revealed that calcite dissolved continuously in the injector and with a dissolution rate higher than the rate found in the carbonated water case. This happened because the injected CO_2 dissolved in the injected water and enhanced the mineral dissolution process. This higher dissolution rate produced higher amount of dissolved calcium, which then continuously precipitated in all other downstream blocks after a brief period of dissolution caused by the injected CO_2 gas (which arrives first).

Similar results were obtained for CO_2 SWAG with half of the injection rate because the total injected amounts of water during the two methods are equal after one WAG cycle ends. However, we observed that during CO_2 SWAG the dissolution in block 2 is lower than during CO_2 WAG, and will cause significant porosity and permeability decrease earlier.

The dissolution rate during CO_2 WAG was observed to increase with higher amounts of water over gas (higher WAG ratio). On the other hand, no strong trend in the reaction rate was detected when varying the WAG cycle length.

Moreover, we observed that higher injection rates yield higher dissolution rates, which confirmed that kinetic modelling is not required because equilibrium was immediately reached (at least for the parameters used in the simulations).

This knowledge is valuable when planning CO_2 WAG projects in carbonate reservoirs. Since higher dissolution rates around the injector trigger higher precipitation downstream (including at the producer wellbore), scale prevention must consider the equilibration process between the injected CO_2-rich water and calcite rock. In addition, the pressure drop along a flow path is also important because it decreases the CO_2 concentration in water and raises the saturation ratio for calcite. Moreover, more permeable reservoirs will show faster porosity changes because of higher flow rate. For these conditions, the injector wellbore integrity will be compromised earlier and a more severe and growing calcite scaling risk around the producer wellbore will occur.

Future work should consider the impact of non-isothermal flow on calcite precipitation. As the temperature around the injection point decreases more dissolution is likely to occur and thus more precipitation may occur in hotter regions. Also, the impact of grid size resolution in the simulations should be investigated.

Acknowledgements

CMG Ltd is thanked for use of the GEM reactive transport reservoir simulator in this study. Foundation CMG is thanked for supporting the studentship held by Ayrton Ribeiro and the Chair in Reactive Flow Simulation held by Eric Mackay. The following are thanked for their support of the FAST5 JIP at Heriot-Watt University: Apache, Baker Hughes, BG Group, BP, Chevron, Clariant, ConocoPhillips, Equion, GALP, Maersk, MI Swaco, Multi-Chem, MWV, NalcoChampion, Nexen, Petrobras, Petronas, REP, Shell, Statoil, Talisman Sinopec, Total and Wintershall.

References

Appelo, C. A. J., Postma, D. 2005. Geochemistry, Groundwater and Pollution, 2nd Edition. Amsterdam: CRC Press.

Christensen et al, 1998. Review of WAG Field Experiences. Presented at SPE International Petroleum Conference and Exhibition of Mexico, Villahermosa, Mexico, 3 – 5 March. SPE-39883-MS.

GEM Manual, 2014, CMG.

Langmuir, D. 1997. Aqueous environmental geochemistry, first edition. Upper Saddle River, New Jersey: Prentice-Hall.

Plummer et al, 1978. The kinetics of calcite dissolution in CO2-water systems at 5 to 60° and 0.0 to 1.0 atm CO2. *Am. J. Sci.* **278,** 179–216.

Plummer, L. N., Busenberg, E., 1982. The solubilities of calcite, aragonite and vaterite in CO_2–H_2O solutions between 0° and 90°, and an evaluation of the aqueous model for the system $CaCO_3$–CO_2–H_2O. *Geochim. Cosmochim. Acta* **46,** 1011–1040.

Pokrovsky et al, 2009. Calcite, dolomite and magnesite dissolution kinetics in aqueous solution at acid to circumneutral pH, 25 to 150°C and to 55 atm pCO_2: New constraints on CO_2 sequestration in sedimentary basins. *Chem. Geol.* **265,** 20–32.

Smith et al, 2013. CO_2-induced dissolution of low permeability carbonates. Part I: Characterization and experiments. *Advances in Water Resources*. **62,** 370–387.

Svec and Grigg, 2001. Physical Effects of WAG Fluids on Carbonate Core Plugs. Presented at SPE Annual Technical Conference and Exhibition, New Orleans, Louisiana, 30 September – 3 October. SPE-71496-MS.

The Impact of Vapor/Liquid-Equilibria Calculations on Scale-Prediction Modeling

Ayrton S. Ribeiro, Duarte Silva, Eric J. Mackay and **Ken Sorbie,** Heriot-Watt University

Summary

Vapor/liquid-equilibria (VLE) calculations, particularly involving the phase behavior of carbon dioxide (CO_2) and hydrogen sulfide (H_2S), are used in scale-prediction modeling. In this work, the impact of VLE calculations for CO_2- and H_2S-rich gas phases and for acid- and sour-gas mixtures on scale-prediction calculations is evaluated.

Three equations of state (EOSs)—Soave-Redlich-Kwong (SRK) (Soave 1972), Peng-Robinson (PR) (Peng and Robinson 1976), and Valderrama-Patel-Teja (VPT) (Valderrama 1990)—are implemented in the Heriot-Watt model and used in VLE calculations. The solubility of single-component CO_2 and H_2S in water and the solubility of a gas mixture in water were compared with experimental data in terms of the absolute relative deviation (ARD). The solubility data were then used in PHREEQC (USGS 2016) to calculate the impact of using different EOSs on carbonate and sulfide scales, particularly on calcium carbonate ($CaCO_3$) and iron sulfide (FeS).

Average ARDs of 6.04, 4.10, and 3.77% between experimental and calculated values for CO_2 solubility in water were obtained for the SRK, PR, and VPT EOSs, respectively. Similarly, for H_2S solubility in water, average ARDs of 6.49, 6.66, and 6.48% were obtained for each EOS, respectively. For the solubility of sour- and acid-gas mixtures in water, average ARDs of 13.92, 13.25, and 10.78% were obtained, respectively. It has thus been concluded that the VPT EOS performs better than the SRK and PR EOSs in VLE calculations for the analyzed data.

The errors introduced in VLE calculations have been found to impact the calculation of the amount of $CaCO_3$ precipitated, with consequences for scale-inhibitor selection. Higher deviations were found in the amount of $CaCO_3$ precipitation for gas mixtures when compared with a single-component, CO_2-rich phase. Furthermore, the large errors occurring in VLE calculations for H_2S solubility have not been found to impact the calculation of the amount of FeS precipitated when H_2S is in excess with respect to Fe^{2+}. In addition to this, a case study that was performed by use of formation-water data from the Brazilian presalt revealed that the choice of EOS can cause errors of 6 kg of precipitate during each day of production.

Scale-prediction calculations carried out with PHREEQC demonstrate that VLE calculations can have a high impact on mineral precipitation. Thus, it is recommended that the best VLE model available should always be used for scale-prediction modeling, particularly when mixtures of gases are present.

Introduction

CO_2 injection for tertiary oil recovery or CO_2/water-alternating-gas schemes [used, for example, in the development of the Lula Field in the Brazilian presalt (Cruz et al. 2016)] poses scaling issues associated with the deposition of carbonates in production wells. In addition, the development of sour reservoirs [e.g., Khuff Formation in Ghawar Field, Saudi Arabia (Leal Jauregui et al. 2007)] also poses scaling issues associated with the deposition of sulfide scales. Scale-prediction modeling uses VLE calculations to assess the solubility of gases in the aqueous phase. These calculations play a critical role in scale-prediction modeling for two primary reasons. First, VLE is used to calculate the amount of carbon and sulfur dissolved in the aqueous phase, which has a direct impact on the scaling tendency of carbonates and sulfides (in other words, the gas phase is a source of carbon and sulfur). Second, dissolution of CO_2 and H_2S alters the acid equilibria and, consequently, the scaling tendency of pH-dependent scales (such as carbonates or sulfides). In this paper, we study the impact of VLE modeling in scale-prediction calculations; particularly, we study the impact of the dissolution of CO_2 and H_2S in the aqueous phase on the precipitation of $CaCO_3$ and FeS.

VLE Calculations and EOSs

The condition for thermodynamic equilibrium of a liquid mixture with a vapor at a specific pressure and temperature is given (for every component in the mixture) by the equality of the component's fugacities in the liquid and in the gas phases; thus, by using an activity model and an EOS to describe, respectively, the behavior of the liquid and the gas, the following equation is obtained for the VLE of component i [see Prausnitz et al. (1999, pp. 586–603) for further reading]:

$$x_i = \frac{y_i \phi_i P}{\gamma_i H_{i,j}} \exp\left[\frac{-(P - P_{vp})\overline{V}_i^{\infty}}{RT}\right], \quad \ldots\ldots\ldots\ldots\ldots (1)$$

where x and y are the aqueous and gaseous molar fractions, ϕ_i is the fugacity coefficient, P_{vp} is the vapor pressure of the solvent, $\overline{V}_i^{\infty}$ is the partial molar volume at infinite dilution, γ is the activity coefficient, and $H_{i,j}$ is the Henry constant. The fugacity coefficient, ϕ_i, is calculated from an EOS; specifically, we studied three EOSs—namely, SRK, PR, and VPT—to calculate ϕ_i. The vapor pressure of the solvent P_{vp} was calculated from the approach detailed in Wagner and Pruss (1993). The activity coefficients may be considered, to a first approximation here, equal to unity. The Henry constants for CO_2, H_2S, and CH_4 are readily available in the literature [see, for example, Li and Nghiem (1986) and Harvey (1996)].

Most common cubic EOSs can be described with one general expression that uses four parameters—*a, b, u,* and *w*—as (Muller and Olivera-Fuentes 1989):

$$P = \frac{RT}{v - b} - \frac{a}{v(v + ub) + wb^2}, \quad \ldots\ldots\ldots\ldots\ldots (2)$$

where the parameters u and w are given in Appendix A. Alternatively, Eq. 2 may be written in terms of the compressibility factor $Z = Pv/RT$, as

$$Z^3 + [(u-1)B - 1]Z^2 + [(w-u)B^2 - uB + A] \times Z - [w(B^2 + B^3) + AB] = 0, \quad \ldots\ldots\ldots\ldots (3)$$

where

$$A = \frac{aP}{(RT)^2}; \quad B = \frac{bP}{RT}. \quad \ldots\ldots\ldots\ldots\ldots\ldots (4)$$

This paper (SPE 179885) was accepted for presentation at the SPE International Oilfield Scale Conference and Exhibition, Aberdeen, 11–12 May 2016, and revised for publication. Original manuscript received for review 8 March 2016. Revised manuscript received for review 10 August 2016. Paper peer approved 15 August 2016.

Parameters a, b, and c are given by

$$a = \Omega_a \frac{(RT_c)^2}{P_c}\alpha; \quad b = \Omega_b \frac{RT_c}{P_c}; \quad c = \Omega_c \frac{RT_c}{P_c}, \quad \ldots\ldots (5)$$

where the parameters Ω_a, Ω_b, and Ω_c are given in Appendix A. The α function may be written in the general form

$$\alpha = \left[1 + F(1 - T_r^{1/2})\right]^2, \quad \ldots\ldots\ldots\ldots\ldots\ldots (6)$$

where $T_r = T/T_c$ is the reduced temperature and F (given in Appendix A) is a function specific to the EOS being used.

For gas mixtures, a, b, and c in Eq. 5 should be replaced by a_{mix}, b_{mix}, and c_{mix}, which are calculated by use of a mixing rule. The EOSs used in this work use the classical van der Waals mixing rules:

$$a_{\text{mix}} = \sum_i \sum_j x_i x_j (a_i a_j)^{1/2}(1 - k_{ij});$$
$$b_{\text{mix}} = \sum_i x_i b_i; \quad c_{\text{mix}} = \sum_i x_i c_i, \quad \ldots\ldots\ldots\ldots (7)$$

where k_{ij} is the binary interaction coefficient between components i and j. The fugacity coefficient can be written in terms of the compressibility factor Z, as shown in Eqs. 9, 11, and 13 for the SRK, PR, and VPT EOSs, respectively. In practice, the calculation of fugacity coefficients is preceded by the calculation of the compressibility factor. The expressions to calculate compressibility factors are thus also written explicitly in Eqs. 8, 10, and 12 for the respective EOSs [see Muller and Olivera-Fuentes (1989) and Poling et al. (2001) for a general expression to calculate fugacity coefficients and respective thermodynamic derivation].

- Redlich-Kwong EOS, modified by Soave (SRK),

$$Z^3 - Z^2 + (A - B - B^2)Z - AB = 0. \quad \ldots\ldots\ldots\ldots (8)$$

$$\ln\phi_i = \frac{b_i}{b}(Z - 1) - \ln(Z - B)$$
$$-\frac{A}{B}\left(\frac{2}{a}\sum y_i a_{ij} - \frac{b_i}{b}\right)\ln\left(1 + \frac{B}{Z}\right). \quad \ldots\ldots\ldots\ldots (9)$$

- PR EOS,

$$Z^3 - (1 - B)Z^2 + (A - 3B^2 - 2B)Z$$
$$-(AB - B^2 - B^3) = 0. \quad \ldots\ldots\ldots\ldots (10)$$

$$\ln\phi_i = \frac{b_i}{b}(Z - 1) - \ln(Z - B)$$
$$-\frac{A}{2\sqrt{2}B}\left(\frac{2}{a}\sum_j y_j a_{ij} - \frac{b_i}{b}\right)\ln\left[\frac{Z + (\sqrt{2} + 1)B}{Z - (\sqrt{2} - 1)B}\right]. \quad \ldots (11)$$

- Patel-Teja EOS, modified by Valderrama (VPT),

$$Z^3 + (C - 1)Z^2 + (A - 2BC - B - C - B^2)Z$$
$$-(BC - B^2C - AB) = 0. \quad \ldots\ldots\ldots\ldots (12)$$

$$RT\ln\phi_i = -RT\ln(Z - B) + RT\left(\frac{b_i}{v - b}\right)$$
$$-\frac{1}{d}\sum_j y_j a_{ij}\ln\left(\frac{Q + d}{Q - d}\right) + \frac{a(b_i + c_i)}{2(Q^2 - d^2)}$$
$$+\frac{a}{8d^3}[c_i(3b + c) + b_i(3c + b)]$$
$$\times\left[\ln\left(\frac{Q + d}{Q - d}\right) + \frac{2Qd}{Q^2 - d^2}\right], \quad \ldots\ldots\ldots\ldots (13)$$

where

$$v = ZRT/P, \quad Q = v + \frac{b + c}{2}, \quad d = \sqrt{bc + \frac{(b + c)^2}{4}},$$
$$\text{and } a_{ij} = (a_i a_j)^{1/2}(1 - k_{ij}).$$

$CaCO_3$ and FeS Scales

To find the scale-formation dependence on the solubility of gases, one may consider the following chemical reactions:

$$Ca^{2+} + CO_3^{2-} \rightarrow CaCO_3(s),$$
$$CO_2(aq.) + H_2O \rightarrow HCO_3^- + H^+,$$
$$HCO_3^- \rightarrow CO_3^{2-} + H^+,$$
$$Fe^{2+} + S^{2-} \rightarrow FeS(s),$$
$$H_2S(aq.) \rightarrow HS^- + H^+,$$
$$HS^- \rightarrow S^{2-} + H^+.$$

The combined reactions can be written as global (reversible) reactions with $K_{\text{carbonate}}$ and K_{sulfide} as the equilibrium constants (Plummer et al. 1978; Benning et al. 2000):

$$Ca^{2+} + 2 \cdot HCO_3^- = CaCO_3(s) + CO_2(aq.) + H_2O.$$
$$Fe^{2+} + 2 \cdot HS^- = FeS(s) + H_2S(aq.).$$

For the purpose of writing the concentrations of Ca^{2+} and Fe^{2+} as functions of CO_2 and H_2S, we treat each system separately. For carbonate scales, we consider pure water in contact with $CaCO_3(s)$ and $CO_2(g)$, while for sulfide scales we have pure water in contact with $FeS(s)$ and $H_2S(g)$. We assume that both solutions have circumneutral pH in equilibrium (i.e., $4 < pH < 8$). In these conditions, the charge balance for each solution can be written in terms of the dominant ionic species only:

$$2m_{Ca^{+2}} = m_{HCO_3^-}; \quad 2m_{Fe^{+2}} = m_{HS^-}. \quad \ldots\ldots\ldots\ldots (14)$$

Using these expressions with the equilibrium relations associated from the global reactions, we can write

$$m_{Ca^{2+}} = \sqrt[3]{\frac{a_w \gamma_{CO_2}}{\gamma_{Ca}\gamma_{HCO_3}}\frac{K_{\text{carbonate}}}{4} \cdot m_{CO_2}};$$
$$m_{Fe^{2+}} = \sqrt[3]{\frac{\gamma_{H_2S}}{\gamma_{Fe}\gamma_{HS}}\frac{K_{\text{sulfide}}}{4} \cdot m_{H_2S}}. \quad \ldots\ldots\ldots\ldots (15)$$

We disregard the dependence of activity coefficients on m_{CO2} and calculate the following derivative:

$$\frac{\partial m_{Ca^{2+}}}{\partial m_{CO_2}} \approx \sqrt[3]{\frac{a_w \gamma_{CO_2}}{\gamma_{Ca}\gamma_{HCO_3}}\frac{K_{\text{carbonate}}}{4}} \cdot \frac{1}{3}(m_{CO_2})^{-\frac{2}{3}} = \frac{1}{3} \cdot \frac{m_{Ca^{2+}}}{m_{CO_2}}. \quad \ldots\ldots\ldots\ldots (16)$$

Thus, the impact of gas solubility in scale formation may be approximated by

$$\frac{\Delta m_{Ca^{2+}}}{\Delta m_{CO_2}} \approx \frac{1}{3} \cdot \frac{m_{Ca^{2+}}}{m_{CO_2}} \quad \text{or} \quad ARD_{CaCO_3} \approx \frac{ARD_{CO_2}}{3}. \quad \ldots (17)$$

Following the same procedure, a similar estimation can be obtained for sulfide scales:

$$\frac{\Delta m_{Fe^{2+}}}{\Delta m_{H_2S}} \approx \frac{1}{3} \cdot \frac{m_{Fe^{2+}}}{m_{H_2S}} \quad \text{or} \quad ARD_{FeS} \approx \frac{ARD_{H_2S}}{3}. \quad \ldots\ldots (18)$$

Simulation Results

CO_2-, H_2S-, and CH_4-Rich Phase Solubilities in Water. The solubility of single components of CO_2, H_2S, and CH_4 in water was modeled using Eq. 1. The fugacity coefficients of the components were calculated using the three EOSs (all other parameters in Eq. 1, including the Henry constant, were kept constant). **Table 1** presents the results obtained in terms of the average absolute

	Temperature (°C)	Pressure (bar)	Number of Data Points, *N*	Reference	AARD* (%)
CO_2	25 to 100	3.25 to 709.3	62	Spycher et al. (2003)	
SRK					6.04
PR					4.10
VPT					3.77
H_2S	25 to 65	4.83 to 39.62	31	Chapoy et al. (2005)	
SRK					6.49
PR					6.66
VPT					6.48
CH_4	25 to 100	9.73 to 179.98	16	Chapoy et al. (2004)	
SRK					3.58
PR					3.69
VPT					3.29

* $AARD(\%) = \frac{1}{N}\sum\left|\left(x_{exp} - x_{calc}\right)/x_{exp}\right| \times 100.$

Table 1—AARD between the experimental and the calculated values for CO_2, H_2S, and CH_4 solubility data by use of the SRK, PR, and VPT EOSs.

relative deviation (AARD) between the experimental and the calculated values for CO_2, H_2S, and CH_4 solubility data.

The results presented in Table 1 suggest that VPT performs better than the remaining EOSs for the solubility of CO_2, H_2S, or CH_4 in water. The VPT EOS was thus selected to illustrate graphically the relation between experimental and calculated values, even though this relation was studied for all EOSs presented previously. Results are shown in **Fig. 1.**

The results shown in Fig. 1 suggest a very good prediction for the solubility of CO_2 and CH_4 in water for the respective pressure and temperature ranges. The model does not perform as well for the solubility of H_2S in water, especially for high pressures, even though this deviation may still be considered acceptable for the purposes of scale-precipitation modeling (i.e., the deviation is still in the ARD range of 0–15%).

The best-performing EOS is not evident for gas-mixture solubility modeling, especially if we consider the results obtained for H_2S solubility. The ARD% for the solubility of H_2S at 37.8°C and 125.2 bar is 8.84% with the PR EOS and 36.21% with the VPT EOS, whereas at 107.2°C and 83.6 bar, the ARD% is 21.60% with the PR EOS and 8.12% with the VPT EOS. See **Table 2.**

Impact of VLE Calculations on Scale-Prediction Modeling. To determine the impact of VLE calculations on scale formation, we use PHREEQC to simulate the mineral precipitation during degassing with different initial concentrations of dissolved gas. We first perform this calculation by use of gaseous dissolution data from the literature. Then, we repeat the simulation for the concentrations given by each EOS and calculate the errors in gas solubility and in mineral precipitation.

The first set of simulations comprises equilibrating pure water with CO_2(g) and $CaCO_3$(s) at either 50 or 100°C with pressures of 500, 200, and 25.33 bar. For this system, we used the PITZER database of the software (Parkhurst and Appelo 2013; Appelo 2015), which provides more accurate activity coefficients. In

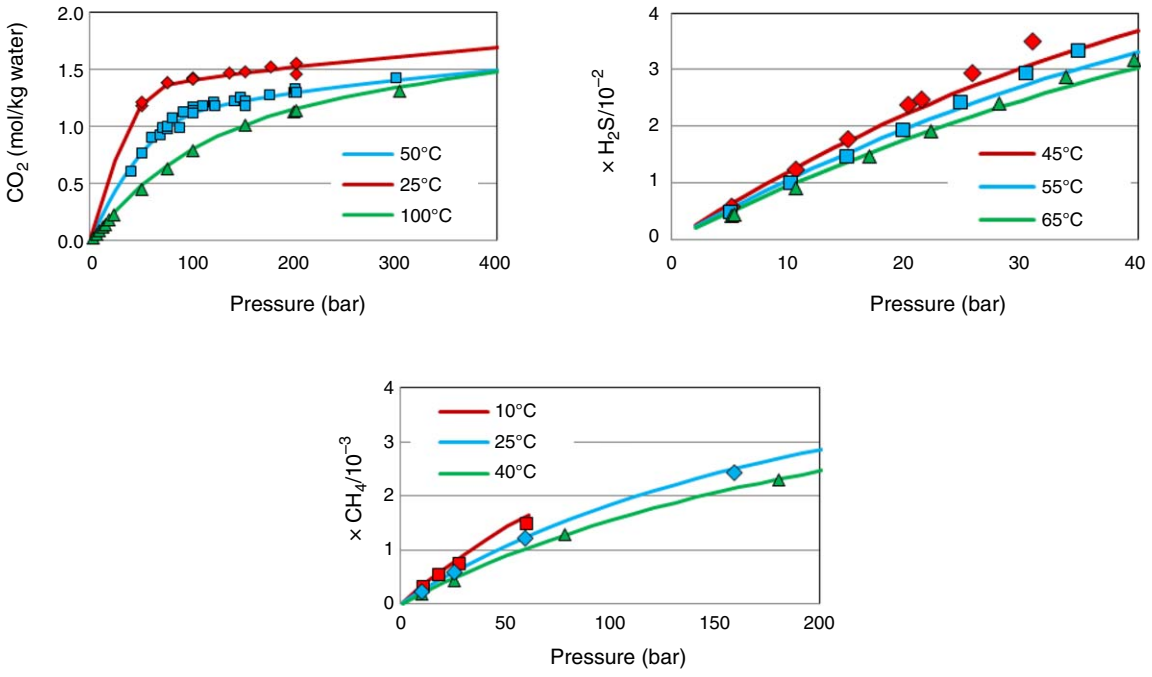

Fig. 1—Experimental (symbols) and predicted (lines) values for the solubility of CO_2, H_2S, and CH_4 in water with varying pressure for different temperatures. The VPT EOS was used for the VLE calculations.

Temperature (°C)	Pressure (bar)		Exp.	SRK	PR	VPT	ARD[1] (%) SRK	PR	VPT
37.8	48.2	CH_4	0.028	0.027	0.027	0.027	1.04	1.93	1.71
		CO_2	0.930	0.981	0.967	0.962	5.44	4.02	1.31
		H_2S	0.503	0.470	0.487	0.463	6.65	3.20	11.26
	76	CH_4	0.047	0.041	0.041	0.041	11.07	12.60	1.01
		CO_2	1.210	1.291	1.272	1.254	6.70	5.09	2.42
		H_2S	0.540	0.564	0.611	0.553	4.53	13.06	19.75
	125.2	CH_4	0.080	0.068	0.065	0.067	14.00	18.58	3.89
		CO_2	1.510	1.490	1.494	1.431	1.34	1.06	5.58
		H_2S	0.595	0.521	0.648	0.509	12.41	8.84	36.21
	169.3	CH_4	0.099	0.087	0.083	0.085	12.09	15.97	2.75
		CO_2	1.540	1.557	1.559	1.482	1.09	1.24	6.71
		H_2S	0.608	0.480	0.629	0.466	21.04	3.47	44.63
107.2	83.6	CH_4	0.038	0.043	0.035	0.035	13.21	8.51	2.71
		CO_2	0.698	0.973	0.747	0.744	39.38	7.08	7.68
		H_2S	0.342	0.495	0.416	0.398	44.74	21.60	8.12
	129.3	CH_4	0.058	0.051	0.050	0.051	12.55	12.65	2.54
		CO_2	0.959	1.079	0.999	0.991	12.48	4.20	6.64
		H_2S	0.447	0.523	0.530	0.492	17.03	18.51	21.59
	171.7	CH_4	0.078	0.064	0.064	0.065	17.35	18.15	2.63
		CO_2	1.130	1.229	1.170	1.155	8.76	3.53	5.93
		H_2S	0.473	0.545	0.594	0.536	15.28	25.56	32.16
					AARD[2] (%)		13.92	13.25	10.78

[1] $ARD(\%) = \left|\left(x_{exp} - x_{calc}\right)/x_{exp}\right| \times 100.$

[2] $AARD(\%) = \frac{1}{N}\sum\left|\left(x_{exp} - x_{calc}\right)/x_{exp}\right| \times 100.$

[3]Calculation does not consider the mole fraction of water in the gas phase.

Table 2—Solubility of a gas mixture (0.3 CH_4, 0.6 CO_2, and 0.1 H_2S in mole fraction) in water. Experimental data taken from Zirrahi et al. (2012).

Tables 3 and 4, one can see that higher dissolution of gas yields higher dissolution of mineral for all conditions.

Moreover, EOS-based calculations produced mineral dissolutions with smaller deviations than gaseous dissolution. For example, at 100°C and 200 bar, the SRK EOS overestimates CO_2 dissolution by 6.99%, while for $CaCO_3$ dissolution, the error is 0.92%.

By subtracting the dissolution values between physical conditions, one can obtain the amounts of evolved gas and mineral precipitation during isothermal depressurization for the experimental data and EOSs **(Tables 5 and 6).**

For simulation at 50°C, the SRK EOS overestimates the quantity of gas that is released from solution during a pressure decrease. On the other hand, the PR and VPT EOSs predict less scale because of lower CO_2 degassing. However, at 100°C, the SRK EOS underestimates calcite precipitation, while the evolution of gas is overestimated for depressurization processes that include 25.33 bar. In addition, the PR- and VPT-EOS calculations showed higher errors for scale formation than for CO_2 evolution for the same processes. These results are influenced by the fact that at pressures lower than the CO_2 critical pressure (73.9 bar),

Pressure (bar)	CO_2 Dissolved (mol/kg water) Exp.	SRK	PR	VPT	$CaCO_3$ Dissolved (mol/kg water) Exp.	SRK	PR	VPT
500	1.59900	1.75165	1.54221	1.56902	0.02450	0.02475	0.02439	0.02444
200	1.30674	1.37165	1.28253	1.29300	0.02059	0.02074	0.02053	0.02055
25.33	0.43651	0.44378	0.43838	0.43916	0.01474	0.01481	0.01476	0.01477

Table 3—Simulation results from PHREEQC for CO_2 and $CaCO_3$ dissolution at 50°C.

Pressure (bar)	CO_2 Dissolved (mol/kg water) Exp.	SRK	PR	VPT	$CaCO_3$ Dissolved (mol/kg water) Exp.	SRK	PR	VPT
500	1.59899	1.77685	1.57797	1.60008	0.00891	0.00899	0.00890	0.00891
200	1.13281	1.21202	1.13759	1.14561	0.00771	0.00778	0.00771	0.00772
25.33	0.24143	0.26412	0.26141	0.26176	0.00528	0.00539	0.00538	0.00538

Table 4—Simulation results from PHREEQC for CO_2 and $CaCO_3$ dissolution at 100°C.

Pressure (bar)	Evolved CO_2 (mol/kg water)				$CaCO_3$ Precipitation (mol/kg water)			
	Exp.	SRK	PR	VPT	Exp.	SRK	PR	VPT
500 → 200	0.29226	0.38000	0.25968	0.27602	0.00391	0.00401	0.00386	0.00389
Rel. Error	–	30.02%	–11.15%	–5.56%	–	2.40%	–1.20%	–0.56%
500 → 25.33	1.16248	1.30787	1.10383	1.12986	0.00976	0.00994	0.00963	0.00968
Rel. Error	–	12.51%	–5.05%	–2.81%	–	1.86%	–1.28%	–0.82%
200 → 25.33	0.87022	0.92787	0.84415	0.85384	0.00585	0.00593	0.00577	0.00579
Rel. Error	–	6.62%	–3.00%	–1.88%	–	1.49%	–1.33%	–0.99%

Table 5—CO_2 evolution and $CaCO_3$ precipitation during depressurization at 50°C.

Pressure (bar)	Evolved CO_2 (mol/kg water)				$CaCO_3$ Precipitation (mol/kg water)			
	Exp.	SRK	PR	VPT	Exp.	SRK	PR	VPT
500 → 200	0.46618	0.56483	0.44038	0.45447	0.00120	0.00121	0.00119	0.00119
Rel. Error	–	21.16%	–5.53%	–2.51%	–	0.60%	–1.28%	–0.96%
500 → 25.33	1.35756	1.51274	1.31657	1.33831	0.00364	0.00360	0.00352	0.00353
Rel. Error	–	11.43%	–3.02%	–1.42%	–	–1.11%	–3.19%	–2.93%
200 → 25.33	0.89138	0.94790	0.87618	0.88385	0.00243	0.00239	0.00233	0.00234
Rel. Error	–	6.34%	–1.71%	–0.85%	–	–1.95%	–4.14%	–3.90%

Table 6—CO_2 evolution and $CaCO_3$ precipitation during depressurization at 100°C.

all analyzed models overestimate CO_2 solubility, and this effect increases with temperature.

We can apply this methodology again to evaluate the impact of H_2S solubility on FeS precipitation by finding the equilibrium states at 65.19°C and pressures of 39.62 and 16.88 bar. This time we adopted the PHREEQC database (Parkhurst and Appelo 2013), which uses the B-dot model to calculate activity coefficients because data regarding Fe^{2+} activities are missing from the PITZER database. **Table 7** shows that, as before, higher dissolution values of gas were linked to higher dissolution of mineral. However, even though H_2S dissolved more than CO_2 in similar conditions of pressure and temperature, the dissolution of FeS was one order of magnitude lower than the dissolution of $CaCO_3$.

Moreover, the relative errors between gas and mineral changes are very similar, as opposed to $CaCO_3$-scale calculations that were more than three times more accurate than CO_2 evolution. However, this propagation of errors in the simulation of FeS deposition is not significant because the absolute difference in iron concentration between simulations is less than 0.000089 mol/kg of water (< 5 ppm Fe^{2+}) and may not be measureable in the field.

Finally, we investigated the $CaCO_3$ precipitation when water is in contact with a mixture of sour and acid gases. Results showed that the presence of additional gases interferes in the calculation of carbonate scale. In **Tables 8 through 11,** one can see that, although the SRK EOS simulations yield higher amounts of dissolved CO_2, the obtained $CaCO_3$ dissolution for this EOS is sometimes smaller than for the others. Moreover, EOS-based calculations produced scale predictions with larger errors than in CO_2 evolution (more than double for some cases). The only exception was the simulation with the VPT EOS at 107.2°C, which shows a slight (but not significant) reduction in the error.

Case Study: Presalt Reservoir. We have also analyzed the impact of each EOS-based calculation on scale predictions by use of formation-water composition from an oil field in the Brazilian presalt. The selected case is a high-pressure, high-temperature, and high-salinity field and poses difficulties in scale-predicition modeling.

Reservoirs in the presalt layer off the coast of Brazil have been developed recently, and scale deposition was already detected.

Pressure (bar)	H_2S Dissolved (mol/kg water)				FeS Dissolved (mol/kg water)			
	Exp.	SRK	PR	VPT	Exp.	SRK	PR	VPT
39.62	1.82647	1.74441	1.713697	1.781423	0.00165	0.00161	0.00160	0.00163
16.88	0.829423	0.860835	0.854174	0.86941	0.00108	0.00111	0.00110	0.00111
Change	0.99705	0.88358	0.85952	0.91201	0.00057	0.00050	0.00049	0.00052
Rel. Error	–	–11.38%	–13.79%	–8.53%	–	–10.95%	–12.72%	–8.83%

Table 7—H_2S evolution and FeS precipitation during depressurization at 65.19°C.

Pressure (bar)	CO_2 Dissolved (mol/kg water)				Calcite Dissolved (mol/kg water)			
	Exp.	SRK	PR	VPT	Exp.	SRK	PR	VPT
169.3	0.87522	0.88363	0.88633	0.84059	0.03984	0.03930	0.04014	0.03849
76	0.68452	0.73113	0.72030	0.70962	0.02297	0.03467	0.03476	0.03425

Table 8—Simulation results from PHREEQC for CO_2 and $CaCO_3$ dissolution at 37.2°C (with H_2S and CH_4).

Pressure (bar)	CO_2 Dissolved (mol/kg water)				Calcite Dissolved (mol/kg water)			
	Exp.	SRK	PR	VPT	Exp.	SRK	PR	VPT
171.7	0.63851	0.69557	0.66204	0.65299	0.00853	0.00884	0.00913	0.00885
83.6	0.39200	0.54877	0.42026	0.41822	0.00768	0.00845	0.00814	0.00803

Table 9—Simulation results from PHREEQC for CO_2 and $CaCO_3$ dissolution at 107.2°C (with H_2S and CH_4).

Pressure (bar)	Evolved CO_2 (mol/kg water)				Calcite Precipitation (mol/kg water)			
	Exp.	SRK	PR	VPT	Exp.	SRK	PR	VPT
169.3 → 76	0.19070	0.15250	0.16603	0.13097	0.01687	0.00463	0.00538	0.00424
Rel. Error	–	–20.03%	–12.94%	–31.32%	–	–72.55%	–68.11%	–74.87%

Table 10—CO_2 evolution and $CaCO_3$ precipitation during depressurization at 37.2°C (with H_2S and CH_4).

Pressure (bar)	Evolved CO_2 (mol/kg water)				Calcite Precipitation (mol/kg water)			
	Exp.	SRK	PR	VPT	Exp.	SRK	PR	VPT
171.7 → 83.6	0.24651	0.14680	0.24178	0.23477	0.00085	0.00040	0.00099	0.00082
Rel. Error	–	–40.45%	–1.92%	–4.76%	–	–53.58%	16.18%	–4.10%

Table 11—CO_2 evolution and $CaCO_3$ precipitation during depressurization at 107.2°C (with H_2S and CH_4).

	Formation water		Low-Sulfate Seawater	
T (°C)	136		136	
P (bar)	472		472	
pH	4.8		7.6	
Composition	(mg/L)	(mol/kg water)	(mg/L)	(mol/kg water)
CO_2	280	0.0084	< 2	< 0.0001
Ca	14 920	0.4895	57	0.0014
Na	71 085	4.0560	10 283	0.4600
K	4074	0.1371	75	0.0020
Mg	1207	0.0660	297	0.0117
Ba	23	0.0002	< 2	<0.0001
Sr	1547	0.0233	< 2	0.0000
Cl	144 506	5.3420	17 000	0.4867
SO_4	346	0.0047	44	0.0004
Br	5	0.0001	–	–
Fe	23	0.0005	–	–

Table 12—Equilibrated waters at reservoir conditions (calculated by PHREEQC).

Thus, we have considered a field in the Santos Basin (Field P) that is at 136°C and 472 bar (Bezerra et al. 2013).

Before performing scale-prediction calculations, we have used PHREEQC with the PITZER database to check if the formation-water composition that was reported in the literature is in equilibrium. We have noted that carbonate and sulfate minerals were supersaturated. Therefore, we forced the precipitation of calcite and anhydrite because these minerals have been observed in the Lula Field (Boyd et al. 2015). Moreover, because there was no information in the literature about the H_2S content, FeS precipitation was not considered, and, therefore, we concentrate our analysis on the precipitation of $CaCO_3$ during depressurization along the production tubing.

A CO_2/water-alternating-gas process with low-sulfate seawater is considered here because (a) CO_2 injection is the preferred enhanced-oil-recovery method for the presalt province and (b) high-sulfate water may cause sulfate-scale precipitation. The equilibrated waters at reservoir conditions are shown in **Table 12.**

During CO_2/water-alternating-gas injection, the injected water becomes saturated with CO_2 at reservoir conditions near the injector wellbore, and then mixes with the formation water. Therefore, the water that arrives in the producer wellbore has a higher scale tendency because of higher concentrations of calcium (from formation water) and bicarbonate (from CO_2 dissolution in injected water). To calculate the impact of CO_2 concentration in scale formation, we chose to saturate with CO_2 (by use of different EOSs) a mixture of 0.75 seawater fraction at reservoir pressure and at 100 bar.

The solubility of gases in water decreases with increasing salinity. Therefore, we have calculated the CO_2 solubility in pure water, and then divided it by the activity coefficient proposed by Harvie et al. (1984), which has been used successfully to model experimental results in different conditions of temperature, pressure, and salinity (Appelo 2015). In **Table 13,** we show the CO_2

		CO_2 Solubility (mol/kg water)								
		Pure Water			Low-Sulfate Seawater			75% Low-Sulfate Seawater + 25% Formation Water		
T (°C)	*P* (bar)	SRK	PR	VPT	SRK	PR	VPT	SRK	PR	VPT
136	472	2.2709	2.0373	2.0616	1.8459	1.6560	1.6758	1.0870	0.9752	0.9868
136	100	0.8841	0.8551	0.8589	0.7186	0.6951	0.6981	0.4232	0.4093	0.4111

Table 13—CO_2 solubility (in mol/kg water) in waters of different salinities at initial conditions and after depressurization according to different EOSs.

		$CaCO_3$ Precipitation (mol/kg water)		
		SRK	PR	VPT
136°C	472 bar	0.02711	0.02438	0.02466
136°C	100 bar	0.02751	0.02472	0.02501
	Difference	0.00040	0.00034	0.00035

Table 14—$CaCO_3$ precipitation (in mol/kg water) during mixing of 75% low-sulfate seawater with 25% formation water at different pressures. The low-sulfate seawater was saturated with CO_2 before mixing with formation water.

solubility in different waters at reservoir temperature according to each EOS.

Thus, the calcite precipitation during the mixing of waters was calculated by PHREEQC using the different EOS-based CO_2 solubilities. **Table 14** shows the precipitation at the two pressures and the difference between them. This difference is interpreted as the precipitation caused by depressurization of the mixture.

The choice of EOS produced discrepancies in the predicted precipitation from 0.00001 to 0.00006 mol $CaCO_3$/kg water. To understand how these deviations affect the amount of precipitation during production, we assume a water-flow rate of 1000 m^3/d and conclude that the error between EOSs may generate an additional approximately 6 kg of $CaCO_3$ precipitation during each day, while the error between actual CO_2 solubility and any of the predicted values (which is not known because of lack of experimental data) may cause higher differences in scale prediction. Such an amount of scale could cause an appreciable difference to scale management if deposition were to take place close to sensitive equipment, such as subsurface safety valves or electrical submersible pumps, and more than a year would amount to more than 2 t of scale.

Conclusions

We have explored the accuracy of VLE calculations with cubic EOSs and their impact on scale-formation prediction. When the solubility of single-component gases in water was investigated, the VPT EOS performed better (especially for CO_2). However, for the data concerning mixtures of acid and sour gases, there was not enough evidence to determine the best EOS because the calculated errors varied from 1.01 to 44.74% for different temperatures and pressures. This result presents a warning to those modeling scale precipitation in real fields and demonstrates the importance of conducting more experiments with a mixture of gases to calibrate model parameters.

To estimate the errors of mineral scale prediction, we used PHREEQC to calculate mineral dissolution during gaseous dissolution in pure water. Then, the difference in solubility between states with different pressure was understood as the amount of gas evolution and mineral precipitation. For carbonates, errors in $CaCO_3$ solubility were smaller than CO_2, and calcite precipitation was generally more accurate than calculations of released gas during depressurization. However, simulations at 100°C showed that deviations in scale prediction can surpass the initial ARD from VLE calculations if the pressure is low. Therefore, predictions of scale deposition in production tubing and equipment near the surface should be made with more caution.

On the other hand, when we applied the same methodology to FeS and H_2S systems, the resulting errors were very similar to each other, which suggests that the use of the SRK, PR, or VPT EOSs had little impact on sulfide-scale prediction (at the analyzed conditions).

Simulations with a mixture of CO_2, H_2S, and CH_4 resulted in significantly larger errors in scale prediction (sometimes more than double the VLE calculations). Moreover, the case study revealed that errors of 1 to 6 kg of $CaCO_3$ precipitate per day can emerge simply by chosing a less-accurate EOS. Additional errors will certainly exist. However, there are limited data on gas solubility in mixed salt solutions at reservoir conditions (especially at high pressure and high temperature), which makes the estimation of errors for natural waters more difficult than for pure water or sodium chloride solutions.

Again, these findings increase the demand for experimental data (or better models) to calculate the solubilities of acid and sour gases in real oilfield reservoir systems and improve scale-prediction calculations. Furthermore, solubility of mixed gases in saline waters should be investigated when more experimental data are available to improve the applicability of this and future studies.

Nomenclature

a_w = activity of water
$H_{i,j}$ = Henry constant of component i and solvent j
$k_{i,j}$ = binary interaction coefficient between components i and j
K_β = equilibrium constant of precipitation reaction of mineral β
m_i = molality (molal concentration) of component i
P = pressure, bar
P_c = critical pressure
P_{vp} = vapor pressure of solvent
R = universal constant of gases
T = temperature, K
T_c = critical temperature, K
T_r = reduced temperature
v = volume
$\overline{V}_i^\infty$ = partial molar volume at infinite dilution
Z = compressibility factor
Z_c = critical compressibility factor
x_i = molar fraction of component i in aqueous phase
y_i = molar fraction of component i in gas phase
γ_i = activity coefficient of aqueous component i
ϕ_i = fugacity coefficient of gaseous component i

Acknowledgments

Foundation CMG is thanked for supporting the studentship held by Ayrton Ribeiro and the Chair in Reactive Flow Simulation held by Eric Mackay. Galp Energia is thanked for supporting the studentship held by Duarte Silva. The following are thanked for their support of the Flow Assurance and Scale Team joint-industry project at Heriot-Watt University: Apache, Baker Hughes, BG Group, BP, Chevron, Clariant, ConocoPhillips, Equion, Galp, Maersk, M-I SWACO, Multi-Chem, MWV, Nalco Champion, Nexen, Petrobras, Petronas, REP, Shell, Statoil, Talisman Sinopec, Total, and Wintershall.

References

Appelo, C. A. J. 2015. Principles, Caveats and Improvements in Databases for Calculating Hydrogeochemical Reactions in Saline Waters From 0 to 200°C and 1 to 1000 atm. *Applied Geochemistry* **55:** 62–71. http://dx.doi.org/10.1016/j.apgeochem.2014.11.007.

Benning, L. G., Wilkin, R. T., and Barnes, H. L. 2000. Reaction Pathways in the Fe–S System Below 100°C. *Chemical Geology* **167** (1–2): 25–51. http://dx.doi.org/10.1016/S0009-2541(99)00198-9.

Bezerra, M. C. M., Rosario, F. F., and Rosa, K. R. S. A. 2013. Scale Management in Deep and Ultradeep Water Fields. Presented at the Offshore Technology Conference-Brasil, Rio de Janeiro, 29–31 October. OTC-24508-MS. http://dx.doi.org/10.4043/24508-MS.

Boyd, A., Souza, A., Carneiro, G. et al. 2015. Presalt Carbonate Evaluation for Santos Basin, Offshore Brazil. *Petrophysics* **56** (6): 577–591. SPWLA-2015-v56n6a2.

Chapoy, A., Mohammadi, A. H., Richon, D. et al. 2004. Gas Solubility Measurement and Modeling for Methane–Water and Methane–Ethane–*n*-Butane–Water Systems at Low Temperature Conditions. *Fluid Phase Equilibria* **220** (1): 111–119. http://dx.doi.org/10.1016/j.fluid.2004.02.010.

Chapoy, A., Mohammadi, A. H., Tohidi, B. et al. 2005. Experimental Measurement and Phase Behavior Modeling of Hydrogen Sulfide–

Water Binary System. *Ind. Eng. Chem. Res.* **44** (19): 7567–7574. http://dx.doi.org/10.1021/ie050201h.

Cruz, R., Rosa, M. B., Branco, C. et al. 2016. Lula NE Pilot Project - An Ultra-Deep Success in the Brazilian Pre-Salt. Presented at the Offshore Technology Conference, Houston, 2–5 May. OTC-27297-MS. http://dx.doi.org/10.4043/27297-MS.

Harvey, A. H. 1996. Semiempirical Correlation for Henry's Constants Over Large Temperature Ranges. *AIChE Journal* **42** (5): 1491–1494. http://dx.doi.org/10.1002/aic.690420531.

Harvie, C. E., Møller, N., and Weare, J. H. 1984. The Prediction of Mineral Solubilities in Natural Waters: The Na-K-Mg-Ca-H-Cl-SO_4-OH-HCO_3-CO_3-CO_2-H_2O System to High Ionic Strengths at 25°C. *Geochimica et Cosmochimica Acta* **48** (4): 723–751. http://dx.doi.org/10.1016/0016-7037(84)90098-X.

Leal Jauregui, J. A., Solares, J. R., Nasr-El-Din, H. A. et al. 2007. A Systematic Approach To Remove Iron Sulphide Scale: A Case History. Presented at the SPE Middle East Oil and Gas Show and Conference, Manama, Bahrain, 11–14 March. SPE-105607-MS. http://dx.doi.org/10.2118/105607-MS.

Li, Y. and Nghiem, L. X. 1986. Phase Equilibria of Oil, Gas and Water/Brine Mixtures From a Cubic Equation of State and Henry's Law. *The Canadian Journal of Chemical Engineering* **64** (3): 486–496. http://dx.doi.org/10.1002/cjce.5450640319.

Muller, E. A. and Olivera-Fuentes, C. 1989. General Expressions for Multicomponent Fugacity Coefficients and Residual Properties from Cubic Equations of State. *Latin American Applied Research* **19:** 99–109.

Parkhurst, D. L. and Appelo, C. A. J. 2013. Description of Input and Examples for PHREEQC Version 3—A Computer Program for Speciation, Batch-Reaction, One-Dimensional Transport, and Inverse Geochemical Calculations: U. S. Geological Survey Techniques and Methods, Book 6, Chapter A43, 132–138. Denver: USGS, http://pubs.usgs.gov/tm/06/a43/.

Peng, D.-Y. and Robinson, D. B. 1976. A New Two-Constant Equation of State. *Ind. Eng. Chem. Fundamen.* **15** (1): 59–64. http://dx.doi.org/10.1021/i160057a011.

Plummer, L. N., Wigley, T. M. L., and Parkhurst, D. L. 1978. The Kinetics of Calcite Dissolution in CO_2-Water Systems at 5° to 60°C and 0.0 to 1.0 atm CO_2. *American Journal of Science* **278** (2): 179–216. http://dx.doi.org/10.2475/ajs.278.2.179.

Poling, B. E., Prausnitz, J. M., and O'Connell, J. P. 2001. *The Properties of Gases and Liquids*, fifth edition, McGraw-Hill.

Prausnitz, J. M., Lichtenthaler, R. N., and Azevedo, E. G. D. 1999. *Molecular Thermodynamics of Fluid-Phase Equilibria*. Upper Saddle River, New Jersey: Prentice Hall PTR.

Soave, G. 1972. Equilibrium Constants From a Modified Redlich-Kwong Equation of State. *Chemical Engineering Science* **27** (6): 1197–1203. http://dx.doi.org/10.1016/0009-2509(72)80096-4.

Spycher, N., Pruess, K., and Ennis-King, J. 2003. CO_2-H_2O Mixtures in the Geological Sequestration of CO_2. I. Assessment and Calculation of Mutual Solubilities From 12 to 100°C and up to 600 bar. *Geochimica et Cosmochimica Acta* **67** (16): 3015–3031. http://dx.doi.org/10.1016/S0016-7037(03)00273-4.

U.S. Geological Survey (USGS). 2016. PHREEQC (Version 3)--A Computer Program for Speciation, Batch-Reaction, One-Dimensional Transport, and Inverse Geochemical Calculations. http://wwwbrr.cr.usgs.gov/projects/GWC_coupled/phreeqc/index.html (last modified 13 September 2016).

Valderrama, J. O. 1990. A Generalized Patel-Teja Equation of State for Polar and Nonpolar Fluids and Their Mixtures. *Journal of Chemical Engineering of Japan* **23** (1): 87–91. http://dx.doi.org/10.1252/jcej.23.87.

Wagner, W. and Pruss, A. 1993. International Equations for the Saturation Properties of Ordinary Water Substance. Revised According to the International Temperature Scale of 1990. Addendum to *J. Phys. Chem. Ref. Data* **16**, 893 (1987). *J. Phys. Chem. Ref. Data* **22:** 783–787. http://dx.doi.org/10.1063/1.555926.

Zirrahi, M., Azin, R., Hassanzadeh, H. et al. 2012. Mutual Solubility of CH_4, CO_2, H_2S, and Their Mixtures in Brine Under Subsurface Disposal Conditions. *Fluid Phase Equilibria* **324:** 80–93. http://dx.doi.org/10.1016/j.fluid.2012.03.017.

Appendix A

Tables A-1 and A-2 provide the parameters for the different EOSs for use in Eqs. 2 and 5. **Table A-3** provides the function F values for use in Eq. 6.

EOS	Notation	u	w
Soave (1972)	SRK	1	0
Peng and Robinson (1976)	PR	2	–1
Valderrama (1990)	VPT	$(b + c)/b$	$-c/b$

Table A-1—Parameters u and w for the seven different EOSs to be used in Eq. 2.

EOS	Ω_a	Ω_b	Ω_c
Soave (1972)	0.42747	0.08664	0
Peng and Robinson (1976)	0.45724	0.07780	0
Valderrama (1990)	$0.66121 - 0.76105Z_c$	$0.02207 + 0.20868Z_c$	$0.57765 + 1.87080Z_c$

Table A-2—Ω_a, Ω_b, and Ω_c values for SRK, PR, and VPT EOSs to be used in Eq. 5. Z_c is the critical compressibility factor.

EOS	Function F
Soave (1972)	$0.480 + 1.574\omega - 0.176\omega^2$
Peng and Robinson (1976)	$0.37464 + 1.54226\omega - 0.26992\omega^2$
Valderrama (1990)	$0.46283 + 3.58230(\omega Z_c) + 8.19417(\omega Z_c)^2$

Table A-3—Function F to be used in Eq. 6. Z_c is the critical compressibility factor.

Ayrton S. Ribeiro is part of a joint PhD-degree program between Heriot-Watt University and Universidade Federal de Pernambuco. His research interests include the study of multiphase flow and geochemical reactions in porous media. Ribeiro holds a BSc degree in physics from the Universidade Federal do Pará and an MSc degree in physics from Pontifícia Universidade Católica do Rio de Janeiro. He is a member of SPE.

Duarte Silva is currently pursuing a PhD degree from the Institute of Petroleum Engineering at Heriot-Watt University. His research interests include modeling of mineral scale in

enhanced-oil-recovery processes and the study of fluid flow and geochemical reactions in porous media. Silva holds an MSc degree in chemical engineering from Instituto Superior Técnico, Portugal. During his studies, he was an exchange student at Politecnico di Milano, Italy, and IFP Energies Nouvelles, France. In his thesis, Silva investigated different pathways to synthesize borinic acids used in the design of new olefin metathesis catalysts. He is a member of SPE.

Eric J. Mackay holds the Foundation CMG Chair in Reactive Flow Simulation in the Institute of Petroleum Engineering at Heriot-Watt University, where he is a principal investigator for the Flow Assurance and Scale Team joint-industry project. His research interests include the study of fluid flow and geochemical reactions in porous media. Mackay has authored or coauthored more than 150 publications related primarily to inorganic scale management and to carbon capture and storage. He was appointed SPE Distinguished Lecturer on the topic of scale management during the 2007–2008 season. Mackay has taught reservoir simulation at Heriot-Watt University since 1990. He holds a BSc degree in physics from the University of Edinburgh and a PhD degree in petroleum engineering from Heriot-Watt University. Mackay is a member of SPE.

Ken Sorbie is a principal investigator within the Flow Assurance and Scale Team at the Institute of Petroleum Engineering at Heriot-Watt University. His research interests include oilfield chemistry, reservoir characterization, and fundamentals of multiphase fluid flow in porous media. Sorbie holds a degree in chemistry from Strathclyde University and a PhD degree in theoretical chemistry and applied mathematics from Sussex University. He has served on several SPE committees.

Journal of Natural Gas Science and Engineering 35 (2016) 703–719

Contents lists available at ScienceDirect

Journal of Natural Gas Science and Engineering

journal homepage: www.elsevier.com/locate/jngse

Geochemical modelling of formation damage risk during CO_2 injection in saline aquifers

Min Jin [a], Ayrton Ribeiro [a, b], Eric Mackay [a, *], Leonardo Guimarães [b], Usman Bagudu [c]

[a] Heriot-Watt University, Edinburgh, UK
[b] Universidade Federal de Pernambuco, Recife, Brazil
[c] National Grid, Warwick, UK

ARTICLE INFO

Article history:
Received 30 March 2016
Received in revised form
27 July 2016
Accepted 11 August 2016
Available online 16 August 2016

Keywords:
CO_2 injection
Mineral reactions
Halite precipitation

ABSTRACT

This study provides an understanding of the impact of geochemical reactions during and after CO_2 injection into a potential storage site. The results of calculations of geochemical reactivity of reservoir rock and of cap rock during and after CO_2 injection were performed using a geochemical simulator, with the calculations showing that for these conditions up to 0.5 mol of CO_2 can be dissolved per kg of water. The risk of dissolution of primary cements was considered and identified. In addition, the potential of carbonation reactions to permanently sequester CO_2 was considered, although these reactions were shown to be very slow relative to other processes. The implications for security of storage are that while dolomite nodules exist in the sandstone formation, these do not contribute significantly to the overall rock strength, and hence the risk of dissolution of the formation or caprock causing significant leakages pathways is very low. Further calculations were performed using a commercial reservoir simulation code to account for brine evaporation, halite precipitation and capillary pressure re-imbibition. The impact on injectivity was found not to be significant during continuous and sustained injection of CO_2 at a constant rate. Capillary pressure effects did cause re-imbibition of saline brine, and hence greater deposition, reducing the absolute porosity by up to 13%. The impact of the halite deposition was to channel the CO_2, but for the configuration used there was not a significant change in injection pressure.

1. Introduction

Injection of CO_2 into saline aquifers will cause carbonation of contacted *in situ* brines, disturbing the chemical equilibrium that was established over geological time frames between the brine and the host rock. This may result in dissolution and or precipitation reactions that affect the integrity of the target storage formation rock, the overburden rock, the injectivity of the wells and the security of storage. Continuous injection of dry CO_2 into saline aquifers may also cause the evaporation of the resident brine and eventually lead to formation dry-out in the vicinity of the injector, with associated salt precipitation (André et al., 2007; Giorgis et al., 2007; Pruess, 2009; Qiao et al., 2016). The precipitate may reduce formation effective porosity, permeability, and consequently impact the injectivity.

To investigate these changes, researchers have been using reactive transport simulations using different software packages (Lichtner, 1985; Steefel and Lasaga, 1994; Xu et al., 2011; Nghiem et al., 2011; Parkhurst and Appelo, 2013; Lichtner et al., 2013). A concise explanation and comparison between the available codes can be found in Steefel et al. (2015).

The object of the study is to develop models of carbon dioxide injection into a saline aquifer that includes a detailed mineralogical description of the sandstone formation and a good characterisation of the formation water system, to assess the formation damage near the wellbore and the risk of injectivity impairment by using thermodynamic simulation and geochemical reservoir modelling. The calculations are performed using the PHREEQC thermodynamic model (Appelo and Postma, 2010) and the GEM-GHG reservoir simulation and coupled geochemical code (CMG, 2015a), which has been adapted specifically for use in Green House Gas storage modelling. Using the former, thermodynamic (0D) calculations have been performed to assess the impact of dissolution of CO_2 in the formation water on the reactivity of the primary minerals present in the reservoir, and the precipitation of secondary minerals. Using the later, a 2D reactive transport model was built

* Corresponding author. Heriot-Watt University, Edinburgh, UK.
E-mail address: eric.mackay@pet.hw.ac.uk (E. Mackay).

http://dx.doi.org/10.1016/j.jngse.2016.08.030
1875-5100/

corresponding to simulations that couple hydrodynamic and geochemical modelling to assess the impact of halite precipitation.

2. CO_2 storage injection site

2.1. Geological data

The sandstone formation was deposited in a broad, gradually subsiding offshore basin. The dominant facies type is very fine to fine grained fluvial laminated sandstone. The reservoir is relatively shallow (1000 mm–1500 mm) and has been subdivided into three main zones, Sandstone_L1 at the base, Sandstone_L2 in the middle and Sandstone_L3 at the top of the formation.

The rock properties were interpreted by data from wells which are within an area covering 40 × 50 km. The pore volume of the model was calculated based on the depth map of the structural closure. As the modelling focuses on the region near the wellbore, the exact value of the pore volume is not important for the study. Because the injection site is part of connected structural closures, and especially as there is evidence of a subcrop to seabed to the south east of the main structure, a numerical aquifer is required as a boundary condition for the flow modelling.

A summary of the reservoir parameters is given in Table 1. The average porosity of the cored area ranges from 17% in the Lower Model to 24% in the Upper Model, with corresponding estimated average permeabilities of 100md to 800md. The average net pore volume is 4.6×10^9 m^3. The uncertainty workflows calculated the spill point ranges between 1416 m and 1533 m, the net to gross between 0.752 and 0.986.

There are no significant barriers to horizontal flow. The only impermeable barriers to vertical flow are mudstone beds, and they are thought unlikely to extend laterally for more than around 100 m. Most such beds are rather silty, and probably act only as baffles to vertical flow rather than wholly impermeable barriers.

2.2. Geochemical data

The formation water analysis shows that all water samples were highly saline (TDS 250000 ± 10000 mg/L) sodium chloride dominated brines with significant concentrations of common rock constituents, such as calcium, magnesium and sulphate.

The modelling of CO_2 injection into the high salinity aquifer involves the solution of the component transport equations, the equations for thermodynamic equilibrium between the gaseous and aqueous phases, and the equations for geochemical reactions between the aqueous species and mineral precipitation and dissolution. A fully coupled approach is implemented in the software GEM used for the study to achieve adaptive-implicit multiphase multicomponent flow simulation with phase and chemical equilibrium and rate-dependent mineral dissolution/precipitation (CMG, 2015a).

2.2.1. Geochemical composition of the formation

Overlying the entire system is a halite-dominated evaporitic sequence, referred to as the Halite. The unit is composed mostly of quite coarsely crystalline halite with inclusions and irregular thin beds of anhydrite. The clay present between the sandstone intervals and the Halite is regarded as a playa mudstone throughout, and is referred to as the Clay.

The mineralogy data comes from 15 core plugs; two plugs were from the Halite, four from the Clay and the remaining from the Sandstone intervals, L3, L2 and L1. Sample depths and the corresponding volume fractions are listed in Table 2 and shown in Fig. 1. The average values for each zone are listed at the bottom of the table; these are the values used in the simulation model.

Based on the mineralogy analysis in Table 2, eight mineral components are chosen as the conceptualization of mineralogy in the geochemical model. They are quartz, illite, calcite, dolomite, K-feldspar, anhydrite, halite, and albite. Among these, albite is used to model plagioclase as the latter is not in the GEM database (CMG, 2015b). The average values in the bottom rows of Table 2 are used for the L3 + L2 + L1 zone and the Clay zone as the input for initial mineral volume fractions.

2.2.2. Formation water composition

Comparing the depth at which water samples were taken for testing (Table 3) with the depth where the cores were sampled for mineralogy analysis in Table 2 and Fig. 1, it is found that three water samples match or are close to the core samples, two in Sandstone L1 and L2 (1575 m and 1440 m), one in Sandstone L3 (1412 m) and one in Clay (1400 m). As the thermodynamic model is 0D, and as the 2D radial geochemical model is a homogeneous model, the initial aqueous concentration data were chosen based on the rock and formation water data from the three depths.

3. Batch 0D modelling using PHREEQC

It is very useful to run a batch geochemical model to identify the main chemical reactions in the formation and to validate the equilibrium state based on the given water composition data and rock mineral analysis data before building a complex 2D or 3D geochemical model. The batch modelling was performed using the PHREEQC code (Appelo and Postma, 2010).

In total, six sets of calculations were performed using PHREEQC. Initial calculations were performed to identify the initial equilibrium water composition, and how this varied compared to the supplied water composition (although it is evident that great care was taken with sampling and analysis of water, inevitably the process alters the initial equilibrium state, even if the analysis is performed quickly, and thus recalibration of the initial water composition to ensure equilibrium with the primary minerals identified is required). Subsequent calculations then consider the impact of dissolving CO_2 in this brine.

The six sets of calculations correspond to six locations in the sequence at various depths, and their corresponding supplied water compositions. These include three locations within the cap rock (C1, C2 and C3) and three layers of the reservoir (L1, L2 and L3). All simulations were performed using 1 L of water @ 57.2 °C and 14.2 MPa. The conditions are identified in Table 4.

The chemical reactions for the PHREEQC modelling were chosen based on the minerals identified in Fig. 2 and the brine composition. The primary concern is formation damage in the near wellbore zone and the impact CO_2 saturated brine could have on the integrity of the cap rock. For this reason, the precipitation and dissolution of the following minerals was considered in the main thermodynamic modelling activity:

Table 1
Summary of reservoir parameters.

Reservoir parameter	Value	Units
Depth to top reservoir	1020	m
Thickness	200–250	m
Spill point	1460	m
Porosity (average)	20	%
Permeability (average)	260	mD
Datum	1300	m
Reservoir temperature at datum	57.2	°C
Temperature gradient	3.16	°C per 100 m
Reservoir pressure at datum	14.12	MPa
Pressure gradient	0.0115	MPa/m

Table 2
Mineral composition of formation from water analysis.

plug	Depth (m)	Illite+Mica*	Chlorite	Quartz	K Feldspar	Plagioclase	Calcite	Dolomite	Magnesite	Halite	Anhydrite	Hematite
1	1387**	0.0	0.0	TR	0.0	0.0	0.0	0.0	0.0	99.7	0.3	0.0
2	1391	0.0	0.0	0.5	0.0	0.0	0.0	0.0	1.4	28.0	70.1	0.0
3	1398	23.6	4.2	11.5	TR	1.9	0.0	14.8	0.0	0.0	43.2	0.8
4	1404	36.8	3.2	20.9	TR	4.8	0.0	27.2	0.0	0.0	5.5	1.6
5	1407	35.2	2.4	31.1	2.2	2.3	0.0	18.5	0.0	2.5	4.0	1.8
6	1408	TR	TR	62.7	5.9	2.1	0.0	1.3	0.0	1.9	26.0	TR
7	1423	5.0	0.7	15.3	0.7	1.6	62.8	4.2	0.0	0.0	8.7	1.1
8	1433	3.3	0.8	66.4	7.1	6.3	0.3	3.9	0.0	7.1	4.3	0.4
9	1448	3.9	0.6	75.0	4.9	5.6	0.0	6.8	0.0	2.6	0.0	0.6
10	1463	13.1	2.1	56.2	4.2	11.8	0.0	4.3	0.0	2.8	2.9	2.6
11	1486	9.5	2.1	64.4	4.4	10.8	0.0	1.4	0.0	3.6	2.0	1.9
12	1503	7.9	1.2	63.1	6.1	8.8	6.1	1.3	0.0	3.2	1.5	0.7
13	1521	7.3	1.5	67.2	4.6	8.0	4.4	1.3	0.0	2.8	2.0	1.1
14	1540	5.0	0.8	69.8	7.1	8.2	TR	1.9	0.0	5.2	1.3	0.7
15	1556	12.1	0.8	63.5	4.0	10.6	3.8	1.0	0.0	2.4	1.1	0.9
	average of L3+L2+L1	7.8		65.7	5.3	8.8	2.1	2.7	0.0	3.7	1.9	1.1
	average of Clay	31.9		21.2	2.2	3.0	0.0	20.2	0.0	0.8	17.6	1.4

*the coloured cells on the heading show the minerals used in the study

** the coloured cells in the column show the formation

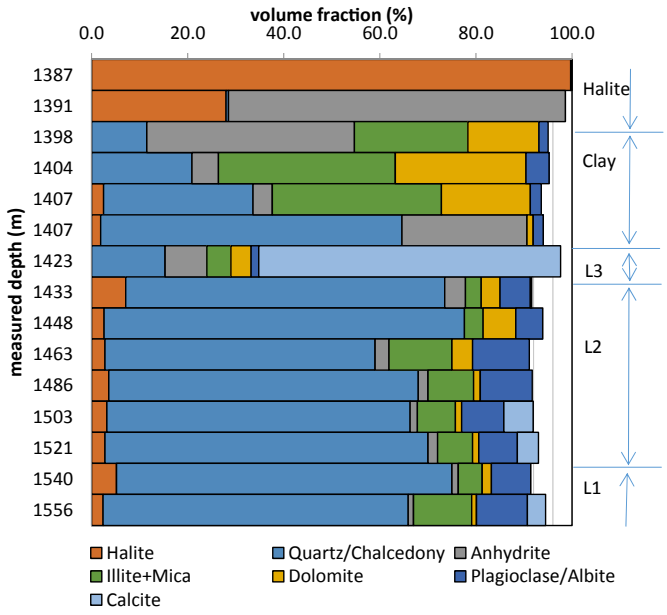

Fig. 1. Initial major mineral volume fractions (for minerals > 10%) from core analysis.

- Dolomite

$$CaMg(CO_3)_{2(s)} = Ca^{+2} + Mg^{+2} + 2 \cdot CO_3^{-2}$$

- Calcite

$$CaCO_{3(s)} = Ca^{+2} + CO_3^{-2}$$

- Anhydrite

$$CaSO_{4(s)} = Ca^{+2} + SO_4^{-2}$$

- Halite

$$NaCl_{(s)} = Na^{+} + Cl^{-}$$

Furthermore, the Pitzer thermodynamic database, which is the most comprehensive database for systems at the pressure, temperature and particularly the salinity of this system, is limited to these reactions.

Table 5 identifies the change in mineral fractions as a result of the equilibration process, and it may be seen that the changes in all cases are minor. Fig. 2 shows the new mineral compositions graphically (identifying only minerals that are present in fractions > 10%) (see Table 6).

Table 3
Formation water composition (mg/kg).

	L1	L2	L3	Clay
Sampling Point/Depth (m)	1575	1440	1412	1400
Chloride	154100	148800	148200	155400
Sulphate	300	360	380	360
Bromide	470	460	440	470
Strontium	110	110	100	120
Calcium	8860	8610	8040	9130
Magnesium	2540	3010	3190	3100
Sodium	85500	79700	80000	84800
Potassium	1400	1470	1480	1530
Sulphur	80	100	110	110
Total Dissolved Solids	253360	242620	241940	255020

Table 4
Selected brine and aquifer sections for PHREEQC simulations.

	Simulation 1	Simulation 2	Simulation 3	Simulation 4	Simulation 5	Simulation 6
Brine Location (m)	1575	1440	1412	1412	1400	1400
Mineralogy Location (m)	1556 (L1)	1448 (L2)	1423 (L3)	1407 (C1)	1398 (C2)	1391 (C3)

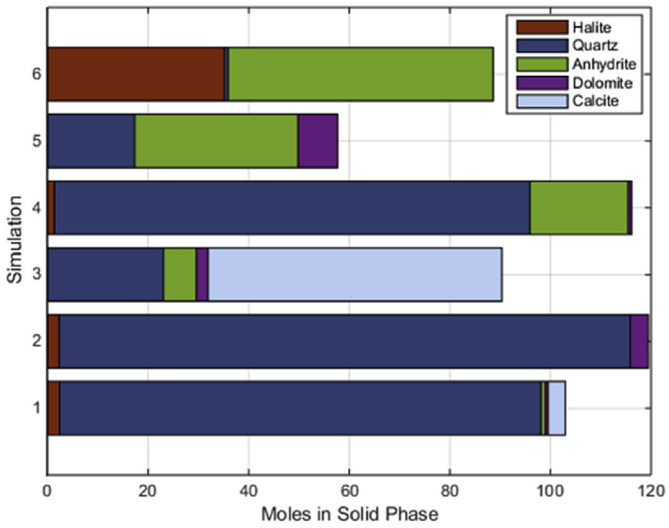

Fig. 2. Equilibrium mineral fractions from PHREEQC simulations in graphical format.

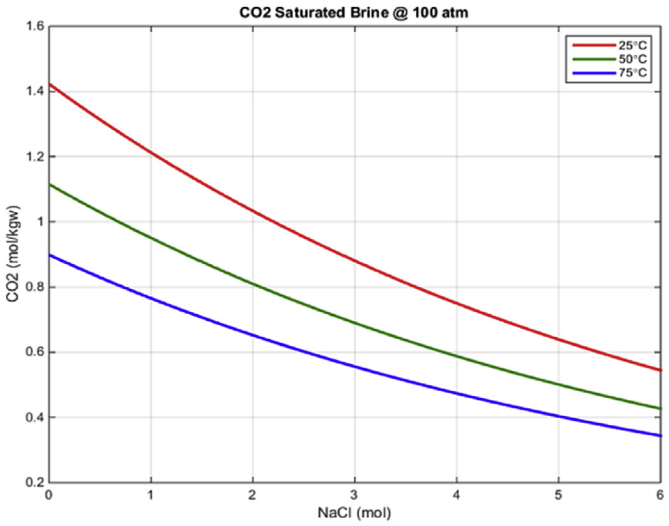

Fig. 3. Solubility of CO_2 at 10.1 MPa as a function of salinity, calculated by PHREEQC.

Table 5
Equilibrium mineral fractions from PHREEQC simulations.

Mineral	Initial size fraction	Final size fraction	Delta	Initial size fraction	Final size fraction	Delta
Simulation 1				Simulation 4		
Anhydrite	1.10%	1.09%	−0.01 p.p.	25.99%	25.99%	<0.01 p.p.
Calcite	3.80%	3.68%	−0.12 p.p.	0%	0%	0 p.p.
Dolomite	0.99%	1.10%	0.11 p.p.	1.30%	1.30%	<0.01 p.p.
Halite	2.40%	1.86%	−0.54 p.p.	1.89%	1.08%	−0.81 p.p.
Quartz	63.50%	63.50%	<0.01 p.p.	62.70%	62.70%	<0.01 p.p.
Simulation 2				Simulation 5		
Anhydrite	0%	0%	0 p.p.	43.19%	43.19%	<0.01 p.p.
Calcite	0%	0%	0 p.p.	0%	0%	0 p.p.
Dolomite	6.79%	6.79%	<0.01 p.p.	14.80%	14.80%	<0.01 p.p.
Halite	2.59%	1.80%	−0.79 p.p.	0%	0%	0 p.p.
Quartz	63.50%	63.50%	<0.01 p.p	11.50%	11.50%	<0.01 p.p.
Simulation 3				Simulation 6		
Anhydrite	8.69%	8.69%	<0.01 p.p.	70.09%	70.09%	<0.01 p.p.
Calcite	62.80%	62.63%	−0.17 p.p.	0%	0%	0%
Dolomite	4.20%	4.35%	0.15 p.p.	0%	0%	0%
Halite	0%	0%	0 p.p.	27.99%	27.50%	−0.49 p.p.
Quartz	15.30%	15.30%	<0.01 p.p	0.50%	0.50%	<0.01 p.p.

Table 6
Ca/Mg mass ratio in formation water for our simulations and observations from different oilfield reservoirs.

	T (°C)	P (MPa)	Ca (mg/L)	Mg (mg/L)	Ca/Mg	K (mg/L)	App SR	App SI	Mineralogy
Middle Eastern	37	2.3	1279	484	2.6	3.2	0.8	−0.1	Dolomite
C1	57	14.0	10640	4157	2.5	1.5	1.7	0.2	Sand. + Dolomite
L2	57	14.0	11345	3929	2.9	1.5	1.9	0.3	Sand. + Dolomite
C2	57	14.0	12322	4114	3.0	1.5	2.0	0.3	Sand. + Dolomite
C3	57	14.0	12279	4112	3.0	1.5	2.0	0.3	Halite
L3	57	14.0	13861	2239	6.2	1.5	4.1	0.6	Sand. + Limestone
L1	57	14.0	14047	2075	6.8	1.5	4.5	0.7	Sand. + Limestone
Brazilian Pre-salt	60	50.0	22000	4500	4.9	0.09	54.4	1.7	Chalk
Ekofisk	131	48.4	22000	1700	12.9	0.02	645.0	2.8	Chalk
Gyda	160	60.0	30185	2325	12.9	0.002	5863.6	3.8	Sand. + Calcite stringers

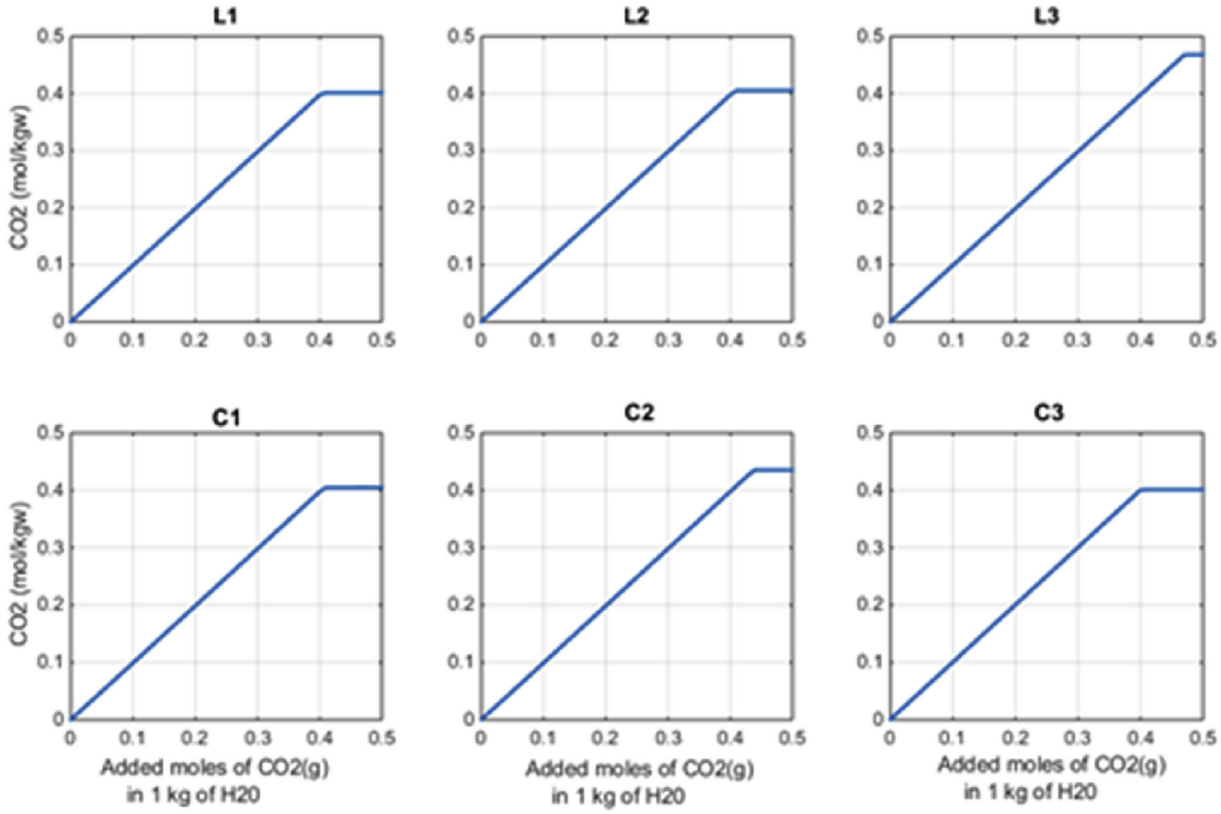

Fig. 4. Solubility of CO_2 for six scenarios. Maximum saturation can be identified in each case as solubility at which plot becomes horizontal.

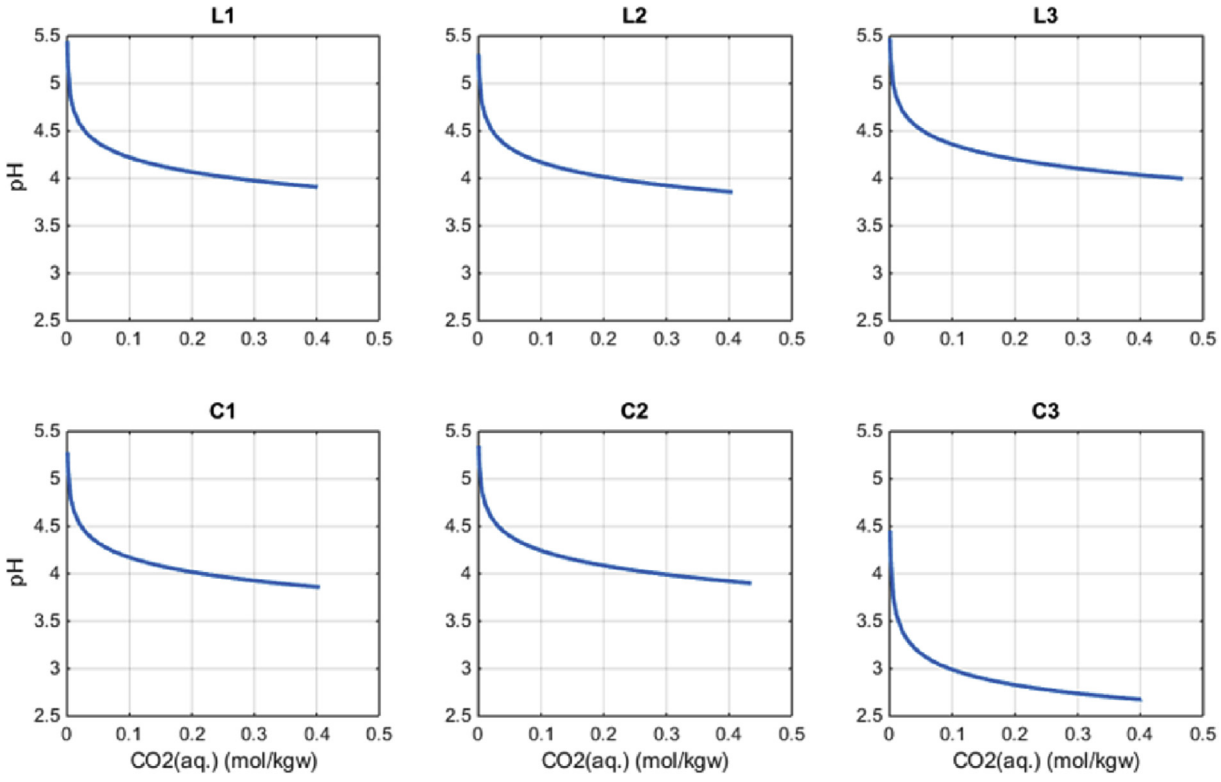

Fig. 5. pH vs CO_2 concentration for six scenarios. Water becomes more acidic in C3 because of the absence of carbonate minerals.

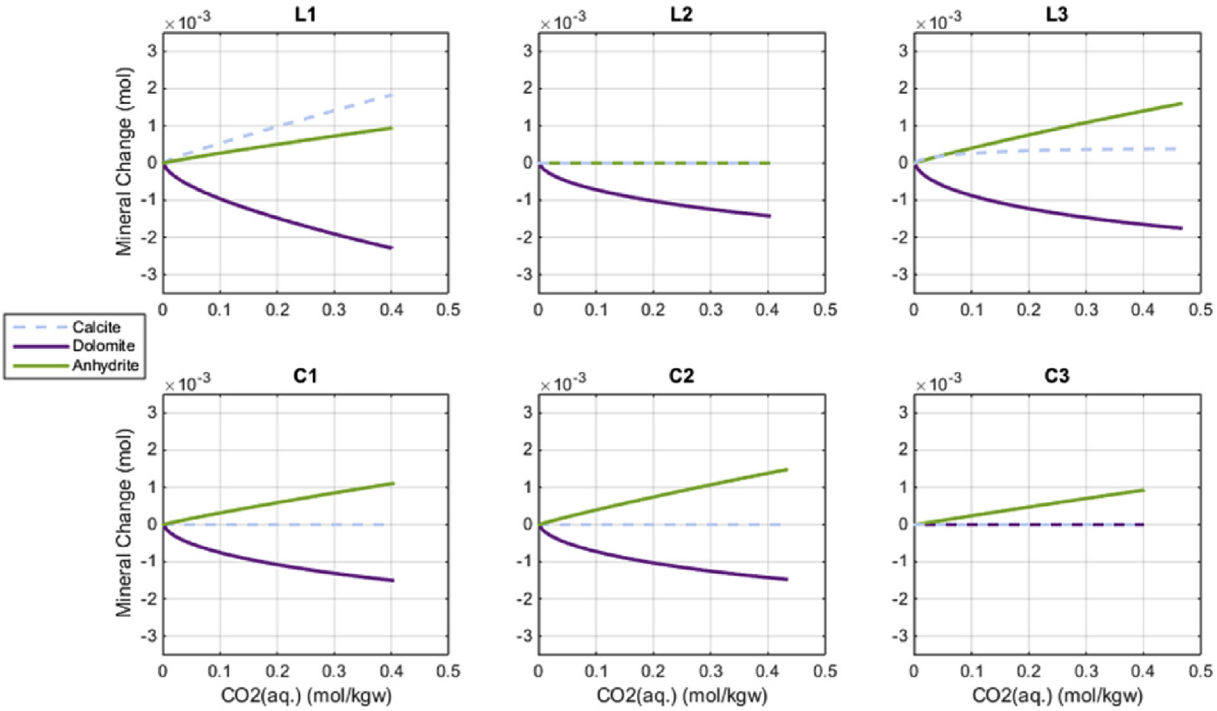

Fig. 6. Mineral changes resulting from increase in CO_2 concentration for six scenarios, for calcium bearing minerals.

3.1. CO_2 storage capacity

Having established the initial equilibrium conditions, the next step was to identify the impact of injection of CO_2 in a highly saline brine. This process was broken down into various steps. The first of these steps was to identify the solubility of CO_2 in brine for each of the 6 scenarios. To do this, PHREEQC was used to calculate the solubility of CO_2 in brine at various salinities and temperatures, as shown in Fig. 3. PHREEQC uses the Peng-Robinson Equation-of-State (EoS) with corrections for high pressure and high salinity to determine the solubility of gases (Appelo et al., 2014; Appelo, 2015).

The solubility of CO_2 in brine decreases with increasing salinity and with increasing temperature. When 5 mol NaCl is added into 1 LL of pure water @ 50 °C and 10.1 MPa, the maximum

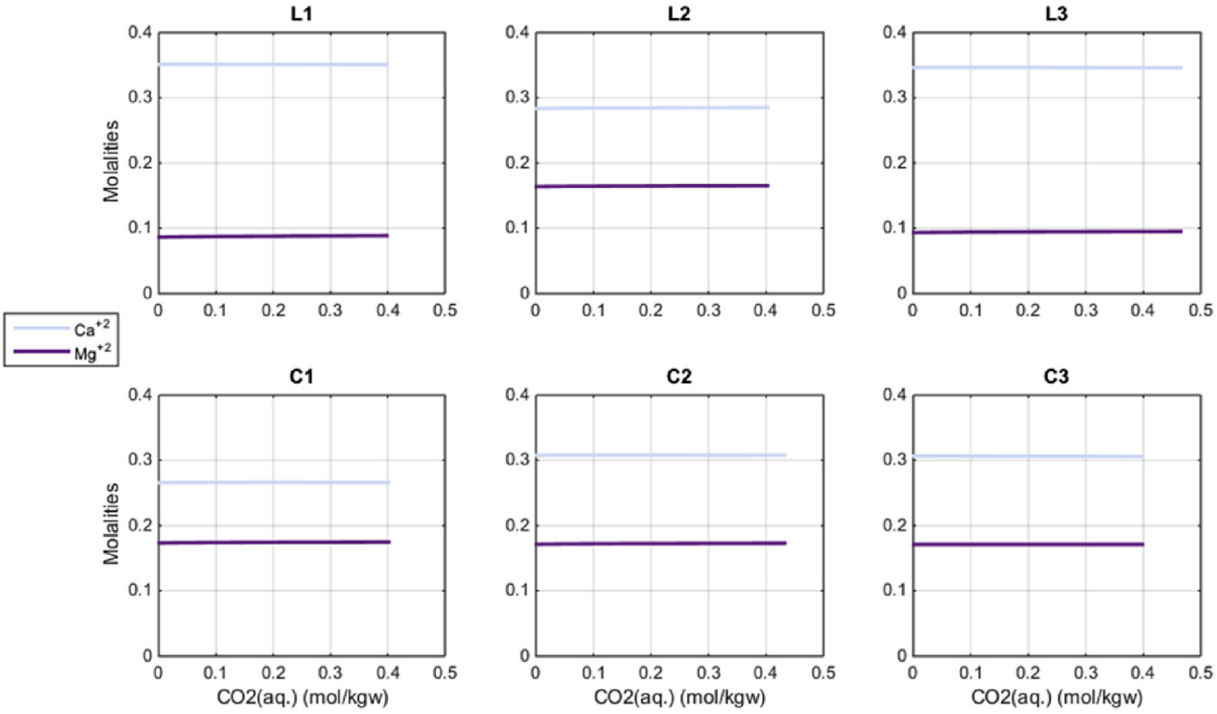

Fig. 7. Molalities of Ca and Mg vs CO_2 concentration for six scenarios.

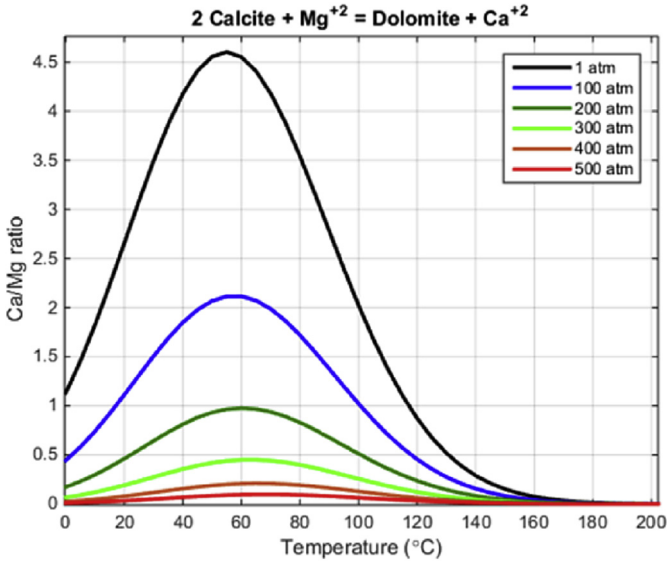

Fig. 8. Equilibrium Ca/Mg mass ratio (assuming equal activity coefficients) for different pressures and varying temperatures.

concentration of dissolved CO_2 decreases from 1.116 to 0.502 mol/kgw. Therefore, for solutions with more NaCl and other dissolved species the CO_2 solubility is lower than the above value. The temperature effect is not considered further here, but it is worth bearing in mind, since CO_2 will be injected cooler and will then warm up to formation temperature once injected.

The solubility of CO_2 for each of the six scenarios was then calculated, as shown in Fig. 4.

The CO_2 solubility for the analysed system is between 0.4 and 0.5 mol/kgw for all intervals (around 15000 ppm). The higher saturations in C2, and especially in L3, were achieved because the ion concentrations are significantly lower.

The injection of CO_2 creates carbonic acid, and an important indicator is the resulting pH of the brine. As shown in Fig. 5, pH decreases for increasing amounts of CO_2 (dissociation of carbonic acid). Lower pH values are reached in C3 because there are no carbonate minerals present to buffer the brine.

3.2. Mineral reactions

Increased concentrations of CO_2 in water trigger dissolution of carbonate minerals. However, we observed (see Fig. 6) that dolomite was the preferred mineral to dissolve and forced calcite to precipitate in intervals where both minerals were initially present (L1 and L3). Because reactions were coupled in these areas, dolomite dissolution was slightly greater when compared to regions where calcite did not precipitate. Moreover, no net mineralisation of CO_2 is predicted to happen in the reservoir since calcite precipitation was null or lower than dolomite dissolution. In addition, in most simulations anhydrite precipitates, even when carbonate minerals are not present (C3). This precipitation is linked to a continuous increase in overall activity coefficients during CO_2 dissolution in water, which will be explained below.

The competition between calcite and dolomite for dissolution is related to the Ca/Mg ratio in formation waters (see Fig. 7) and it can be understood by equilibrating water with both minerals (Parkhurst and Appelo, 2013).

$$2 \cdot CaCO_{3(s)} + Mg^{+2} = CaMg(CO_3)_{2(s)} + Ca^{+2}$$

If this reaction is in equilibrium, the following relation holds:

$$K_{dolomte} - (K_{calcite})^2 = \frac{[Ca^{+2}]}{[Mg^{+2}]} = \frac{\gamma_{Ca^{+2}}}{\gamma_{Mg^{+2}}} \cdot \frac{m_{Ca^{+2}}}{m_{Mg^{+2}}}$$

In Fig. 8, we plotted the apparent (ideal) Ca/Mg mass ratio, i.e. neglecting activity coefficients, for varying temperature and different pressure values. Values above a specific curve indicate the tendency for coupled dolomite dissolution and calcite precipitation.

Moreover, when observed Ca/Mg ratio is much higher than the equilibrium value, for a given temperature and pressure, means that all dolomite had been previously dissolved and only calcite is left to react. This scenario is observed for different oilfield reservoirs with known water compositions (see Table 7). In addition, with regard to the simulations performed here, calcite precipitation was observed when the apparent SI was high enough.

Table 7
Input data for simulation models.

Property	Unit	Value
Grid type		2D Radial model
Grid dimension (I × J × K)		699 × 1 × 48
datum	m	1300
Pressure	kPa	14120
Pressure gradient	MPa/m	0.0115
Temperature	C	57.2
Temperature gradient	Degree C/m	0.0316
Pore compressibility	1/kPa	5.0×10^{-7}
Porosity (o/u burden)	fraction	0.1
Porosity (BSS)	fraction	0.22
Permeability (o/u' burden)	mD	0.0001
Permeability (BSS)	mD	500
Deepest inj. point	m	1459.0
Top perforation	m	1292.0
Pressure change	MPa	1.1 @2019m

Increase in HCO_3 is a consequence of CO_2 dissolution in water. However, in this case most of the HCO_3 is produced by dolomite dissolution, while only a relatively small amount comes from the dissociation of carbonic acid. One can see this by comparing the HCO_3 maximum concentration between C3 (where there are no carbonate minerals) and all the other scenarios (see Fig. 9). On the other hand, SO_4 decreases when anhydrite precipitates.

Furthermore, CO_2 dissolution in water also changes the activity coefficients of species related to mineral reactions. Although the activities of cations generally increase and the activities of anions decrease (see Fig. 10), the net change is non-zero and therefore the impact of activity on mineral precipitation can be determined by multiplying the coefficients.

One can see in Fig. 11 that activity coefficients associated with undersaturated minerals change more than the others. The actual dependency is defined by the Pitzer parameters. On the other hand, for reacting minerals, changes in molalities act as constraints on the increase in activity coefficients. In this sense, anhydrite activity shows a steeper increase in L2 because the mineral is not initially present, while for other scenarios the activity increase triggers mineral precipitation which lowers SO_4 molalities and controls the growth of the activity.

Na and Cl, shown in Fig. 12, are the dominant species and their concentrations set the maximum CO_2 solubility. For areas where halite is initially present, the concentration of these ions decreases

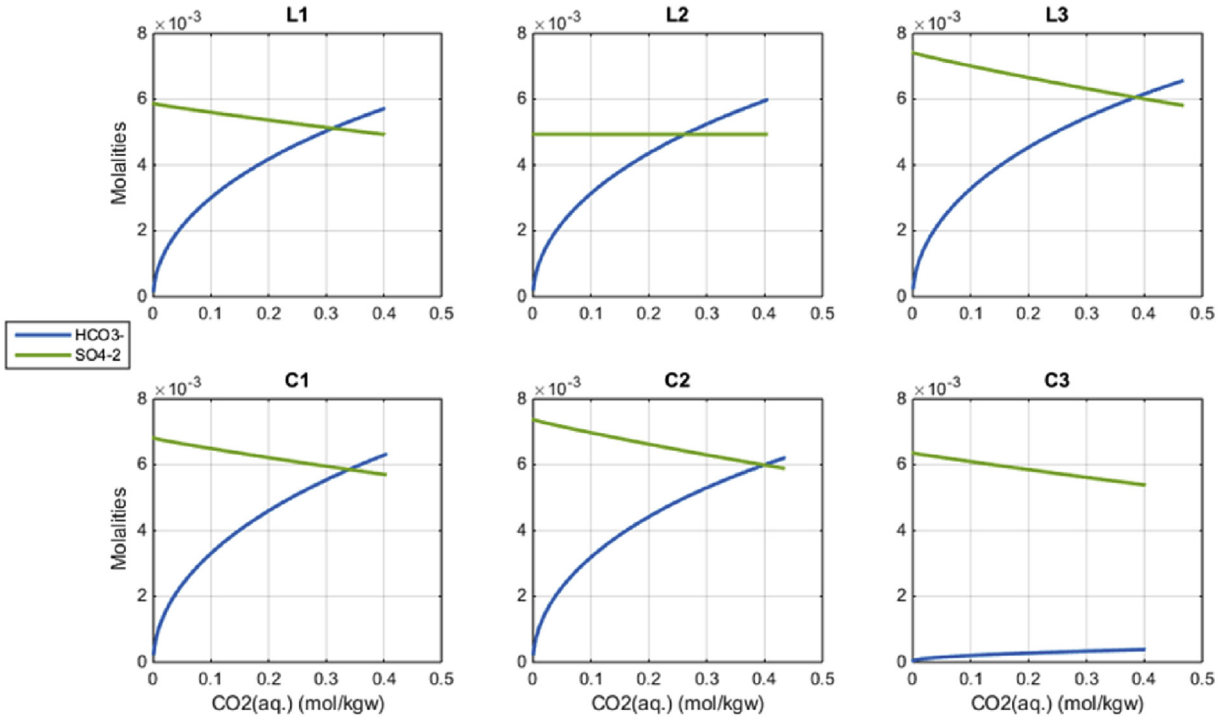

Fig. 9. Molalities of HCO_3 and SO_4 vs CO_2 concentration for six scenarios.

because CO_2 dissolution in water triggers halite precipitation by the same mechanism of anhydrite precipitation (see Fig. 13).

3.3. Rock integrity and porosity change

The most significant outcome of these calculations is that only dolomite dissolves in this system – where present – during CO_2 injection. All other minerals will precipitate. The key issue is whether or not dolomite contributes to the integrity of the rock, and if the dolomite is not present as a cement then the risk of formation damage from its dissolution is low.

Also of note is the fact that increasing CO_2 concentration will tend to increase the amount of halite precipitation due to evaporation. Moreover, halite precipitation dominates over the others in terms of moles of deposit and in volume change because all analysed minerals have molar volumes of the same order of magnitude. Therefore, if we assume pores completely filled by water, i.e. the porous volume is equivalent to the solution volume, we can estimate the relative changes in porosity ($\Delta\varnothing/\varnothing_o$) due to mineral reactions by dividing the halite volume changes by the PHREEQC solution volumes. As shown in Fig. 14, the volume change ratio ($\Delta V/V_{Solution}$) associated with halite is in the order of up to 3×10^{-3} (precipitation).

4. Coupled modelling of fluid flow and geochemical reactions

All simulations in this study were performed using GEM, a general three-dimensional compositional reservoir simulator, using Peng-Robinson EoS (CMG, 2015a).

4.1. Model geometry and properties

Because of computing time constraints due to the multi reactions and multi components in the fluid flow and geochemical coupling simulation, the problem was simplified to a 2D homogeneous model with a radial mesh geometry including 2 layers of cap rock, 45 layers of Sandstone, and one layer of underburden. Two regions were defined to represent cap rock (Halite and Clay) and Sandstone. The underburden has the same properties as the cap rock. The dimensions of the model are 4000 m in radius, 375 m in thickness with a dip angle of 2°. The top of the model is at a depth of 1200 m. A numerical aquifer is connected at the outer boundary of the model and the spill point is in the top layer at the outer boundary.

In the 2D model the mesh contains 699 cells in the radial direction and 48 layers in the vertical direction. In the tangential direction there is only one cell with an angle of 360° because of the homogeneous and axisymmetric features. The well radius is 0.1 m. The first cell that is connected with the wellbore is 0.1 m in size in the radial direction, and is followed by 642 cells with a constant radial increase of 5 mm. These are then followed by 57 cells with increments $\Delta Rn+1 = c1 \times \Delta Rn$ and $c1 = 1.03826$ until the total radius reaches 4000 mm.

The injector is in the centre of the model as shown in Fig. 15. The perforations go through the L2 and L3 zones (layers 22 to 47). Injection of CO_2 is simulated at 0.6 Mt/year for 15 years. A pre-injection run was carried out to establish the formation equilibrium.

Fig. 15 also illustrates the grid top contour on a cross section of the 2D model to show the location of the cap rock, dip angle and the depth of spill point. It can be seen from the figure that the spill point is at the outermost column of cells with the depth of about 1480 mm. Because a numerical aquifer is connected with the horizontal boundary of the model, CO_2 can migrate to the numerical aquifer with brine.

Viking 2 relative permeability curves (Bennion and Bachu, 2008) and capillary pressure curve were used in the generic model, in which Van Genuchten function (van Genuchten, 1980) was used for the calculation of liquid relative permeability and capillary pressure; Corey function (Corey, 1954) was used for gas relative

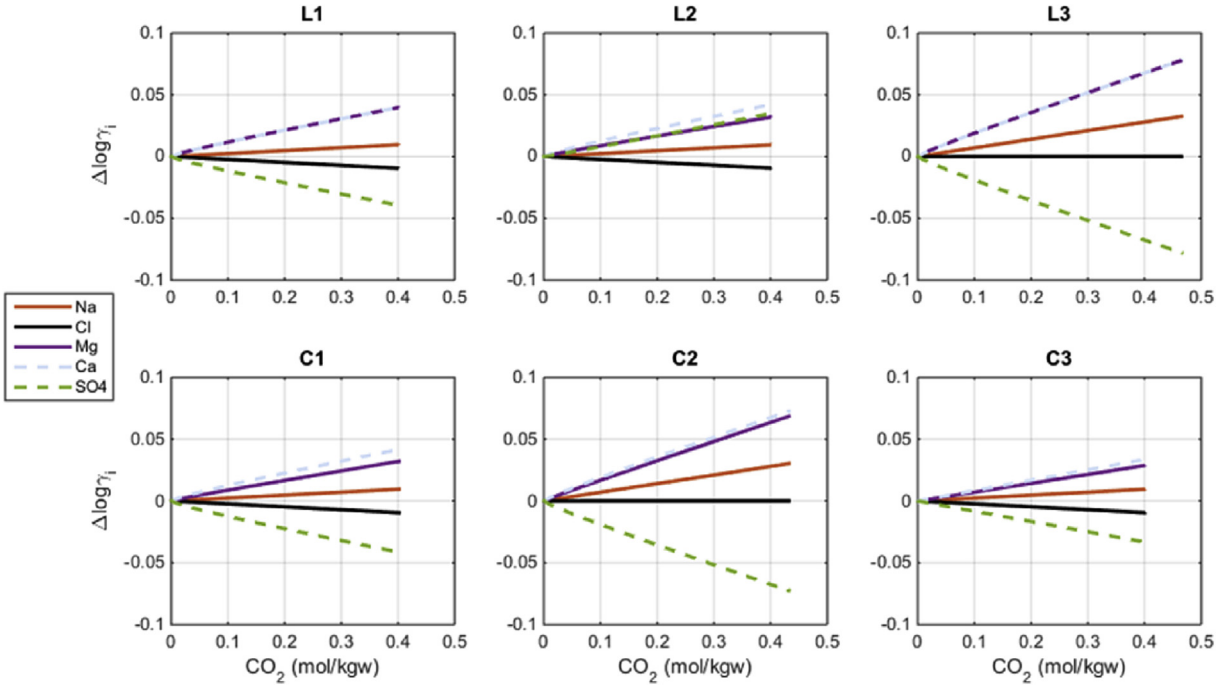

Fig. 10. Activity coefficients change for representative ions.

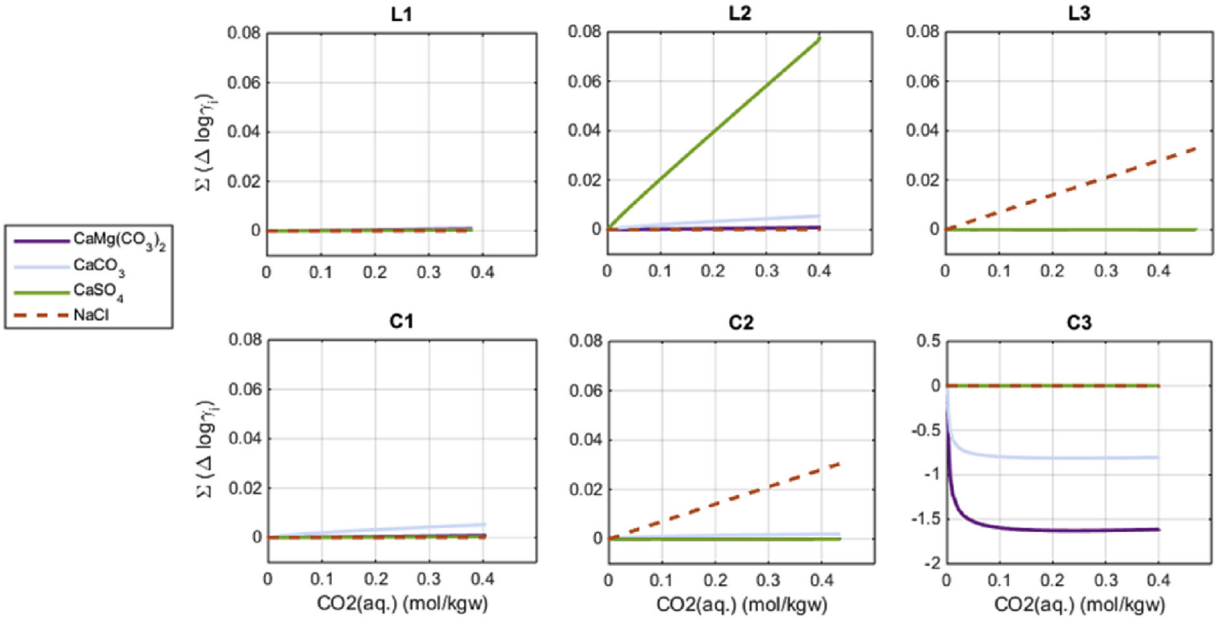

Fig. 11. Effective change in activity coefficients for each mineral. Large variations indicate undersaturated brines.

permeability. The sensitivity study of capillary pressure was performed with low, medium, and high entry pressure (up to 15 MPa) (see Table 7).

In the geochemical and fluid flow coupled simulation the irreducible brine saturation will play an important role in determining the mass of minerals that may dissolve. Therefore, a relative permeability function taken from the cores in the area of interest is very important. As no relative permeability functions were made available at the outset of this study, an assumed function was chosen based on the regional permeability and porosity. Brine properties are a function of brine composition, as discussed in Section 2.

4.2. Thermodynamic data and chemical reactions

The gaseous phase and the aqueous phase are assumed to be in thermodynamic equilibrium. GEM allows a choice of activity model for the aqueous phase: the ideal model, the Debye-Hückel model or the B-dot model. The accuracy of these models reduces for brines with salinities above 2 M, but since the more appropriate Pitzer model used in PHREEQC is not available in GEM, the B-dot model was used instead. However, this will introduce some errors relative

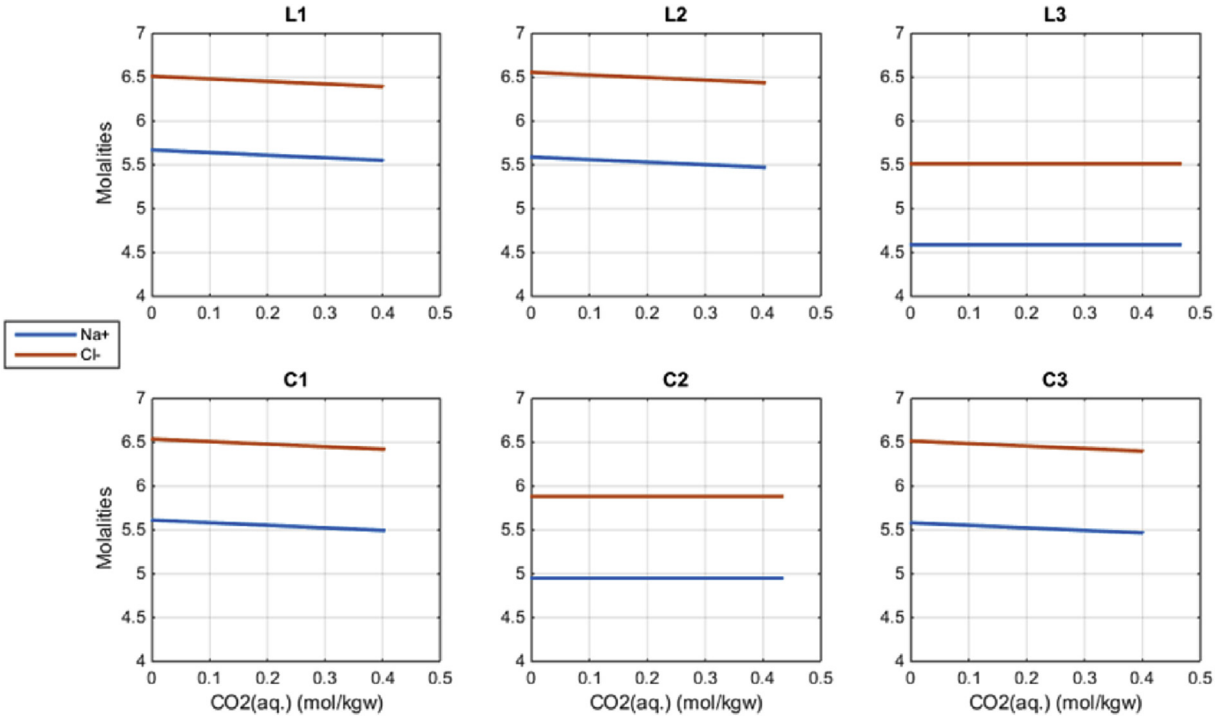

Fig. 12. Molalities of Na and Cl vs CO_2 concentration for six scenarios.

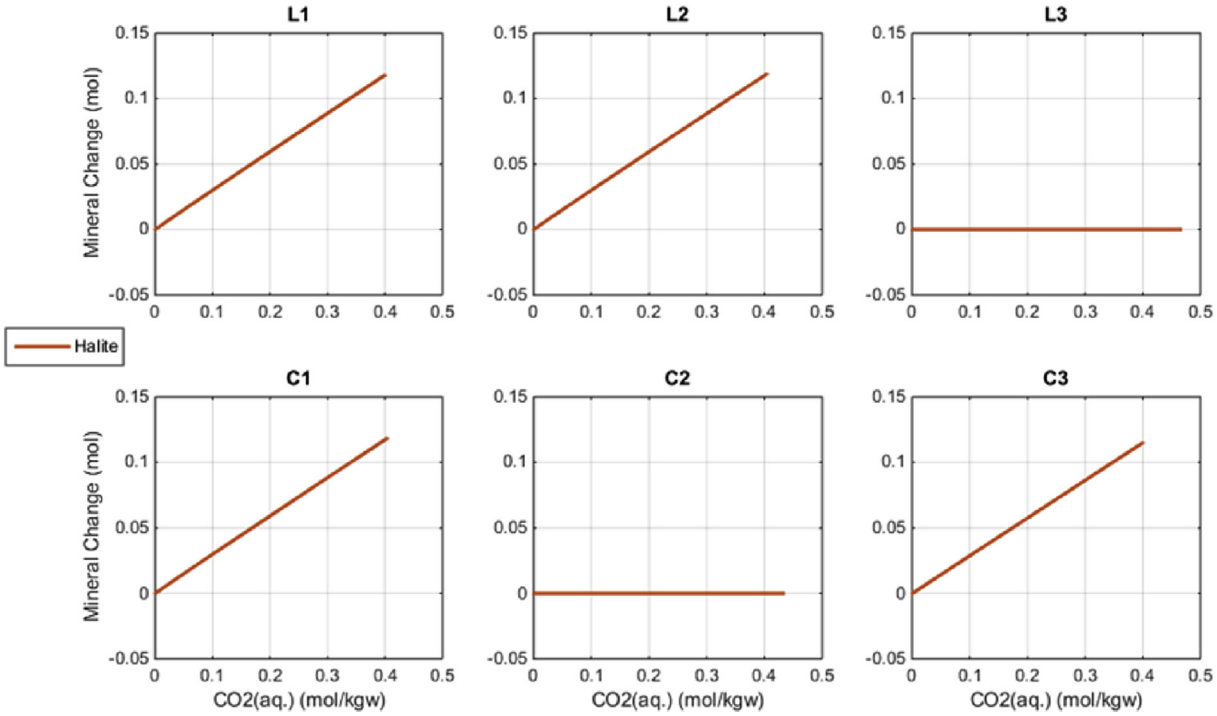

Fig. 13. Mineral changes resulting from increase in CO_2 concentration for six scenarios, for halite.

to the PHREEQC calculations. To check the compatibility between the two different models, we have performed thermodynamic simulations (with no transport) using GEM with B-dot for the data related to Section L1. Fig. 16 shows the mineral changes for different CO_2 concentrations. One can compare these results with the PHREEQC simulations and see some differences. First, calcite (for high CO_2 concentrations) and anhydrite (entire range) dissolve. Second, the mineral changes in moles calculated by GEM's B-dot are lower than the results from PHREEQC's Pitzer, with the largest difference being associated with halite (more than one order of magnitude). On the other hand, both codes reproduce the precipitation of halite as the dominant mineral reaction. Nevertheless,

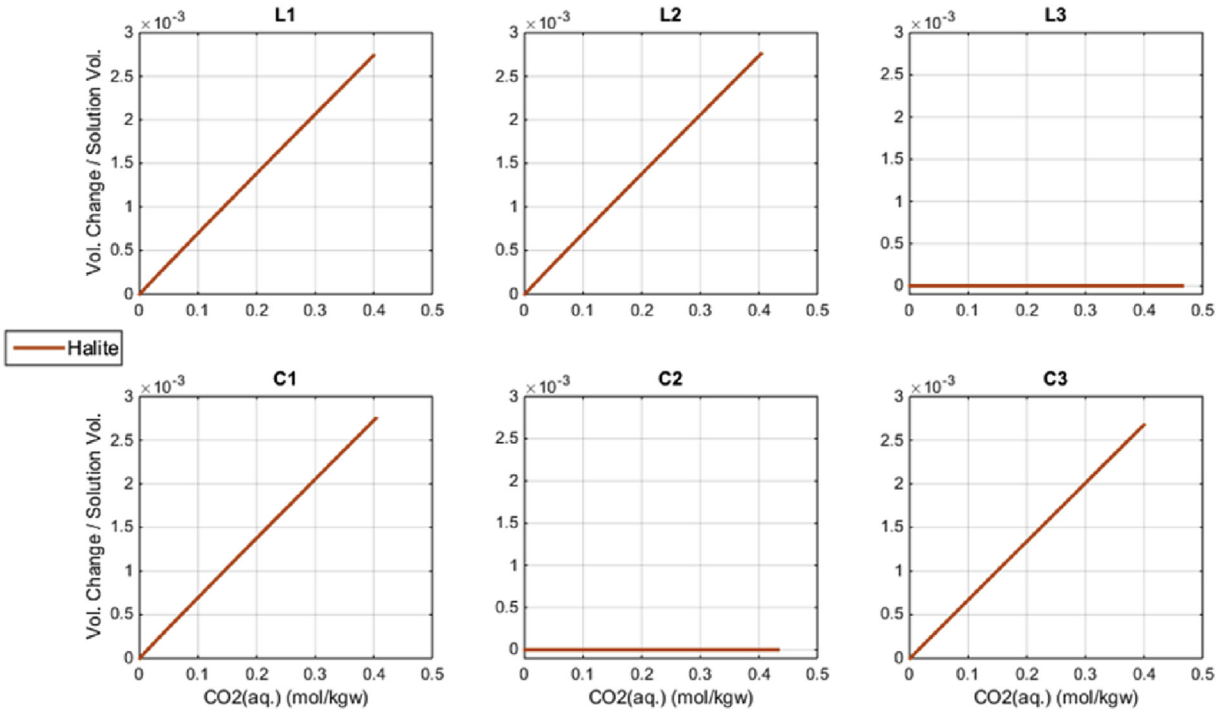

Fig. 14. Volume changes resulting from increase in CO_2 concentration for six scenarios, for halite. Curves are estimates of relative porosity change.

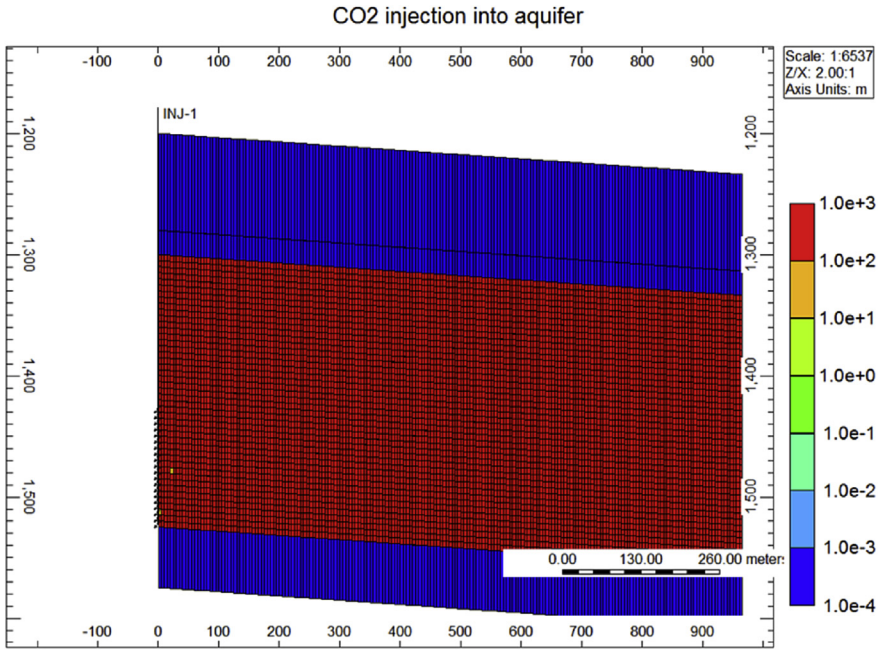

Fig. 15. The model gridding with permeability contour to show the location of cap rock, formation depth and dip angle, and the well perforation.

GEM has the capability of multiphase transport and additional precipitation occurs (because of evaporation) during gas injection, while PHREEQC is limited to unidimensional transport of water only. Moreover, it has been reported that TOUGHREACT, which uses the extended Debye-Huckel activity model (Xu et al., 2011), can produce results similar to PHREEQC and GEM if the same thermodynamic database is used in each of them (Gundogan, 2011). Thus we use GEM as it is at least as good as any other model in terms of ability to include the impact of both transport and evaporation for the halite deposition calculations, although it is recognised that the activity model used has limitations. However, since the initial concentrations of sodium and chloride are the same for both models, and in the GEM model which accounts for transport and evaporation, such differences are small in the near wellbore region since the majority of the deposited mass is due to the evaporation of the brine, not due to the change in solubility of halite.

Henry's law is used to calculate the fugacity of gaseous

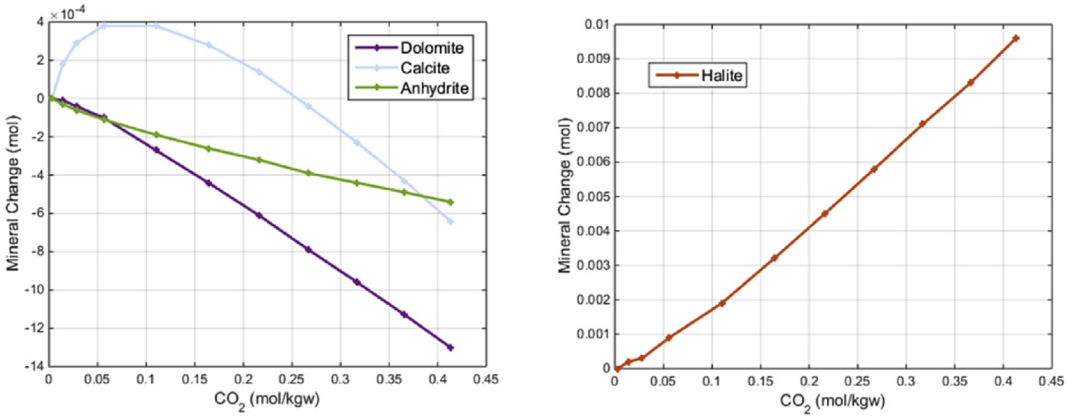

Fig. 16. Mineral changes (in moles) for section L1 calculated by GEM using B-dot activity model. Static simulations were performed with a reservoir model with 1 L of porous volume saturated with water and different amounts of dissolved CO_2.

components soluble in the aqueous phase. The Henry's constants are functions of pressure, temperature and salinity. The salting-out process includes the phenomenon where the solubility of CO_2 decreases with the increasing salinity. To model H_2O vaporization, which may form a dry zone near the injector and cause a decrease of CO_2 injectivity, a thermodynamic equilibrium of H_2O is applied.

At the same time, chemical reactions take place between minerals and aqueous components (identified as heterogeneous reactions) and among components in the aqueous phase (homogeneous reactions), including gaseous components such as CO_2 that are soluble in the aqueous phase as well as components that exist only in the aqueous phase. Normally intra-aqueous reactions are represented as chemical-equilibrium reactions as they are fast relative to mineral dissolution/precipitation reactions that are represented as rate-dependent reactions. In the following we list the relevant equations that are implemented in GEM.

The rate law for the mineral dissolution and precipitation reaction is (Bethke, 1996):

$$r_\beta = \widehat{A}_\beta k_\beta \left(1 - \frac{Q_\beta}{K_{eq,\beta}}\right) \qquad (4-1)$$

where r_β is the rate, $\widehat{A}_\beta$ is the reactive surface area for mineral β, k_β is the rate constant of mineral reaction β, $K_{eq,\beta}$ is the chemical equilibrium constant for mineral reaction β and Q_β is the activity product of mineral reaction β.

The reactive surface area $\widehat{A}_\beta$ is another important parameter in the calculation of the rate. Eq (4–2) is used to calculate the reactive surface area with change in the moles of minerals through dissolution or precipitation:

$$\widehat{A}_\beta = \widehat{A}^0_\beta \frac{N_\beta}{N^0_\beta} \qquad (4-2)$$

where $\widehat{A}^0_\beta$ is the reactive surface area at time T_0, N_β is the mole number of mineral β per unit grid block volume at current time and N^0_β is the mole number of mineral β per unit grid block bulk volume at time T_0.

The ratio $(Q_\beta/K_{eq,\beta})$ in Equation (4–1) is called the saturation index of the reaction. If $(Q\beta/K_{eq,\beta}) > 1$, mineral dissolution occurs; otherwise, mineral precipitation occurs.

Three aqueous reactions and seven mineral reactions are selected, based on the PHREEQC modelling in Section 3, and reactions reported in the literature for minor minerals. Table 8 shows the reactions and kinetic rate parameters used in the modelling with references. The initial aqueous-component concentrations and mineral volume fractions are listed in Table 9. As noted above, the choice of activity model for the aqueous phase is not suitable for very high salinity brines, and the brine composition used here has lower overall salinity than that used in the batch modelling above (Section 3).

There are two key cut off values to control the chemical reactions in the simulation. The minimum aqueous phase saturation, under which all geochemical reactions, including mineral precipitation/dissolution, will stop, was set to 1×10^{-4}. The residual aqueous phase saturation for H_2O vaporization, under which the vaporization ceases, was set to 1×10^{-2}. As the precipitation and dissolution of halite is very rapid, it is often treated by means of a local equilibrium process (Alkan et al., 2010) or by a reaction, but setting the reaction rate to a high value (Noh et al., 2004).

4.3. Porosity-permeability relationship in dynamic simulation

Mineral dissolution and precipitation change the void volume of the porous medium. The porosity, φ, altered as a result of mineral precipitation or dissolution is updated in each timestep, and is calculated from the mineral volume fraction at the current time, as follows:

$$\widehat{\phi}^* = \phi^* - \sum_{\beta=1}^{n_m} \left(\frac{N_\beta}{\rho_\beta} - \frac{N^0_\beta}{\rho_\beta}\right) \qquad (4-3)$$

$$\varphi = \widehat{\phi}^* \left[1 + c_\varphi (p - p^*)\right] \qquad (4-4)$$

where $\widehat{\phi}^*$ is the reference porosity including mineral precipitation/dissolution, ρ_β is the mineral molar density, ϕ^* is the reference porosity without mineral precipitation/dissolution, φ is the updated porosity, and c_φ is the rock compressibility, p^* is the reference pressure (CMG, 2015a).

By using an experimental relationship or analytical models between porosity and permeability, a permeability change induced by mineral dissolution or precipitation can be calculated. There are several published porosity-permeability relationships, such as the commonly used and the simplest power law model, the classical Kozeny-Carman model (Carman, 1956), Verma and Pruess's 'tubes-in-series' model (Verma and Pruess, 1988), and the extended Verma-Pruess model (V-P) (Xu and Pruess, 2004). Only the first two relations are currently included in GEM.

The Kozeny-Carman (K-C) equation is used in the study as

Table 8
Reactions modelled. The first three are aqueous reactions and assumed to be equilibrium. The others are mineral reactions and require kinetic parameters to be specified. (The Na and Cl concentrations will mean that halite precipitation will dominate all other reactions).

Reaction	Source for values of kinetic parameters
$CO_2(aq)+H_2O = H^+ + HCO3^-$	
$CO_3^{--} + H^+ = HCO3^-$	
$OH^- + H^+ = 2H_2O$	
Anhydrite $= Ca^{++} + SO_4^{--}$	(Audigane et al., 2005)
Calcite $+ H^+ = Ca^{++} + HCO_3^-$	(Noh et al., 2004)
Dolomite $+ 2\ H^+ = Ca^{++} + Mg^{++} + 2\ HCO_3^-$	(Pokrovsky and Schott, 2001)
Halite $= Na^+ + Cl^-$	(Alkattan et al., 1997)
Illite $+ 8H^+ = 5\ H_2O + 0.6K^+ + 0.25\ Mg^{++} + 2.3\ Al^{++} + 3.5SiO_2(aq)$	Set to muscovite rate (Nagy, 1995)
K-feldspa $+ 4H^+ = 2\ H_2O + 0.6K^+ + Al^{++} + 3SiO_2(aq)$	(Nagy, 1995)
Quartz $= SiO_2(aq)$	(Rimstidt and Barnes, 1980)

follows:

$$ResistanteFactor(rf) = \frac{k}{k_0} = \left(\frac{\varphi}{\varphi_0}\right)^3 \left(\frac{1-\varphi^0}{1-\varphi}\right)^2 \quad (4-5)$$

where k_0 and φ_0 are the initial permeability and porosity, respectively, and the K-C constant is assumed to be independent of porosity.

The extended V-P model is as follows:

$$\frac{k}{k_0} = \left(\frac{\varphi-\varphi_c}{\varphi_o-\varphi_c}\right)^n \quad (4-6)$$

where ϕ_c is the value of a "critical" porosity at which permeability tends to zero, and n is a power law exponent.

Comparing with the K-C equation, which resulted in a modest decrease in permeability, the V-P model was found more sensitive and more consistent with the observed significant loss of injectivity from field data and lab experiments (Peysson et al., 2011; Xu et al., 2004).

(Graham, 1973) found the permeability to be proportional to $(\phi-\phi_c)^n$, and n = 1.8 for sintered metallic powders (Vaughan et al., 1985). indicated that a mere 8% reduction in original porosity resulted in 96% reduction in permeability of a granite rock core from geothermal laboratory experiments. (Wyble, 1958) conducted an experimental study on the effects of confining pressure on porosity and permeability for three different types of sandstones. Their results can be restated by factoring out pressure, to provide a relationship that is very similar to the V-P model. There are also several types of porosity-permeability models developed from stress-sensitivity studies (Jin, 1999).

The complexity of the problem is due to the variety of geometric properties, such as the size distribution, pore shapes, and connectivity, among the reservoir formations, and the variety of mechanisms that cause porosity changes, such as mechanical deformation which may primarily affect the wider portion of pores, and mineral precipitation or dissolution which may affect the pore throats (Verma and Pruess, 1988). The simple cubic K-C model is based on the assumption of a 'uniform channel'. The 'bottle-neck' effect, that a major permeability reduction occurs due to only a minor reduction in porosity, cannot be accounted for by using the K-C model. Therefore, this model gives the upper bound on permeability reduction. By contrast, as it is unknown where the halite will deposit - in pore bodies and/or pore throats - and whether once precipitated it will be static, mobile, or mobile until hydrodynamically trapped, the extended V-P model represents the lower bound of permeability reduction.

Considering the very high salinity in the system, and the need to identify the risk of formation damage that may be caused by salt precipitation near the wellbore based on field data in similar situations, the permeability reduction was also calculated by using the V-P model for comparison, although it should be recognised that this represents an extreme end member, and in fact any detailed assessment would require appropriate and specific experimental data. The permeability reduction calculations performed in the study in the absence of appropriate and specific experimental data should provide an envelope of possible outcomes.

Because the V-P model is not included in the simulator, a staggered coupling has to be used, i.e. the current permeability, k_n, has to be calculated outside of the program, then the updated value, k_{n+1}, is inputted into the model for the next timestep. The timesteps are 10, 20, 30, 50, 80, 110 days in this study. Thereafter, the property was updated every 1000 days. Critical porosity $\phi_c = 0.90^*\phi_o$ and n = 8 in Eq. (4–6) were used in this staggered simulation. The permeability-porosity relationship is shown in Fig. 17.

Table 9
Initial input data for aqueous components and mineral components for cap rock and reservoir.

Aqueous component	Concentration for cap rock (molality)	Concentration for reservoir (molality)	Mineral component	Concentration for cap rock (volume fraction)	Concentration for reservoir (volume fraction)
H	1.00E-07	1.00E-07	Albite	0.03	0.088
Na	3.6882	3.7196	Anhydrite	0.176	0.019
Al	1.00E-07	1.00E-07	Calcite	0.0	0.021
$SiO_2(aq)$	1.00E-07	1.00E-07	Dolomite	0.202	0.027
Ca	0.2278	0.2210	Halite	0.008	0.037
SO_4	1.00E-07	1.00E-07	Illite	0.319	0.078
Mg	0.1277	0.1046	K-feldspar	0.022	0.053
Cl	4.3834	4.3479	Quartz	0.212	0.657
K	0.0339	0.0358			
HCO_3	1.00E-07	2.00E-04	Total	0.969	0.980
CO_3	1.00E-07	1.00E-07			
OH	1.00E-07	1.00E-07			

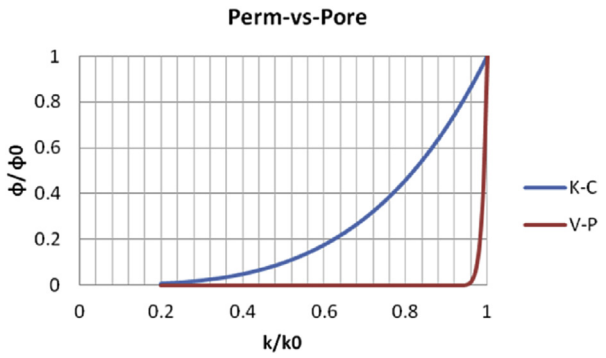

Fig. 17. Comparison of K-C model with V-P model at $\phi_c = 0.90\phi_o$ when k = 0, and n = 8.

4.4. Discussion of the results from 2D base case model with K-C permeability-porosity model

In this section the results from the base-case model are presented. The output parameters for analysis include porosity change, concentration of halite vs. radial distance and well bottom hole pressure (WBHP) against time. The injector is controlled firstly by CO_2 injection rate, then by WBHP, i.e. if the pressure exceeds the maximum allowed pressure (30 MPa in the study), the injection rate will be reduced. Therefore, the impact of loss of injectivity will be reflected in the pressure change or reduction in flow rate.

Fig. 18 shows the porosity change due to mineral reactions. As discussed in the previous section, the main porosity change induced by CO_2 injection is from halite precipitation because the concentrations of Na and Cl are so high relative to the other components that halite is the dominant mineral that precipitates during evaporation, and in addition the rates of the other reactions are relatively low.

As shown in Fig. 18 a low porosity zone was formed gradually at the edge of CO_2 plume. The pronounced vertical solid saturation trend and the emergence of a localized region with very large salt precipitation near the lower portion of the dry-out front was found from a previous study by (Pruess and Müller, 2009) using TOUGH2 simulation, and was noticed by Giorgis et al. (2007). It is caused by a backflow of brine toward to injector under the capillary force, which provides a continuous supply of salt that increases the local salinity and the precipitable solid (Pruess, 2009). Gravity override effects accelerate the accumulation of solids. The edge of the dry-out zone does not move outward due to the buoyancy force acting on the CO_2. A sensitivity study of injection rate was performed and the results are discussed in the next section. As the injection rate in the base case is already very high (0.6 Mt/y), a much higher injection rate ($\times$10, for example) may not be realistic for the one well in the study. Therefore, a lower injection rate is chosen to provide a comparison with the base case.

The permeability reduction due to halite precipitation at different time steps is shown in Fig. 19. The permeability at the advancing front at 5000 days reduces to about 1/3 to 1/2 of its initial value based on the K-C model. It is also noticeable that a low permeability region is also developed along the top perforations.

Besides the precipitation in the saline aquifer, Fig. 20 shows the distribution of precipitated halite in the cap rock at 2000 days (left)

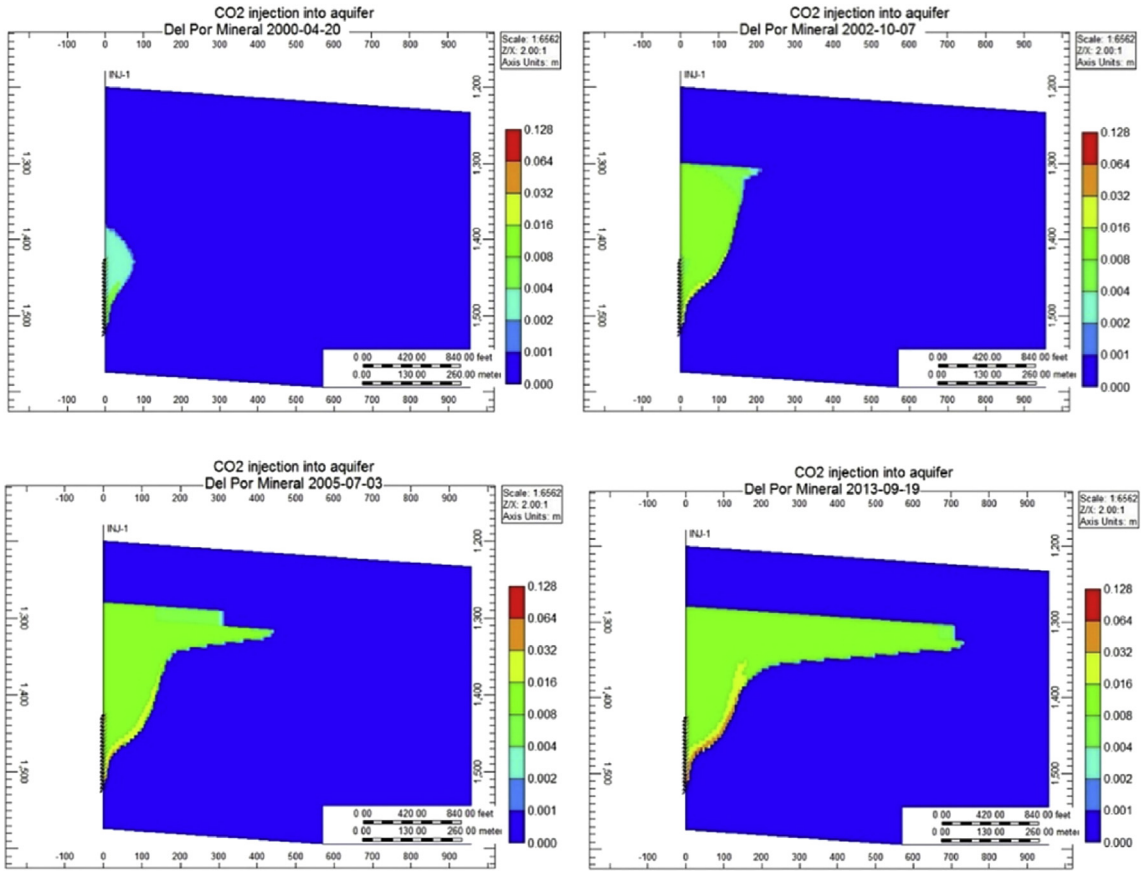

Fig. 18. Porosity change due to CO_2 injection and salt precipitation at time step = 10, 100, 1000, and 5000 days in the 2D model. The barrier was formed gradually as shown in the figure, and may block the perforations and force a change in the migration path during the rest of the injection period.

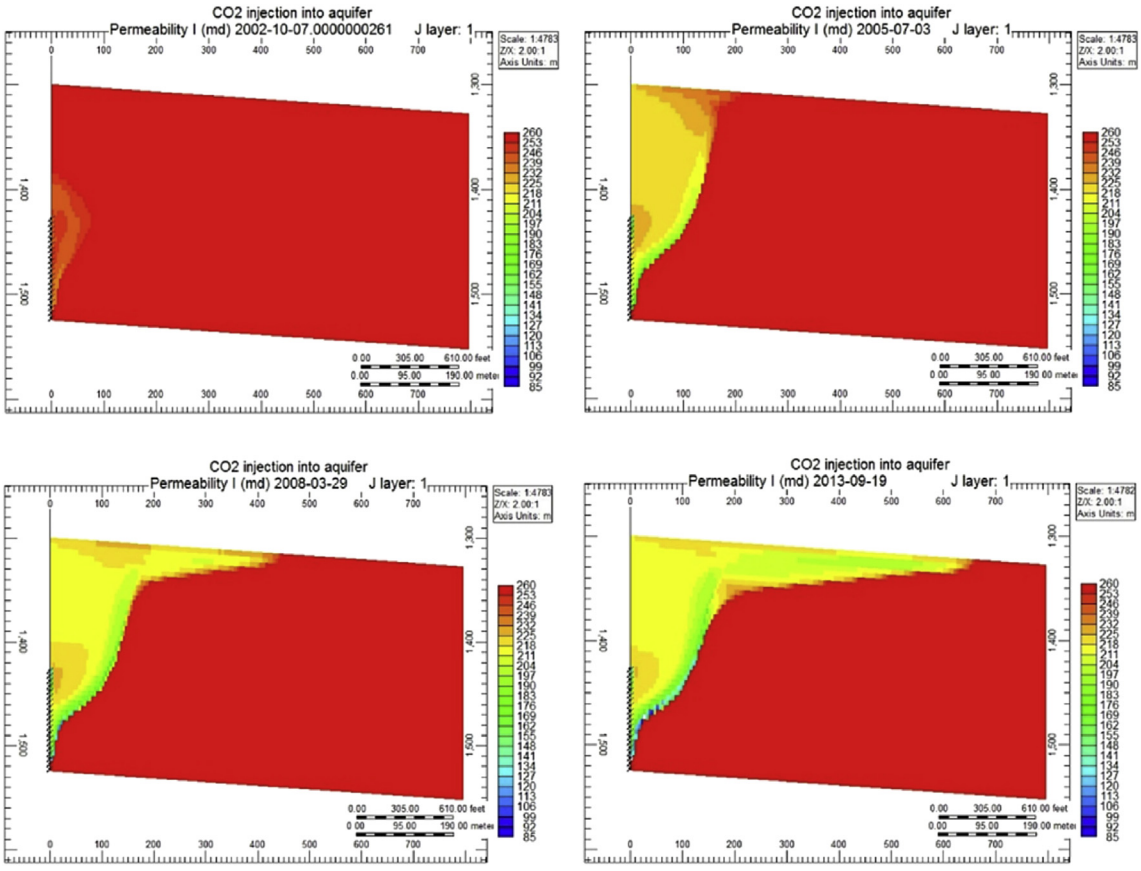

Fig. 19. Permeability reduction due to halite precipitation at different time steps. The permeability in the front at 5000 days reduces to about 1/3–1/2 of its initial value. It is also noticeable that the low permeability region is also developed along the perforation at the top of the injection layer.

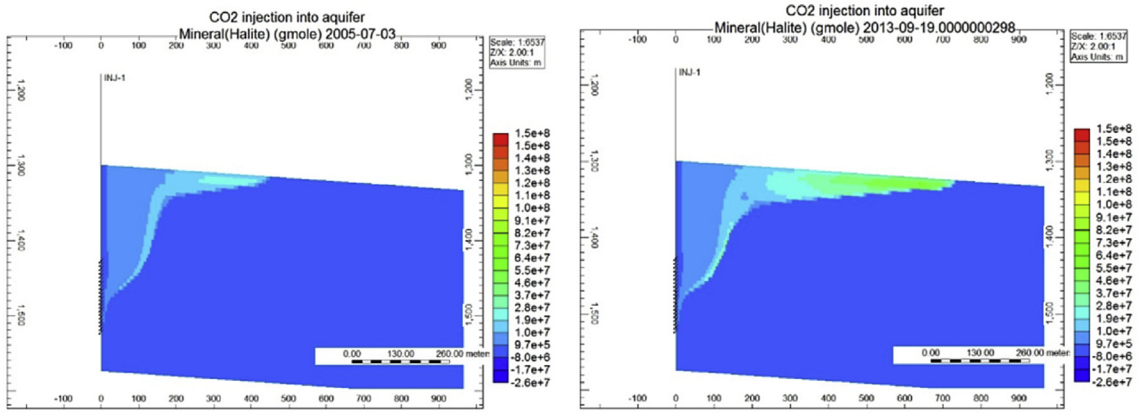

Fig. 20. The distribution of precipitated halite at 2000 days (left) and 5000 days (right) show that the CO_2 flowing into the cap rock (2000 days after injection in the simulation) may reduce the porosity further, and therefore reduce the permeability of the cap rock. (These results are derived using the model with capillary pressure.)

and 5000 days (right). This may reduce the porosity, and therefore, the permeability in the cap rock, which may improve the sealing capacity of the caprock. The results are from the model with low capillary pressure.

4.5. Discussion of the results from 2D models with V-P permeability-porosity model

It is worth re-emphasizing that these results represent an extreme end member, with the values being obtained from literature matching silicate precipitation, not halite – and thus they illustrate what damage could be induced in a worst case scenario. A pre-CO_2 injection fresh water flush may be used as a treatment to prevent the damage in the near-well area. In a potential injection site, experimental data for the current system would be required for accurate modelling.

As discussed in Section 4.3, the K-C model cannot be used to represent a sharp permeability decrease as a result of a moderate

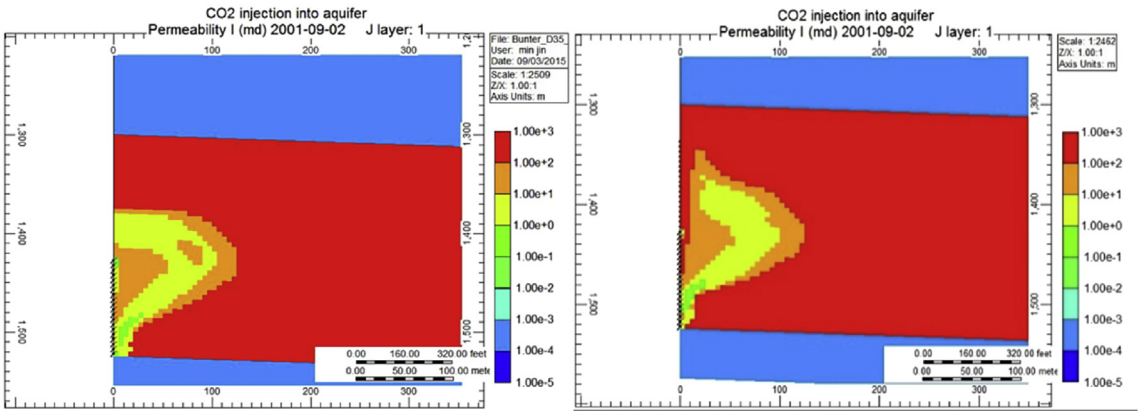

Fig. 21. Permeability distribution after injection of CO_2 for 600 days, left – without fresh water pre-flush, right – with a 10-day pre-injection water flush.

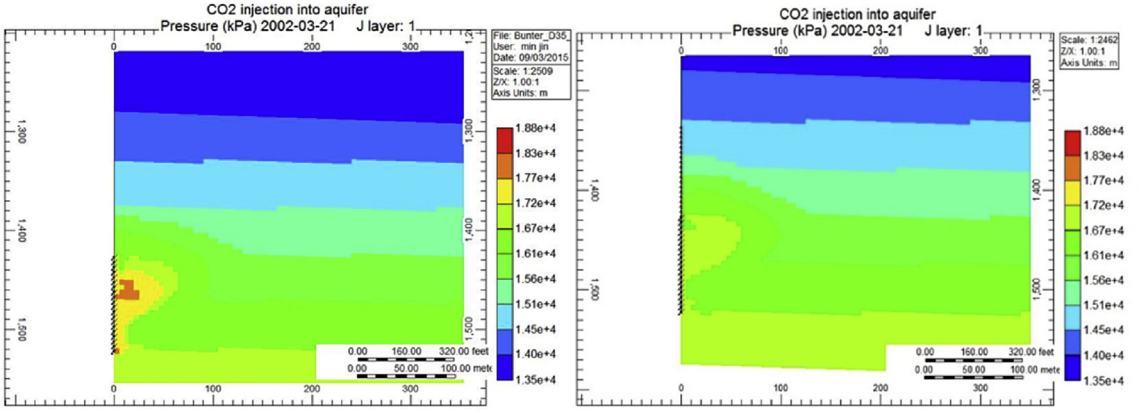

Fig. 22. Pressure distribution after 600 days for models without (left) and with (right) pre-injection fresh water flushing. As a consequence of the deposition zone in the region near the wellbore the local pressure increases quickly.

porosity reduction. Such behaviour can be reproduced by the V-P model, but as this model is not included in the simulator, to use the V-P model in this case the permeability in the simulator is updated after each time step based on Eq. (4–6) with parameters $\phi_c = 0.90$ ϕ_o and $n = 8$, i.e. when the porosity reduces to 90% of its initial value, the permeability reduces to zero. There is a short time lag between porosity and permeability changes because the permeability at timestep n+1 is calculated based on the porosity at timestep n.

Figs. 21 and 22 show a comparison of the permeability reduction and pressure in the model without fresh water pre-flush (left) and with pre-flush (right) at the same timestep. In the case without the pre-flush, as shown in Fig. 21 (left), the salt deposition zone gradually surrounds the entire zone where CO_2 can migrate. As a consequence of this flow restriction in the region near the wellbore due to the salt precipitation, the local pressure increases quickly, as shown in Fig. 22 (left). The pressure within the dry-out zone starts to increase significantly within a two-year injection period.

In the sensitivity study, a freshwater flush is simulated before the injection of CO2 to reduce the salinity of the brine near the wellbore to reduce the damage caused by salt precipitation in this area. Considering that the greatest porosity reduction occurred in the immediate vicinity of the injection well, and water injection may increase the formation pressure and reduce the capacity of storage if too much is injected, and so the pre-flush is only performed for 10 days at an injection rate of 1000 m^3/day. Comparing the results in Figs. 21 and 22, after this short period of water flush, the low salinity region was sufficient to create a relatively protected zone that permitted CO2 displacement and pressure release. The maximum well bottom hole pressure value after 3 years injection of CO2 is reduced by 1280 kPa, about a 40% decrease.

5. Conclusions

The risk of dissolution of primary cements was considered in this study, and it was identified that only dolomite would dissolve under the specified conditions, with all other minerals precipitating. The implications for security of storage are that while dolomite nodules exist in the sandstone, these do not contribute significantly to the overall rock strength, and hence the risk of dissolution of the formation or caprock causing significant leakages pathways is very low.

Mineralisation of CO_2 may occur, but this requires further study, with attention in this work being devoted to the main mineral that precipitates, which is halite. Furthermore, provided dissolution of CO_2 in brine does not create a significant risk of mineral dissolution, the precipitation of minerals will only affect CO_2 already dissolved in the brine phase, and this CO_2 is already very effectively secured due to the greater density of brine saturated CO_2.

The impact on injectivity was found not to be significant during continuous and sustained injection of CO_2 at a constant rate. Capillary pressure effects did cause re-imbibition of saline brine, and hence greater deposition. The impact of the halite deposition was to channel the CO_2, but for the configuration used there was

not a significant change in injection pressure, except where extreme modelling assumptions were made.

To make the geochemical simulation more accurate, experiments should be carried out to identify the permeability reduction that will occur due to evaporation in this formation, and to test the change in rock strength and in water composition arising from the contact between the CO_2 saturated brine and the rock. Using such experimental data it would be possible to more accurately identify the impact on injectivity, and remediation opportunities, such as the fresh water pre-flush shown here to have potential, or periodic brine flushes, can be considered in more detail.

Acknowledgements

CMG Ltd is thanked for the use of the GEM reservoir simulation model in this work. Foundation CMG are thanked for funding the PhD studentship held by Ayrton Ribeiro, the Chair in Reactive Flow Simulation held by Eric Mackay and the Chair in Oil and Gas Reservoir Modeling held by Leonardo Guimarães. National Grid is thanked for funding this work.

References

André, L., Audigane, P., Azaroual, M., Menjoz, A., 2007. Numerical modeling of fluid-rock chemical interactions at supercritical CO2-liquids interface during CO2 injection into a carbonate reservoir, the Dogger aquifer (Paris Basin, France). Energy Convers. Manag. 48, 1782–1797.

Alkan, H., Cinar, Y., Ülker, E.B., 2010. Impact of capillary pressure, salinity and in situ conditions on CO_2 injection into saline aquifers. Transp. Porous Media 84 (3), 799–819. http://dx.doi.org/10.1007/s11242-010-9541-8.

Alkattan, M., Oelkers, E.H., Dandurand, J., Schott, J., 1997. Experimental studies of halite dissolution kinetics, 1 the effect of saturation state and the presence of trace metals. Chem. Geol. 137, 201–219.

Appelo, C.A.J., Postma, D., 2010. In: Geochemistry, Groundwater and Pollution, second ed. A.A. Balkema Publishers, The Netherlands (Leiden, a member of Taylor & Francis Group Plc).

Appelo, C.A.J., Parkhurst, D.L., Post, V.E.A., 2014. Equations for calculating hydrogeochemical reactions of minerals and gases such as CO2 at high pressures and temperatures. Geochim. Cosmochim. Acta 125, 49–67.

Appelo, C.A.J., 2015. Principles, caveats and improvements in databases for calculating hydrogeochemical reactions in saline waters from 0 to 200 °C and 1 to 1000 atm. Appl. Geochem. 55, 62–71.

Audigane, P., Gaus, I., Pruess, K., Xu, T., 2005. Reactive transport modeling using TOUGHREACT for the long term CO2 storage at Sleipner, North Sea. In: Paper Presented at the Fourth Annual Conference on Carbon Capture and Sequestration DOE/NETL.

Bennion, D.B., Bachu, S., 2008. Drainage and imbibition relative permeability relationships for supercritical CO_2/brine and H2S/brine systems in intergranular sandstone, carbonate, shale, and anhydrite rocks. SPE Reserv. Eval. Eng. 487–492.

Bethke, C.M., 1996. Geochemical Reaction Modelling. Oxford University Press, New York.

Carman, P.C., 1956. Flow of Gases Through Porous Media. Butterworth, London.

CMG, 2015a. User's Guide for GEM Compositional and Unconventional Reservoir Simulator.

CMG, 2015b. WinProp User Guide for Phase-behaviour and Fluid Property Program. C.M. G. Ltd. (Ed.).

Corey, A.T., 1954. The interrelation between gas and oil relative permeabilities. Prod. Mon. 38–41.

Giorgis, T., Carpita, M., Battistelli, A., 2007. 2D modeling of salt precipitation during the injection of dry CO_2 in a depleted gas reservoir. Energy Convers. Manag. 48 (6), 1816–1826. http://dx.doi.org/10.1016/j.enconman.2007.01.012.

Graham, R.A., 1973. A Quantitative Determination of Microstructure on Gas Permeability of UO2 and Ni Sintered Bodies. University of Florida Gaineville, U.S.A.

Gundogan, O., 2011. Geochemical Modelling of CO_2 Storage. Heriot-Watt University, Edinburgh, UK.

Jin, M., 1999. The Numerical Modelling of Coupled Rock Mechanics/fluid-flow and its Application in Petroleum Engineering. Heriot-Watt University, Edinburgh, UK.

Lichtner, P.C., 1985. Continuum model for simultaneous chemical reactions and mass transport in hydrothermal systems. Geochimica Cosmochimica Acta 49, 779–800.

Lichtner, P.C., Hammond, G.E., Lu, C., Karra, S., Bisht, G., Andre, B., Mills, R.T., Kumar, J., 2013. PFLOTRAN User Manual: a Massively Parallel Reactive Flow and Transport Model for Describing Surface and Subsurface Processes.

Nagy, K.L., 1995. Dissolution and precipitation kinetics of sheet silicate. In: White, A.F., Barantley, S.L. (Eds.), Chemical Weathering Rate of Silicates Minerals, vol. 31. Mineralogical Society of America, pp. 173–273.

Nghiem, L., Shrivastava, V., Kohse, B., 2011. Modeling aqueous phase behavior and chemical reactions in compositional simulation. In: Paper SPE 141417 presented in SPE Reservoir Simulation Symposium 1, pp. 454–468 (The Woodlands, Texas, USA).

Noh, M., Lake, L.W., Bryant, S.L., Maraque-Martinez, A., 2004. Implications of Coupling Fractional Flow and Geochemistry for CO_2 Injection. Paper Presented at the 2004 SPE/DOE Fourteenth Symposium on Improved Oil Recovery. Oklahoma, U.S.A, Tulsa.

Parkhurst, D.L., Appelo, C.A.J., 2013. Description of input and examples for PHREEQC version 3—a computer program for speciation, batch-reaction, one-dimensional transport, and inverse geochemical calculations. book 6, chap. A43 U.S. Geological Survey Techniques and Methods, p. 497. available only at. http://pubs.usgs.gov/tm/06/a43.

Peysson, Y., Bazin, B., Magnier, C., Kohler, E., Youssef, S., 2011. Permeability alteration due to salt precipitation driven by drying in the context of CO_2 injection. Energy Procedia 4, 4387–4394. http://dx.doi.org/10.1016/j.egypro.2011.02.391.

Pokrovsky, O.S., Schott, J., 2001. Kinetics and mechanism of dolomite dissolution in neutral to alkaline solutions revisited. Am. J. Sci. 301, 597–626.

Pruess, K., 2009. Formation dry-out from CO_2injection into saline aquifers: 2. Analytical model for salt precipitation. Water Resour. Res. 45 (3) http://dx.doi.org/10.1029/2008wr007102 n/a-n/a.

Pruess, K., Müller, N., 2009. Formation dry-out from CO_2injection into saline aquifers: 1. Effects of solids precipitation and their mitigation. Water Resour. Res. 45 (3) http://dx.doi.org/10.1029/2008wr007101 n/a-n/a.

Qiao, C., Li, L., Johns, R.T., Xu, J., 2016. Compositional modeling of dissolution-induced injectivity alteration during CO2 flooding in carbonate reservoirs. SPE J. (June) 1, 809–826. http://dx.doi.org/10.2118/170930-PA.

Rimstidt, J.D., Barnes, H.L., 1980. The kinetics of silica-water reactions. Geochimica Cosmochimica Acta 44 (11), 1683–1699.

Steefel, C.I., Lasaga, A.C., 1994. A coupled model for transport of multiple chemical species and kinetic precipitation/dissolution reactions with application to reactive flow in single phase hydrothermal systems. Am. J. Sci. 294 (5), 529–592.

Steefel, C.I., Appelo, C.A.J., Arora, B., Jacques, D., Kalbacher, T., Kolditz, O., Lagneau, V., Lichtner, P.C., Mayer, K.U., Meeussen, J.C.L., Molins, S., Moulton, D., Shao, H., Simunek, J., Spycher, N., Yabusaki, S.B., Yeh, G.T., 2015. Reactive transport codes for subsurface environmental simulation. Comput. Geosci. 19, 445–478.

van Genuchten, M.T., 1980. A closed-form equation for predicting the hydraulic conductivity of unsaturated soils. Soil Sci. Soc. Am. 44 (5), 892–898.

Vaughan, P.J., Moore, D.E., Morrow, C.A., Byerlee, J.D., 1985. The Mechanism of Permeability Reduction during Flow of Hydrothermal Fluids through Westerly Granite (United States Depertment of the Interior Geological Survey).

Verma, A., Pruess, K., 1988. Thermohydrological conditions and silica redistribution near high-level nuclear wastes emplaced in saturated geological formations. J. Geophys. Res. 93 (B2), 1159. http://dx.doi.org/10.1029/JB093iB02p01159.

Wyble, D.O., 1958. Effect of applied pressure on the conductivity, porosity and permeability of sandstone. Trans. AIME 213, 430–432.

Xu, T., Ontoy, Y., Molling, P., Spycher, N., Parini, M., Pruess, K., 2004. Reactive transport modeling of injection well scaling and acidizing at Tiwi field. Philipp. Geotherm. 33 (4), 477–491. http://dx.doi.org/10.1016/j.geothermics.2003.09.012.

Xu, T., Pruess, K., 2004. Numerical Simulation of Injectivity Effects of Mineral Scaling and Clay Swellilng in a Fractured Geothermal Reservoir. Lawrence Berkeley National Laboratory.

Xu, T., Spycher, N., Sonnenthal, E., Zhang, G., Zheng, L., Pruess, K., 2011. TOUGHREACT version 2.0: a simulator for subsurface reactive transport under non-isothermal multiphase flow conditions. Comput. Geosci. 37, 763–774.

Introduction

Calcite ($CaCO_3$) is the main constituent of limestone rocks and its solubility in water increases with pressure and decreases with temperature. In addition to this, when mixing waters of different chemical compositions, precipitation of calcite may occur if the product of the concentration of Ca and CO_3 is higher than a given value, namely the equilibrium constant divided by activity coefficients. Moreover, solutions containing inorganic carbon exhibit a chemical equilibrium between dissolved CO_2 and its ionised species, HCO_3 and CO_3, which is related to the solution pH (e.g. CO_2-rich waters show lower pH compared to HCO_3-rich waters). Finally, the solubility of gases in solvents is a convex (or concave upward) function of temperature (Harvey, 1996) and the increase of CO_2 solubility with temperature is only obtained at pressures high enough to suppress the total vapourisation of water.

The implications of these thermodynamic facts concerning calcite is that dissolution and precipitation of this mineral are likely to happen during injection of waters with higher CO_2 and/or lower Ca (André et al., 2003; Mackay and de Souza, 2014; Ribeiro et al., 2016; Qiao et al., 2016). In particular, for CO_2 WAG (water-alternating-gas) injection, mineral reactions occur along the flow path within a carbonate formation because of multiple fluid-fluid and fluid-rock interactions combined with temperature and pressure changes. While calcite dissolution can increase injectivity and porosity, precipitation causes formation damage and scale deposition around the producer wellbore. The physical and chemical mechanisms that lead to mineral reactions during multiphase transport still need to be studied, understood, assessed and remediated/mitigated since they present risks to the economic success of the proposed WAG projects.

Geochemical Consequences of CO_2 WAG Flooding on the Production Process

Injectors

The repeated process of brine injection followed by CO_2 injection and CO_2 dissolution into the brine acidifying it will, similarly to carbonated water injection, result in dissolution of the carbonate minerals before the brine is buffered.

Producers

For all scenarios where CO_2 is injected to enhance oil production it is to be expected that there will be a greater calcite scaling tendency at the producers than if only water were injected – although consideration must be given to not only the chemical composition of the produced water, but also the volume, and pure CO_2 injection may increase the scaling tendency for calcite, but reduce the volume of water being produced.

The extent to which brine is acidified prior to or after injection will determine the amount of carbonate dissolution that takes place, and the dissolved carbonate may then re-precipitate in the production wells as pressure decreases, with carbonate water injection likely to lead to the greatest mass of calcite precipitation, and pure CO_2 injection the least mass.

Topside

Depending on the kinetics of the scaling reaction, the risk of calcite deposition may extend beyond the well and into the topside facilities. Any heat exchangers would also exacerbate the risk. However, this can readily be mitigated by appropriate choice of metallurgy.

Whether in the injection wells, production wells or topside facilities, the presence of acid brine will increase the corrosion risk.

The CO_2 WAG injection may introduce geochemical challenges that lead to issues for managing the facilities at production wells, topside facilities and possibly at injectors; the degree of risk is identified in **Table 1**.

Table 1. Geochemical impacts of CO_2 WAG EOR method across the reservoir to the process facility

Injectors			Producers			Topside Process	
Calcite dissolution	Corrosion at end of cycles		Carbonate precipitation	Corrosion		Carbonate precipitation	Corrosion

Predicting and Mitigating Scale in CO_2 WAG EOR Systems

The well published (Jordan et al., 1994; Jordan et al., 1995) approach to evaluation of the scale risk for a new field development has been focused on assessment of the inhibitor performance in a range of formation water to injection water ratio that would guide the scale inhibitor selection. This follows well established tests to measure minimum inhibitor concentration leading to reservoir condition coreflood studies and finally scale squeeze designs via software packages (Mackay and Jordan, 2003). **Table 2** shows the changes that CO_2 WAG flooding will have on the elements that control scale management.

Table 2. Impact of CO_2 WAG on scale control testing

Brine composition change	Scale Prediction	Chemical brine compatibility	Inhibitor performance testing	Coreflood retention studies	Squeeze treatment volumes
Lowered pH	Higher carbonate solubility	Better chemical solubility in brine	Lower MIC	Reduced retention	Larger chemical volume
Elevated HCO_3	Higher SR and mass for calcite	NA[1]	Higher MIC	NA[1]	Larger chemical volume
Elevated Ca	Higher SR and mass for calcite	Poorer chemical solubility in brine	Higher MIC for calcium scales but lower for other scales	Better retention	Larger chemical volume, depending on balance between MIC and retention
Elevated Mg?	Higher SR and mass for $CaMgCO_3$	Poorer chemical solubility in brine	Higher MIC for all scales	Better retention	Larger chemical volume, depending on balance between MIC and retention

Note.
[1] HCO_3 and SO_4 normally removed from test brine other than for inhibitor performance testing
minimum inhibitor concentration (MIC)
Saturation Ratio (SR)

If squeeze treatments are to be avoided in higher pressure fields (or during initial water production) and delayed in lower pressure fields then there is a need to consider downhole chemical injection to the production packer to control scale formation risk from the packer to the wellhead and through the topside process. The installation of deep downhole injection can only be carried out during the well completion so the risk assessment of the carbonate formation (location of formation and amount) requires to be carried out during the field evaluation phase not once the wells are completed and in production.

Reactive Transport Simulation

Since we want to understand calcite dissolution and precipitation within a carbonate reservoir containing injection and producing wells located hundreds of meters apart, we chose to perform reactive transport simulations using a commercial software (CMG GEM) which is a multiphase and multicomponent flow simulator, hereinafter called Simulator. The Simulator solves simultaneously several differential equations associated to transport: (i) fluids (oleic, gaseous and aqueous phases), (ii) components (oil, gas and aqueous species) and (iii) heat between components and rock. Moreover, the Simulator solves fully coupled to the transport equations: (a) chemical equilibrium equations for aqueous (homogeneous) reactions and gaseous dissolution in oil and water and (b) kinetic rate laws for mineral reactions.

We have simulated the injection of CO_2 WAG in a 2D model of a chalk reservoir for 30 years. Information on reservoir properties, water composition and oil components are described in **Tables 3, 4 and 5**, respectively.

Table 3. Reservoir and well properties

Model Dimensions	**600 x 600 x 20 m**
Grid Resolution	**20 x 20 x 20 m**
Porosity	**0.22**
Permeability	**400 mD**
Reservoir Temperature	**60°C**
Temperature of injected fluids	**25°C**
Rock heat capacity	**1046.7 J/kg.K**
Rock thermal conductivity	**3.46 W/m.K**
Well Position Pattern	**$^1/_4$ five-spot**
Maximum Bottom-hole Fluid Rate in injector well	**500 m^3/day**
Maximum Bottom-hole Pressure in producer well	**500 bar**

Table 4. Water composition

	Formation Water (mol/kgw)	**Seawater (mol/kgw)**
Ca	**0.575**	**0.010**
K	**0.047**	**0.010**
Cl	**3.500**	**0.570**
Mg	**0.026**	**0.050**
SO4	**0.004**	**0.029**
Na	**2.267**	**0.500**
HCO3	**0.0001**	**0.001**
CO3	**<0.0001**	**<0.0001**
pH	5.8	7.6

Table 5. Initial oil phase composition (API = 28.8°)

	N2 to C1	**CO_2**	**C2 to C3**	**IC4 to NC5**	**C6 to C9**	**C10 to C19**	**C20 to C29**	**C30A+**	**C30B+**
Moles (%)	**4.8**	**0.3**	**8.6**	**11.2**	**26.3**	**25.3**	**20.6**	**1.7**	**1.3**

In previous research (Ribeiro et al., 2016), it was observed that calcite dissolution is stronger near the injector and is more intense for higher WAG ratio ($\boldsymbol{W_R}$), where this is defined as

$$W_R = \frac{Volume\ of\ Water\ Injected}{Volume\ of\ Gas\ Injected}$$

We have first simulated a base case with unity $\boldsymbol{W_R}$ and WAG half-cycle of 60 days.

Simulation Results

Our analysis of simulation results revealed three distinct zones of calcite dissolution and precipitation that emerge from the propagation of different fluid fronts, namely the oil/formation water front, the formation water/injected water front and the temperature front. In this sense, as the oil phase is being displaced, formation water moves toward the produced and hence the oil/formation water saturation front propagates (see **Figure 1**).

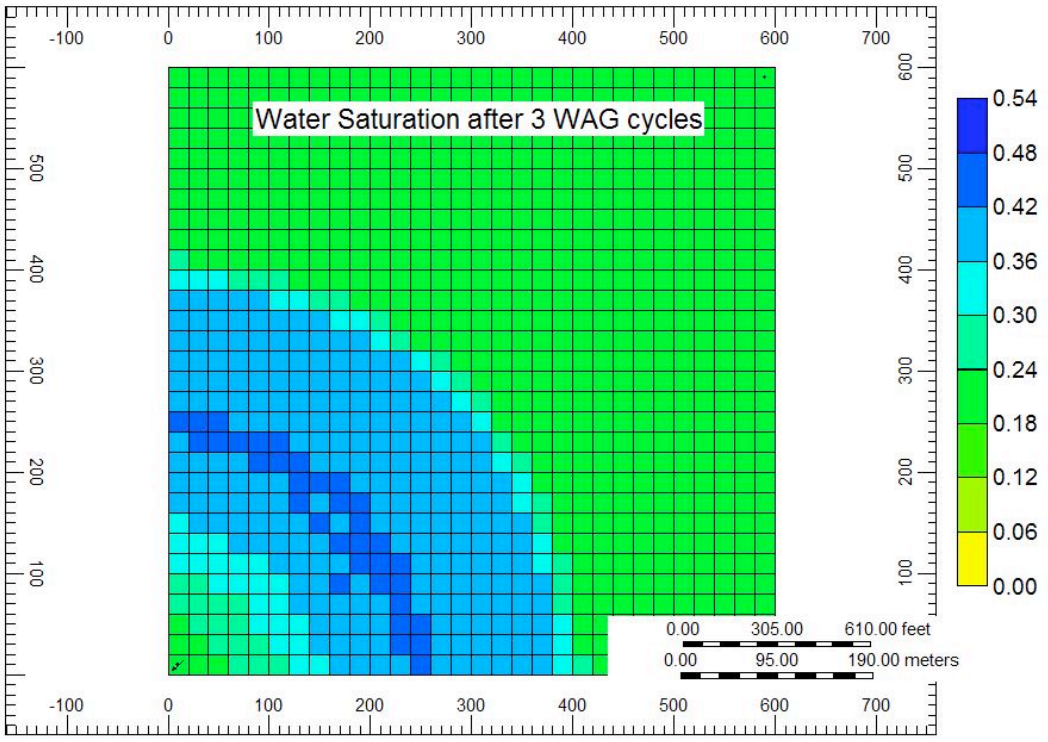

Figure 1. Water saturation after 360 days of injection (base case). An oil/formation water front was developed and is currently at 400 meters away from the injector.

The formation water is then displaced by the injected seawater, which carries a higher amount of dissolved CO_2. This also occurs in isothermal injection of seawater or CO_2-bearing fluids in aquifers (André et al., 2013; Mackay and de Souza, 2014; Ribeiro et al., 2016). Therefore, a group of aqueous concentration fronts propagate together: CO_2, HCO_3, SO_4, etc. As these fronts propagate calcite is first dissolved and then precipitated through the model. Moreover, the injection of cooler fluids creates an additional zone with CO_2-rich water around the injector wellbore (see **Figure 2**).

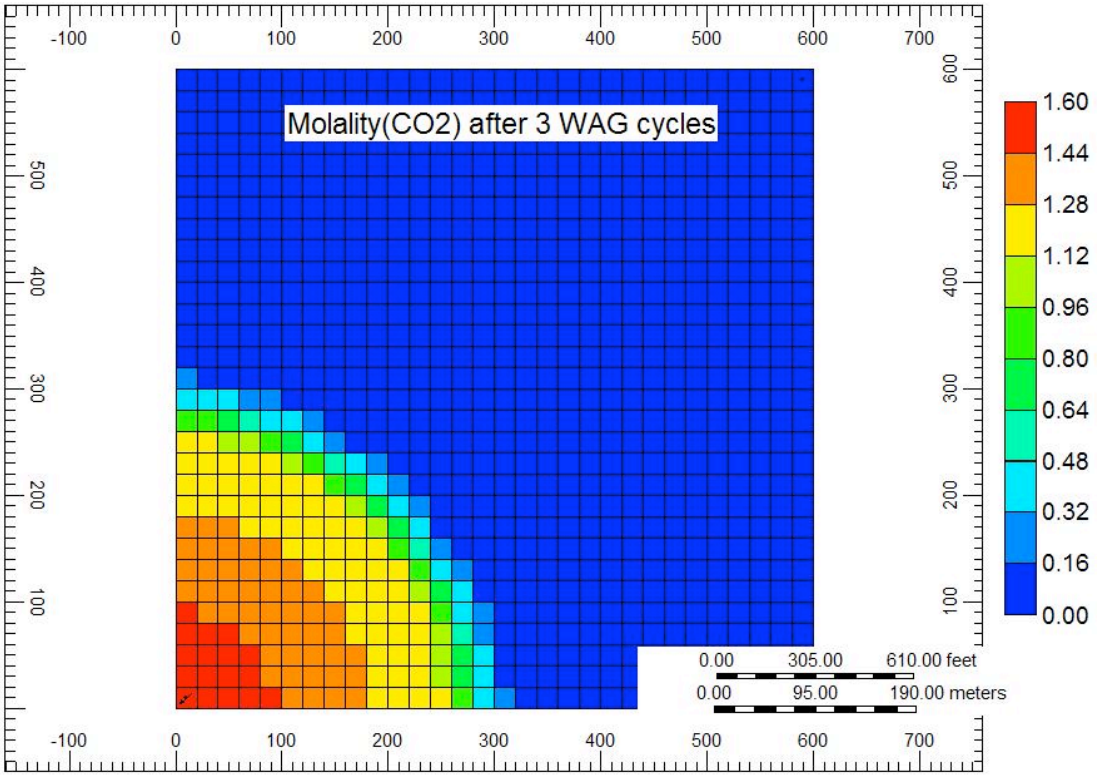

Figure 2. CO_2 molality after 360 days of injection (base case). Two distinct aqueous CO_2 fronts are developed during non-isothermal flow and they are currently at 300 and 100 meters away from the injector.

The temperature drop in the area moves this portion of the system closer to chemical equilibrium and therefore calcite reactions are supressed beyond 20m away from the injector. On the other hand, when this near-equilibrium water moves to warmer locations precipitation starts. Therefore, the porosity more than 20m away from the injector is stationary after an initial dissolution (see **Figure 3**).

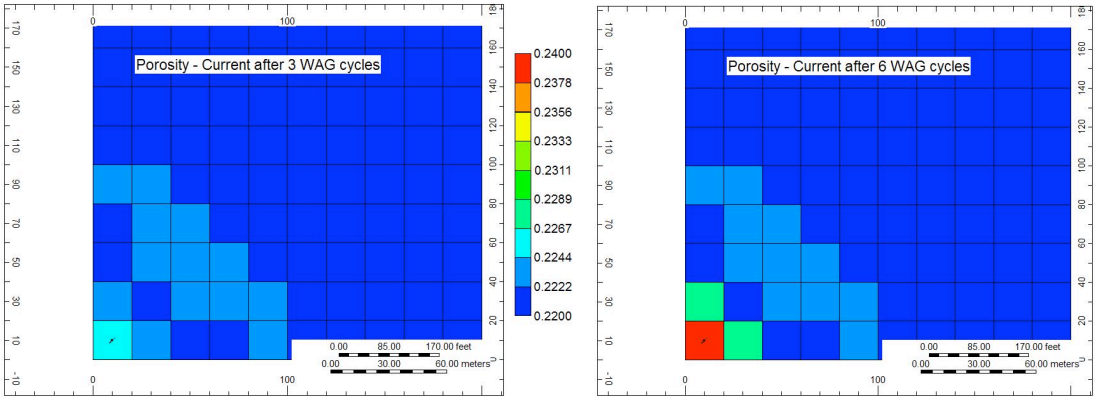

Figure 3. Porosity after 360 (left) and 720 days (right) of injection (base case). Porosity increases because calcite is dissolving. However, continuous dissolution occurs only very close to the injector.

Impact of Heat Exchange

To address the impact of heat exchange in calcite reactions, we have simulated the base case using the temperature of injecting fluids equal to the reservoir temperature and compared the results. We have found that during non-isothermal flow calcite dissolution in the near injector wellbore (<20m) is stronger, which is due to higher solubility at lower temperature. On the other hand, deeper in the reservoir, dissolution is suppressed as the injected fluids move from cooler to warmer zones. Thus, although the reservoir becomes cooler, scale deposition around the producer is higher when compared to isothermal calculation. In fact, after 30 years of injection of cooler fluids 56.4 thousands kg of calcite precipitated within 20 meters from the producer wellbore, while under isothermal assumption dissolution of 8.7 thousands kg were calculated.

A deeper analysis of the consequences of heat exchange reveals that they are dependent on the amount of dispersion involved, which can be controlled by the size of time step. Table 4 shows that for smaller time steps, hence less numerical dispersion, the ratio between calcite dissolution with and without heat exchange in the full field is smaller. (The fraction of all time steps that are solved implicitly is given in the table: implicit solution of the pressure equation permits longer time steps and hence reduced overall model run time, but results in more dispersion.).

Table 6. Impact of heat exchange for different time step sizes.

Max Time Step (day)	Isothermal		Non-isothermal		Error in Dissolution (%)
	Dissolution (MM kg)	Implicit steps (%)	Dissolution (MM kg)	Implicit steps (%)	
1.8	**26.5**	**42**	**14.5**	**46**	**82**
1.6	**23.0**	**35**	**14.7**	**43**	**60**
1.4	**25.3**	**32**	**19.4**	**40**	**30**
1.2	**24.0**	**36**	**21.1**	**36**	**14**
1.0	**20.3**	**31**	**19.7**	**33**	**3**

Moreover, as it can be seen in **Figure 4** the fastest dissolution occurred before five years independent of time step size or temperature. We could explain this by calculating the time for breakthrough as six years.

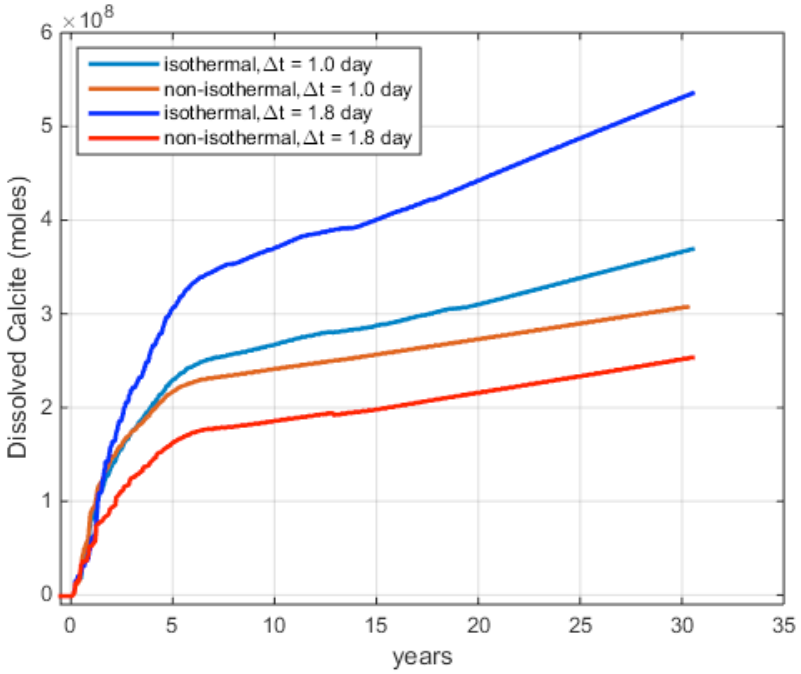

Figure 4. Dissolved calcite in the reservoir with or without heat exchange for different time step sizes.

Impact of WAG scheme

Injector wellbore

The total volume of water injected during the lifetime of a development plan can be partitioned in several ways to control the production rate and prevent operating problems such as gas override and channelling. Hence, it is important to know if the size of the water slugs has any impact on calcite dissolution even if the sum of the slugs is constant. To investigate this we have performed simulation of the following scenarios of 30 years of CO_2 WAG injection:

Table 7. Simulated scenarios of CO_2 WAG

Scenario Code	W_R	Water Slug (days)	Gas Slug (days)	WAG Cycle (days)	Total Volume of Water Injected (m^3)
A1	0.5	60	120	180	1 825 000
A2	1	60	60	120	2 737 500
A3	2	60	30	90	3 650 000
B1	0.5	120	240	360	1 825 000
B2	1	120	120	240	2 737 500
B3	2	120	60	180	3 650 000
C1	0.5	180	360	540	1 825 000
C2	1	180	180	360	2 737 500
C3	2	180	90	270	3 650 000

It is shown in **Figure 5** that for each water slug size there is a strong linear relationship between injected volume of water and calcite dissolution around the injector wellbore. On the other hand, shorter WAG slugs cause slightly more calcite dissolution because of greater contact occurring between water and gas phases (which cause more dissolution of gaseous CO_2 into water). However, for very short WAG cycles with high W_R (scenario A3), the gas slug may be not large enough to support gaseous dissolution and therefore the total dissolved calcite will be less.

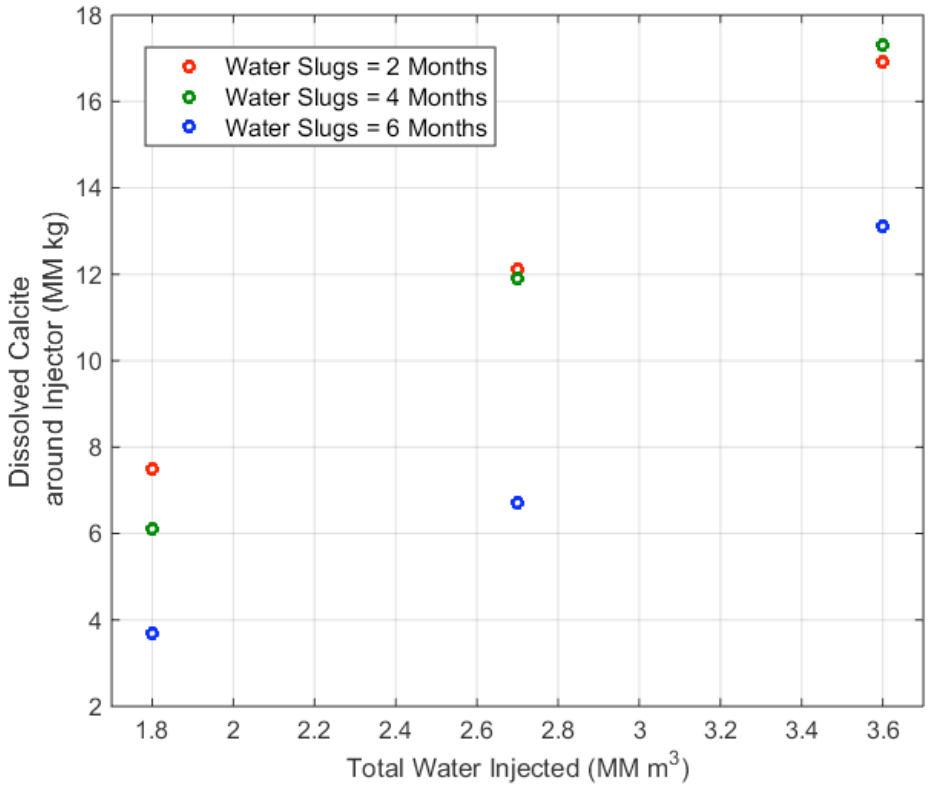

Figure 5. Dissolved calcite around injector for different WAG schemes.

Hence, W_R is a key operational parameter to control calcite dissolution during CO_2 WAG injection and it is preferred over water slug size because of its higher impact and also because of operational constraints on the minimum slug size, which limits the maximum dissolution.
However, the size of the water slug has been found to control the size of the dissolution zone around the injector wellbore independently of W_R. Higher W_R yield more dissolution close to the well. On the other hand, the maximum range for which porosity changes are relevant grows linearly with the duration of the water flood per WAG cycle. Moreover, as seen in **Figure 5**, the volume of dissolved calcite for fixed W_R changes very little with water slug size. This is a very important result since the spatial distribution of the mineral dissolution impacts the increase of injectivity. While tight dissolution zones have faster increase of porosity, a deeper penetration of the dissolution into the reservoir will be more beneficial for fluid displacement and, in addition, contributes to a lower risk of wellbore collapse.

Producer wellbore

Calcite changes at the producer wellbore occur in three steps. First, calcite dissolves during the arrival of the injected CO_2 at the wellbore, which dissolves into formation water and reduces pH close to the well. Then, the injected water mixes with the formation water and strong precipitation begins. After that, when most of the formation water has been produced, the precipitation rate decreases but remains constant because of degassing.

For fixed $\boldsymbol{W_R}$, calcite dissolution around the producer is greater for larger water slugs; this is because larger slugs delay the dissolution of injected CO_2 into the injected water, and thus reduces the degree of interaction around the injector, delaying this interaction such that it increasingly occurs around the producer. Effectively, although there will be dissolution along the entire flow path, the point at which most dissolution occurs moves gradually away from the injector and towards the producer as the sizes of the injected slugs increase. Moreover, higher $\boldsymbol{W_R}$ yields greater precipitation and at faster rates, since high HCO_3 concentration water propagates faster through the reservoir (see **Figure 6**).

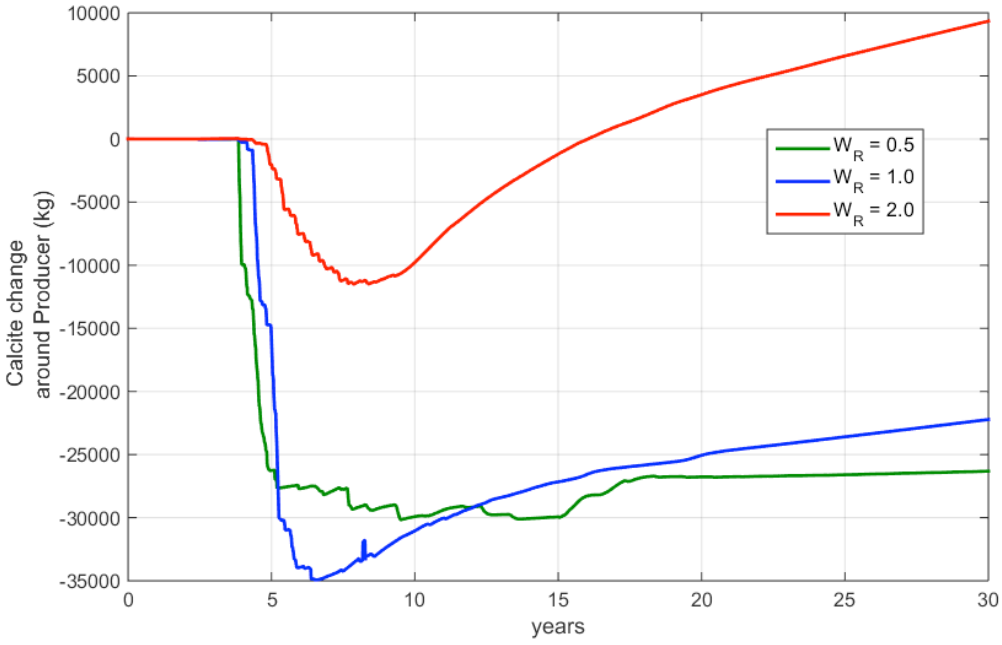

Figure 6. Calcite change around producer for different WAG schemes (scenarios B1, B2 and B3).

Finally, we have confirmed that an increase in W_R causes earlier breakthrough of seawater and a longer time elapses before the injected CO_2 starts to be produced (see Figure 7). The moment when the gas saturation first increases is an indication of the start of the precipitation caused by CO_2 evolution. On the other hand, when the seawater fraction approaches 100%, the precipitation caused by mixing of incompatible waters terminates and the mechanism of precipitation is restricted to depressurisation/degassing along the flow path.

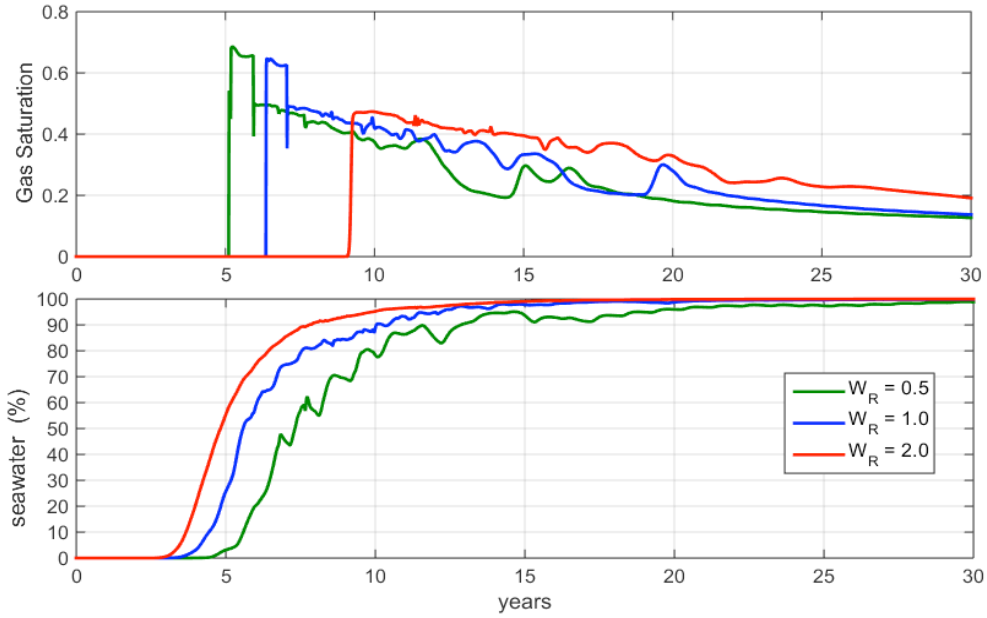

Figure 7. Gas breakthrough (top) and seawater breakthrough (bottom) for scenarios B1, B2 and B3.

Conclusions

EOR presents challenges different from those encountered during primary and secondary recovery processes. In the CO_2 WAG example cited, pH change is the most significant difference from conventional water flooding, as the pH at the production well declines over time. The implications for scale management are as follows:

- The $CaCO_3$ scaling risk at the production wells may be higher than in a waterflood case due to the additional dissolution of carbonate resulting from the carbonation of water.
- Dissolution of carbonate matrix will generally result in a higher scaling risk than dissolution of calcite cements within a sandstone reservoir due to the volume difference.
- Nonetheless, the dissolution of carbonate matrix or cements will result in buffering of the brine, such that pH values in the produced water will typically be within one pH unit of the formation water pH.
- The extra carbonate scaling potential in the production wells will mean that larger chemical volumes are required for treatment.

In this work a compositional model was used to simulate the impact of implementing CO_2 WAG in a model of chalk reservoir from the point of view of important mineral reactions, namely the dissolution and precipitation of calcite between injector and producer wellbores.

Simulation results show dissolution of calcite concentrates around the injector while precipitation is stronger around the producer, which is attributed to the short equilibration time of calcite reactions and the CO_2 solubility dependency on pressure. These results have been presented before by different authors (André et al., 2007; Qiao et al., 2016; Mackay and de Souza, 2014; Ribeiro et al. 2016).

On the other hand, this research has investigated the impact of cooling the injector wellbore by simulating non-isothermal flow. It was shown that when cooler fluids are injected calcite dissolution is stronger in the near wellbore area because of increasing solubility at lower temperature. However, as the propagated fluids are getting heated to the reservoir temperature, calcite dissolution is suppressed deep in the reservoir including the producer wellbore where higher precipitation occurs. Moreover, since the suppression of calcite dissolution is linked to temperature transition zone, the impact of heat exchange on the calcite reactions through the flowpaths will be stronger on reservoirs with higher heterogeneities, as we have demonstrated with simulations of increasing numerical dispersion.

Another aspect of this work was the impact of the WAG scheme, which is important for the link between EOR and scale management. The main variable of the WAG scheme is the WAG ratio (W_R), both for oil recovery and scale deposition. Simulation results show that implementing higher W_R causes an earlier seawater breakthrough, which affects not only oil production rate but also the rate of scale deposition at the producer. The calcite around the producer wellbore first dissolves with arrival of a CO_2-rich front. Then, strong precipitation starts because of mixing of high HCO_3 water with high Ca formation water. The high HCO_3 water is obtained through the dissolution and further dissociation of CO_2 in the injected seawater while high Ca formation water is characteristic of carbonate formation. Therefore, the precipitation by mixing causes the faster increase in scale risk. Nevertheless, after most of the formation water is produced (seawater fraction approaches unity), a slower but continuous scale deposition occurs as CO_2 evolves along the flowpaths.

Finally, this research highlights the importance of the understanding of different but coupled phenomena related to CO_2 EOR in carbonates which impact scale management. Since the injection of CO_2 causes the precipitation of $CaCO_3$ either by mixing or degassing, the WAG scheme affects the scale deposition. Higher W_R yields higher precipitation because it increases the interaction of injected water with the reservoir and accelarate seawater breakthrough. Moreover, the injection of cooler fluids may cause significantly higher scale deposition, especially in carbonates reservoirs, which are very heterogeneous. Thus, scale prediction during CO_2 WAG in carbonates may be regarded as optimistic if the WAG scheme and heat exchange are not considered as part of the analysis.

Acknowledgements
The authors would like to thank Nalco Champion an Ecolab Company and Heriot-Watt University for permission to publish this work. Foundation CMG are thanked for funding Eric Mackay and Leonardo Guimarães's research chairs and Ayrton Ribeiro's studentship. CMG are thanked for access to the GEM simulator.

References

André, L., Audigane, P., Azaroual, M. and Menjoz, A., 2007. Numerical modeling of fluid-rock chemical interactions at supercritical CO_2-liquids interface during CO_2 injection into a carbonate reservoir, the Dogger aquifer (Paris Basin, France). Energy Conversion & Management, 48, 1782-1797.

Jordan, M.M., Sorbie, K.S., Jiang, P., Yuan, M.D., Todd, A.C. and Hourston, K.E.: "Scale Inhibitor Adsorption/ Desorption and the Potential for Formation Damage in Reconditioned Field Core," presented at the SPE International Symposium on Formation Damage Control, Lafayette, Louisiana, 7-10 February 1994.

Jordan, M.M., Sorbie, K.S., Griffin, P., Hennessey, S. Houston, K.E. and Waterhouse, P.: "Scale Inhibitor Adsorption/Desorption vs. Precipitation: The Potential for Extending Squeeze Life While Minimising Formation Damage," SPE 30106, presented at the European Formation Damage Conference, Hague, Netherlands, 15-16 May 1995.

Mackay, E.J. and Jordan, M.M.: "SQUEEZE Modelling: Treatment Design and Case Histories" paper SPE 82227, presented at the SPE European Formation Damage Conference, The Hague, The Netherlands, 13-14 May 2003.

Mackay, E. and Martins de Souza, A. P.: "Modelling of CO_2 and Seawater Injection in Carbonate Reservoirs to Evaluate Inorganic Scaling Risk," presented at the SPE International Oilfield Scale Conference and Exhibition, Aberdeen, Scotland, 14-15 May 2014.

Qiao, C., Li, L., Johns, R. T. and Xu, J., 2016. Compositional Modeling of Dissolution-Induced Injectivity Alteration During CO_2 Flooding in Carbonate Reservoirs. SPE Journal (June). SPE-170930-PA

Ribeiro, A., Mackay, E. J. and Guimarães, L.: "Predicting Calcite Scaling Risk Due to Dissolution and Re-Precipitation in Carbonate Reservoirs During CO_2 Injection," presented at the SPE International Oilfield Scale Conference and Exhibition, Aberdeen, Scotland, 11-12 May 2016.

References

AGADA, S., GEIGER, S. & DOSTER, F. 2016. Wettability, hysteresis and fracture–matrix interaction during CO2 EOR and storage in fractured carbonate reservoirs, *Int. J. Greenh. Gas Control*, 46, 57-75, doi:10.1016/j.ijggc.2015.12.035.

AKINFIEV, N. N & DIAMOND, L. W. 2010. Thermodynamic model of aqueous CO2–H2O–NaCl solutions from −22 to 100°C and from 0.1 to 100MPa, *Fluid Phase Equilibria*, 295, 1, 104-124, doi:10.1016/j.fluid.2010.04.007.

ANDRÉ, L., AUDIGANE, P. & MENJOZ, A. 2007. Numerical modeling of fluid-rock chemical interactions at supercritical CO_2-liquids interface during CO_2 injection into a carbonate reservoir, the Dogger aquifer (Paris Basin, France). *Energy Conversion & Management*, 48, 1782-1797, doi:10.1016/j.enconman.2007.01.006

APPELO, C. A. J. & POSTMA, D. 2013. Geochemistry, groundwater and pollution. 2nd Ed. CRC Press.

APPELO, C. A. J., PARKHURST, D. L. & POST, V. E. A. 2014. Equations for calculating hydrogeochemical reactions of minerals and gases such as CO2 at high pressures and temperatures. *Geochim. Cosmochim. Acta,* 125, 49-67, doi:10.1016/j.gca.2013.10.003.

APPELO, C. A. J. 2015. Principles, caveats and improvements in databases for calculating hydrogeochemical reactions in saline waters from 0 to 200 °C and 1 to 1000 atm. *Applied Geochemistry,* 55, 62-71., doi:10.1016/j.apgeochem.2014.11.007.

BAKKER, R.J. 2003. Package FLUIDS 1. Computer Programs for Analysis of Fluid Inclusion Data and for Modelling Bulk Fluid Properties, *Chemical Geology*, 194, 3-23.

BEAR, J. 1972. Dynamics of Fluids in Porous Media. Dover Publications.

BETHKE, C.M. 1996. Geochemical Reaction Modelling. Oxford University Press.

BLOUNT, C.W. 1977. Barite solubilities and thermodynamic quantities up to 300°C and 1400 bars. *Am. Mineral.*, 62, 942–957.

BLOUNT, C.W. & DICKSON, F.W. 1969. The solubility of anhydrite (CaSO4) in NaCl–H2O from 100 to 450 °C and 1–1000 bars. Geochim. Cosmochim. Acta 33, 227–245.

BLOCK, J. & WATERS, O.B. 1968. The CaSO4–Na2SO4–NaCl–H2O system at 25–100 °C. *J. Chem. Eng. Data*, 13, 336–344.

BRADLEY, D. J. & PITZER, K. S. 1979. Thermodynamics of electrolytes. 12. Dielectric properties of water and Debye-Hückel parameters to 350 °C and 1 kbar. *J. Phys. Chem.* 83, 1599-1603.

BRANNAN, G. & WHITINGTON, H. M. 1977. Enriched-Gas Miscible Flooding: A Case History of the Levelland Unit Secondary Miscible Project. *SPE Journal*. SPE-5826-PA

BROSSE, E., MAGNIER, C. & VINCENT, B. 2005. Modelling Fluid-Rock Interaction Induced by the Percolation of CO2-Enriched Solutions in Core Samples: The Role of Reactive Surface Area. *Oil & Gas Science and Technology*, 60 (2), 287–305.

CALLEN, H. B. 1985. Thermodynamics and An Introduction to Thermostatistics. 2nd Ed. John Wiley & Sons.

CARROLL, J. J. & MATHER, A. E. 1992. The system carbon dioxide−water and the Krichevsky−Kasarnovsky equation. *J. Sol. Chem.*, 21, 607−621.

CASTELLAN, G. 1986. Fundamentos de físico-química. LTC.

CHEN, Z., HUAN, G., MA, Y. 2006. Computational Methods for Multiphase Flows in Porous Media. Society for Industrial and Applied Mathematics.

CHOU, L., GARRELS, R. M., WOLLAST, R., 1989. Comparative Study of the Kinetics and Mechanisms of Dissolution of Carbonate Minerals. *Chem. Geol.*, 78 (3), 269−282.

CHRISTENSEN, J. R., STENBY, E. H. & SKAUGE, A. 1998. Review of WAG Field Experiences. Presented at SPE International Petroleum Conference and Exhibition of Mexico, Villahermose, Mexico, 3 – 5 March. SPE-39883-MS.

CORBETT, P.W.M. & GOMES, J.S., 2000. Variation in permeability in a Middle East carbonate reservoir, presented at the 2000 SCA Annual Technical Conference, Abu Dhabi, UAE, Oct. 18-22. SCA 2000-52.

CORBETT, P.W.M. & POTTER, D., 2004. Petrotyping: A basemap and atlas for navigating through permeability and porosity data for reservoir comparison and

permeability prediction, presented at the 2004 SCA Annual Technical Conference, Abu Dhabi, UAE, Oct. 5-9. SCA2004-30.

CHITALE, D.V., ALABI, G., GRAMIN, P. LEPLEY, S. & PICCOLI, L., 2015. Reservoir Characterization Challenges, due to the multiscale spatial heterogeneity in the Presalt Carbonate Sag Formation, North Campos Basin, Brazil. *Petrophysics*, v50(6), 552-576.

CRUZ, R., ROSA, M. B., BRANCO, C., PIZARRO, J. O. S. & SILVA, C. T. S. 2016. Lula NE Pilot Project - An Ultra-Deep Success in the Brazilian Pre-Salt. Presented at Offshore Technology Conference, Houston, Texas, USA, 2 – 5 May. SPE-27297-MS.

DEBYE, P. & HÜCKEL, E., 1923. Zur Theorie der Elektrolyte. *Phys. Z.*, 24, 185-208; 24, 305-325.

DIAMOND, L. AKINFIEV, N, 2003. Solubility of CO2 in water from −1.5 to 100 ◦C and from 0.1 to 100MPa: evaluation of literature data and thermodynamic modelling. *Fluid Phase Equilibria*, 208, 1–2, 265-290, doi:10.1016/S0378-3812(03)00041-4.

DRUMMOND, S.E. 1981. Boiling and mixing of hydrothermal fluids: chemical effects on mineral precipitation. PhD thesis, Pennsylvania State University.

DUAN, Z., MOLLER, N. & WEARE, J.H., 1992. An equation of state for the CH4–CO2–H2O system: I. Pure systems for 0 to 1000 °C and 0 to 8000 bar. *Geochim. Cosmochim. Acta*, 56, 2605– 2617.

DUAN, Z. & SUN, R. 2003. An improved model calculating CO2 solubility in pure water and aqueous NaCl solutions from 273 to 533 K and from 0 to 2000 bar. *Chem. Geol.*, 193, 257–271.

ETTEHADTAVAKKOL, A., LAKE, L. W. & BRYANT, S. L. 2014. CO2-EOR and storage design optimization, *Int. J. Greenh. Gas Control*, 25, 79-92, doi:10.1016/j.ijggc.2014.04.006.

ELWY, M., ZEKRI, A. Y., ALMEHAIDEB, R. A., & AL-ATTAR, H. H. 2012. Optimization of CO2 WAG Processes in Carbonate Reservoirs-An Experimental Approach. Presented at Abu Dhabi International Petroleum Conference and Exhibition, 11-14 November , Abu Dhabi, UAE. SPE-161782-MS.

ELLIS, A.J., 1963. Solubility of calcite in sodium chloride solutions at high temperatures. *Am. J. Sci.*, 261, 259–267.

FANCHI, J. R., 2006. Principles of Applied Reservoir Simulation. 3rd ed. Elsevier Inc.

GARCIA, J.E. 2001. Density of Aqueous Solutions of CO2, Lawrence Berkeley National Laboratory.

GEM Manual, 2014, CMG.

GRAHAM, G. M., MACKAY, E. J., DYER, S. J., & BOURNE, H. M. 2002. The Challenges for Scale Control in Deepwater Production Systems: Chemical Inhibition and Placement. NACE International.

GREEN, D. W. & WILLHITE, G. P., 1997. Enhanced Oil Recovery. SPE Textbook Series, Volume 6. Society of Petroleum Engineers.

GUIMARÃES, L. do N., GENS, A. & OLIVELLA, S., 2007. Coupled Thermo-Hydro-Mechanical and Chemical Analysis of Expansive Clay Subjected to Heating and Hydration. *Transport in Porous Media*, 66, 341–372.

FINNERAN, D.M. & MORSE, J.W., 2009. Calcite dissolution kinetics in saline waters. *Chem. Geol.*, 268, 137–146.

HARVEY A. H, 1996. Semiempirical correlation for Henry's constants over large temperature ranges. *AIChE J.*, 42, 1491–1494.

HARVIE, C.E. & WEARE, J.H., 1980. The prediction of mineral solubilities in natural waters: the Na–K–Mg–Ca–Cl–SO4–H2O system from zero to high concentration at 25℃. *Geochim. Cosmochim. Acta*, 44, 981–997.

HARVIE, C.E. & WEARE, J.H., 1984. The prediction of mineral solubility in natural waters: the Na–K–Mg–Ca–H–Cl–SO4–OH–HCO3–CO3–CO2–H2O systems from zero to high concentration at 25℃. *Geochim. Cosmochim. Acta*, 48, 723–751.

HELGESON, H. C. & KIRKHAM, D. H., 1976. Theoretical predictions of thermodynamic behavior of aqueous electrolytes by high pressures and temperatures: III. Equation of state for aqueous species at infinite dilution. Am. J. Sci. 276, 97-240.

HELGESON, H.C., KIRKHAM, D.H. & FLOWERS, G.C., 1981. Theoretical prediction of the thermodynamic behavior of aqueous electrolytes by high pressures and temperatures: IV. Calculation of activity coefficients, osmotic coefficients, and apparent molal and standard and relative partial molal properties to 600℃ and 5 kb. *Am. J. Sci.*, 281, 1249–1516.

HENRY, R. L., FEATHER, G. L., SMITH, L. R., FUSSELL, D. D., 1981. Utilization Of Composition Observation Wells In A West Texas CO2 Pilot Flood. Presented

at SPE/DOE Second Joint Symposium on Enhanced Oil Recovery, Tulsa, Oklahoma, 5 – 8 April. SPE-9786-MS

HERZER, J. & KINZELBACH, W., 1989. Coupling Transport and Chemical Processes in Numerical Transport Models.

HILL, P. G. J., 1990. A Unified Fundamental Equation for the Thermodynamic Properties of H2O. *Phys. Chem. Ref. Data*, 19, 1233–1274.

IZGEC, O., DEMIRAL, B., BERTIN, H. J., & AKIN, S. 2005. CO2 Injection in Carbonates. Presented at SPE Western Regional Meeting, 30 March-1 April, Irvine, California. SPE-93773-MS.

KANE, A. V. 1979. Performance Review of a Large-Scale CO2-WAG Enhanced Recovery Project, SACROC Unit Kelly-Snyder Field. *SPE Journal*. SPE-7091-PA.

LANGMUIR, D. 1997. Aqueous environmental geochemistry. Prentice-Hall.

LICHTNER, P. C., 1985. Continuum Model for Simultaneous Chemical Reactions and Mass Transport in Hydrothermal Systems. *Geochim. Cosmochim. Acta*, 49, 779-800.

LICHTNER, P. C., HAMMOND, G.E., LU, C., KARRA, S., BISHT, G., ANDRE, B., MILLS, R.T. & KUMAR, J. 2013. PFLOTRAN User manual: A Massively Parallel Reactive Flow and Transport Model for Describing Surface and Subsurface Processes.

MACDONALD, R. W. & NORTH, N. A., 1974. The effect of pressure on the solubility of CaCO3, CaF2, and SrSO4 in water. Can. J. Chem. 52, 3181–3186.

MACKAY, E. & SOUZA, A. P. M., 2014. Modelling of CO_2 and Seawater Injection in Carbonate Reservoirs to Evaluate Inorganic Scaling Risk. Presented at SPE International Oilfield Scale Conference and Exhibition, 14-15 May, Aberdeen, Scotland. SPE-169766-MS.

MANRIQUE, E. J., MUCI, V. E. & GUFINKEL, M. E. 2007. EOR Field Experiences in Carbonate Reservoirs in the United States. *SPE Reservoir Evaluation & Engineering*. SPE-100063-PA

MOHAMED, I. & NASR-EL-DIN, H. A., 2013. Fluid/Rock Interactions During CO2 Sequestration in Deep Saline Carbonate Aquifers: Laboratory and Modeling Studies. *SPE Journal*. SPE-151142-PA

MOLLER, N., 1988. The prediction of mineral solubilities in natural waters: A chemical equilibrium model for the Na-Ca-CI-S04-H20 system, to high temperature and concentration. *Geochim. Cosmochim. Acta*, 52, 821– 837.

NGHIEM, L. X., SHRIVASTAVA, V. K. & KOHSE, B. F. 2011. Modeling Aqueous Phase Behavior and Chemical reactions in Compositional Simulation. Presented at SPE Reservoir Simulation Symposium, 21-23 February, The Woodlands, Texas, USA. SPE-141417-MS.

PARKHURST, D. L. 1990. Ion association models and mean activity coefficients of various salts. In D. C. Melchior and R. L. Basset (eds), Chemical modelling of aqueous systems II. ACS Symp. Ser. 416, 30-43.

PARKHURST, D.L. & APPELO, C.A.J. 2013. Description of input and examples for PHREEQC version 3 -- a computer program for speciation, batch-reaction, one-dimensional transport, and inverse geochemical calculations, U.S. Geological Survey Techniques and Methods, book 6, chap. A43, 497 p., available only at http://pubs.usgs.gov/tm/06/a43

PEACEMAN, D. W., 1977. Fundamentals of numerical reservoir simulation. Elsevier Scientific Publishing Company.

PLUMMER, L. N., WIGLEY, T. M. L. & PARKHURST, D. L. 1978. The kinetics of calcite dissolution in CO_2-water systems at 5 to 60℃ and 0.0 to 1.0 atm CO_2. *Am. J. Sci.* 278, 179 – 216.

PLUMMER, L.N. & BUSENBERG, E. 1982. The solubilities of calcite, aragonite and vaterite in CO2–H2O solutions between 0℃ and 90℃, and an evaluation of the aqueous model for the system CaCO3–CO2–H2O. *Geochim. Cosmochim. Acta*, 46, 1011–1040.

PITZER K. S. 1973. Thermodynamics of Electrolytes I: Theoretical basis and general equations. *J. Phys. Chern.* 77, 268-277.

PITZER, K. S. 1987. Thermodynamic model for aqueous solutions of liquid-like density. In *Thermodynamic modeling of geological materials*: Minerals, fluids and melts, ed. I. S. E. Carmichael and H. P. Eugster, Reviews in Mineralogy 17, pp. 97-142. Min. Soc. Am.

POKROVSKY, O. S., GOLUBEV, S. V., SCHOTT, J. & CASTILLO, A. 2009. Calcite, dolomite and magnesite dissolution kinetics in aqueous solution at acid to circumneutral pH, 25 to 150℃ and 1 to 55 atm pCO_2: New constraints on CO_2

sequestration in sedimentary basins. *Chem. Geol.*, 265, 20-32. doi: 10.1016/j.chemgeo.2009.01.013.

QIAO, C., LI, L., JOHNS, R. T. & XU, J. 2016. Compositional Modeling of Dissolution-Induced Injectivity Alteration During CO2 Flooding in Carbonate Reservoirs. *SPE Journal*. SPE-170930-PA

RUMPF, B., NICOLAISEN, H., OCAL, C. & MAURER, G., 1994. Solubility of carbon dioxide in aqueous solutions of sodium chloride: experimental results and correlation. *J. Solution Chem.*, 23 (3), 431– 448.

SAUL, A. & WAGNER, W. 1987. International Equations for the Saturated Properties of Ordinary Water Substance, *J. Phys. Chem. Ref. Data*, 16, 4. 893-901.

SMITH, M. M., SHOLOKHOVA, Y., HAO, Y. & CARROLL, S. A. 2013. CO_2-induced dissolution of low permeability carbonates. Part I: Characterization and experiments. *Advances in Water Resources*, 62, 370 – 387.

SPAN, R. & WAGNER, W. 1996. A New Equation of State for Carbon Dioxide Covering the Fluid Region from the Triple-Point Temperature to 1100 K at Pressures up to 800 Mpa. J. Phys Chem. Ref. Data, Vol. 25, No. 6.

STEEFEL, C. I. 2008. Chapter 11. Geochemical kinetics and transport. *In: Brantley S., Kubicki J., White A. (eds) Kinetics of Water-Rock Interaction. Springer.*

STEEFEL, C. I. & LASAGA, A. C. 1994. A coupled model for transport of multiple chemical species and kinetic precipitation/dissolution reactions with application to reactive flow in single phase hydrothermal systems. *Am. J. Sci.*, 294 (5), 529-592.

SVEC, R. K. & GRIGG, R. B. 2001. Physical Effects of WAG Fluids on Carbonate Core Plugs. Presented at SPE Annual Technical Conference and Exhibition, New Orleans, Louisiana, 30 September – 3 October. SPE-71496-MS.

TANNER, C. S. & BAXLEY, P. T. 1992. Production Performance of the Wasson Denver Unit CO_2 Flood. Presented at SPE/DOE Eight Symposium on Enhanced Oil Recovery, Tulsa, Oklahoma, 22 – 24 April. SPE-24156.

TAKENOUCHI, S. & KENNEDY, G. C. 1964. The binary system H2O–CO2 at high temperatures and pressures. *Am. J. Sci.*, 262, 1055– 1074.

TAKENOUCHI, S. & KENNEDY, G. C. 1965. The solubility of carbon dioxide in NaCl solutions at high temperatures and pressures. *Am. J. Sci.*, 263, 445–454.

TEMPLETON, C.C., 1960. Solubility of barium sulfate in sodium chloride solutions from 25°C to 95°C. *J. Chem. Eng. Data*, 5, 514–516.

TONG, D., TRUSLER, J. P. M. & VEGA-MAZA, D. 2013. Solubility of CO2 in aqueous solutions of CaCl2 or MgCl2 and in a synthetic formation brine at temperatures up to 423 K and pressures up to 40 Mpa. *Journal of Chemical and Engineering Data*, 58, 7, 2116–2124.

TRUESDELL, A. H. & JONES, B. F., 1969. Ion association in natural brines. *Chem. Geol.* 4, 51-62.

TUTOLO, B. M., KONG, X. Z., SEYFIRED, W. E. & SAAR, M. O. 2015. High performance reactive transport simulations examining the effects of thermal, hydraulic, and chemical (THC) gradients on fluid injectivity at carbonate CCUS reservoir scales, *Int. J. Greenh. Gas Control*, 39, 285-301. doi:10.1016/j.ijggc.2015.05.026.

UCHAMEYSHVILI, N.Y., MALININ, S.D. & KHITAROV, N.I. 1966. Solubility of barite in con- centrated chloride solutions of some metals at elevated temperatures in relation to problems of the genesis of barite deposits. *Geochem. Int.*, 10, 951–963.

VAZQUEZ, O., ROSS, G., JORDAN, M., BASKORO, D. A. A., MACKAY, E., JOHNSON, C., & STRACHAN, A. 2017. Automatic Optimisation of Oilfield Scale Inhibitor Squeeze Treatments Delivered by DSV. Presented at International Symposium on Oilfield Chemistry, 3-5 April, Montgomery, Texas. SPE-184535-MS

WALTER, L.M. & MORSE, J.W. 1984. Reactive surface area of skeletal carbonates during dissolution: effect of grain size. *J. Sediment. Petrol*., 54, 1081–1090.

WELLMAN, T. P., GRIGG, R. B., MCPHERSON, B. J., SVEC, R. K., & LICHTNER, P. C. 2003. Evaluation of CO_2-Brine-Reservoir Rock Interaction with Laboratory Flow Tests and Reactive Transport Modeling. Presented at International Symposium on Oilfield Chemistry, 5-7 February, Houston, Texas. SPE-80228-MS

WIEBE, R. & GADDY, V.L. 1939. The solubility in water of carbon dioxide at 50°C, 75°C, and 100 °C at pressures to 700 atm. *J. Am. Chem. Soc.,* 61, 315– 318.

WIEBE, R. & GADDY, V.L. 1940. The solubility of carbon dioxide in water at various temperatures from 12 to 40°C and at pressures to 500 atm. *J. Am. Chem. Soc.,* 62, 815– 817.

XU, T., SPYCHER, N., SONNENTHAL, E., ZHANG, G., ZHENG, L. & PRUESS, K. 2011. TOUGHREACT Version 2.0: a simulator for subsurface reactive

transport under non-isothermal multiphase flow conditions. *Computers & Geosciences*, 37, 763-774.

ZHAO, H., FEDKIN, M. V., DILMORE, R. M. & LVOV, S. N. 2015. Carbon dioxide solubility in aqueous solutions of sodium chloride at geological conditions: Experimental results at 323.15, 373.15, and 423.15 K and 150 bar and modeling up to 573.15 K and 2000 bar. *Geochim. Cosmochim. Acta,* 149, 165-189.

ZICK, A. A. 1986. A combined condensing/vaporizing mechanism in the displacement of oil by enriched gases. Presented at SPE Annual Technical Conference and Exhibition, 5-8 October, New Orleans, Louisiana. SPE-15493-MS.